

DISSERTATION
SUBMITTED TO THE
COMBINED FACULTIES OF THE NATURAL SCIENCES AND MATHEMATICS
OF THE RUPERTO-CAROLA-UNIVERSITY OF HEIDELBERG, GERMANY
FOR THE DEGREE OF
DOCTOR OF NATURAL SCIENCES

PUT FORWARD BY
DIPLOM-PHYSICIST ANDRÉ MÜLLER
BORN IN: PLAUEN, GERMANY
ORAL EXAMINATION: JUNE 21st, 2012

CHARACTERIZATION OF
HERBIG AE/BE STARS
and
PRIMA FSU-A AS A
FRINGE TRACKER FOR MIDI

REFEREES: PROF. DR. THOMAS HENNING
 PROF. DR. ANDREAS QUIRRENBACH

Dedicated to the European taxpayer.

Zusammenfassung Herbig Ae/Be Sterne sind junge Vorhauptreihensterne mit Massen zwischen 2 und 10 M_{\odot} . Es sind die massereichsten Sterne, die noch eine Vorhauptreihenphase besitzen und damit das Bindeglied zwischen massearmen T Tauri Sternen und massereichen Sternen bilden. Im ersten Teil der Arbeit werden anhand von drei Herbig Ae/Be Sternen deren Charakterisierung mit einer Vielzahl von hochauflösenden Beobachtungsmethoden und anspruchsvollen Auswertungen vorgestellt. Neben der Bestimmung der stellaren Parameter konnten jeweils einzigartige Entdeckungen bei jedem einzelnen Objekt gemacht werden.

HD 144432 konnte als junges hierarchisches Dreifachsystem klassifiziert werden. Die Rotationsperiode von HD 135344B ist mit 3.9 h so kurz, dass dieser Stern kurz vor dem Zerreißen steht. Um den nur vier Millionen Jahre jungen Herbig Stern HD 142527 konnte mittels Spektroskopie im optischen und nahinfraroten Spektralbereich ein massereicher Planet in kurzer Entfernung um diesen Stern nachgewiesen werden.

Der zweite Teil der Arbeit stellt einen neuen Beobachtungsmodus am VLTI vor. Das im mittleren Infrarot arbeitende Interferometer MIDI wird in Kombination mit einem im nahen Infrarot arbeitenden Strahlvereiniger betrieben, der sogenannten PRIMA FSU-A. Letzteres ist in der Lage, die von der Atmosphäre erzeugten Veränderungen in der optischen Wegdifferenz in Echtzeit zu korrigieren. Das führt zu einem stabilisierten interferometrischen Signal in MIDI, was eine gesteigerte Sensitivität zur Folge hat. Der Aufbau, die Datenreduktion und erste Ergebnisse, sowie notwendige Modifikationen für die endgültige Implementierung werden vorgestellt und beschrieben.

Summary Herbig Ae/Be stars are intermediate-mass (2-10 M_{\odot}) pre-main-sequence stars and they are the most massive stars with a pre-main-sequence phase. They are the higher-mass counterparts to the T Tauri stars, hence fill the parameter space between TTSs and high-mass young stars in addressing the question of star formation as a function of mass. In the first part of this work, the characterization of three Herbig Ae/Be stars using several high-resolution observation methods is presented. Besides the determination of various stellar parameters, unique discoveries were made for each object. HD 144432 was discovered to be a hierarchical triple system. The rotation period of HD 135344B is found to be only 3.9 h. It is so short that this star is rotating at or close to the break-up velocity. Around the four million years young Herbig star HD 142527, a massive planet with a semi-major axis of only 0.6 AU was discovered using high-resolution optical and near-infrared spectroscopy.

In the second part of this work, a new observation mode at VLTI is presented. The mid-infrared interferometric instrument MIDI is used with a near-infrared beam-combiner, called PRIMA FSU-A. The latter one enables the correction for changes in the optical path difference caused by Earth's atmosphere in real time. Therefore, the interferometric signal on MIDI is highly stabilized and results in a significant increase of its sensitivity. The setup, the data reduction process with first results, and requirements for the final implementation are presented and described.

Contents

Table of Contents	i
List of Figures	v
List of Tables	ix
1 Introduction and thesis scope	1
2 HD 135344B: A young star has reached its rotational limit	3
2.1 Introduction	4
2.2 Observations and data reduction	4
2.3 Astrophysical parameters of HD 135344B	5
2.3.1 Stellar parameters	6
2.4 Data analysis and results	8
2.4.1 Radial velocity measurements	8
2.4.2 Radial velocity variations	9
2.4.3 Bisector analysis	11
2.4.4 $H\alpha$ measurements	12
2.5 Discussion	19
2.5.1 HD 135344B is rotating close to break-up velocity	19
2.5.2 Possible origins of the observed periodicity	20
2.6 Conclusions	24
2.7 RV_* and $H\alpha$ measurements	25
3 HD 144432: A young triple system	27
3.1 Introduction	28
3.2 Observations and data reduction	29
3.2.1 NACO	29
3.2.2 FEROS	29
3.3 Data analysis and results	30
3.3.1 Imaging	30
3.3.2 Spectral classification of HD 144432 A	30

3.3.3	Spectral classification of HD 144432 B and C	33
3.3.4	Signatures of youth in HD 144432 B and C	36
3.4	Discussion and conclusions	36
4	A massive planet inside the disk of the Herbig star HD 142527	39
4.1	Introduction	40
4.2	HD 142527: a young star-disk system	41
4.2.1	Disk properties	41
4.2.2	Stellar parameters	42
4.3	Observations and data reduction	43
4.3.1	FEROS	43
4.3.2	HARPS	44
4.3.3	CRIRES	45
4.4	Data analysis and results	45
4.4.1	Optical <i>RV</i> measurements	45
4.4.2	NIR <i>RV</i> measurements	46
4.4.3	Radial velocity variations	47
4.4.4	Orbital parameters	51
4.4.5	Stellar rotation period: <i>Hipparcos</i> photometry	55
4.5	Accretion tracers	55
4.5.1	Line profiles and variance	57
4.5.2	Velocity correlation matrices	58
4.5.3	Residual line profiles and temporal variations	60
4.6	Discussion	66
4.6.1	Planet or brown dwarf?	66
4.6.2	Properties of HD 142527 b	67
4.6.3	Magnetospheric accretion?	68
4.6.4	Gas-disk simulation	69
4.7	Conclusions	71
5	PRIMA FSU-A as a Fringe Tracker for MIDI	73
5.1	Introduction	74
5.1.1	MIDI	74
5.1.2	PRIMA FSU	76
5.1.3	MIDI + PRIMA FSU-A	79
5.2	Observations	81
5.2.1	Observing sequence	86
5.2.2	Estimation of visibility	89
5.3	Data reduction	90
5.3.1	Reduction using EWS	90

5.3.2	Reduction of MIDI + PRIMA FSU-A data	91
5.4	Calibration	96
5.4.1	Construction of the Transfer Function	96
5.4.2	Calibration of $F_{\text{corr, raw}}$	96
5.5	Results	98
5.5.1	Comparison between <i>EWS</i> and <i>Koresko</i>	98
5.5.2	Calibrated correlated N -band fluxes	101
5.5.3	Correlations	108
5.6	Requirements for implementation at VLTI	112
5.6.1	IRIS	112
5.6.2	MIDI	112
5.6.3	PRIMA FSU-A	115
5.6.4	Observing Template and Observing Sequence	115
5.6.5	Generated Files	116
5.7	Discussion and conclusions	116
6	Outlook	119
	Abbreviations	121
	Bibliography	123
A	HD 142527 - Radial velocity measurements	131
B	HD 142527 - Line profiles	133
C	HD 142527 - Circumstellar components	145
D	Simulation of velocity correlation matrices	157

List of Figures

2.1	A pictographic sketch of the HD 135344B system	7
2.2	The spectral windows used for fitting the synthetic spectrum	8
2.3	The position of HD 135344B in an H-R diagram	9
2.4	Measured RVs for HD 135344B	10
2.5	GLS periodogram and window function of RV data of HD 135344B	12
2.6	Close-up view of the GLS	13
2.7	Close-up views of the window function	14
2.8	Phase-folded plot of the RV_{\star} data	15
2.9	GLS periodogram of the residual RV_{\star} data	15
2.10	Bisector quantities versus RV_{\star}	16
2.11	H α line profiles of HD 135344B	17
2.12	Phase-folded plot of the $W_{10}(H\alpha)$ data	18
2.13	Dark spot model	22
2.14	Hot spot model	23
3.1	NACO image of HD 144432	31
3.2	The spectral windows used for fitting the synthetic spectrum	32
3.3	The position of the A, B, and C components of HD 144432 in an HRD	33
3.4	Combined synthetic spectrum of components A, B, and C	35
3.5	Li I line at 6708 Å	37
4.1	The spectral windows used for fitting the synthetic spectrum	43
4.2	The position of HD 142527 in an H-R diagram	44
4.3	Measured RVs for HD 142527	47
4.4	GLS periodogram and window function of RV data of HD 142527	48
4.5	Close-up view of the window function	49
4.6	Close-up view of the GLS	50
4.7	CLEANed amplitude spectrum of all RV data	51
4.8	Kepler fit to optical RV data	52
4.9	Kepler fit to NIR RV data	53
4.10	Final Kepler fit	54

4.11	GLS periodogram of the RV residuals	54
4.12	GLS periodogram of Hipparcos data	56
4.13	CLEANed amplitude spectrum of Hipparcos data	56
4.14	Phase-folded Hipparcos data	57
4.15	Average line profiles	59
4.16	Velocity correlation matrices	61
4.17	CLEANed amplitude spectrum of EW_{CSC}	64
4.18	CLEANed amplitude spectrum of simulated EW_{CSC}	65
4.19	A pictographic sketch of the HD 142527 system	67
4.20	Gas-disk simulation	70
4.21	Age distribution of all exoplanet host stars	72
5.1	The MIDI instrument	75
5.2	Schematic optical layout of MIDI	76
5.3	Schematic optical layout of PRIMA FSU	77
5.4	ABCD algorithm	78
5.5	VLT laboratory configuration	80
5.6	MIDI + PRIMA FSU-A first light	80
5.7	Fringe scan of β Pic	87
5.8	Close-up view of the detected fringe from the scan	88
5.9	SNR fit	89
5.10	Phase unwrapping HD1014 (perfect case)	94
5.11	Phase unwrapping HD1014	95
5.12	Transfer functions	97
5.13	Measured and predicted GD and DISP	99
5.14	Calibrated correlated N -band fluxes	102
5.15	FSU-A GD correlation plots	109
5.16	FSU-A PD correlation plots	110
5.17	FSU-A LR correlation plots	111
5.18	Modified MIDI RTD	113
B.1	Ca II H line profiles	134
B.2	Ca II K line profiles	135
B.3	H α line profiles	136
B.4	H β line profiles	137
B.5	H γ line profiles	138
B.6	H δ line profiles	139
B.7	He I line profiles	140
B.8	Na I D line profiles	141
B.9	Ca II λ 8498 line profiles	142

B.10 Ca II λ 8662 line profiles	143
C.1 Ca II H CSC	146
C.2 Ca II K CSC	147
C.3 H α CSC	148
C.4 H β CSC	149
C.5 H γ CSC	150
C.6 H δ CSC	151
C.7 He I CSC	152
C.8 Na I D CSC	153
C.9 Ca II λ 8498 CSC	154
C.10 Ca II λ 8662 CSC	155
D.1 Velocity correlation matrix case 1	158
D.2 Velocity correlation matrix case 2	159
D.3 Velocity correlation matrix case 3	160
D.4 Velocity correlation matrix case 4	161
D.5 Velocity correlation matrix case 5	162
D.6 Velocity correlation matrix case 6	163
D.7 Velocity correlation matrix case 7	164
D.8 Velocity correlation matrix case 8	165
D.9 Velocity correlation matrix case 9	166

List of Tables

2.1	Stellar parameters of HD 135344B	7
2.2	Results of the sinusoidal fit to the RV_{\star} data	11
2.3	Measured RV_{\star} , $EW(H\alpha)$, and $W_{10}(H\alpha)$	25
3.1	Relative astrometric measurements of HD 144432	30
3.2	Stellar parameters of HD 144432 A, B, and C	32
4.1	Stellar parameters of HD 142527	42
4.2	Sampling and alias frequencies	50
4.3	Orbital parameters of HD 142527 b	53
5.1	List of targets	83
5.2	Overview of the observations	84
5.3	NULL values	92
5.4	Fringe track performance and used MIDI frames	99
5.5	FITS keyword parameters	114

Chapter 1

Introduction and thesis scope

Herbig Ae/Be (HAeBe) stars (Herbig 1960; Finkenzeller & Mundt 1984; Waters & Waelkens 1998) are intermediate-mass ($2-10 M_{\odot}$) pre-main-sequence stars. They are believed to be higher-mass counterparts to the T Tauri stars (TTS), hence fill the parameter space between TTSs and high-mass young stars in addressing the question of star formation as a function of mass (Appenzeller 1994). In addition, HAeBe are the most massive stars with a visible pre-main-sequence phase.

The **stellar parameters** of HAeBe stars are poorly determined and are only available for a small number of stars. This lack of knowledge makes it very difficult to understand the systematic dependencies behind the large variety of observational properties and thus hampers our understanding of the physical mechanisms that distinguish high- from low-mass star formation. The accurate knowledge of stellar parameters is crucial for understanding the structure and evolution of their circumstellar disks where the formation of planets occurs. I have developed tools, which allow the fit of synthetic spectra to the observed spectra and derive fundamental parameters such as metallicity, effective temperature, surface gravity, and projected rotational velocity. This parameter set allows the determination of the most fundamental parameter, the stellar mass, which is crucial for understanding the formation and evolution of stars. In addition, these spectra enable the measurement of stellar accretion rates and ages of HAeBe stars. The projected rotational velocity, $v \sin i$, of these objects is significantly higher (Davis et al. 1983; Finkenzeller 1985; Boehm & Catala 1995) than that of TTSs (Weise et al. 2010) because of the missing strong magnetic fields, which break down the rotation of the star due to star-disk locking mechanisms. The evolution of $v \sin i$ depending on the mass and age of a HAeBe star is still unknown. With the spectroscopic tools I have developed, all parameters can be determined and will provide a global picture for HAeBe stars.

The developed tools and present data set allow the determination of the stellar parameters for most of the HAeBe stars, which can be also used to validate or falsify the evolutionary status of HAeBe candidates listed in the literature.

Double or **multiple stellar systems** are of great interest with respect to star formation theories, as they provide constraints for star formation models, such as fragmentation, accretion, N-body dynamics, and orbit migration (e.g. Tokovinin 2008, and references therein). One very interesting aspect of unequal mass binary systems is that the lower-mass companions allow for much more robust and precise age determination than would be possible on the Herbig stars themselves, thus constraining the system age under the reasonable assumption of co-eval formation. Hence, such systems, once identified, provide the unique opportunity to measure ages of HAeBe stars. Although several imaging surveys have indicated that HAeBe stars have close companions (e.g. Leinert et al. 1997; Pirzkal et al. 1997; Kouwenhoven et al. 2005), there are relatively few studies constraining the physical properties of such companions.

The discovery of **extrasolar planets** is one of the greatest scientific and philosophical achievements of our time and offers for the first time in human history a perspective to understand the role of mankind in the universe. While we already have a good census of planetary systems around solar type stars from large surveys carried out by, e.g. HARPS and *Kepler* (e.g. Howard et al. 2011; Mayor et al. 2011), we currently do not know up to what stellar mass stars can form planets. Due to strong stellar winds and radiation pressure originating from high-massive stars, the lifetime of a circumstellar disk around such a star is too short to enable planet formation. In contradiction, planet formation around TTSs is expected to be frequent. The transition, where planet formation occurs, is expected to be in the intermediate-mass regime, i.e. in the parameter space of HAeBe stars. The detection of extrasolar planets around HAeBe stars is a challenging topic. High projected rotational velocities, stellar activity, and ongoing accretion make the discovery of sub-stellar objects around these objects especially difficult.

The circumstellar disks of several objects, HAeBe stars as well as TTSs, show large gaps at radial distances $\gtrsim 30$ AU that cannot be explained by processes like photo-evaporation and grain growth but are likely caused by disk clearing due to forming giant planets (e.g. Verhoeff et al. 2011). In addition, discovering such systems are of high interest, as they provide the strongest constraint on the time available to form and migrate planets. The combined usage of high-resolution optical (e.g. FEROS, HARPS, and ESPRESSO in the near future) and near-infrared spectrographs (e.g. CRIFES with gas cell) are mandatory to distinguish between periodic RV signals, which can be caused either by a planetary companion or strong stellar activity.

More detailed explanations on the different subjects are provided in the individual chapters. In this thesis we will address these issues on three individual HAeBe stars in detail (Chapter 2 to 4) using data gathered with state of the art instruments, including high-angular resolution imaging and high-resolution optical and near-infrared spectroscopy methods. The second part of this thesis (Chapter 5) is instrumental related and presents a new interferometric observing mode at VLTI where a *K*-band fringe tracker (PRIMA FSU-A) is used to stabilize the interferometric signal on the Mid-infrared Interferometric instrument (MIDI).

Chapter 2

HD 135344B: A young star has reached its rotational limit

Abstract We search for periodic variations in the radial velocity of the young Herbig star HD 135344B to determine a rotation period.

We analyze 44 high-resolution optical spectra taken over a time period of 151 days. The spectra were acquired with FEROS at the 2.2m MPG/ESO telescope in La Silla. The stellar parameters of HD 135344B are determined by fitting synthetic spectra to the stellar spectrum. To obtain radial velocity measurements, the stellar spectra are cross-correlated with a theoretical template computed from determined stellar parameters.

We report the first direct measurement of the rotation period of a Herbig star from radial velocity measurements. The rotation period is found to be 0.16 d (3.9 h), which makes HD 135344B a rapid rotator at or close to its break-up velocity. The rapid rotation could explain some of the properties of the circumstellar environment of HD 135344B such as an inner disk with properties (composition, inclination) that differ significantly from the outer disk.

adapted from Müller, A., van den Ancker, M. E., Launhardt, R., Pott, J. U., Fedele, D., and Henning, Th., 2011, A&A, 530, A85

2.1 Introduction

Herbig Ae/Be (HAeBe) stars (Herbig 1960; Finkenzeller & Mundt 1984; Waters & Waelkens 1998) are intermediate-mass (2-10 M_{\odot}) pre-main-sequence stars. They are believed to be higher-mass counterparts to the T Tauri stars (TTS), hence fill the parameter space between TTSs and high-mass young stars in addressing the question of star formation as a function of mass (Appenzeller 1994).

Stellar rotation is a crucial parameter in the evolution of angular momentum, magnetic fields, and accretion processes. It is known that HAeBe stars exhibit significantly larger projected rotational velocities, $v \sin i$, than TTSs. Typical $v \sin i$ values for HAeBe stars are in the range from 60 to 225 km s^{-1} (Davis et al. 1983; Finkenzeller 1985; Boehm & Catala 1995), whereas most TTSs have $v \sin i$ values of about 10 km s^{-1} (e.g. Weise et al. 2010). This result indicates that mechanisms of angular momentum dispersal are much less efficient in HAeBe stars than in TTSs (Boehm & Catala 1995). Star-disk locking and subsequent rotational braking might even be absent in HAeBe stars. Only for low-mass HAeBe stars ($M \leq 2.6 M_{\odot}$) did Boehm & Catala (1995) find indications of a loss of angular momentum due to stellar winds.

However, no extensive study to determine the rotation periods of HAeBe stars has yet been presented. Only for a few HAeBe stars, rotation periods have so far been found. Observed variations of Ca II K and Mg II h and k of AB Aur were interpreted as rotational modulation (e.g. Praderie et al. 1986; Catala et al. 1986). Hubrig et al. (2011) detected a rotationally modulated magnetic field of the HAeBe star HD 101412. In this work, we determine the rotation period of the Herbig star HD 135344B by measuring radial velocity variations using multi-epoch high resolution optical spectra.

The chapter is organized as follows. Section 2.2 presents the observations and data reduction. The determination of the stellar parameters and the radial velocity measurements are presented in Sects. 2.3 and 2.4. A discussion of the results and conclusions can be found in Sects. 2.5 and 2.6. The Appendix provides a table of measured quantities.

2.2 Observations and data reduction

The observations were carried out in two observing campaigns with the Fiber-fed Extended Range Optical Spectrograph (FEROS; Kaufer et al. 1999) at the 2.2m MPG/ESO telescope at La Silla Observatory in Chile. FEROS covers the whole optical spectral range from 3600 Å to 9200 Å and provides a spectral resolution of $\approx 48\,000$. The fibre aperture of FEROS is 2 arcsec on the sky. A contamination of the spectra due to other stars around HD 135344B can thus be ruled out (Sec. 2.3). In total, 44 spectra of HD 135344B were obtained over a time range of five months between March and July 2010. Depending on the conditions, we observed the star up to four times a night with a separation of two hours between the observations. The average exposure time was 16 minutes per spectrum, which results in an average signal-to-noise ratio

(SNR) of 230 at 5500 Å for our spectroscopic data set. A set of 40 spectra were obtained using the object-calibration mode where one of the two fibers is positioned on the target star and the other fiber is fed with the light of a ThAr+Ne calibration lamp. This mode allows us to monitor and correct for the intrinsic velocity drift of the instrument. An additional four spectra were obtained using the object-sky mode where the second fiber points to the sky, allowing the subtraction of the sky background from the target spectrum. The reduction of the raw data was performed using the online data reduction pipeline available at the telescope¹. The pipeline does the bias subtraction, flat-fielding, traces and extracts the single echelle orders, applies the wavelength calibration, and corrects for the barycentric motion. For each exposure, it produces 39 individual sub-spectra representing the individual echelle orders, as well as one merged spectrum.

2.3 Astrophysical parameters of HD 135344B

HD 135344B (SAO 206462) belongs to the Sco OB2-3 (Upper Centaurus Lupus, UCL) star-forming region, whose center is at a distance of 140 ± 2 pc (de Zeeuw et al. 1999).

Preibisch & Mamajek (2008) also list the individual distances of 81 group members. The median and standard deviation of these values indicate that the distance is 142 ± 27 pc. This spread reflects the true extent of Sco OB2-3, rather than observational errors in distances to individual stars. We thus adopt a value of 142 ± 27 pc for the distance of HD 135344B in the following.

HD 135344B is the secondary star of the visual binary system of HD 135344 (SAO 206463). The two components are separated by $21''$ (PA= 197° , Mason et al. 2001), which translates into a projected separation of 3000 ± 600 AU for the given distance of 142 ± 27 pc. Therefore, a gravitational interaction between the primary and the disk of HD 135344B can be ruled out for this large separation. Using the HST/NICMOS2 camera at $\lambda = 1.6 \mu\text{m}$, Augereau et al. (2001) found a close binary system lying $5.8''$ from HD 135344B. A companionship was ruled out by the detection of different proper motions by Grady et al. (2009), who used the same instrument.

The disk around HD 135344B has been the subject of numerous studies carried out over a large wavelength range using imaging, spectroscopy, and interferometry (e.g., Thi et al. 2001; Dent et al. 2005; Doucet et al. 2006; Brown et al. 2007; Fedele et al. 2008; Pontoppidan et al. 2008; Grady et al. 2009; Verhoeff et al. 2010) that have identified a complex structure. An outer radius of 200 AU for the dusty disk was derived by Doucet et al. (2006) at $20.5 \mu\text{m}$. By modeling the Spitzer spectrum, Brown et al. (2007) found a gap in the dusty disk between 0.45 AU and 45 AU. We should note that Brown et al. (2007) do not resolve the inner disk but estimate the location of the inner rim of the gap based on potentially ambiguous SED model fits. This agrees with the mid-IR observations of Verhoeff et al. (2010). One explanation of a gap in the

¹<http://www.eso.org/sci/facilities/lasilla/instruments/feros/>

disk, besides grain growth and photo-evaporation, is that a (sub-)stellar companion has formed causing a dynamical clearing. Pontoppidan et al. (2008) rule out the presence of a stellar companion around HD 135344B based on their detection of molecular CO gas ($\lambda = 4.7 \mu\text{m}$) at 0.3–15 AU.

The value of the disk inclination derived from different observations at different wavelengths varies from 11° to 61° (Dent et al. 2005; Doucet et al. 2006; Fedele et al. 2008; Pontoppidan et al. 2008; Grady et al. 2009). We note, however, that different methods probe different spatial scales in the disk. Therefore, these different values may not contradict each other but may reflect the presence of a more complex morphology than assumed in the simple symmetric models from which these values are derived. Grady et al. (2009) ruled out inclinations greater than 20° for the outer disk, which is in good agreement with the value of $11^\circ \pm 2^\circ$ measured by Dent et al. (2005). Therefore, the outer disk is seen almost face-on as it is already indicated by direct imaging (Doucet et al. 2006; Grady et al. 2009). Interferometric N-band observations of the inner part of the star-disk system identified a much higher inclined (53° – 61°) structure with an estimated inner radius of about 0.05 AU and an outer radius of 1.8 AU (Fedele et al. 2008).

The disk of HD 135344B contains $(2.8 \pm 1.3) \cdot 10^{-3} M_\odot$ of gas and dust (Thi et al. 2001). The detection of polycyclic aromatic hydrocarbon (PAH) features (e.g. Coulson & Walther 1995; Brown et al. 2007; Fedele et al. 2008) implies that there is rich chemistry in the vicinity of the star. From J=3-2 ^{12}CO measurements, Dent et al. (2005) derived an inner radius of ≤ 10 AU and 75 ± 5 AU for the outer radius where emitting gas is present.

HD 135344B also displays signs of active mass accretion. This matches the findings of Pott et al. (2010), who studied young transitional disk systems with a gap in the circumstellar dust distribution, similar to HD 135344B (Fig. 2.1). They systematically found sub-AU scale dust in accreting transitional disk systems. Garcia Lopez et al. (2006) derived a value for the mass accretion rate of $\dot{M}_{acc} \approx 5.4 \cdot 10^{-9} M_\odot \text{yr}^{-1}$ using the Br γ emission line in the NIR. From FUV data, Grady et al. (2009) concluded that HD 135344B drives no jet, but found indications of a stellar wind leading to a mass-loss rate between 10^{-11} and $10^{-8} M_\odot \text{yr}^{-1}$.

On the basis of all previous observations, the disk can be assumed to contain dust within an inner ring from 0.05 AU to 1.8 AU. This structure is highly inclined relative to the outer disk. There is evidence of mass accretion from the inner disk onto the star. Between 1.8 AU and 45 AU, a large gap is present. At 45 AU, the outer disk, seen almost pole-on, begins extending to about 200 AU. We refer to Figure 2.1 for a pictographic sketch.

2.3.1 Stellar parameters

Table 2.1 lists the derived stellar parameters of HD 135344B. The luminosity, L_\star , was computed by integrating the total flux under the SED. The parameters T_{eff} , $\log g$, and $v \sin i_\star$ were computed using a self-developed tool for retrieving stellar parameters of Herbig stars based on

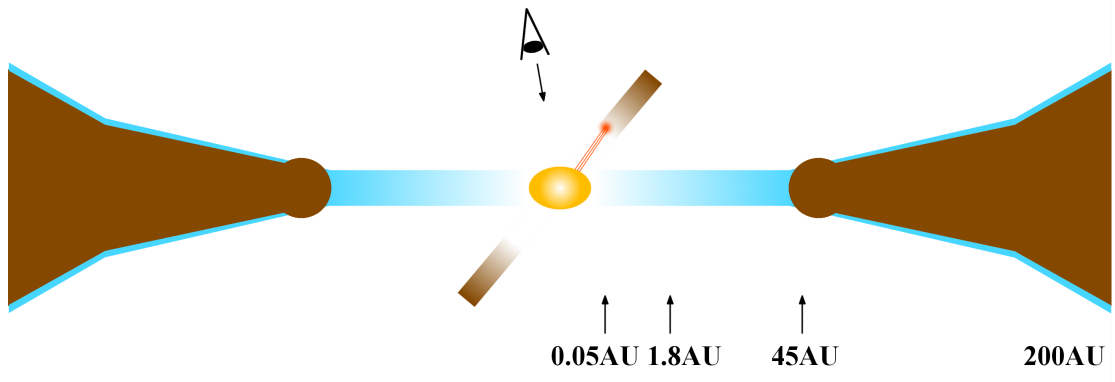


Figure 2.1: A pictographic sketch of the HD 135344B system. The star, the dusty disk (brown color) with its large inner gap, the gaseous disk (blue), and an hot spot emerging from the inner rim of the inner disk caused by active accretion (red) are shown.

fitting synthetic spectra to the observed stellar spectrum. The computation of the synthetic spectrum was carried out using SPECTRUM² (Gray & Corbally 1994) with the ATLAS9 atmosphere models (Castelli & Kurucz 2004). Figure 2.2 shows a part of a stellar spectrum of HD 135344B (black line, observed at JD=2455347.63521) that is well fitted by a single star synthetic spectrum (red line).

From the position of HD 135344B in the H-R diagram (Fig. 2.3), we derived its stellar mass, radius, and age. The derived parameters are in close agreement with literature values, e.g., van der Plas et al. (2008), Manoj et al. (2006), van Boekel et al. (2005), and Dunkin et al. (1997). The measured effective temperature is comparable to that of an F3Ve to F4Ve main-sequence star and agrees with the value found by Dunkin et al. (1997).

Table 2.1: Stellar parameters of HD 135344B.

Parameter	Value
<i>distance</i>	142 ± 27 pc
$\log L_{\star}$	$1.02^{+0.18}_{-0.10} L_{\odot}$
T_{eff}	6810 ± 80 K
$\log g$	4.4 ± 0.1 cm s ⁻²
M_{\star}	$1.7^{+0.2}_{-0.1} M_{\odot}$
<i>age</i>	9 ± 2 Myr
R_{\star}	$1.4 \pm 0.25 R_{\odot}$
$\langle RV_{\star} \rangle$	2.5 ± 1.5 km s ⁻¹
$v \sin i_{\star}$	82.5 ± 2.9 km s ⁻¹

Notes. $\langle RV_{\star} \rangle$ represents the mean value of the observed RVs. The error does not present the accuracy of the determined RV_{\star} but reflects the scatter in RV_{\star} around the mean value.

²<http://www.phys.appstate.edu/spectrum/spectrum.html>

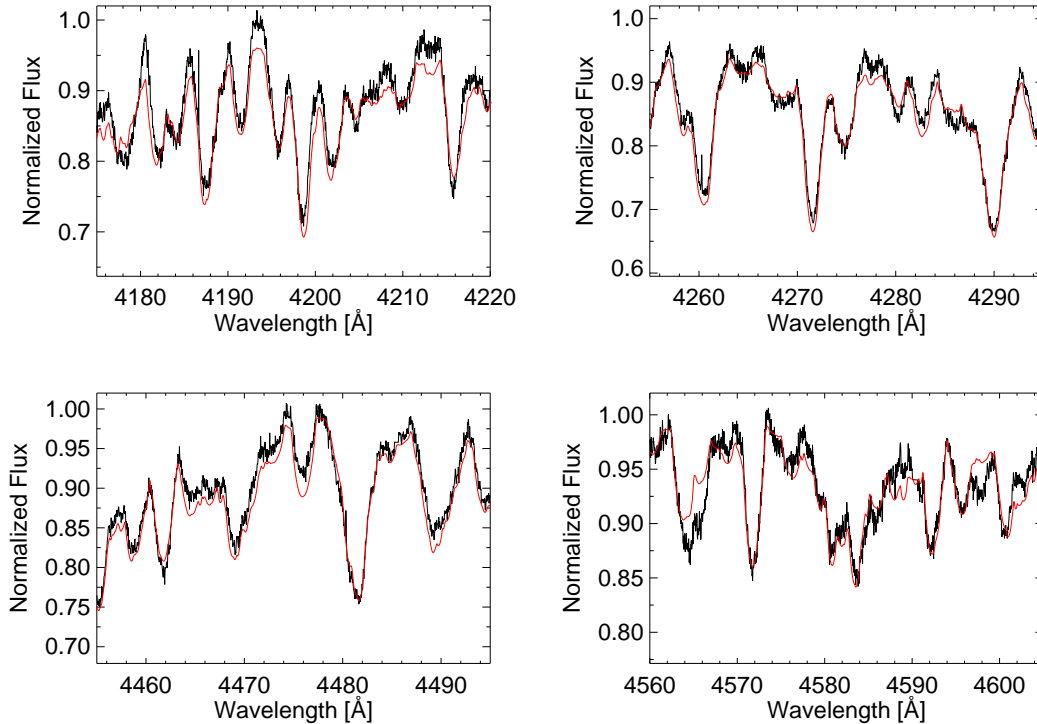


Figure 2.2: The spectral windows used for fitting the synthetic spectrum (red line) to the observed stellar spectrum (black line, JD=2455347.63521) of HD 135344B.

2.4 Data analysis and results

2.4.1 Radial velocity measurements

We measured the stellar RV by cross-correlating the stellar spectrum with a template spectrum. The template was a synthetic spectrum representing the fitted stellar parameters of HD 135344B (Table 2.1). We measured a projected rotational velocity, $v \sin i_*$, of 82.5 km s^{-1} (Sec. 2.3.1). Therefore, all stellar spectral lines are highly broadened and blended, which makes a determination of RV_* difficult because the accuracy is limited to some 100 m s^{-1} . For the cross-correlation, only the spectral range between 4000 \AA to 7875 \AA was considered because the instrument efficiency drops significantly outside this spectral range. In addition, areas with strong emission lines, telluric lines, and Balmer lines were carefully excluded. The resulting cross-correlation function was fitted by a Gaussian function. The position of the center of the Gaussian yields RV_* . After the individual RV_* values were derived separately for each echelle order, the median value and standard deviation of RV_* were computed. We applied to the RV_* values a $1\text{-}\sigma$ clipping to remove anomalous velocity values, similar to e.g. Barnes et al. (2005) and Jeffery et al. (2007). The deficient RV_* estimates, rejected by this σ clipping, do not follow a simple Gaussian noise statistics but are far from the median RV_* , which indicates that there are individual, systematic biases in the RV_* estimate in the rejected orders. The final RV_* were

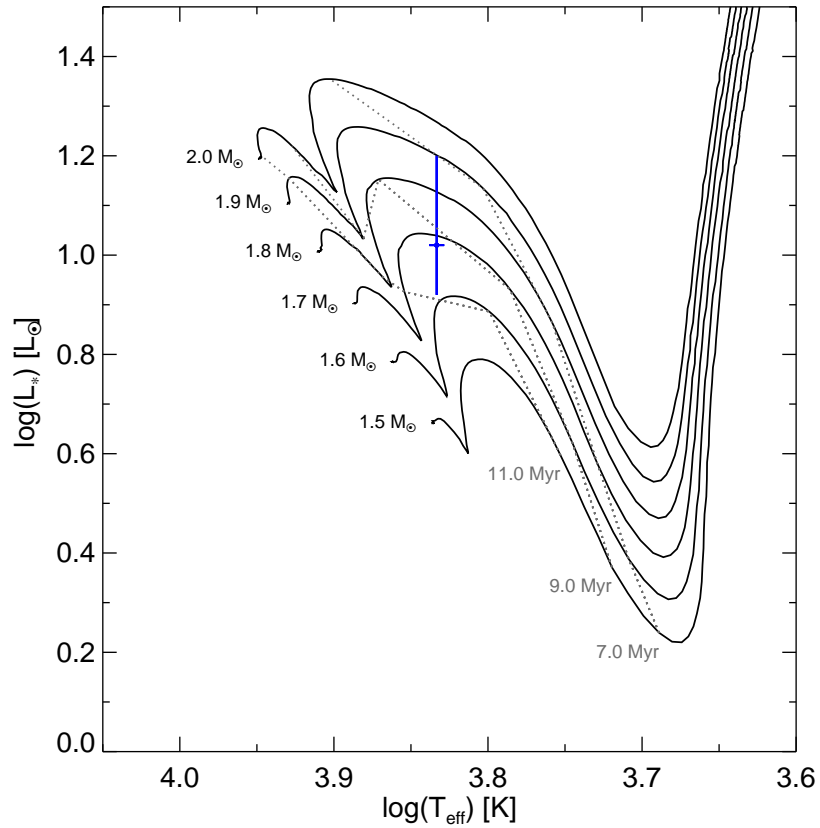


Figure 2.3: The position of HD 135344B in an H-R diagram along with the evolutionary tracks of Siess et al. (2000) for a metal abundance of $Z=0.02$.

then computed based on averaging ten to twelve remaining individual orders. The error in the final RV_* is the standard deviation of the mean. All measured RV_* values are listed in Table 2.3 provided in the appendix. Figure 2.4 shows the measured RVs for all 44 spectra with a mean RV_* value of 2.5 km s^{-1} , indicated by the gray horizontal dashed line. Peak-to-peak variations of up to 2.9 km s^{-1} are present.

2.4.2 Radial velocity variations

To identify periodicities present in the RV_* data, we computed the generalized Lomb-Scargle (GLS) periodogram (Zechmeister & Kürster 2009) and its window function (Fig. 2.5). The GLS exhibits a strong peak at a period of 0.16045 d (in the following, we use 0.16 d), marked by the red arrow. Its false-alarm probability (FAP) is 0.64%. In addition, several other peaks in the GLS are present that are less or not significant compared to the 0.16 d period. This complicates the interpretation of a periodogram. To identify alias frequencies caused by uneven sampled data in time, we have to consider the window function. Significant peaks in the window

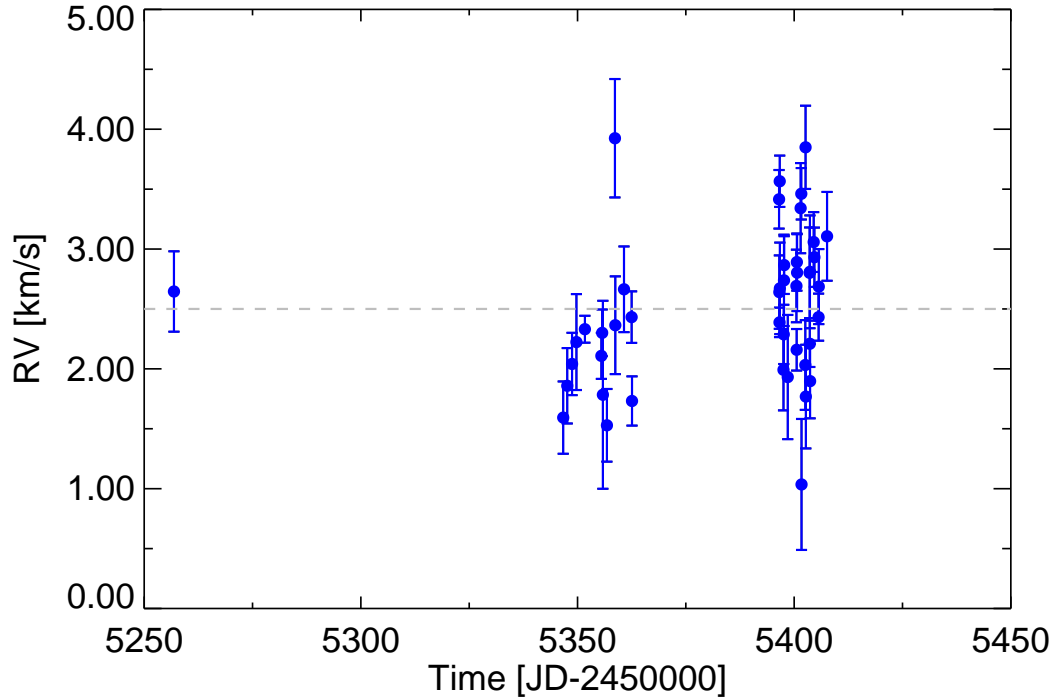


Figure 2.4: Measured RVs for HD 135344B. The horizontal gray dashed line represents the mean value of the measurements.

function can produce aliases in the GLS that are separated from the true peak by the frequency difference. Figure 2.6 shows a close-up view of the GLS, centered on the 0.16 d period (or at the frequency of 6.232 d^{-1} , respectively). The two strongest other but less significant peaks are located at 5.230 d^{-1} and 7.234 d^{-1} . The difference of both frequencies with respect to 6.232 d^{-1} is 1.002 d^{-1} , which corresponds to the sidereal day. Figure 2.7 b) shows a close-up view of the window function centered around the significant frequency 1.0 d^{-1} . The highest peak is at a frequency of 1.002 d^{-1} . We can therefore conclude that the peaks to both the left and right of the 0.16 d period in the GLS are aliases. Each of the three peaks in Fig. 2.6 display side lobes separated by 0.021 d^{-1} for all cases. From the close-up view of the window function (Fig. 2.7 a), we can identify a significant frequency at 0.021 d^{-1} , which is exactly the measured frequency difference between the side lobes of three main peaks. The 0.021 d^{-1} frequency corresponds to a period of about 48 d. By looking at the distribution of observations in Fig. 2.4, we can identify three separate data sets (the first data set consisting of the first single data point only). The time difference between the first and the second data set is about 100 d, and the difference between the second and the third data set is about 50 d. This explains the observed aliases at this frequency difference in the GLS and the presence of a significant peak in the window function. The observations cover a time range of about 150 d. Therefore, the window function (Fig. 2.7 a) shows a significant peak for frequencies smaller than 0.006 d^{-1}

(or periods greater than 150 d respectively), but they are not visible as side lobes of the main peaks in the GLS. In addition, we subtracted a sinusoidal fit from the RV_{\star} data and computed a GLS periodogram of the residuals (Fig. 2.9) to verify that the 0.16 d period is present in the RV_{\star} data. The GLS periodogram of the residuals clearly shows that the peak at 0.16 d as well as its corresponding aliases was removed. There are no additional significant peaks at other periods. From this analysis, we assume that the 0.16 d period is significant and indeed the only real period in the observed RV_{\star} data.

Figure 2.8 shows the phase-folded RV_{\star} data for the 0.16 d period. The solid line represents a sinusoidal fit to the data with a period of $0.16045 \pm 2 \cdot 10^{-5}$ d and an amplitude of 493 ± 86 m s $^{-1}$. The results of the fit are presented in Table 2.2.

Table 2.2: Results of the sinusoidal fit to the RV_{\star} data.

Parameter	Value
χ_{red}^2	2.5
<i>rms</i>	478 m s $^{-1}$
<i>period</i>	$0.16045 \pm 2 \cdot 10^{-5}$ d
<i>amplitude</i>	493 ± 86 m s $^{-1}$
<i>phase</i> (to JD $_{\text{min}}$)	0.95 ± 0.03
<i>offset</i>	2508 ± 61 m s $^{-1}$

2.4.3 Bisector analysis

Stellar activity such as cold and hot spots, granulation, and pulsation can mimic significant RV variations that can be periodic because of stellar rotation. For a cold (i.e. dark) spot, the line profile becomes asymmetric because of the fainter stellar light. Stellar rotation leads to a modulation of the asymmetry and causes RV variations depending on the stellar inclination and latitude of the spot. The analysis of the line profile (in the following bisector) is routinely applied to search for extrasolar planets when the RV technique is used to determine whether the observed periodic RV variations are caused by stellar activity or a companion (e.g. Queloz et al. 2001). A correlation between RV_{\star} and bisector velocity span would indicate that the RV_{\star} variation is caused by line shape asymmetries, i.e. by rotational modulation caused, for example, by a spot. The shape of the computed cross-correlation function (CCF) represents the mean line profile of the selected lines in the observed spectra. We measured the bisector velocity span (BVS), bisector displacement (BVD), and bisector curvature (BC) for all our spectra following the definition of Povich et al. (2001). To construct the bisector, the middle points of the horizontal segments, which connect a point on the left to the right side of the CCF at the same flux level, are computed. The bisector is divided into three zones. The BVS is simply the difference between the upper and lower zones. The BC is defined as the difference between the upper and lower bisector spans. To derive the BVD, we calculate the average of the three bisector velocity zones. To compute the individual quantities, we chose heights of 30%, 50%, and 85% of the

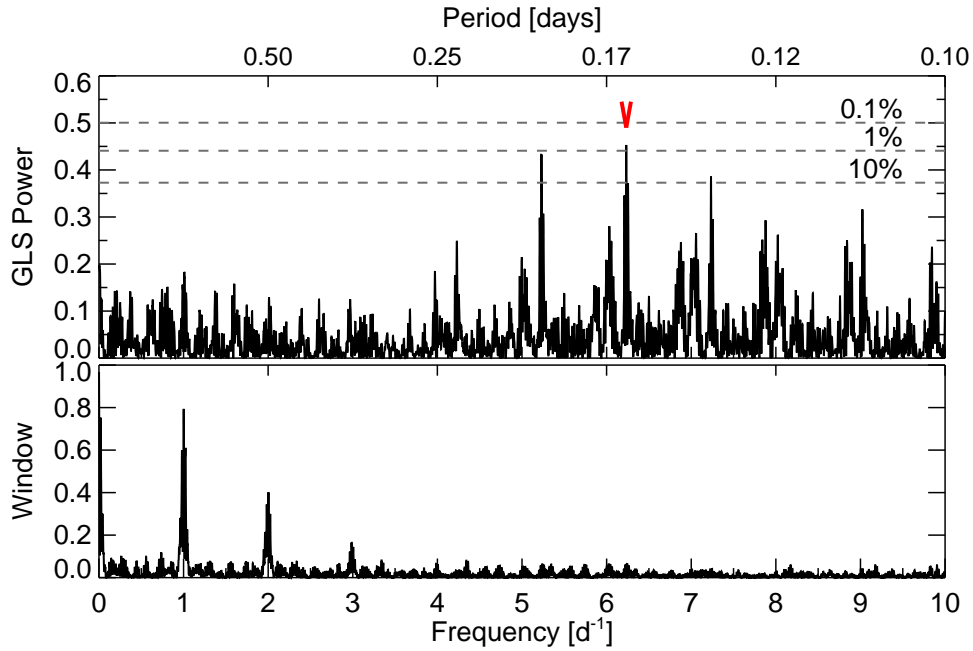


Figure 2.5: GLS periodogram (upper plot) and window function (lower plot) of the RV_* data. The significant period at 0.16 d is marked by the red arrow. FAP thresholds for 0.1%, 1%, and 10% are indicated by the horizontal dashed lines. The data are plotted over frequency but the upper x-axis gives the corresponding period. Note that periods greater than 1 d are in the frequency range between 0 and 1 d⁻¹.

bisector. As for the RV_* measurements, we measured BVS, BVD, and BC for each computed CCF. The final bisector values were derived by averaging the single values. The errors in BVS, BVD, and BC are the standard deviations of the means. In Figure 2.10, we have plotted all three bisector quantities against RV. The computed linear correlation coefficients r are noted in the upper right corner of each plot. We find that there is a significant linear correlation for none of the three quantities. Only a weak trend might be present for BVS and BD. However, the sensitivity of the bisector method decreases rapidly when it comes to low stellar inclinations (e.g. Desort et al. 2007). For HD 135344B, we can assume that we see the star almost pole-on (Sec. 2.5), hence we do not expect there to be a strong correlation between BVS and RV.

2.4.4 H α measurements

The H α line profile of HD 135344B undergoes rapid and significant changes. Finkenzeller & Mundt (1984) classified the H α line profile of HAeBe stars into three categories: single-peak, double-peak, and P Cygni profiles. The H α line profile of HD 135344B adopt each of these types at different times. Figure 2.11 shows the H α line profiles of our spectroscopic data set of HD 135344B ordered with respect to their phase value according to a 5.77 d period. A double-peaked profile corresponds to accretion, whereas a blue-shifted absorption (P Cygni profile) rep-

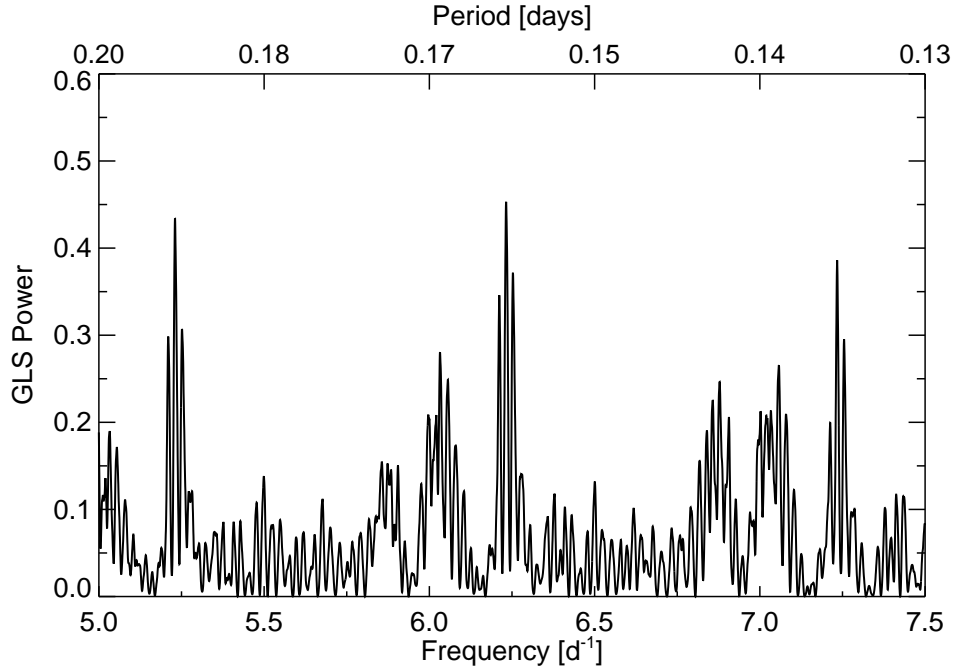


Figure 2.6: Close-up view of the GLS centered around the most significant peak at 0.16 d. Two less significant peaks at 5.230 d^{-1} and 7.234 d^{-1} are present in addition and are aliases caused by the sidereal day. All three peaks show side lobes with a difference of 0.021 d^{-1} in frequency, caused by the uneven sampling of our data.

resents an outflow of material. We measured the equivalent width, $EW(H\alpha)$, of HD 135344B in our FEROS spectra. The measured values are listed in Table 2.3 in the appendix. To measure $EW(H\alpha)$, we selected several distinct wavelength intervals on both sides of the $H\alpha$ line and used a second order polynomial to describe the continuum. This was repeated four times for different intervals. The deviation of all four measurements defines our error. For $EW(H\alpha)$, we obtained a mean value of -10 \AA . We were unable to reliably determine a period from the GLS periodogram of the $EW(H\alpha)$ values.

We also measured the full width of $H\alpha$ at 10% height, $W_{10}(H\alpha)$, which is frequently used for TTSs to distinguish between chromospheric activity and accretion of circumstellar material (White & Basri 2003; Natta et al. 2004; Jayawardhana et al. 2006). We applied the same method to normalize the spectra as for $EW(H\alpha)$. We measured a mean value of 9.8 \AA for $W_{10}(H\alpha)$, which corresponds to an accretion rate of $3 \cdot 10^{-9} \text{ M}_{\odot} \text{ yr}^{-1}$ if Eq. 5 in Natta et al. (2004) is applied. The measured values of $W_{10}(H\alpha)$ are listed in Table 2.3 provided in the appendix. The periodogram of $W_{10}(H\alpha)$ has a significant period at 5.77 d with a FAP of $1.9 \cdot 10^{-6}$. A phase-folded plot for the $W_{10}(H\alpha)$ data (black data points) and the sinusoidal fit (red line) is shown in Fig. 2.12. Assuming Keplerian rotation of the circumstellar gas, this period corresponds to a radial distance of $\approx 0.07 \text{ AU}$. The error bars of $W_{10}(H\alpha)$ are the statistical errors in the single measurements and reflect the precision of the individual measurements. These error

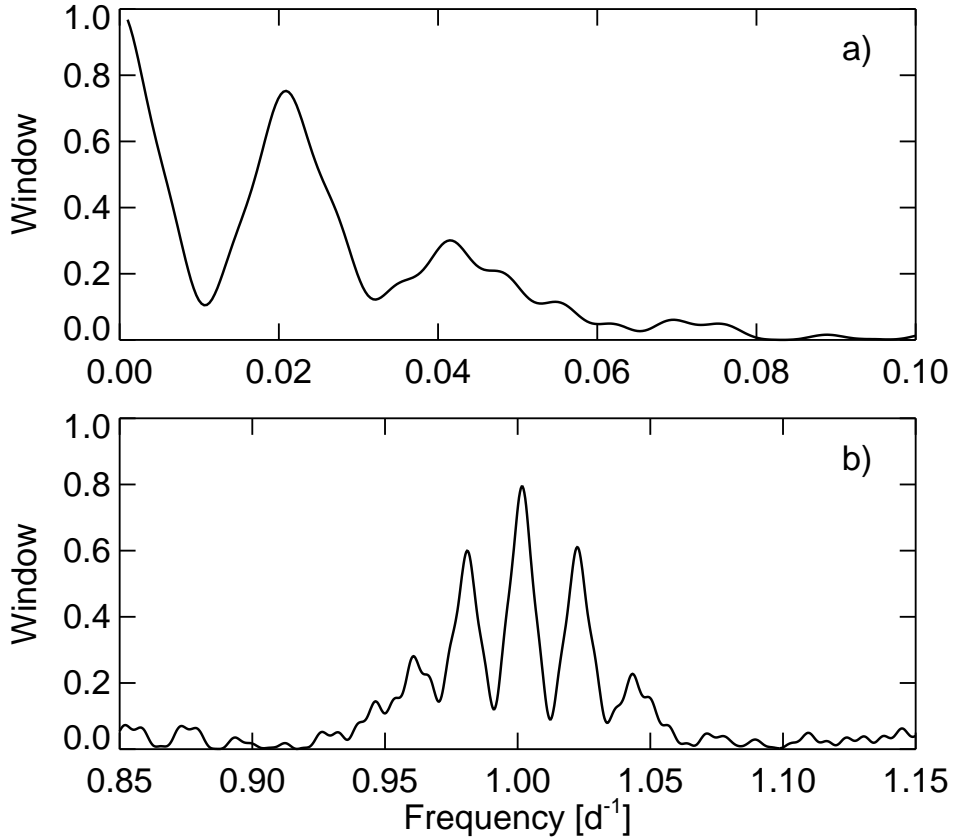


Figure 2.7: Close-up views of the window function for the significant peaks at $<0.006 \text{ d}^{-1}$, 0.021 d^{-1} , and 1.002 d^{-1} .

bars most likely overestimate the accuracy of each measurement, since the distance of the data points to the sinusoidal fit often exceeds the error bars significantly. A possible reason for an accuracy bias in the individual $W_{10}(H\alpha)$ measurements is that the $H\alpha$ line can form at different locations. The formation might also be caused by different processes, e.g. accretion column, accretion shock on the stellar surface, disk surface, and wind. Therefore, we see a significant scatter in the measured $W_{10}(H\alpha)$ values around the sinusoidal fit, the level of which exceeds the precision of the individual measurements. However, the bias in each individual measurement is statistically spread around the fit. We binned the phase in 0.1 wide bins and averaged the $W_{10}(H\alpha)$ values lying in the corresponding bin. The displayed error is the standard deviation of the values in each bin. These values are overplotted in Fig. 2.12 with green triangles. The green error bars now reflect both the precision and accuracy of the $W_{10}(H\alpha)$ measurements and are described well by the sinusoidal fit.

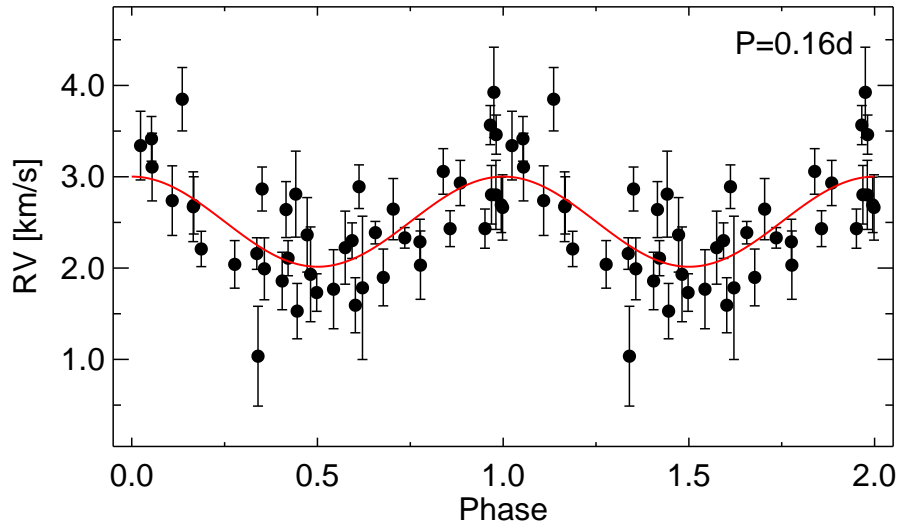


Figure 2.8: Phase-folded plot of the RV_* data. The solid line is a sinusoidal fit with a period of $0.16045 \pm 2 \cdot 10^{-5}$ d and an amplitude of 493 ± 86 m s $^{-1}$.

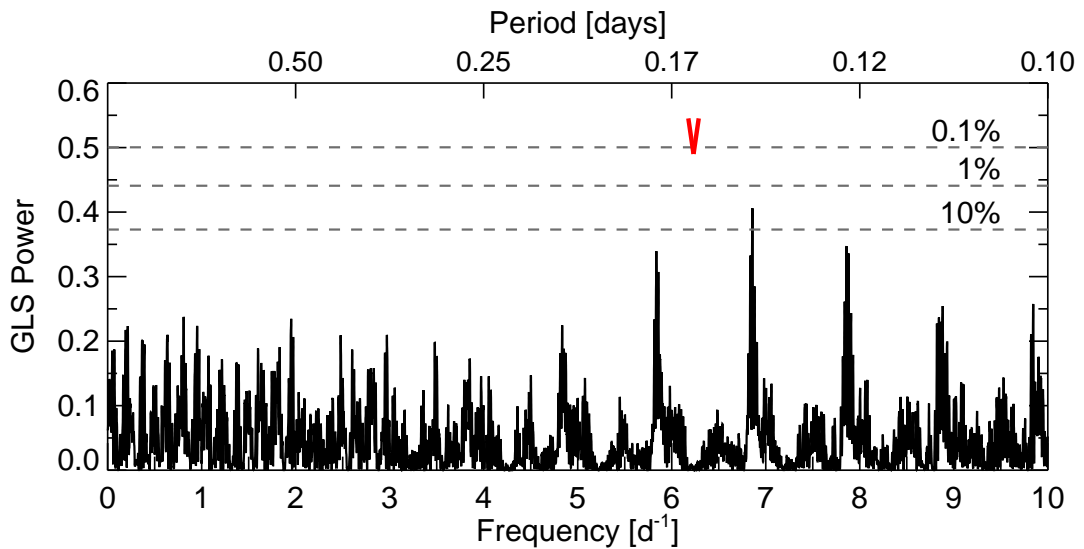


Figure 2.9: GLS periodogram of the residual RV_* data after subtraction of the sinusoidal fit. The red arrow marks the position of the 0.16 d period, which is no longer present, as well as its corresponding aliases. The new peak with the highest power at 0.14 d has a FAP of 3.4% and is therefore insignificant.

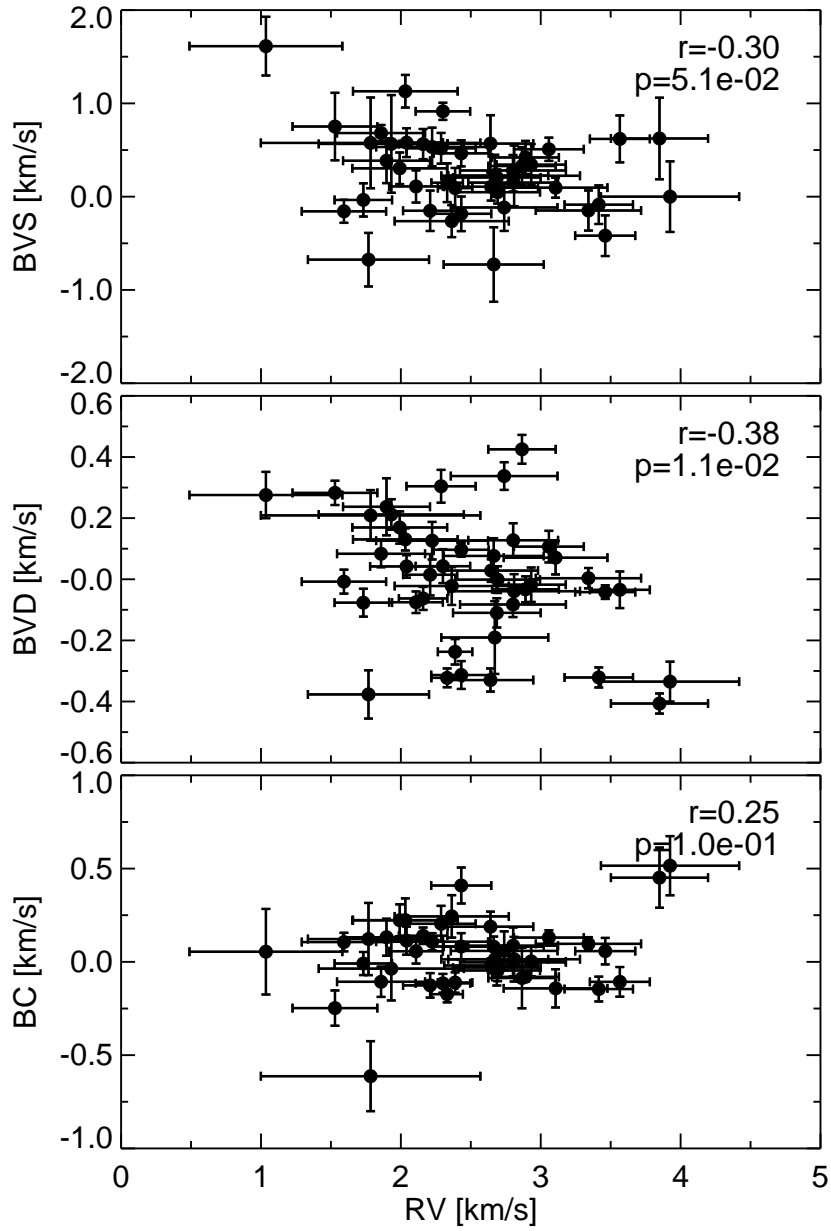


Figure 2.10: Bisector quantities versus RV_{\star} . For each plot, the linear correlation coefficient r and the probability p that the data are linearly uncorrelated are computed (Bevington & Robinson 2003). There is no linear correlation between the bisector quantities and RV_{\star} .

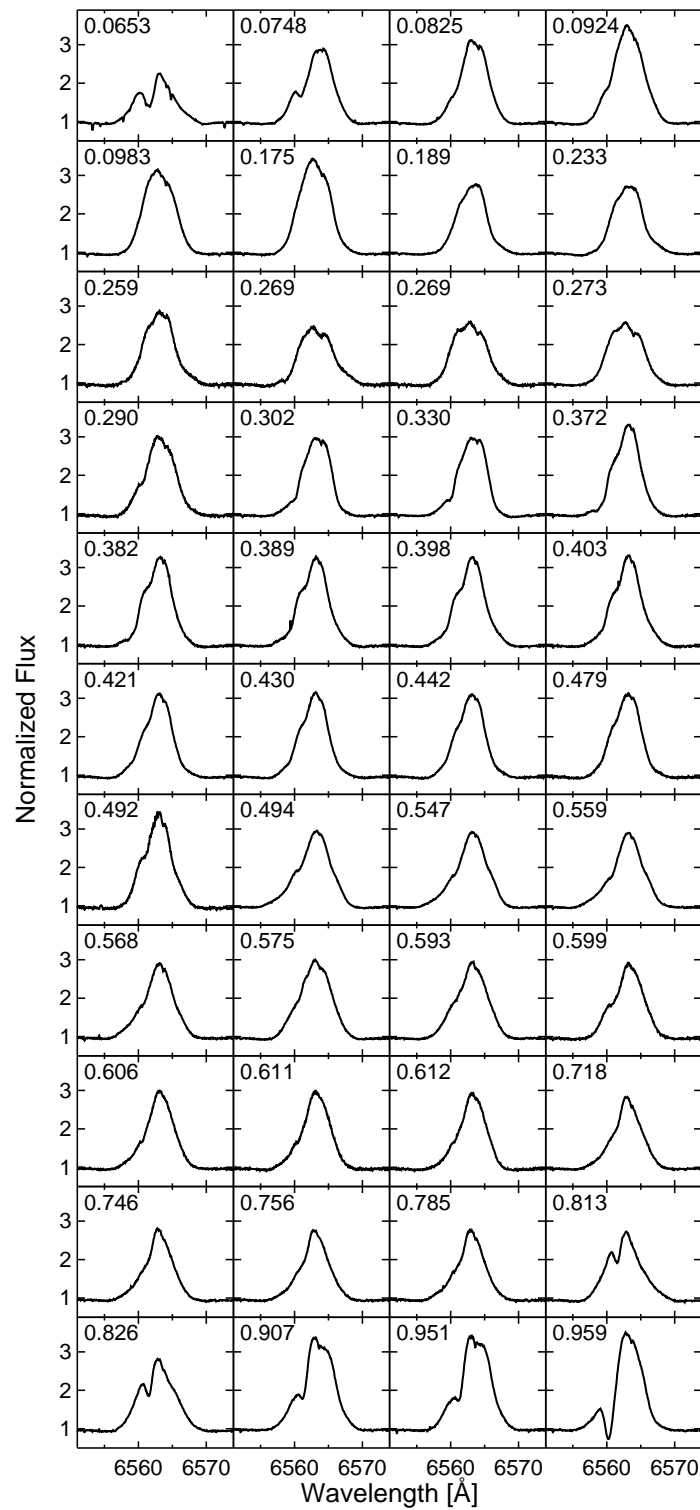


Figure 2.11: $H\alpha$ line profiles of HD 135344B. The plots are ordered with respect to their phase value according to a 5.77 d period, which is shown in the upper left corner of each plot.

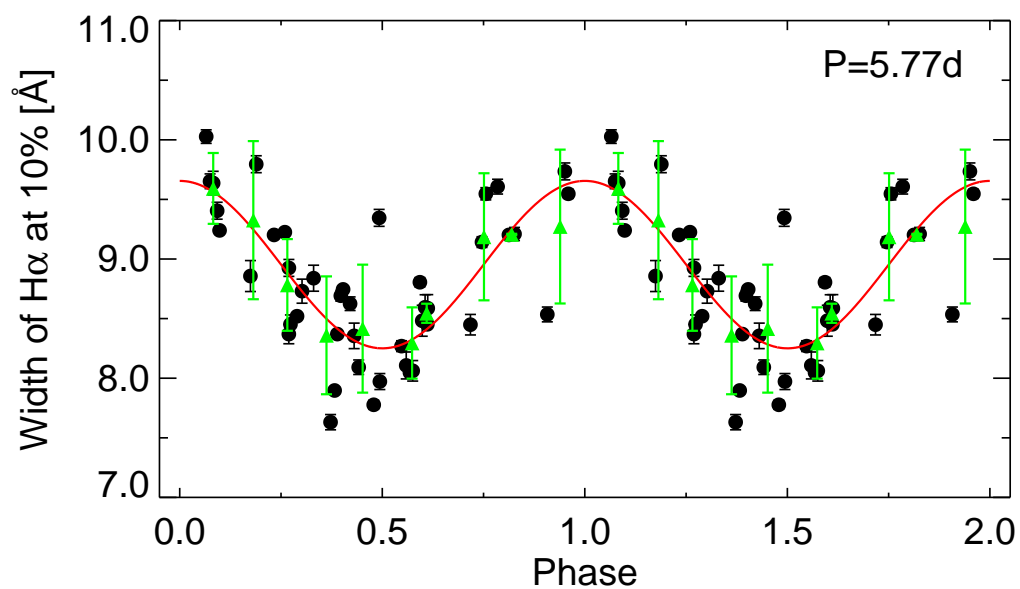


Figure 2.12: Phase-folded plot of the $W_{10}(H\alpha)$ data. The solid line is a sinusoidal fit with a period of 5.77 ± 0.02 d and an amplitude of 0.70 ± 0.08 Å. The green triangles are the average values computed by binning the phase in 0.1 wide bins. Their error bars are derived by computing the standard deviation of the corresponding $W_{10}(H\alpha)$ values in each bin.

2.5 Discussion

The observed 0.16 d period might be caused by the rotational modulation of one or more spot(s) on the stellar surface. Adopting the stellar radius of $1.4 \pm 0.25 R_{\odot}$ and $v \sin i_{\star} = 82.5 \pm 2.9 \text{ km s}^{-1}$ from Table 2.1, the inclination of the stellar rotation axis is $i_{\star} = 11^{\circ} \pm 2^{\circ}$. We thus see the star almost pole-on. This could explain the weak correlation between the BVS and RV_{\star} (Sec. 2.4.3). The disk of HD 135344B is also found to be almost face-on with inclination measurements of $\lesssim 20^{\circ}$ (Grady et al. 2009) and $11^{\circ} \pm 2^{\circ}$ by Dent et al. (2005), i.e., the orientation of the stellar rotation axis, based on the assumption that the 0.16 d RV_{\star} period represents the stellar rotation period, is almost perpendicular to the mid-plane of the outer disk. This supports the hypothesis that the 0.16 d period is caused by photospheric effects.

Another approach to verifying the origin of the 0.16 d period is to apply a Keplerian fit to the data. Under the assumption of a circular orbit (eccentricity is set to 0) and a period of 0.16 d, the semi-major axis is $7 \cdot 10^{-3}$ AU, which corresponds to $1.5 R_{\odot}$. For HD 135344B, we found the stellar radius to be $1.4 \pm 0.25 R_{\odot}$ (Table 2.1), i.e., the semi-major axis to be in the range of the stellar radius. This shows that the companion hypothesis is implausible, thus favors the photospheric interpretation. Thus, the rotational period of 0.16 d or 3.9 hours makes HD 135344B an extremely rapid rotator.

2.5.1 HD 135344B is rotating close to break-up velocity

The break-up velocity $v_c = \sqrt{GM_{\star}/R_{\star}}$ of the star, where G is the gravitational constant, has a value of $480 \pm 60 \text{ km s}^{-1}$. Using the value of $i_{\star} = 11^{\circ} \pm 2^{\circ}$ derived from the stellar parameters leads to a true rotational velocity of $432 \pm 81 \text{ km s}^{-1}$. Therefore, HD 135344B is rotating at or close to the break-up velocity at its equator.

Aufdenberg et al. (2006) interferometrically measured the polar and equatorial radius of Vega, which rotates at 91% of its break-up velocity. They measured a difference of 20% between the equatorial and polar radius and found the temperature gradient to be 2250 K. For HD 135344B, similar effects are expected. Because the star is seen almost pole-on, we might overestimate its luminosity, thus its mass and temperature. The angular stellar diameter of HD 135344B is about $100 \mu\text{as}$ and not resolvable by current stellar interferometric facilities, preventing a direct confirmation and determination of its true stellar parameters.

The continuous accretion of circumstellar material onto the star could have caused the spin-up of the stellar rotation up to v_c . HD 135344B has only a very weak magnetic field (Hubrig et al. 2009). Therefore, the star is probably decoupled from its disk, which prevents the star from magnetic braking and losing spin. In contrast, for the majority of TTSs only moderate $v \sin i_{\star}$ values are observed, which indicates that a disk-braking mechanism operates during the accretion phase (e.g. Weise et al. 2010).

2.5.2 Possible origins of the observed periodicity

The von Zeipel effect

Because of its rapid rotation, the stellar atmosphere of the star should be oblate because of the centrifugal force. This causes a redistribution of the flux, which is proportional to the local surface gravity (von Zeipel 1924), i.e., the equatorial zones become darker at a lower T_{eff} than the polar zones. This phenomenon is known as gravity-darkening and is symmetric with respect to the equator. To produce a periodic RV_* signal, i.e. mimic a stellar spot, the flux and temperature gradient has to be off-center from the rotational axis to produce a Doppler shift, i.e. the von Zeipel effect cannot account for the observed periodicity of the spectra. Smith & Worley (1974) and Claret (2000) showed that for differentially rotating radiative stellar atmospheres, the flux over the stellar surface varies more strongly than the surface gravity, which could produce asymmetric flux distributions.

Stellar spots

We computed different spot configurations (temperature differences of the spot with respect to the photosphere ΔT_{spot} , filling factor f_{spot} , and latitude of the spot Θ) by taking the determined stellar parameters into account.

The effects of star spots on photometry and RV_* were numerically derived with a relatively simple model. A sphere with radius R , unit surface brightness I , and one or more round spots with spot filling factor f_{spot} at a specific latitude and longitude was projected onto a 2D Cartesian grid with 200×200 pixels. The relative spot brightness at the considered wavelength was calculated from the ratio of effective photospheric temperature to spot temperature, assuming black-body radiation. To account for opacity effects on the stellar surface, a linear limb darkening law with coefficients adopted from Claret & Hauschildt (2003) was applied. The inclination of the rotation axis can be arbitrarily chosen. Solid-body rotation was assumed, but differential rotation was not considered. Each cell of the star image was thus assigned a brightness and a radial velocity value. The surface brightness distribution at each phase of the stellar rotation (in steps of 1 deg) was then integrated to obtain the total brightness and the position of the photo center (1st moment). The first moment of the radial velocity distribution, weighted with the surface brightness distribution, was adopted as a proxy for the the mean radial velocity. Absorption line shapes were not taken into account.

The two extreme scenarios that can explain the RV_* variations are: 1.) dark spot (Fig. 2.13), $\Delta T_{spot} = -1350$ K, $\Theta = 40^\circ$, $f_{spot} = 5\%$, and 2.) bright spot (Fig. 2.14), $\Delta T_{spot} = 2000$ K, $\Theta = 85^\circ$, $f_{spot} = 56\%$. The large covering fraction of the latter model may more closely resemble the von Zeipel effect than traditional star spots. There is still no available photometric monitoring data for HD 135344B that would set additional constraints on the possible spot configurations. We conclude that both explanations of the origins of the observed RV_* variations, such as stellar spots or the flux and temperature gradient between the pole and equator, can

adequately explain the data.

Owing the accretion process, the $W_{10}(H\alpha)$ variations may trace a hot spot from an accretion funnel flow that has its origin at the inner edge of the inner disk. A periodic variation in 5.77 d is found for $W_{10}(H\alpha)$ (Sec. 2.4.4). This period corresponds to a Keplerian radius of ≈ 0.07 AU, which is close to the inner edge of the disk estimated to 0.05 AU by Fedele et al. (2008), given the uncertainty. A similar effect was observed for $EW(H\alpha)$ variations for the TW Hya system by Setiawan et al. (2008).

Several studies have shown that the disk lifetimes of young stars are expected to be between ~ 5 and ~ 10 Myr (e.g. Haisch et al. 2001; Bouwman et al. 2006; Jayawardhana et al. 2006; Sicilia-Aguilar et al. 2006; Fedele et al. 2010). At this age, stars lose their inner dusty disk and accretion stops. This also seems to coincide with the dissipation of gas in the inner disk (Jayawardhana et al. 2006). In contrast, HD 135344B displays accretion signatures, an inner dusty disk with an inclination, which is much greater than that of the outer disk, as well as a gas-rich inner environment of age 9 ± 2 Myr. A possible explanation might be that HD 135344B loses parts of its outer atmosphere because of its rapid rotation at or close to its break-up velocity, and feeds the inner part of the disk with its own material, which is then accreted back onto the star.

A possible stellar or sub-stellar companion located in the gap of the disk suggested by literature (e.g. Grady et al. 2009) cannot be confirmed or ruled out with our measurements because our spectroscopic data set covers only five months in total and the uncertainties in the RV_* measurements are of about 300 m s^{-1} .

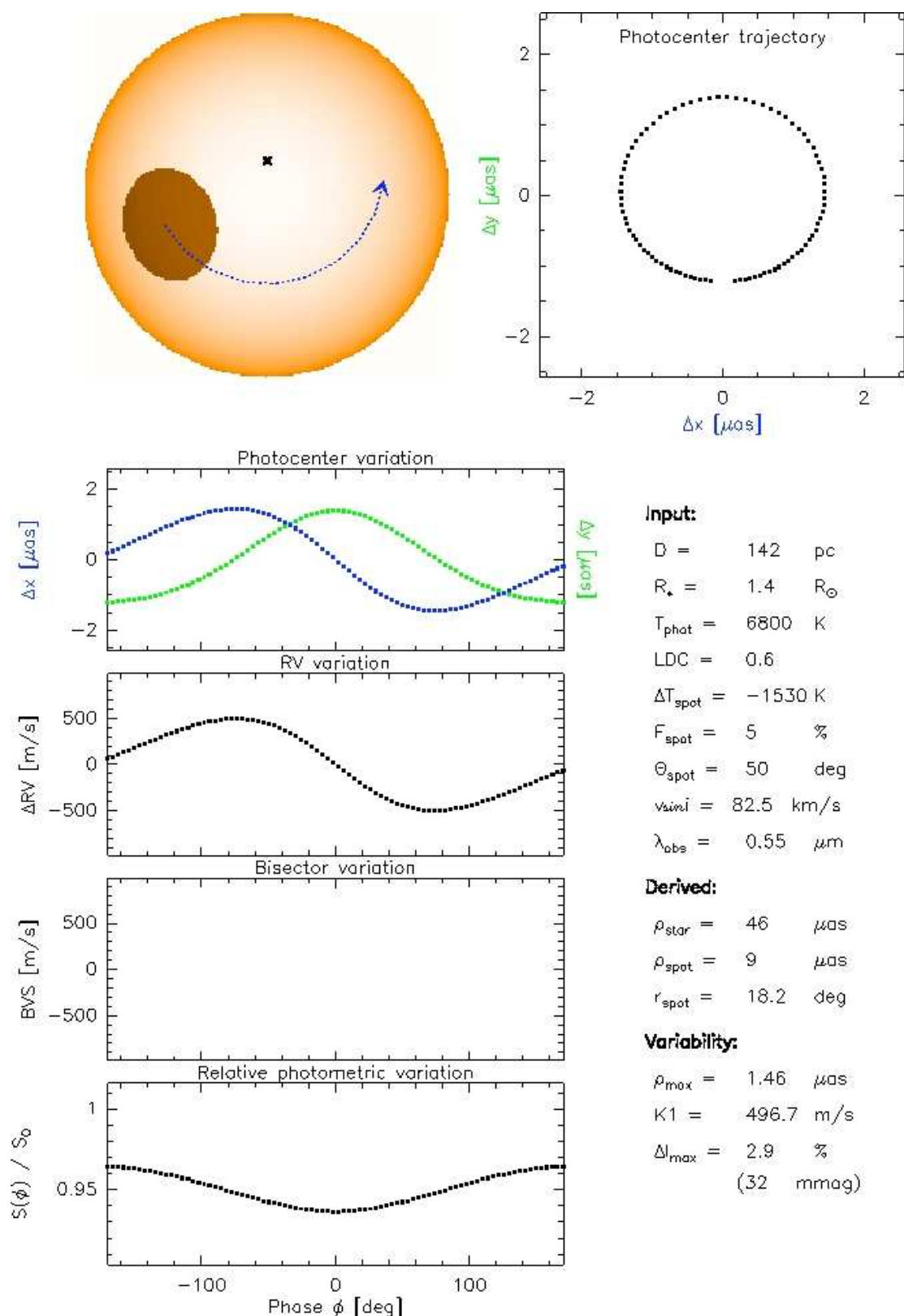


Figure 2.13: Dark spot model to explain the observed RV_* variations. The right panel shows the input parameter used for the modeling and the expected amplitude for RV_* and photometry. The upper left plot shows the star-spot configuration used for the model. The upper right panel displays the computed trajectory of the photocenter. The plots at the lower left display the computed variations as a function of rotational phase. Computation by R. Launhardt.

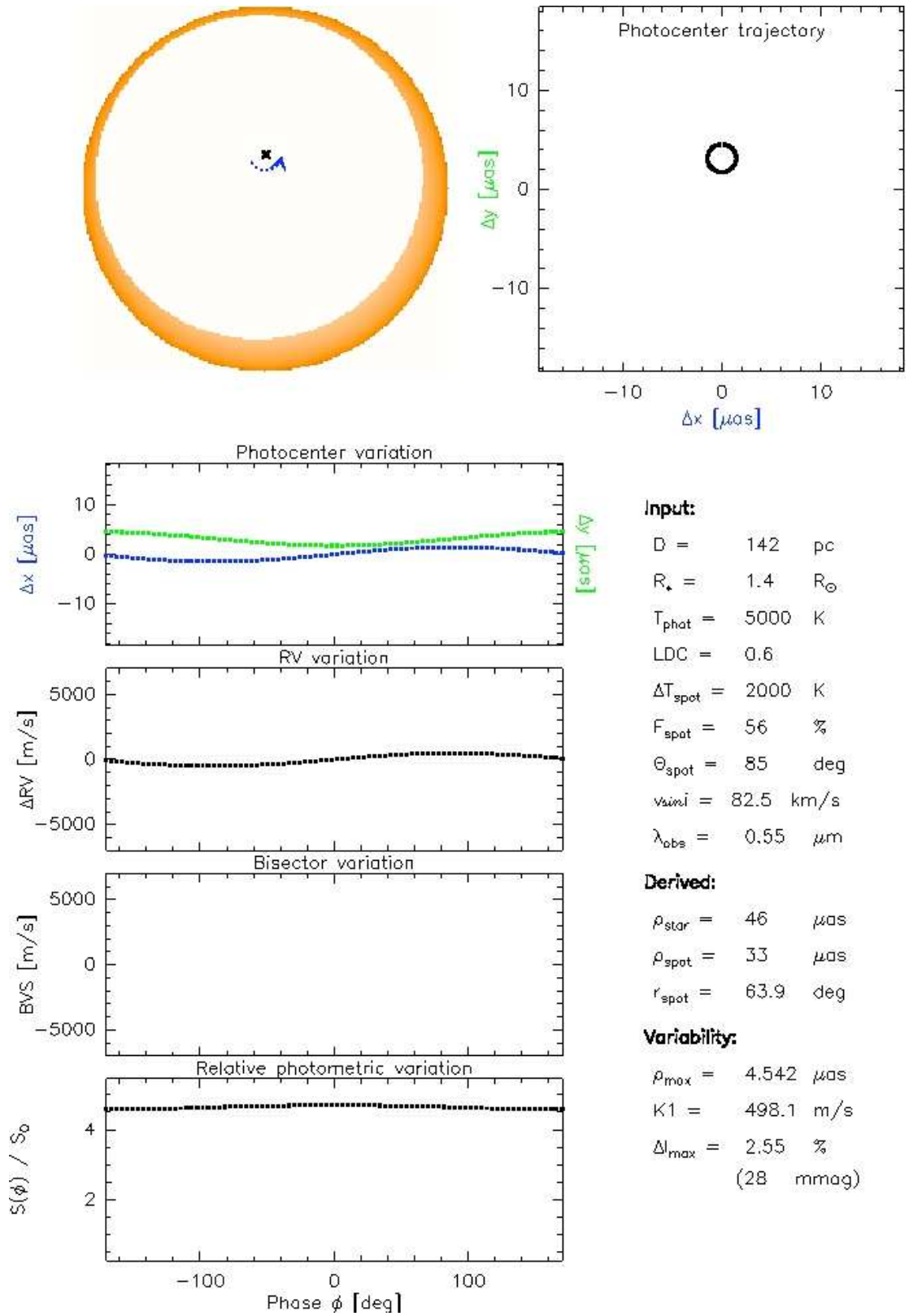


Figure 2.14: Same as Fig. 2.13 but for a hot spot model. Computation by R. Launhardt.

2.6 Conclusions

We have presented the first direct measurement of the stellar rotational period of a Herbig star. The period was derived from RV_{\star} measurements by cross-correlating optical high-resolution spectra with a synthetic spectrum. The rotational period of HD 135344B was found to be 0.16 d. In addition, we have determined new reliable stellar parameters for HD 135344B, independent of previous literature values, and demonstrated that it is possible to measure the RV_{\star} of a Herbig star with a high $v \sin i_{\star}$ value. From the measured stellar parameters, we were able to estimate the stellar inclination to a value of $11^{\circ} \pm 2^{\circ}$. With these data, we concluded that HD 135344B is rotating at or close to its break-up velocity and feeding its stellar vicinity with gas and dust. This is the first piece of observational evidence that a young intermediate-mass star can rotate close to its break-up velocity.

The direct determination of the stellar rotational period by RV_{\star} measurements may also be applicable to other Herbig Ae/Be stars. A larger sample could therefore provide insight into the evolution of angular momentum, the presence of star-disk coupling mechanisms, and the presence of magnetic fields in these young intermediate-mass stars.

We also detected variations in the $W_{10}(H\alpha)$ measurements with a period of 5.77 d, corresponding to a Keplerian radius close to the inner edge of the inner disk of HD 135344B, which could be a hot spot caused by an accretion funnel flow.

2.7 RV_{\star} and $H\alpha$ measurementsTable 2.3: Measured RV_{\star} , $EW(H\alpha)$, $W_{10}(H\alpha)$, and their corresponding uncertainties.

Time [JD-2 400 000 d]	RV_{\star} [m s ⁻¹]	$\sigma_{RV_{\star}}$ [m s ⁻¹]	$EW(H\alpha)$ [Å]	$\sigma_{EW(H\alpha)}$ [Å]	$W_{10}(H\alpha)$ [Å]	$\sigma_{W(H\alpha)}$ [Å]
55256.86690	2645	335	-6.02	0.21	9.80	0.07
55346.70410	1593	302	-9.84	0.13	9.14	0.05
55347.63521	1859	315	-10.44	0.17	8.54	0.06
55348.73788	2041	260	-13.17	0.19	9.24	0.02
55349.74833	2223	400	-11.42	0.20	8.45	0.08
55351.69950	2331	112	-12.80	0.24	8.45	0.03
55355.49994	2108	192	-8.83	0.12	8.37	0.08
55355.68805	2300	195	-8.96	0.13	8.73	0.10
55355.85300	1784	784	-9.85	0.20	8.84	0.11
55356.78750	1529	303	-8.24	0.20	9.35	0.07
55358.63746	3925	494	-9.17	0.15	9.20	0.03
55358.71724	2364	408	-9.15	0.14	9.21	0.06
55360.72711	2664	358	-10.35	0.13	8.86	0.13
55362.48448	2432	215	-9.55	0.15	7.78	0.04
55362.57222	1732	205	-9.67	0.11	7.97	0.07
55396.51686	3415	245	-10.48	0.20	7.63	0.06
55396.57497	2641	306	-10.73	0.08	7.90	0.03
55396.61357	2388	123	-10.91	0.17	8.37	0.02
55396.66325	3566	214	-10.90	0.16	8.69	0.05
55396.69535	2672	382	-11.18	0.08	8.75	0.03
55397.52834	1992	339	-10.01	0.11	8.27	0.05
55397.59554	2288	247	-9.99	0.13	8.11	0.11
55397.64898	2739	381	-10.02	0.30	8.05	0.03
55397.68781	2866	241	-10.27	0.15	8.06	0.09
55398.51102	1932	519	-11.25	0.29	8.45	0.09
55400.51882	2692	303	-10.66	0.14	10.03	0.06
55400.57368	2159	173	-10.18	0.22	9.65	0.06
55400.61784	2891	239	-9.70	0.14	9.64	0.10
55400.67505	2803	321	-9.52	0.20	9.41	0.07
55401.48617	3341	376	-10.65	0.17	9.20	0.03
55401.63979	3461	215	-10.01	0.17	9.23	0.02
55401.69736	1035	546	-9.56	0.21	8.93	0.07
55402.56980	2032	374	-9.41	0.00	8.63	0.06
55402.62734	3849	347	-9.35	0.24	8.36	0.11
55402.69271	1769	433	-8.77	0.18	8.09	0.06
55403.56511	2802	378	-8.49	0.19	8.81	0.04
55403.59827	2209	193	-8.08	0.23	8.48	0.13
55403.63910	2810	471	-8.05	0.19	8.60	0.11
55403.67692	1898	311	-7.99	0.23	8.59	0.11
55404.50509	3058	250	-8.80	0.18	9.55	0.05
55404.67289	2932	247	-9.56	0.18	9.61	0.06
55405.63121	2431	197	-12.65	0.16	9.74	0.07
55405.68095	2686	313	-12.62	0.19	9.55	0.04
55407.58835	3106	371	-10.67	0.16	8.52	0.02

Chapter 3

HD 144432: A young triple system

Abstract We present new imaging and spectroscopic data of the young Herbig star HD 144432 A, which is a well-known binary star with a separation of $1.47''$. High-resolution NIR imaging data obtained with NACO at the VLT reveal that HD 144432 B itself is a close binary pair with a separation of $0.1''$. High-resolution optical spectra, acquired with FEROS at the 2.2m MPG/ESO telescope in La Silla, of the primary star and its co-moving companions are used to determine their main stellar parameters, such as effective temperature, surface gravity, radial velocity, and projected rotational velocity by fitting synthetic spectra to the observed stellar spectra. The two companions, HD 144432 B and HD 144432 C, are identified as low-mass T Tauri stars of spectral type K7V and M1V, respectively. From the position in the HRD, the triple system appears to be co-eval with a system age of 6 ± 3 Myr.

adapted from Müller, A., Carmona, A., van den Ancker, M. E., van Boekel, R., Henning, Th., and Launhardt, R., 2011, A&A, 535, L3

3.1 Introduction

Herbig Ae/Be (HAeBe, Herbig 1960; Finkenzeller & Mundt 1984) stars are intermediate-mass (2-10 M_{\odot}) pre-main sequence stars (PMS). They are the higher-mass counterparts of the T Tauri stars (TTS), hence fill the parameter space between TTSs and high-mass young stars in addressing the question of star formation as a function of mass. Double or multiple stellar systems are of great interest to star formation theories as they provide constraints on the components of star formation models, such as fragmentation, accretion, N-body dynamics, and orbit migration (e.g. Tokovinin 2008, and references therein). Although several imaging surveys have indicated that HAeBe stars have close companions (e.g. Leinert et al. 1997; Pirzkal et al. 1997; Kouwenhoven et al. 2005), relatively few studies have constrained the physical properties of these companions. One interesting question that can be addressed is the age of the HAeBe star by constraining the age of its companions. An independent and more robust age estimate can be derived from the lower-mass companions.

Corporon (1998) pointed out that the companions of Be stars tend to be intermediate-mass stars with spectral types A to F, while the companions of Ae stars are low-mass TTSs with spectral types K to M, which suggests that the mass ratio seems to be quantitatively independent of the primary mass (e.g. Hogeveen 1992).

HD 144432 A is a late A to early F-type star (Thé et al. 1994) at a distance of 160^{+36}_{-25} pc (van Leeuwen 2007) that is associated with the Sco OB2-2 star forming region. The star is surrounded by a protoplanetary disk (e.g. Meeus et al. 2001) and displays signs of active mass accretion. The values found in the literature range from 1.8 to $8.5 \cdot 10^{-8} M_{\odot} \text{ yr}^{-1}$ (Blondel & Djie 2006; Garcia Lopez et al. 2006; Donehew & Brittain 2011). From J=3-2 ^{12}CO measurements and line profile fitting, Dent et al. (2005) derived a dust mass of $2 \cdot 10^{-3} M_{\odot}$ (assuming a constant gas-dust ratio of 100) and an outer radius of 60 ± 20 AU ($i = 48^{\circ} \pm 10^{\circ}$) for the disk around HD 144432 A where emitting gas is present. The system HD 144432 is known to be a binary (Pérez et al. 2004; Carmona et al. 2007). *K*-band observations by Pérez et al. (2004) revealed a 2.4 mag fainter stellar companion at a separation of $1.4''$ ($PA=4^{\circ}$, Carmona et al. 2007). Carmona et al. (2007) reported the detection of Li I (6708 Å) and $H\alpha$ emission in the spectrum of HD 144432 B using the VLT-FORS2 spectrograph.

Pérez et al. (2004) showed that HD 144432 A and B share the same common proper motion and age. In addition, component B was ruled out as a background star by Carmona et al. (2007).

In this chapter, we present NACO observations of HD 144432, which resolve HD 144432 B as a close binary star, thereby revealing HD 144432 as a hierarchical triple system. Using high-resolution optical spectroscopy, we determined the stellar parameters of all components of the triple system.

3.2 Observations and data reduction

3.2.1 NACO

HD 144432 was observed in the night of July 13, 2005, with NACO (Lenzen et al. 2003; Rousset et al. 2003), the adaptive optics (AO), near-infrared (NIR) camera at ESO's VLT. We obtained these unpublished observations from the ESO archive. The data consist of six imaging observations in three different filters (K_s at $\lambda = 2.18 \mu\text{m}$, NB2.12 at $\lambda = 2.122 \mu\text{m}$, and NB2.17 at $\lambda = 2.166 \mu\text{m}$). Each observation consists of eight single exposures at different sky positions (jitter). Standard data reduction (bias subtraction, flat-field correction, bad-pixel interpolation) was applied to each frame by employing the available calibration frames. The average $FWHM$ of the images is $0.07''$. A combined image was produced by applying the shift-and-add method (a two-dimensional cross-correlation routine) to the NB2.17 observation (Fig. 3.1) using NACO pipeline recipes provided by ESO¹.

3.2.2 FEROS

We obtained single-epoch spectra of HD 144432 A (SNR of 350 at 5500 \AA) and a combined spectrum of HD 144432 B and C (SNR of 250 at 5500 \AA) in the night of June 1, 2009, using FEROS (Kaufer et al. 1999) at the 2.2m MPG/ESO telescope at La Silla Observatory in Chile. FEROS covers the optical spectral range from 3600 \AA to 9200 \AA and provides a spectral resolution of ≈ 48000 . The spectra were obtained using the object-calibration mode where one of the two fibers is positioned on the target star and the other fiber is fed with the light of a ThAr+Ne calibration lamp. The reduction of the raw data was performed using the online data reduction pipeline available at the telescope². The pipeline performs bias subtraction and flat-fielding, traces and extracts the single echelle orders, applies the wavelength calibration, and corrects for the barycentric motion. For each exposure, it produces 39 individual sub-spectra representing the individual echelle orders, as well as one merged spectrum.

The fiber aperture of FEROS is $2''$ on the sky. The projected separation between the components B and C is $0.1''$. Therefore, the observed spectrum is a superposition of those of the two companions. In addition, owing to the difference in the brightnesses of B and C in the optical with respect to A ($\delta \sim 5 \text{ mag}$) and a seeing at the time of the observations of $0.8''$, the spectrum of the fainter companions is contaminated by the $\approx 1.5''$ apart and ≈ 20 times brighter primary star.

¹<http://www.eso.org/sci/software/pipelines/naco/naco-pipe-recipes.html>

²<http://www.eso.org/sci/facilities/lasilla/instruments/feros/>

Table 3.1: Relative astrometric measurements of the triple system HD 144432, where ρ is the angular separation, d is the projected separation, and PA is the position angle.

Parameter	A-B	A-C	B-C
ρ ["]	1.465 ± 0.007	1.468 ± 0.007	0.102 ± 0.001
d [AU]	234 ± 44	235 ± 44	16 ± 3
PA [°]	6.31 ± 0.12	2.32 ± 0.12	275.90 ± 0.28

3.3 Data analysis and results

3.3.1 Imaging

To measure the relative position of the companions in the field, i.e. their projected distance and position angle with respect to the primary star, and its relative fluxes, we used the IDL-based program Starfinder (Diolaiti et al. 2000), which is designed to analyze AO images using the extracted point spread function from the image. The final positional values were derived by averaging the single values of all individual NACO exposures (48 in total). Their errors were derived by computing the standard deviations in the means and taken into account the calibrations of Chauvin et al. (2010) for the plate scale (13.25 ± 0.06 mas) and true north orientation ($-0.02^\circ \pm 0.10^\circ$), which were derived from a data set taken in August 2005. Table 3.1 lists the measured distances and position angles of the companions. The K_s magnitudes for B and C were obtained from the relative flux measurements. We computed the zero point of each individual image using HD 144432 A as reference ($K = 5.888$ mag, Cutri et al. 2003) and derived 9.09 mag for B and 9.16 mag for C, respectively.

3.3.2 Spectral classification of HD 144432 A

Table 3.2 lists the derived stellar parameters of HD 144432 A. The luminosity, L_* , was computed by integrating the total flux under the SED. To construct the SED, we used photometric data from de Geus et al. (1990), Sylvester et al. (1996), and Malfait et al. (1998), and data from the ISO and IRAS point-source catalog. We derived an extinction $A_V = 0.15$ for HD 144432 A by fitting a reddened stellar atmosphere model with the T_{eff} and $\log g$ derived from the spectral fit to the observed UV-optical photometric data. The parameters T_{eff} , $\log g$, and $v \sin i$ were computed using a self-developed tool for retrieving stellar parameters of Herbig stars based on fitting synthetic spectra to the observed stellar spectrum. The computation of the synthetic spectra was carried out using SPECTRUM (Gray & Corbally 1994) with the ATLAS9 atmosphere models (Castelli & Kurucz 2004). The grid of synthetic spectra has step sizes of 125 K in T_{eff} , 0.15 in $\log g$, and 5 km s^{-1} in $v \sin i$. The stellar spectrum was divided into four spectral windows (Fig. 3.2). Each window was fitted independently and the individual best fits were averaged to derive the final stellar parameters (Table 3.2). After finding the best-fit value for T_{eff} and $\log g$ at solar metallicity, we tried models with diverse metallicities to find the best fit to the Fe I lines. We found that the optimal match to the spectrum was provided by solar metallicity.

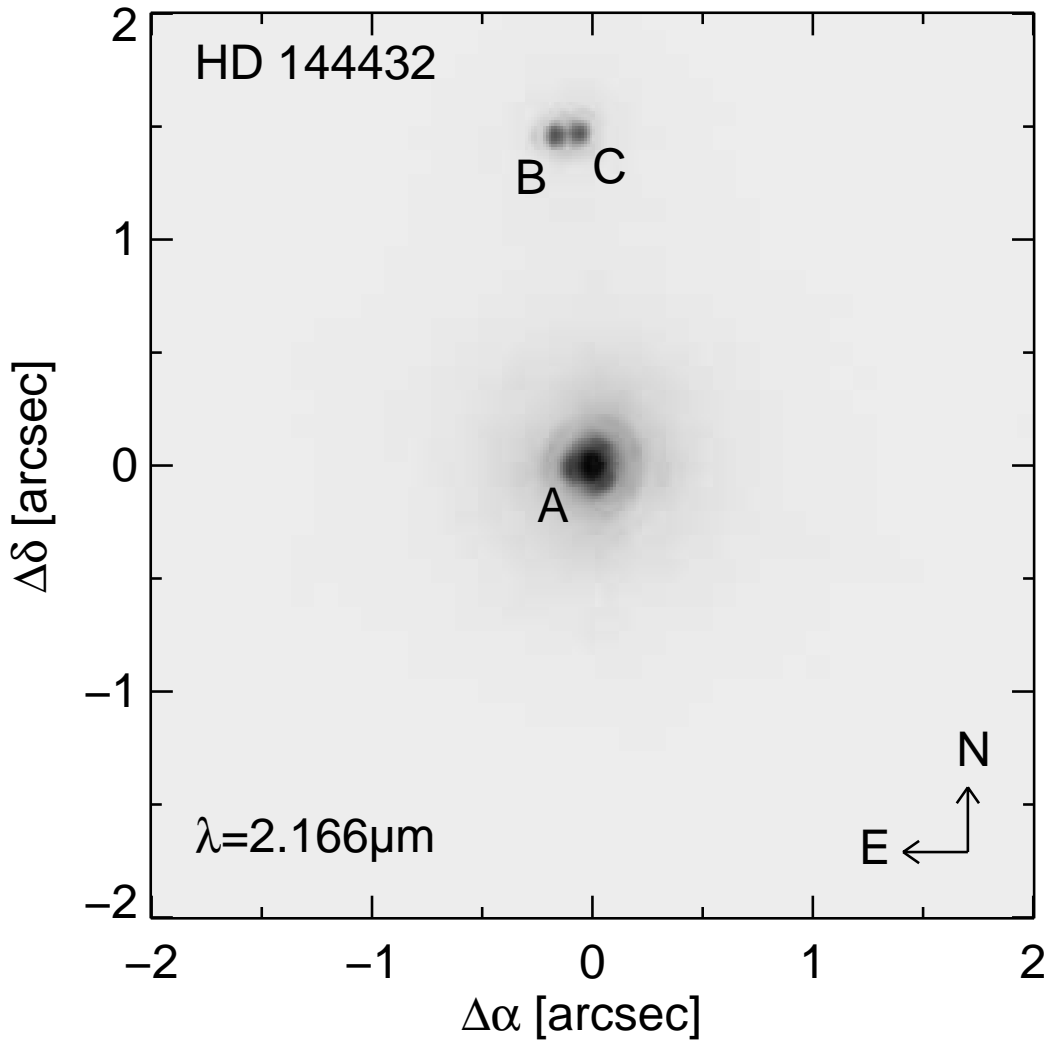


Figure 3.1: Near infrared image (logarithmic scaling in brightness) of the HD 144432 triple system observed with NACO in July 2005. The components are marked by letters in hierarchical order. The separation between A and B is $1.47''$. The components B and C are separated by $0.1''$.

Figure 3.2 shows four related windows of the observed stellar spectrum of HD 144432 A (black line), which is closely fitted by a single star synthetic spectrum (red line).

We measured the stellar radial velocity, RV , by cross-correlating the stellar spectrum with a template spectrum, which was a synthetic spectrum representing the stellar parameters of HD 144432 A (Table 3.2). The resulting cross-correlation function was fitted by a Gaussian function. The position of the center of the Gaussian yields RV .

From the position of HD 144432 A in the HRD (Fig. 3.3), we obtained the stellar mass, radius, and its age using the evolutionary tracks of Siess et al. (2000). We also compared with the

Table 3.2: Stellar parameters of HD 144432 A, B, and C.

Component	A	B	C
Parameter	Value		
Spectral type	F0IIIe	K7V	M1V
L_* / [L_\odot]	$12.7^{+6.4}_{-3.7}$	$0.50^{+0.24}_{-0.20}$	$0.41^{+0.19}_{-0.16}$
T_{eff} / [K]	7220 ± 115	4000 ± 250	3750 ± 250
$\log g$ / [cm s^{-2}]	3.60 ± 0.15	4.0 ± 0.5	4.0 ± 0.5
M_* / [M_\odot]	$1.8^{+0.2}_{-0.1}$	0.8 ± 0.2	0.5 ± 0.2
R_* / [R_\odot]	2.3 ± 0.5	1.5 ± 0.7	1.5 ± 0.7
$v \sin i$ / [km s^{-1}]	75.0 ± 3.5	55 ± 5	40 ± 5
RV / [km s^{-1}]	-2.8 ± 0.4	-5 ± 2	-4 ± 2
age / [Myr]	9 ± 2	4^{+5}_{-2}	3^{+2}_{-1}

evolutionary tracks of Tognelli et al. (2011), which yield the same results. The derived parameters are in close agreement with values derived in other publications, e.g., Dunkin et al. (1997), van Boekel et al. (2005), and Guimarães et al. (2006). The measured effective temperature and surface gravity are comparable to those of an F0IIIe main-sequence star.

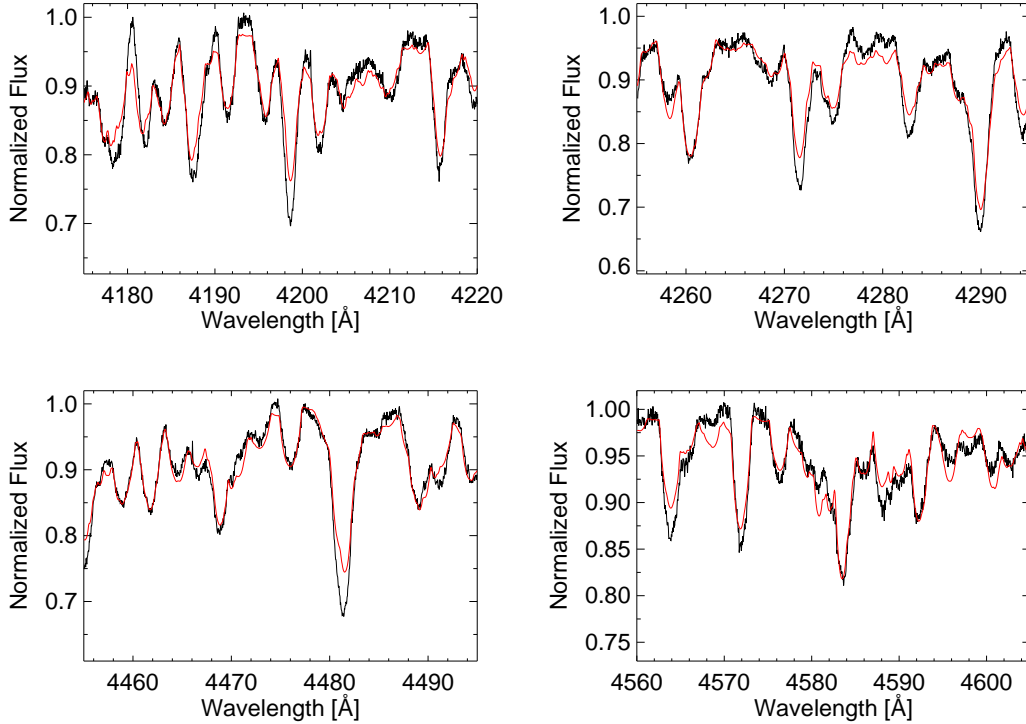


Figure 3.2: The spectral windows used for fitting the synthetic spectrum (red line) to the observed stellar spectrum (black line) of HD 144432 A.

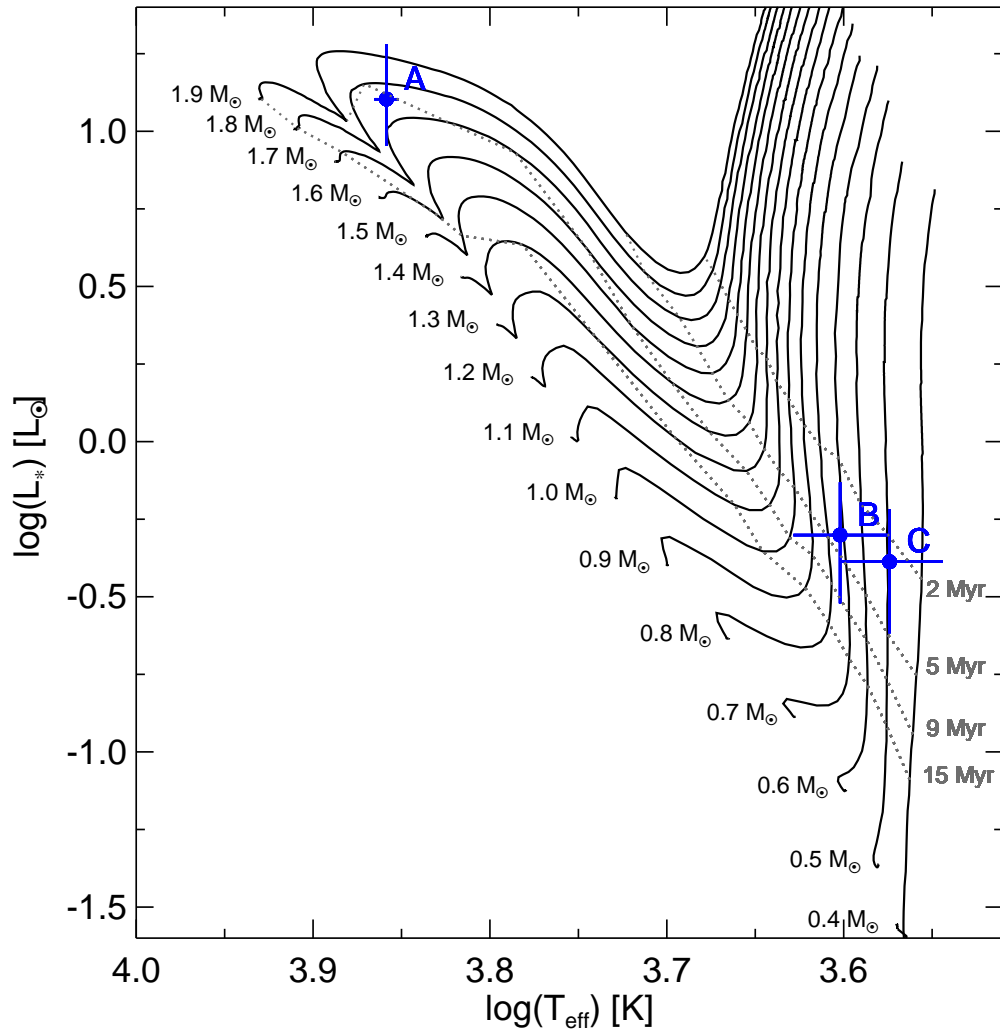


Figure 3.3: The position of the A, B, and C components of HD 144432 in an HRD along with the evolutionary tracks of Siess et al. (2000) for a metal abundance of $Z=0.02$.

3.3.3 Spectral classification of HD 144432 B and C

The observed spectrum of HD 144432 B and C is strongly contaminated by HD 144432 A. The contamination varies as a function of wavelength, with the blue part of the spectrum being the most strongly affected. In addition, the spectra of components B and C are superimposed. To derive the spectral type of B and C, we compared the continuum-normalized B+C observed spectrum with a continuum-normalized synthetic spectrum made of three components: a high-resolution Kurucz theoretical spectra of B and C (computed as described in Sec. 3.3.2), and a scaled observed FEROS spectrum of HD 144432 A.

We employed a custom designed interactive IDL software³ that permitted us to visually compare in real time, after any change of parameters, the observed and the synthetic spectra. The procedure consisted first choosing the spectral types of B and C thereby automatically fixing their absolute magnitudes (M_V); the M_V for the contribution of component A was then varied to match strength of the features of A; and finally, the $v \sin i$ for components B and C was set to reproduce the widths of the absorption lines. The synthetic comparison spectrum was constructed by scaling the flux of each component by its M_V , summing the scaled fluxes, and normalizing the resultant spectrum by dividing it by a second order polynomial fit to the continuum. The χ_{red}^2 statistic was calculated for each synthetic spectrum.

We used as a first guess a K4V spectrum for B and C (Carmona et al. 2007), and searched for a region in the spectrum best suited to the spectral classification. We selected the region at 7695 – 8100 Å because: (i) it has few atmospheric lines; (ii) it is relatively featureless in the spectrum of A; (iii) it has a very strong line at 7700 Å that allows us to differentiate spectral types K and M; (iv) it has several additional weaker absorption lines that aid the spectral classification and determination of RV and $v \sin i$; and (v) it has a strong absorption line at 7775 Å from component A that is not blended with absorption lines of K and M stars.

After defining the spectral window for classification, we searched for the optimal spectral type pair able to reproduce most of the spectral features observed. The best match was given by a binary system composed of a K7V ($T_{\text{eff}}=4000$ K, $\log g=4.0$) and an M1V ($T_{\text{eff}}=3750$ K, $\log g=4.0$) star of $v \sin i=55\pm 5$ and 40 ± 5 km s⁻¹, respectively, plus a contribution by A of similar magnitude as the K7V component. We checked other regions of the spectrum (6020–6420 Å, 6330–6740 Å, 6655–6760 Å, 7250–7585 Å) in addition to the 7695 – 8100 Å region, and confirmed that this binary pair provided a good match (we note that the level of A is different for each region). The uncertainty in the classification is one spectral sub-class and $\Delta \log g=0.5$, owing to the 250 K and 0.5 grid, used for T_{eff} and $\log g$.

Once the spectral types and $v \sin i$ of B and C were derived, we relaxed the assumption that the RV for both components is equal to -3 km s⁻¹ (RV of HD 144432 A, Table 3.2) and shifted their spectra until the Gaussian fit to the cross-correlation function has its center at 0 km s⁻¹. In this way, we obtained heliocentric RV s for components B and C of -5 ± 2 and -4 ± 2 km s⁻¹, respectively. In Fig. 3.4, we display the observed FEROS spectrum, the final combined synthetic spectrum of components B, C, and A, and the relative flux contribution of each component.

Finally, we note that to assume that the flux ratio of components B to C is equal to the M_V ratio, is equivalent to assuming that they are at the same distance and have the same extinction. If we allow for a different brightness for both components, we find that a slightly closer fit to

³IDL widget software available upon request from A. Carmona

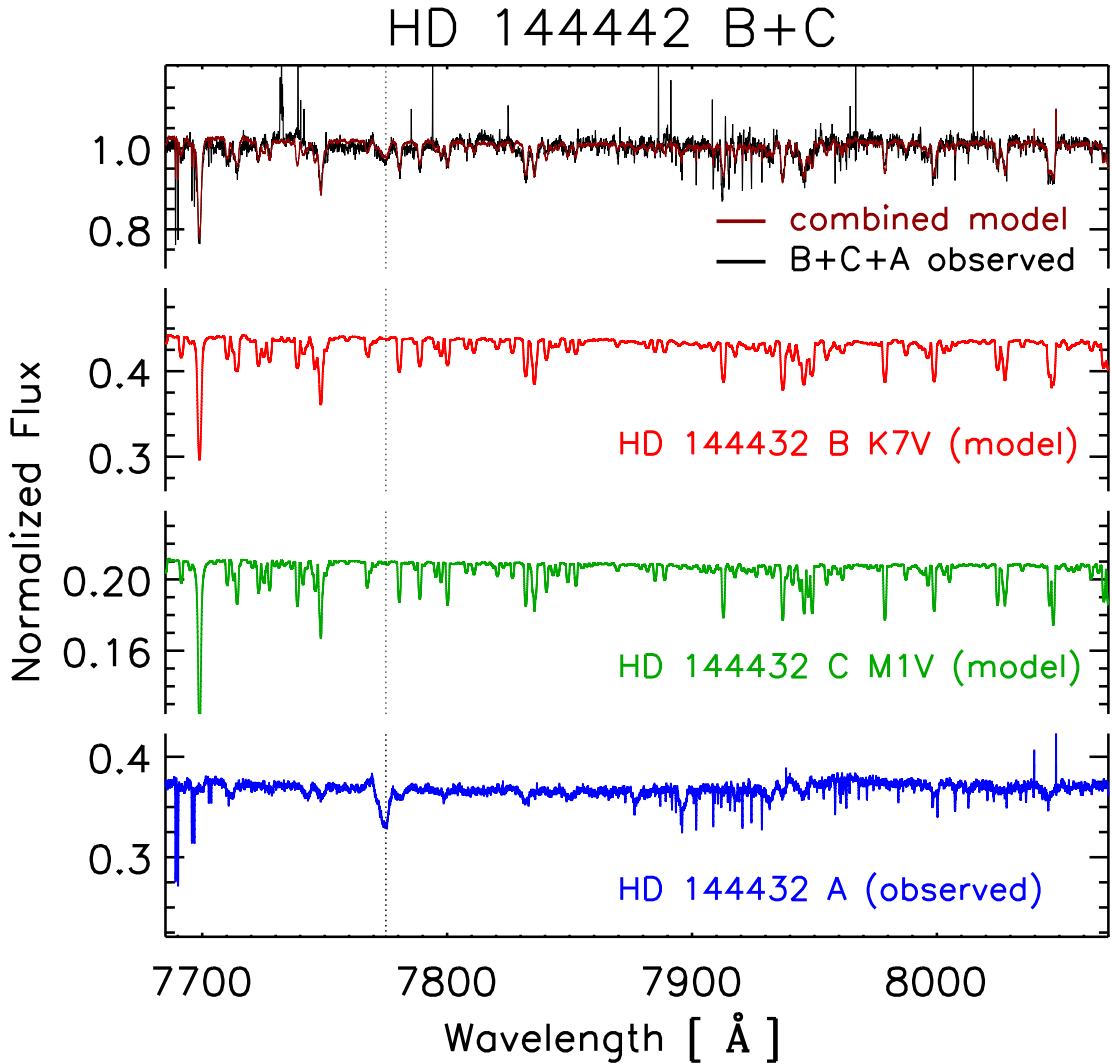


Figure 3.4: *Upper spectra*: observed normalized FEROS spectrum at the position HD 144432 B and C (in black), and the normalized synthetic combined model that most closely describes the observed spectrum (in red). *Lower spectra*: Relative contributions of HD 144432 B, C, and the contamination from HD 144432 A (note the difference in the Y-axis for each spectrum). The vertical dotted line displays the absorption line of HD 144432 A used to scale the flux of HD 144432 A to match the observed spectrum. The strength of the contamination from the A component is similar to the flux of HD 144432 B.

the 7700 Å line can be achieved if C is slightly brighter (by up to a 0.5 mag). However, it is statistically very unlikely that two stars of similar RV , which indicates a common membership, and co-eval evolutionary status are so close together on the sky, thus it is unlikely that C is brighter than B.

From the measured distances between A, B, and C (Table 3.1) and their derived masses (Ta-

ble 3.2), the components B and C orbit component A with a period of 2100 ± 600 yr and B and C orbit each other with a period of 60 ± 20 yr under the assumption of circular orbits and that the triple system is seen pole-on.

3.3.4 Signatures of youth in HD 144432 B and C

The lithium line at 6708 \AA is visible in the combined spectrum of HD 144432 B and C. In Fig. 3.5 we display the spectrum at the position of the line after correction for the contribution of the A component. Because the lithium line of the B+C observed spectrum is stronger (EW $0.52 \pm 0.02 \text{ \AA}$) than the lithium line expected for the combination of a K7V and a M1V spectra (EW $0.42 \pm 0.02 \text{ \AA}$), we conclude that HD 144432 B and C are likely young stars.

To constrain the age of the companions from the position in the HRD (Fig. 3.3), we estimated their luminosities. We used MARCS stellar models (Gustafsson et al. 2008), K_s -band photometry of the NACO images (Sec. 3.3.1), and assumed a constant extinction of $A_V = 0.15$ (Sec. 3.3.2) for all components. We derived a luminosity of $L_B = 0.50^{+0.24}_{-0.20} L_\odot$ for the B component and $L_C = 0.41^{+0.19}_{-0.16} L_\odot$ for the C component. The derived ages and other derived stellar parameters are listed in Table 3.2. The ages of the three stars are comparable taking into account the error bars. Therefore, we estimate that the age of the system is 6 ± 3 Myr (weighted mean of the individual age values), which is in good agreement with the value of 8^{+3}_{-1} Myr derived by Carmona et al. (2007).

3.4 Discussion and conclusions

We have analyzed NIR AO images obtained with NACO of the young Herbig star HD 144432 and discovered that it is a triple system. The components B and C are located $1.47''$ north of the primary star, and B and C themselves are separated by $0.1''$. Using high-resolution optical spectra, we have determined the stellar parameters T_{eff} , $\log g$, L_* , M_* , and $v \sin i$ of all three components and derived a spectral type of A9/F0Ve for component A and K7V and M1V for components B and C, respectively. This is in agreement with the trend suggested by Corporon (1998) that companions of Herbig Ae stars are usually of spectral type K to M.

The equivalent width of Li I as well as the position of HD 144432 B and C in the HRD indicates a young age of the components similar to HD 144432 A. An additional sign of their young age is the detection of X-ray emission at the position of the B and C components by Stelzer et al. (2009). The A component of HD 144432 shows only weak X-ray activity, which is expected for intermediate-mass stars as they are fully radiative and unable to generate strong magnetic fields like T Tau stars. This is supported by the detection of a weak but variable magnetic field of HD 144432 A by Hubrig et al. (2004, 2006, 2007, 2009), which could be a remnant of the primordial magnetic field of the molecular cloud.

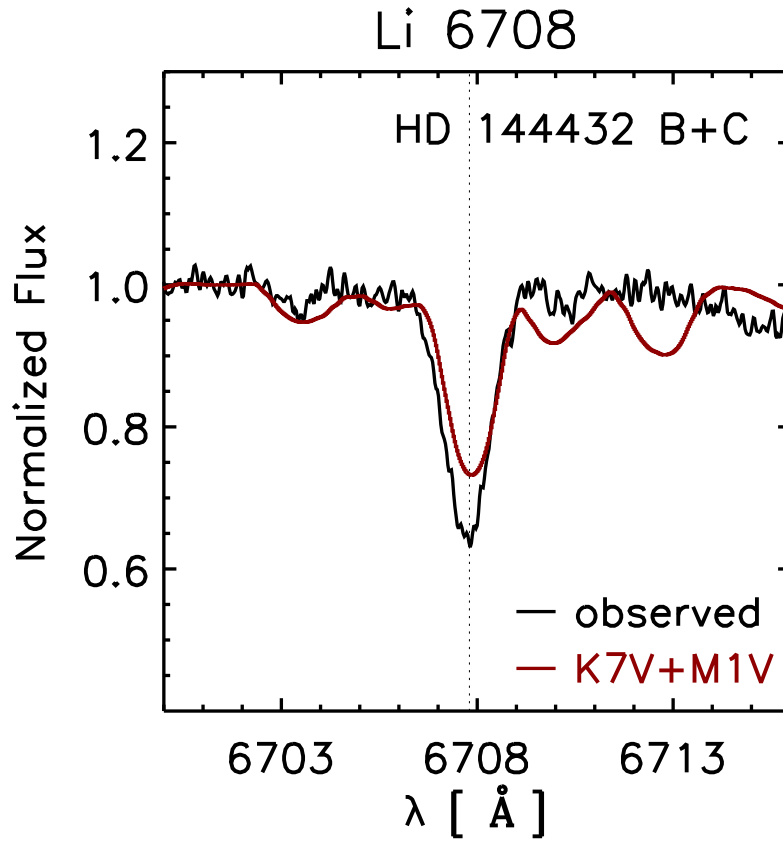


Figure 3.5: Observed (black line) and modeled (red line) HD 144432 B+C spectrum after correction by the contribution from the A component at the position of the Li I line at 6708 \AA .

The derived ages from the position in the HRD of all components are comparable within the error bars and the system age of the triple system can be constrained to be 6 ± 3 Myr. This implies that these stars have a common evolutionary state and therefore supports the scenario of formation via cloud fragmentation.

Chapter 4

A massive planet inside the disk of the Herbig star HD 142527

Abstract The majority of planet search programs nowadays concentrate on evolved stars with late spectral types ranging from F to M as they provide stable radial velocity and photometric measurements, which enables to find Earth size planets. Thus, there is a lack of planets found around young stars resulting in poor statistics. Certainly, such systems and their characterization are needed to set time constraints for planet formation theories.

We search for periodic variations in the radial velocity of the 4 Myr young Herbig star HD 142527. In addition, we investigate the variability of accretion tracers.

We analyze 109 high-resolution optical spectra taken over a time period of 3.7 years. The spectra were acquired with FEROS at the 2.2m MPG/ESO telescope and with HARPS at the 3.6m telescope in La Silla. A set of 10 spectra recorded in the near-infrared with CRIRES at UT1 in Paranal are completing the optical data set.

We report the detection of a 114.5 d periodic signal in the optical and near-infrared radial velocity data. A Kepler fit reveals a low-mass companion on an eccentric orbit ($e = 0.23$) at a distance of $a = 0.60 \pm 0.01$ AU. The mass of the companion is $m \sin i = 8.5 \pm 1.0 M_J$. From measurements of the disk inclination and estimation of the inclination of the stellar rotation axis, we derive a true mass of $25 \pm 6 M_J$. Detailed analysis of spectral lines, which act as accretion tracers, rule out activity related modulations of the radial velocity signal. In addition, we derive a full set of stellar parameters for HD 142527.

This is the first discovery of a low-mass companion around a Herbig star. It is the youngest companion found by the radial velocity method.

adapted from Müller, A., Seifahrt, A., Launhardt, R., Henning, Th., Pott, J. U., Setiawan, J., Sicilia-Aguilar, A., Uribe, A. L., van Boekel, R., and van den Ancker, M. E., 2012, to be submitted

4.1 Introduction

How stars and planetary systems form is a key question in modern astronomy. Our knowledge of the formation mechanism and history of planets has developed strongly since the first detection of an exoplanet by Mayor & Queloz (1995) around a main-sequence star. This and subsequent discoveries showed that many planetary systems have giant gas planets on close (sub-AU) orbits, i.e. their architecture is very different from that of the Solar system. It was soon realized that the solar system is not as typical as it had been assumed to be.

Planet formation theories have been focused around two main principles: that of “Core Accretion” (CA; e.g. Pollack et al. 1996) and “Gravitation Instability” (GI; e.g. Boss 1997, 2001). The GI scenario is the simplest: if a “clump” of gas in a circumstellar disk exceeds the local Jeans mass it will collapse and form a giant planet on time scales of hundreds to thousands of years. In the CA scenario, giant planet formation proceeds along a more complex path. First, small (sub-)micron sized particles engage in low-velocity collisions and stick together, forming ever larger aggregates. Once bodies become approximately kilometer sized they start to exert significant gravitational forces on neighboring bodies, and a period of gravity-assisted “oligarchic” growth begins in which the largest bodies assimilate the smaller ones, and form the cores of future giant planets. Once these cores reach about ten Earth masses, they are able to capture and hold hydrogen and helium gas, and the gas accretion phase ensues. This process is initially slow, but as the planet gathers more mass the accretion accelerates and finally proceeds in a “run-away” fashion during which the giant planet exhausts its local disk region and may open a gap in the disk. In both scenarios, giant planets are subject to (radial) migration due to planet disk interactions.

A very important but still poorly constrained observational boundary condition with which planet formation theories should be confronted, is the time scale on which planet formation proceeds. In particular the observational upper limit for the time it takes to assemble a giant planet of a given mass provides strong constraints on planet formation in the CA scenario (it does so only to a lesser extent for the GI scenario, which is extremely fast by nature). This requires detecting planets around very young stars which have comparatively active photospheres (hindering RV work) and are usually still surrounded by a circumstellar disk. Only direct detection methods were able to discover potentially low mass companions around very young stars with transitional disks (e.g. T Cha by Huélamo et al. 2011 and LkCa 15 by Kraus & Ireland 2012), so far. From statistical studies of young stellar clusters, the dissipation timescales of circumstellar disks are found to be of the order of 5 to 10 Myr (e.g. Bouwman et al. 2006; Sicilia-Aguilar et al. 2007, and reviews by Henning 2008; Hillenbrand 2008), where the formation of a planet has to be succeeded.

Stellar activity originating from cool star spots on the stellar surface can mimic radial velocity variations (e.g. Saar & Donahue 1997). While such variations are often correlated with bisector variations and other photometric, and spectroscopic activity indices (e.g. Queloz et al. 2001; Huerta et al. 2008), these indicators are not always reliable in ruling out stellar activity

as the underlying cause for radial velocity variations in young stars. Due to the diminishing temperature contrast between the star spots and the stellar photosphere at longer wavelength (Vrba et al. 1986), RV measurements in the near-infrared provide an important diagnostics for ruling out star spots as the potential origin of the RV signal (e.g. Prato et al. 2008; Mahmud et al. 2011).

In this chapter, we present multi-epoch RV measurements of the young Herbig star HD 142527 observed with high-resolution optical and NIR spectrographs. The chapter is organized as follows: Sec. 4.2 describes the star-disk system and presents the derived stellar parameter for HD 142527. The spectroscopic observations and data reduction is presented in Sec. 4.3. In Sec. 4.4 the analysis of the RV and photometric measurements is presented. A detailed analysis of accretion tracers is provided in Sec. 4.5. A discussion of the results and conclusions can be found in Sects. 4.6 and 4.7. The Appendix provides a table with the measured RV values and detailed plots of selected lines for accretion analysis.

4.2 HD 142527: a young star-disk system

HD 142527 is an F6 to F7IIIe (Houk 1978; van den Ancker et al. 1998) Herbig star and is associated with the star-forming region Sco OB2-2 (Acke & van den Ancker 2004) located at 145 pc (de Zeeuw et al. 1999).

4.2.1 Disk properties

Verhoeff et al. (2011) carried out a comprehensive analysis of the star and modeled its circumstellar environment using data of different instruments (VISIR, Subaru, MIDI, *Spitzer*, ISO, SEST, ATCA) and observing techniques (imaging, spectroscopy, interferometry, photometry). We will summarize their results of the geometric components in the following.

Inner disk. HD 142527 is surrounded by an inner, thin, and self-shadowed disk (height of puffed up inner rim is $7 \cdot 10^{-3}$ AU) ranging from 0.3 to 30 AU containing only $2.5 \cdot 10^{-9} M_{\odot}$ of small dust grains probably because of already formed planetesimals or larger bodies. Verhoeff et al. (2011) also identified a halo like structure, which contains an estimated dust mass of only $1.3 \cdot 10^{-10} M_{\odot}$. The highly processed dust (crystallinity of 20%, degree of sedimentation is 0.4 compared with the gas) leads to the conclusion of an evolved state.

Gap. The region between 30 and 130 AU is devoid of small dust grains. Verhoeff et al. (2011) argued that the most likely scenario for such a big gap is that it was formed due to the formation of one or more Jupiter-like planets, because photo-evaporation is only effective inward of ≈ 30 AU.

Outer disk. At 130 to ≈ 200 AU a self-shadowed massive outer disk containing $1 \cdot 10^{-3} M_{\odot}$ of dust is present, which is highly processed (containing crystalline H₂O ice and forsterite). Because of the thin inner disk almost all IR radiation emitted by the central star can be processed

Table 4.1: Stellar parameters of HD 142527.

Parameter	Verhoeff et al. (2011)	This work
	Value	Value
Spectral type	F6IIIe	
<i>distance</i> / [pc]	145±15	–
L_{\star} / [L_{\odot}]	20±2	20±2 ^a
T_{eff} / [K]	6250	6400 ± 125
$\log g$ / [cm s^{-2}]	3.62±0.13	3.69±0.38
M_{\star} / [M_{\odot}]	2.2±0.3	2.2±0.1
<i>age</i> / [Myr]	5 ⁺⁷ ₋₃	4±1
R_{\star} / [R_{\odot}]	3.8 ± 0.3	3.6±0.4
$v \sin i$ / [km s^{-1}]	–	50.0±3.5

Notes. ^(a) We adopted the value for the stellar luminosity from Verhoeff et al. (2011).

by the outer disk. Therefore, the height of the inner rim of the outer disk reaches 60 AU. In addition, scattered light images obtained in the *H*- and *K*-band by Fukagawa et al. (2006) revealed the presence of two arcs in the outer disk.

The inclination of the inner and outer disk is found to be similar and has a value of $i_{\text{disk}} = 20^{\circ} \pm 10^{\circ}$ (Verhoeff et al. 2011). This is in agreement with the measured value of 30° by Fukagawa et al. (2006), whose analysis is based on adaptive optics *H*- and *K*-band observations. There are also indications for ongoing accretion onto the star. Garcia Lopez et al. (2006) derived a value for the mass accretion rate of $\dot{M}_{\text{acc}} \approx 7 \cdot 10^{-8} M_{\odot} \text{ yr}^{-1}$ using the Br γ emission line in the NIR.

4.2.2 Stellar parameters

Table 4.1 lists the stellar parameters of HD 142527 derived by Verhoeff et al. (2011) and by us. We derived the stellar parameters T_{eff} , $\log g$, and $v \sin i$ using a self-developed tool for retrieving stellar parameters of Herbig stars based on fitting synthetic spectra to the observed stellar spectrum. The computation of the synthetic spectrum was carried out using SPECTRUM¹ (Gray & Corbally 1994) with the ATLAS9 atmosphere models (Castelli & Kurucz 2004). Figure 4.1 shows a part of the observed stellar spectrum of HD 142527 (black line, observed at JD=2454312.65436) by FEROS, that is well fitted by a single star synthetic spectrum (red line). Using the stellar luminosity value of $20 \pm 2 L_{\odot}$ found by Verhoeff et al. (2011) we obtained the stellar mass, radius, and age of HD 142527 from the position in the H-R diagram (Fig. 4.2). The derived stellar parameters by our method confirm the values found by Verhoeff et al. (2011). The age of 4 ± 1 Myr compares well with the general age of 5 Myr of stars in the Sco OB2-2 region derived by Carpenter et al. (2006).

¹<http://www.phys.appstate.edu/spectrum/spectrum.html>

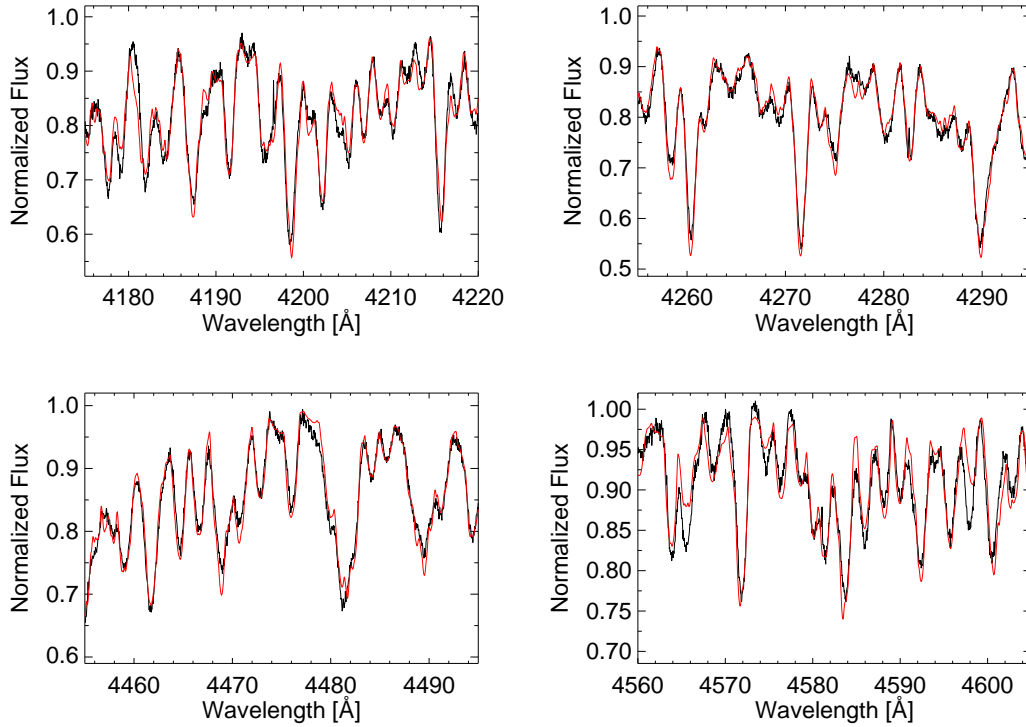


Figure 4.1: The spectral windows used for fitting the synthetic spectrum (red line) to the observed stellar spectrum (black line) of HD 142527.

4.3 Observations and data reduction

We observed HD 142527 using high-resolution optical and NIR spectrographs located at ESO’s La Silla and Paranal observatories over a time period of 3.7 years and obtained 119 spectra in total. In the following sections we describe the observation and data reduction process for each instrument.

4.3.1 FEROS

We obtained 93 multi-epoch spectra between July 2007 and April 2011 using the FEROS² spectrograph (Kaufer et al. 1999) at the 2.2m MPG/ESO telescope at La Silla observatory in Chile. FEROS covers the whole optical spectral range from 3600 Å to 9200 Å and provides a spectral resolution of $\approx 48\,000$.

Except for seven spectra, which were obtained using the object-sky mode, all spectra were obtained using the object-calibration mode where one of the two fibers is positioned on the target star and the other fiber is simultaneously fed with the light of a ThAr+Ne calibration lamp, which serves as a wavelength reference. This mode allows to monitor and correct for the intrinsic velocity drift of the instrument. The reduction of the raw data was performed using

²FEROS stands for Fibre-fed Extended Range Optical Spectrograph

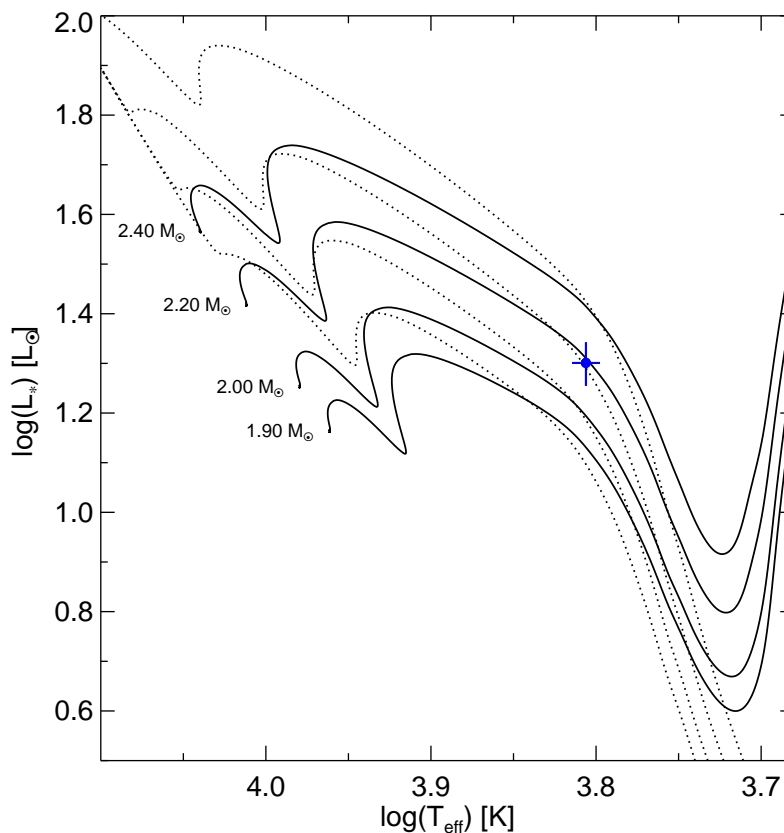


Figure 4.2: The position of HD 142527 in an H-R diagram along with the evolutionary tracks of Tognelli et al. (2011) for solar metallicity.

the FEROS Data Reduction System (DRS) available at ESO's web page³. The pipeline does the bias subtraction, flat-fielding, traces and extracts the individual echelle orders, applies the wavelength calibration, and corrects for the barycentric motion. For each exposure, it produces 39 individual sub-spectra representing the individual echelle orders, as well as one merged spectrum.

The average exposure time was 960 seconds per spectrum, which results in an average signal-to-noise ratio (SNR) of ≈ 300 per pixel at 5500 \AA .

4.3.2 HARPS

HARPS⁴ (Mayor et al. 2003) is a fibre-fed, cross-dispersed echelle spectrograph located at the 3.6m ESO telescope, providing a spectral resolution of 115 000, and covers a spectral range from 3800 to 6900 \AA . Similar to FEROS, HARPS is recoding simultaneously the spectrum of a ThAr lamp.

³<http://www.eso.org/sci/facilities/lasilla/instruments/feros/>

⁴HARPS stands for High Accuracy Radial velocity Planet Searcher

Between April 2008 and March 2009 we observed 16 spectra in total. The data were reduced using the data reduction software (pipeline) available at the telescope. The pipeline corrects for detector bias, dark, flatfield, cosmic ray removal, rebins the spectrum according to the wavelength calibration, and corrects for the barycentric motion. The average exposure time was 540 seconds per spectrum, which results in an average signal-to-noise ratio (SNR) of ≈ 90 at 5500 Å.

4.3.3 CRIRES

CRIRES⁵ (Kaeufl et al. 2004) is a high resolution, near-infrared spectrograph mounted on UT1 at ESOs VLT. We chose a wavelength setting near 1175 nm (order 48) after a careful study of the intrinsic stellar and telluric features in the near-infrared. For this study we constructed a detailed model spectrum of HD 142527, consisting of a reddened and flux calibrated high-resolution PHOENIX model atmosphere kindly provided by Peter Hauschildt ($T_{\text{eff}}=6300$ K, $\log g=3.5$, $[\text{Fe}/\text{H}]=0.0$) after adding additional continuum emission from dust in the circumstellar disk of HD 142527. We compared this model with a model of the Earths atmosphere and simulated the achievable RV precision for different CRIRES settings. Since the near-infrared excess emission of HD 142527 is very strong towards the *K*-band and the intrinsic equivalent widths of photospheric absorption lines are generally higher at shorter wavelengths, we found the best RV performance for HD 142527 can be achieved in the *J*-band. We obtained spectra for HD 142527 in this setting for 10 epochs spread over 62 days between July 2009 and September 2009. We made use of the CRIRES adaptive optics system, which was locked on the target and a 0.2'' slit to achieve the highest spectral resolving power of $R\sim 100,000$. Ten individual spectra per epoch were observed in an ABBA nodding pattern and reduced separately using a custom IDL pipeline described in Bean et al. (2010). The data reduction consisted of steps to correct the non-linearity of the detector, pairwise background and bias subtraction and division by a normalized flat-field. The SNR in the individual, optimum extracted one-dimensional spectra is between 100 and 130. The exposure time was always 30 seconds.

4.4 Data analysis and results

4.4.1 Optical *RV* measurements

The measurement of the stellar *RV* from FEROS spectra has been done by cross-correlating the stellar spectrum with a template spectrum. The template was a synthetic spectrum representing the fitted stellar parameters of HD 142527 (Table 4.1). We measure a projected rotational velocity, $v \sin i$, of 50.0 ± 3.5 km s⁻¹ (Sect. 4.2.2). Therefore, all stellar spectral lines are highly broadened and blended, which makes a determination of *RV* difficult since the accuracy is limited to some 100 m s⁻¹. For the cross-correlation, only the spectral range between 4000 to

⁵CRIRES stands for CRyogenic InfraRed Echelle Spectrograph

6500 Å was considered because the instrument efficiency of FEROS drops significantly outside this spectral range. In addition, areas with emission lines, telluric lines, Balmer lines, and other lines showing variability (e.g., Na I D, He I at 5876 Å) were carefully masked out. After this selection process, 19 individual echelle orders from FEROS were left, which were used to compute RV . The same procedure was used for the HARPS spectra. The only difference was that we had only the merged spectra and not the single echelle orders because the HARPS pipeline is only available at the telescope and only fully reduced and merged spectra are available from the ESO archive. Therefore, we divided the merged HARPS spectrum into 145 Å wide spectral windows, which resulted in 20 artificial single orders ranging from 4000 to 6900 Å. The same spectral regions masked out in the FEROS spectra were also masked out in the HARPS spectra, i.e. we used the same spectral lines for the computation of RV , resulting in 14 usable single orders. The resulting cross-correlation function was fitted by a Gaussian function. The position of the center of the Gaussian yields the RV . After the individual RV values were derived separately for each echelle order, the median value and standard deviation of RV were computed. All measured RV values are listed in Table A.1 provided in the appendix.

In Figure 4.3, we plot chronologically all optical and NIR RV measurements derived from FEROS, HARPS, and CRIRES. The median velocity is subtracted for the individual spectrographs. The rms of the whole data set is 290 m s^{-1} . Four data points from FEROS deviate more than 3σ from the whole sample. We carefully post-processed and checked the calibration, the reduction of the spectra, and the environmental conditions during observation. As we cannot identify any error in the reduction process nor do we see any unusual behavior, e.g. in the cross-correlation function, we assume that a physical effect, such as an increased activity level due to, e.g. accretion, causes the deviation of these data points. We will discuss this further in Sec. 4.5.1.

4.4.2 NIR RV measurements

Radial velocity measurements are obtained by simultaneously fitting a telluric model (see Seifahrt et al. 2010 for details) and a stellar template to all individual CRIRES spectra obtained for HD 142527. The telluric model provides a precise wavelength solution for each spectrum while the fit of the stellar template includes the sought-for RV of the star as a free fit parameter. The stellar template is an empirical spectrum of HD 142527 obtained during one of the observed epochs. Hence, the obtained radial velocities are relative in nature. The four CRIRES chips are always modeled separately. Chip one and the right half of chip four had to be excluded from the analysis due to strong order overlap which is a known feature of CRIRES in the J -band where the spectral orders are shorter than the coverage of the detector mosaic. Chip two does not contribute significantly to the RV signal due to the sparseness of stellar lines. The final per-epoch RV signal is thus entirely dominated by the spectral content of chip three and the uncompromised spectral range on chip four. The strongest limiting factor is the relatively high rotational velocity of HD 142527 ($v \sin i = 50 \text{ km s}^{-1}$) which broadens the photospheric absorption lines

and reduces their contrast significantly. The high line width also produces a cross-talk between the RV parameter and the continuum normalization in the fit, which drastically limits the achievable precision. Our epoch averaged RV uncertainty is thus only $\sim 150 \text{ m s}^{-1}$, falling short by at least an order of magnitude over what normally can be achieved on CRIRES without the use of a dedicated gas absorption cell as a calibrator. The measured NIR RV values are listed in Table A.1 provided in the appendix.

4.4.3 Radial velocity variations

Figure 4.3 shows all 119 RV measurements obtained from all spectrographs. Because the velocity offsets of HARPS and CRIRES relative to FEROS, $\Delta_{\text{HARPS-FEROS}}$ and $\Delta_{\text{CRIRES-FEROS}}$, respectively, are not known at this point of the analysis, we subtracted the median value of the RV for the data set of each spectrograph (see Sec. 4.4.4 fitted offset values). From this plot we can see peak-to-peak variations of 2 km s^{-1} present in RV . To identify periodici-

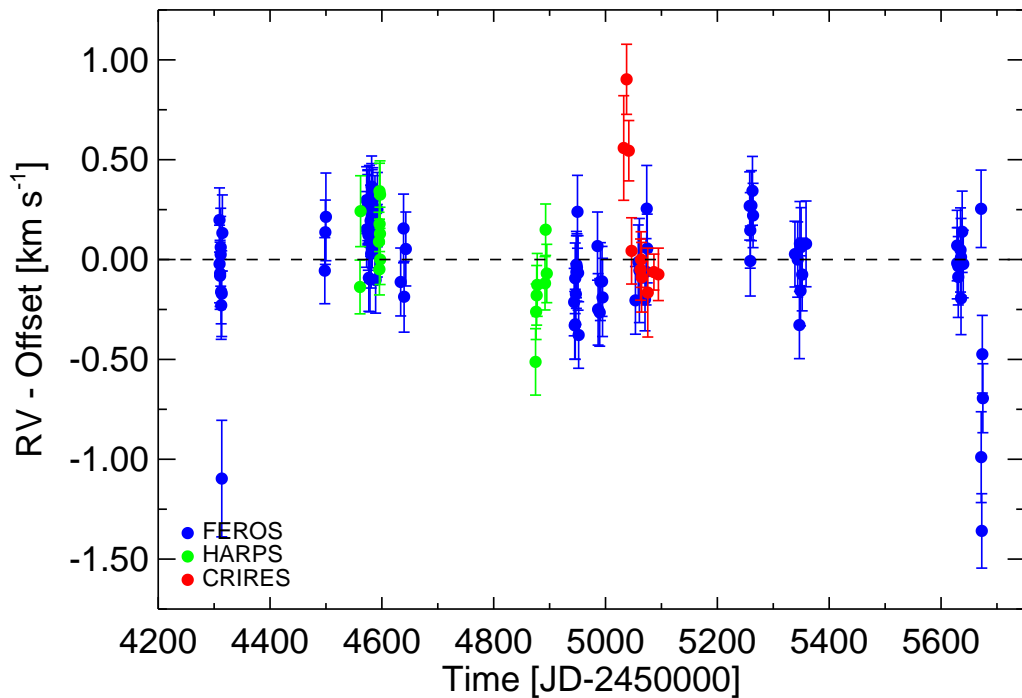


Figure 4.3: All measured RVs for HD 142527. The RV data obtained with FEROS and HARPS in the optical spectral range are blue and green colored, respectively. The NIR RV data obtained with CRIRES are red colored. For each data set the median velocity is subtracted as the relative RV offsets between the spectrographs is not known at this point. Peak-to-peak variations of $\approx 2 \text{ km s}^{-1}$ are present in the data.

ties present in the RV data, we computed the generalized Lomb-Scargle (GLS) periodogram (Zechmeister & Kürster 2009) and its window function (Fig. 4.4). We included all 119 RV

data for the computation, i.e. the optical as well as the NIR measurements. The justification of this step will be given in Sec. 4.4.4. For a better visibility of longer periods, we plotted the GLS periodogram on a logarithmic scale for the period. The GLS periodogram revealed a

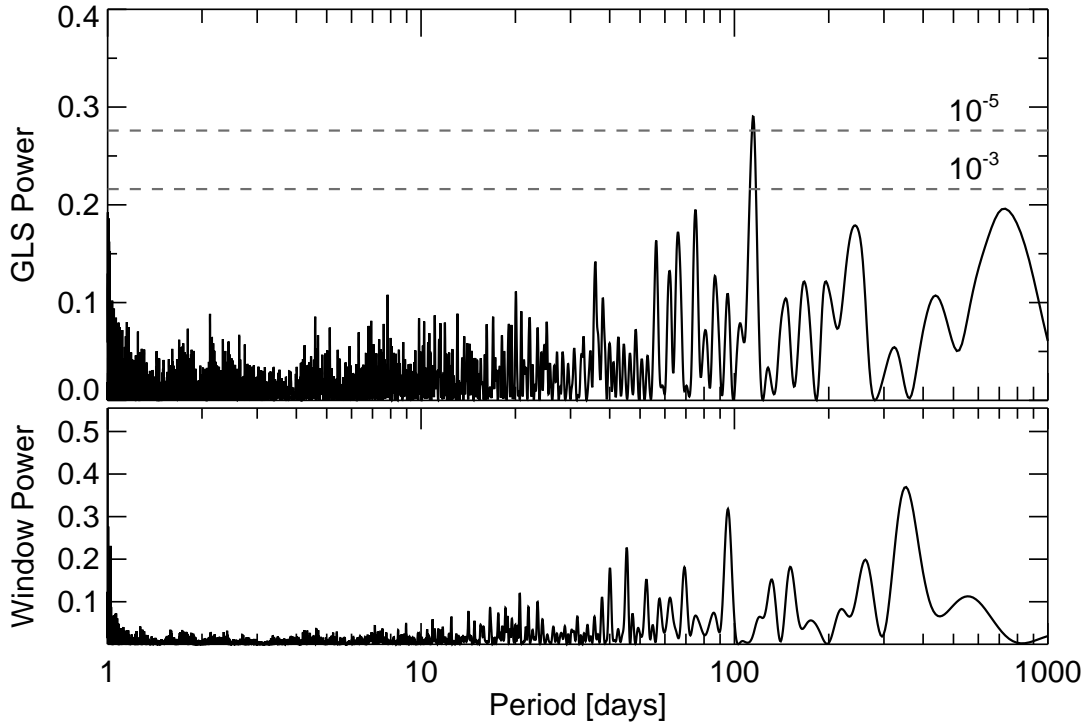


Figure 4.4: GLS periodogram (upper plot) of all, i.e. optical and NIR, RV data, and the corresponding window function (lower plot). The median velocity of the individual data sets was subtracted when the GLS was computed. The two horizontal dashed lines indicate FAP levels of 10^{-3} and 10^{-5} . The highest peak at a period of 114.6 d has a FAP of $3.1 \cdot 10^{-6}$.

significant peak at a period of 114.6 d with a false alarm probability (FAP) of $3.1 \cdot 10^{-6}$. In addition, there are several peaks at shorter and longer periods present, but they are less significant with FAPs higher by four order of magnitudes compared to the 114.6 d period. These other peaks are expected to be aliases as the periodogram is a convolution of the astrophysical signal present in the data and the sampling function of these data (window function). Typical sampling frequencies are caused by Earth’s rotation (daily visibility) and the seasonal visibility of the object. Figure 4.5 is a zoom into the window function on a frequency scale. Major peaks that can cause alias peaks in the periodogram are marked by a different color and a dedicated symbol of type $f_{s,i}$, where s stands for “sampling” and i is the i -th sampling frequency. An alias frequency appears at a position $f_{a,i} = f_0 \pm f_{s,i}$ in the GLS periodogram where f_0 is the assumed true frequency present in the data, which is $8.727 \cdot 10^{-3} \text{ d}^{-1}$ (114.6 d) in our case. In Table 4.2 all sampling frequencies of the window function showing a major peak are listed as well as the expected and identified alias frequencies of the GLS periodogram. Figure 4.6 shows a zoom into the GLS periodogram where the most prominent peaks are present. The

imprinted arrows show the position of the expected alias frequencies computed from Table 4.2. The color of the arrows indicate from which sampling frequency present in the window function they were computed (Fig. 4.5). For example the green arrows in the GLS periodogram, $f_{a,4}$ and $f_{a,5}$, indicate the position of the aliases caused by the sampling frequency $f_{s,1}$ of the window function. All peaks present in the GLS periodogram can be described as alias frequencies using $f_0 = 8.727 \cdot 10^{-3} \text{ d}^{-1}$ (114.6 d). An additional check of our hypothesis, that the 114.6 d

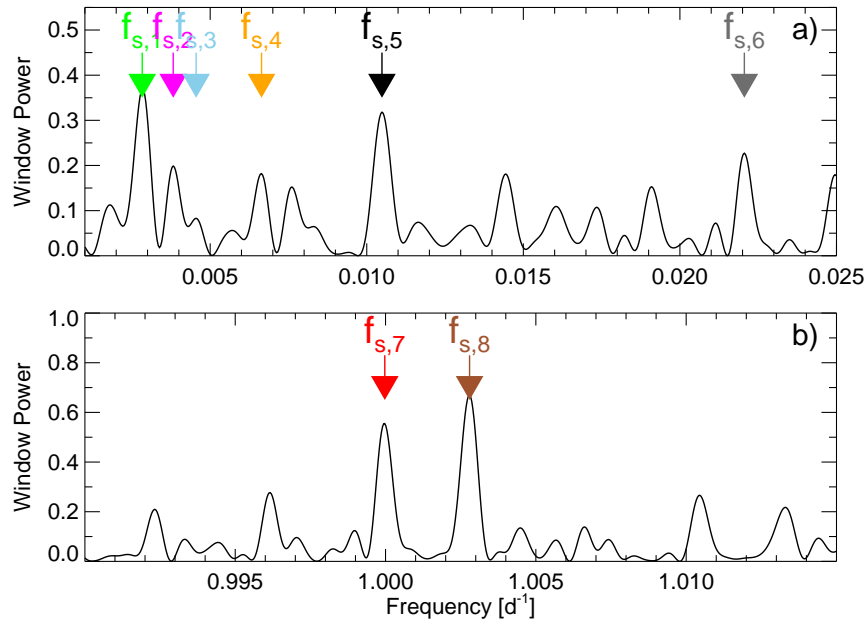


Figure 4.5: Zoom into the window function of the RV data set. Plot a) shows the peaks at short frequencies and plot b) shows the peaks at around 1 d^{-1} . Arrows mark significant alias frequencies present in the window function.

period, which is detected by the GLS periodogram with high significance, is the real period present in the RV data, we computed an amplitude spectrum using the CLEAN deconvolution algorithm (Roberts et al. 1987, written in IDL by A. W. Fullerton). This algorithm deconvolves the window function from the Fourier transform of the RV data set. Therefore, the resulting spectrum should contain only real periods present in the data with their aliases removed. Figure 4.7 shows the CLEANed amplitude spectrum for the entire RV data set (optical and NIR). We used a gain of 0.5 with 100 iterations. As for the GLS periodogram, the median velocity of the individual data sets was subtracted. The only peak present in the CLEANed spectrum appears at 114 d. Together with the computation and analysis of the GLS periodogram we conclude that the 114.6 d period is the real period of the RV variations present in the current data set.

Table 4.2: Sampling frequencies $f_{s,i}$ obtained from the computed window function of the RV data. The expected and identified alias frequencies are computed by $f_{a,j} = f_0 \pm f_{s,i}$, where $f_0 = 8.727 \cdot 10^{-3} \text{ d}^{-1}$.

Sampling frequency $f_{s,i} [\text{d}^{-1}]$	Expected and identified alias frequency	
	$f_0 + f_{s,i} [\text{d}^{-1}]$	$f_0 - f_{s,i} [\text{d}^{-1}]$
^a $f_{s,1} = 2.831 \cdot 10^{-3}$	$f_{a,5} = 1.1559 \cdot 10^{-2}$	$f_{a,4} = 5.896 \cdot 10^{-3}$
$f_{s,2} = 3.820 \cdot 10^{-3}$	–	$f_{a,3} = 4.907 \cdot 10^{-3}$
$f_{s,3} = 4.552 \cdot 10^{-3}$	–	$f_{a,2} = 4.175 \cdot 10^{-3}$
$f_{s,4} = 6.640 \cdot 10^{-3}$	$f_{a,7} = 1.537 \cdot 10^{-2}$	–
$f_{s,5} = 1.0485 \cdot 10^{-2}$	–	$f_{a,1} = -1.758 \cdot 10^{-3} $
$f_{s,6} = 2.2058 \cdot 10^{-2}$	–	$f_{a,6} = -1.3331 \cdot 10^{-2} $
^b $f_{s,7} = 0.99997$	$f_{a,10} = 1.00870$	$f_{a,8} = -0.99125 $
^c $f_{s,8} = 1.00279$	$f_{a,11} = 1.01152$	$f_{a,9} = -0.99408 $

Notes. ^(a) 1 year⁻¹, ^(b) 1 (solar day)⁻¹, ^(c) 1 (sidereal day)⁻¹.

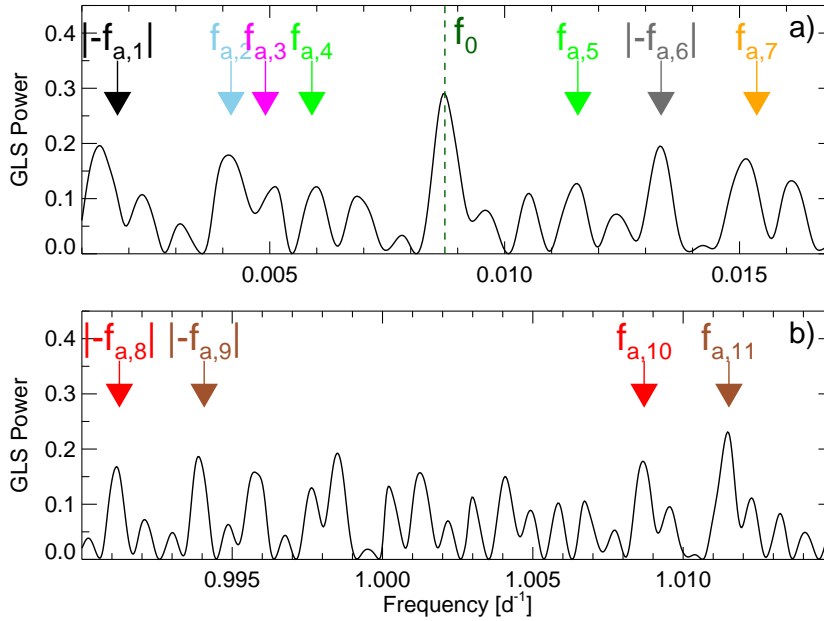


Figure 4.6: Zoom into the GLS periodogram where the most prominent peaks occur, which is at around 0.01 d^{-1} (panel a), long periods) and at around 1 d^{-1} (panel b). The vertical dashed line marks the $8.727 \cdot 10^{-3} \text{ d}^{-1}$ frequency (114.6 d period), which is assumed to be the true frequency of the RV data. Arrows mark the expected positions of the alias frequencies based on identified peaks of the window function. If the sampling frequency $f_{s,i}$ is greater than f_0 than the alias frequencies $f_{a,i} = f_0 - f_{s,i}$ are smaller than 0 frequency and would occur at a symmetric position relative to its positive counterpart, $f_{a,i} = f_0 + f_{s,i}$, in the GLS periodogram if the plot would be flipped across 0 frequency. If this is the case we list the alias frequency as $| -f_{a,i} |$.

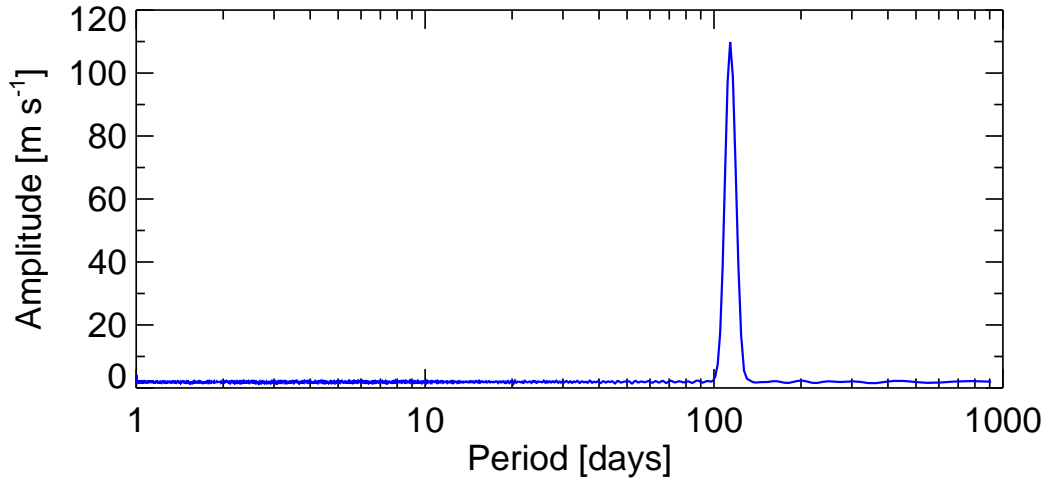


Figure 4.7: CLEANed amplitude spectrum of all, i.e. optical and NIR, RV data. The median velocity of the individual data sets was subtracted for the computation of the CLEANed amplitude spectrum. The highest peak is located at a period of 114 d.

4.4.4 Orbital parameters

Activity features, such as stellar spots, can mimic RV variations due to their temperature contrast with respect to the stellar photosphere. The amplitude of an observed RV variation is independent of wavelength if another body, e.g. planetary companion, is orbiting the star. To test this scenario on our data set, we first performed a full Keplerian fit to the *optical* RV data (Fig. 4.8). The velocity offset $\Delta_{\text{HARPS-FEROS}}$ is treated as free parameter and fitted simultaneously. The best Keplerian fit has a period of 114.7 ± 0.6 d and a semi-amplitude of $K_{\text{VIS}} = 208 \pm 28$ m s $^{-1}$. In a second step, we fitted the CRIRES NIR RV measurements only, while keeping all parameters derived from the fit of the optical data fixed, except semi-amplitude and instrumental offset. Figure 4.9 shows the result of this procedure. The derived semi-amplitude is $K_{\text{NIR}} = 316 \pm 64$ m s $^{-1}$. The NIR RV semi-amplitude K_{NIR} is not lower than K_{VIS} as it would be expected from the rotational modulation caused by, e.g. a stellar spot. In addition, from Figure 4.9 we can also see that the NIR RV data follow qualitatively the proposed Kepler fit from the optical data with respect to amplitude, period, phase, and eccentricity. The bad data sampling (only 50% of the orbit are covered) as well as the difficulty of NIR RV measurements for HD 142527 (high $v \sin i$, few lines), which result in a higher scatter of the data points, makes an independent Keplerian fit of the NIR RV data not meaningful. From this analysis, we still can conclude that the observed RV signal does not depend on the wavelength. Hence, the observed periodic 114.6 d signal in RV can be caused only by a companion. Thus, it is valid to merge the optical and NIR RV data sets and to perform a joined Keplerian fit.

We fitted a Keplerian orbit to all RV data simultaneously. The velocity offsets $\Delta_{\text{HARPS-FEROS}}$

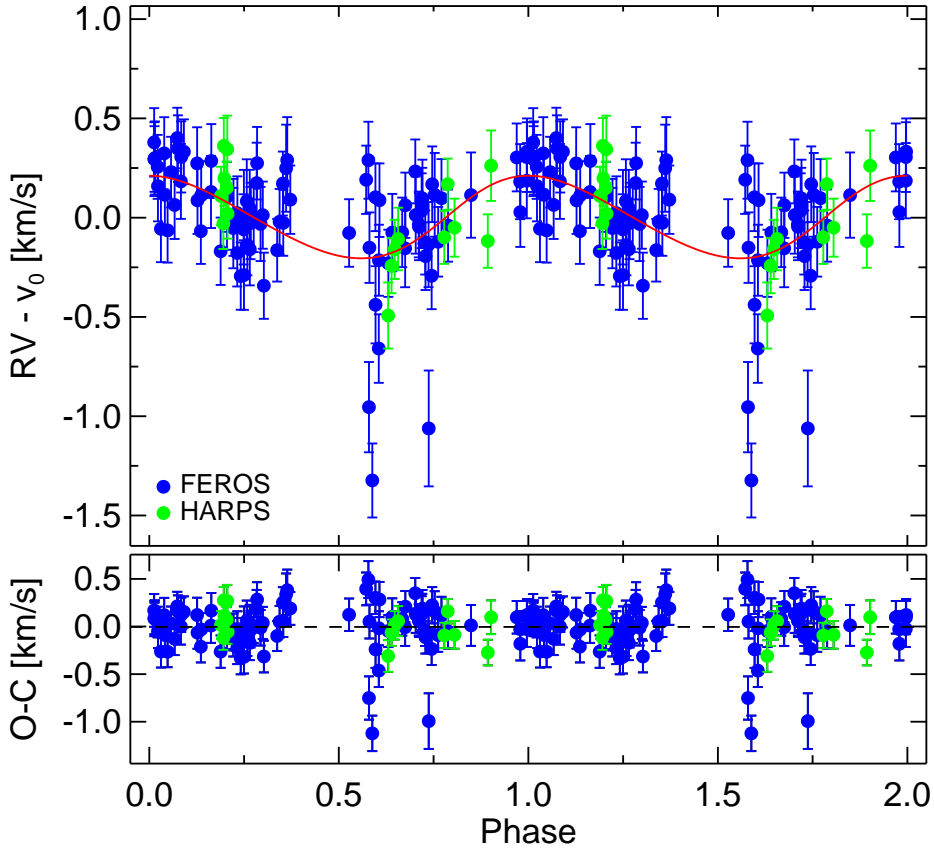


Figure 4.8: Upper panel: Phase-folded plot of the *optical* RV data only. Blue and green data points correspond to FEROS and HARPS measurements, respectively. The red solid line shows the best Keplerian fit for a period of 114.7 ± 0.6 d and an amplitude of 208 ± 28 m s $^{-1}$. The orbit of the planet is slightly eccentric with $e = 0.09^{+0.15}_{-0.09}$. Lower panel: RV residuals.

and $\Delta_{\text{CRIRES-FEROS}}$ are treated as free parameters and fitted simultaneously. The fit revealed a $m \sin i = 8.5 \pm 1.0$ M $_J$ companion on a slightly eccentric orbit ($e = 0.23$) with a semi-major axis of 0.60 AU. Table 4.3 lists the derived orbital and fit parameters. Fig. 4.10 shows the RV data phase-folded with a 114.6 d period. The Kepler fit is imprinted as a black solid line. The lower panel of Fig. 4.10 shows the RV residuals. The rms value of the residuals is 236 m s $^{-1}$, which is higher than the average error of our RV measurements. Therefore, an additional signal present in our RV data set is expected. We computed the GLS periodogram of the RV residuals, which is shown in Fig. 4.11. For a better comparison with the original GLS periodogram (Fig. 4.4) the scale of the axes are identical. No additional significant period is apparent in the RV data. Therefore, the residual rms is not due to additional companion or periodic rotational modulation, but more likely stochastic activity noise. In addition, we used an F -test to evaluate the significance of the Keplerian fit, which yield a confidence of $> 5.6 \sigma$.

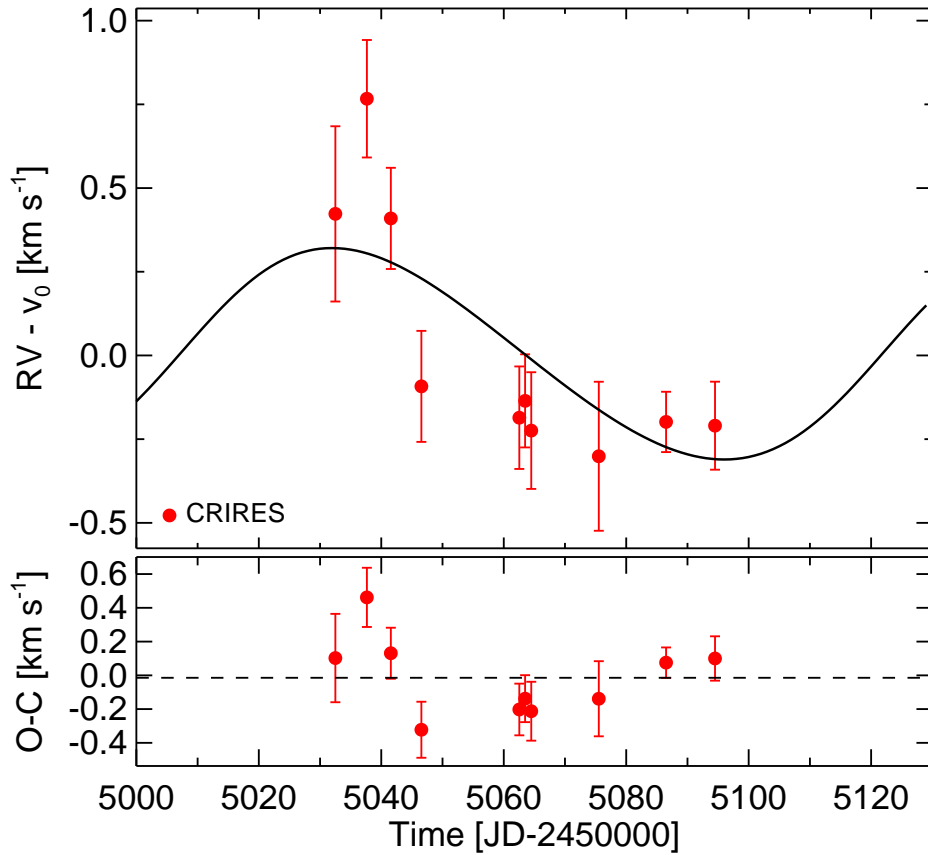


Figure 4.9: Upper panel: Keplerian fit (black line) of the CRIRES NIR RV data only. All parameters derived from the fit of the optical data were fixed, except semi-amplitude and instrumental offset. The semi-amplitude is $K_{\text{NIR}} = 316 \pm 64 \text{ m s}^{-1}$.

Table 4.3: Orbital and physical parameters derived for the best-fit Keplerian model of HD 142527 b.

Parameter	Value
Orbital period P / [d]	114.5 ± 0.6
Velocity amplitude K / [m s^{-1}]	217 ± 24
Eccentricity e	0.23 ± 0.12
Argument of periapsis ω / [deg]	358 ± 28
Periastron time T_0 / [JD-2,400,000]	54348 ± 9
System velocity v_0 / [m s^{-1}]	-1280 ± 20
$\Delta_{\text{HARPS-FEROS}}$ / [m s^{-1}]	512 ± 46
$\Delta_{\text{CRIRES-FEROS}}$ / [m s^{-1}]	1242 ± 53
$m \sin i$ / [M_{J}]	8.5 ± 1.0
Mass function $f(m)$ / [$10^{-7} M_{\odot}$]	1.114
Semimajor axis a / [AU]	0.60 ± 0.01
rms / [m s^{-1}]	236
χ_{red}^2	1.67

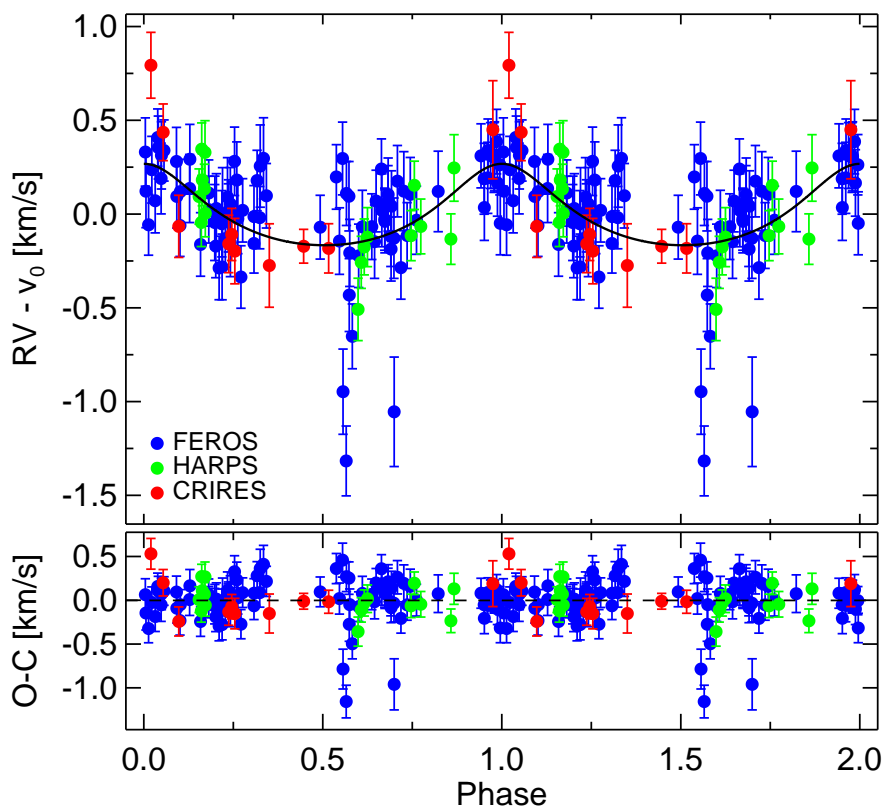


Figure 4.10: Upper panel: Phase-folded plot of the RV data. The black solid line shows the Kepler fit for a period of 114.5 ± 0.6 d and an amplitude of 217 ± 24 m s^{-1} . The orbit of the low-mass companion is slightly eccentric with $e = 0.23 \pm 0.12$. For a better distinction of the data sets of the three spectrographs, the data are colored. FEROS data are shown in blue, HARPS data in green, and CRIRES data in red. Lower panel: RV residuals.

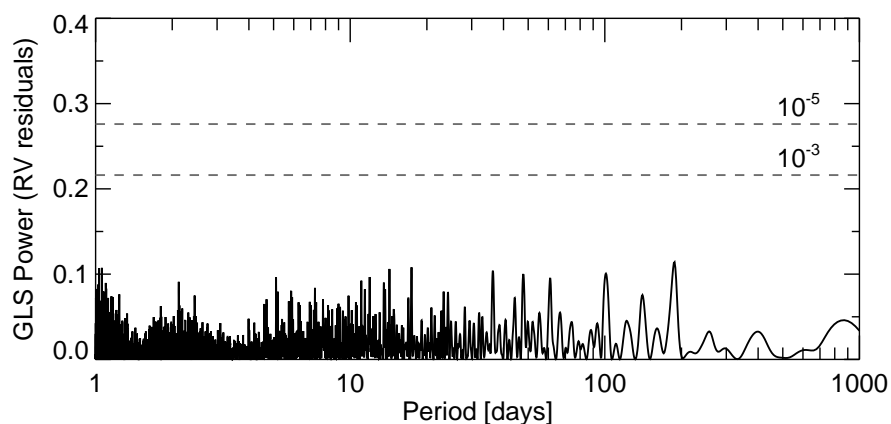


Figure 4.11: GLS periodogram of the RV residuals after the Kepler fit was subtracted. The scale of the axes and the imprinted FAP levels (horizontal dashed lines) are similar to Fig. 4.4 for better comparison. There is no additional significant signal present in the RV data.

4.4.5 Stellar rotation period: *Hipparcos* photometry

The *Hipparcos* photometry (Perryman & ESA 1997) for HD 142527 was analyzed to see whether periodic variations related to its stellar rotation are present. The light curve consists of 91 data points and covers 1123 days. The average sampling between the individual transits of *Hipparcos* was one hour. We only considered measurements where the quality flag was set to bit 0 or bit 1, leaving us 89 data points. Figure 4.12 shows the GLS periodogram of the photometric data after we subtracted a long-term trend. A significant period of 1.21 d with a FAP of $5.8 \cdot 10^{-6}$ is present. In addition, we computed the CLEANed amplitude spectrum of the photometric data (Fig. 4.13) and the most prominent peak is located at a period of 1.21 d, similar to the result of the GLS periodogram. A phase-folded plot for the prewhitened data (black data points) and the sinusoidal fit (red line) is shown in Fig. 4.14.

The maximum rotational period $P/\sin i$ of the star is 3.64 ± 0.48 days based on its stellar radius and the measured $v \sin i$ (Table 4.1). If the 1.21 d period is related to the stellar rotation, the inclination of the stellar rotation axis can be computed to be $20^\circ \pm 3^\circ$ through computed R_\star and measured $v \sin i$, which matches the value of the disk inclination of $20^\circ \pm 10^\circ$ (Sec. 4.2.1). Thus, we conclude that the observed 1.21 d period is the stellar rotational period. Therefore, we can assume that the orientation of the stellar rotation axis is almost perpendicular to the mid-plane of the disk. This allows us to estimate the true mass of the companion to $m = 25 \pm 6 M_J$. In addition, the true equatorial velocity of HD 142527 can be computed to $146 \pm 24 \text{ km s}^{-1}$.

4.5 Accretion tracers

A widely used and routinely applied method to check if RV variations are mimicked by line shape variations, is the measurement of the so called bisector. A correlation between bisector quantities, such as velocity span, velocity displacement, and curvature (e.g. Povich et al. 2001), with RV measurements usually indicate a rotational modulation of the RV signal by stellar activity, which can mimic the presence of a planetary companion (see Queloz et al. 2001 for an example). However, this analysis is not applicable to stars with high $v \sin i$ values. The rotational broadening leads to strong line blends and individual bisectors cannot be measured.

The effect of rotational modulation of RV s caused by activity processes, which might be present on the stellar surface, can be already excluded for HD 142527 as the rotational period of the star with 1.21 d (see Sec. 4.4.5) is two orders of magnitude lower than the observed 114.5 d RV variations. This is supported by the lack of significant periods lower than the companions period in the residual RV GLS periodogram (Fig. 4.11) as well as in the CLEANed amplitude spectrum (Fig. 4.7). But there is still a possibility that the spectra of HD 142527 are affected by physical processes of its inner disk, and therefore, we might trace, e.g. a hot spot from the inner rim of the inner disk where an accretion funnel flow emerges with the RV measurements.

Our large data set of optical spectra (109 in total), covering over 3.7 years, allows us to interpret and characterize physical processes of the inner disk to some extent. In particular, we

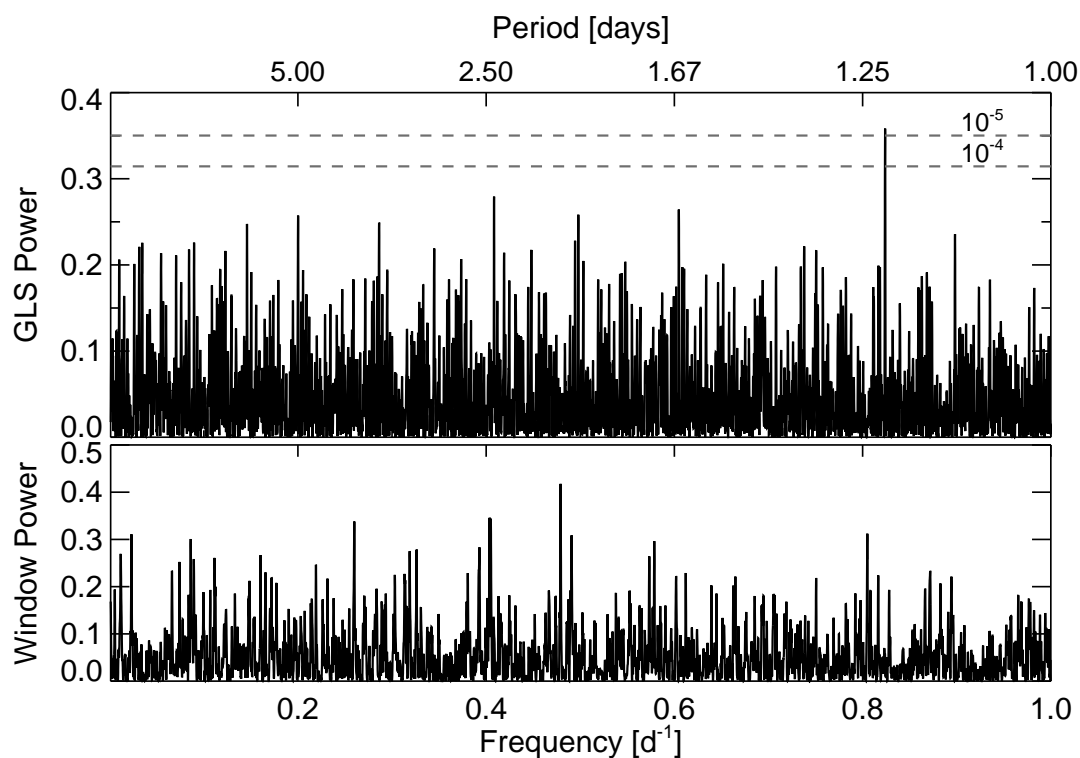


Figure 4.12: GLS periodogram of the *Hipparcos* data after a long term trend has been removed. The two horizontal dashed lines indicate FAP levels of 10^{-4} and 10^{-5} . The most significant peak at 1.21 d has a FAP of $5.8 \cdot 10^{-6}$.

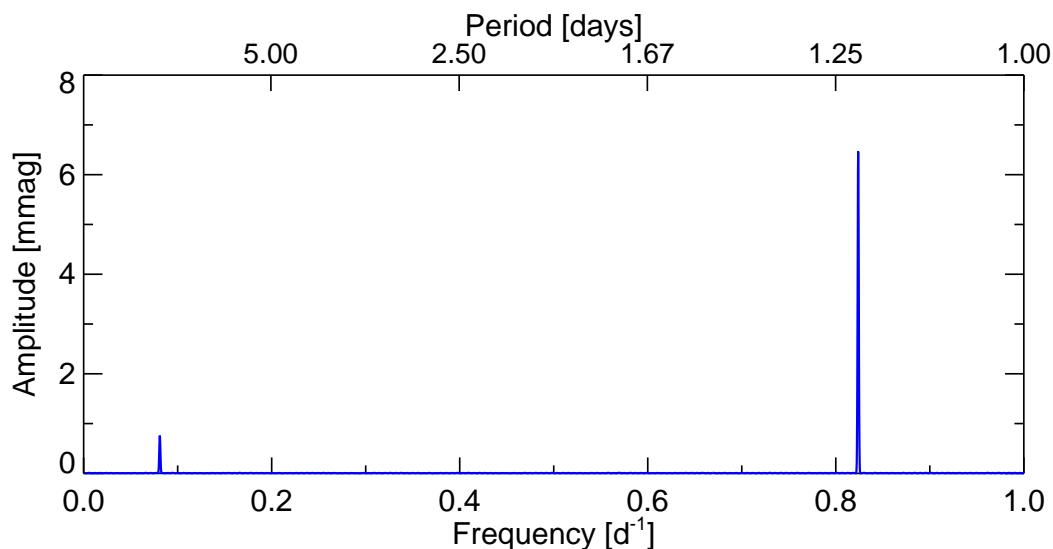


Figure 4.13: CLEANed amplitude spectrum of the *Hipparcos* data after a long term trend has been removed. The highest peak is located at a period of 1.21 d.

examined several lines to be known as accretion tracers, which are: Ca II K and H, $H\alpha$, $H\beta$, $H\gamma$, $H\delta$, He I at $\lambda 5876\text{\AA}$, Na I D doublet, and Ca II at $\lambda 8498\text{\AA}$ and $\lambda 8662\text{\AA}$. We checked for

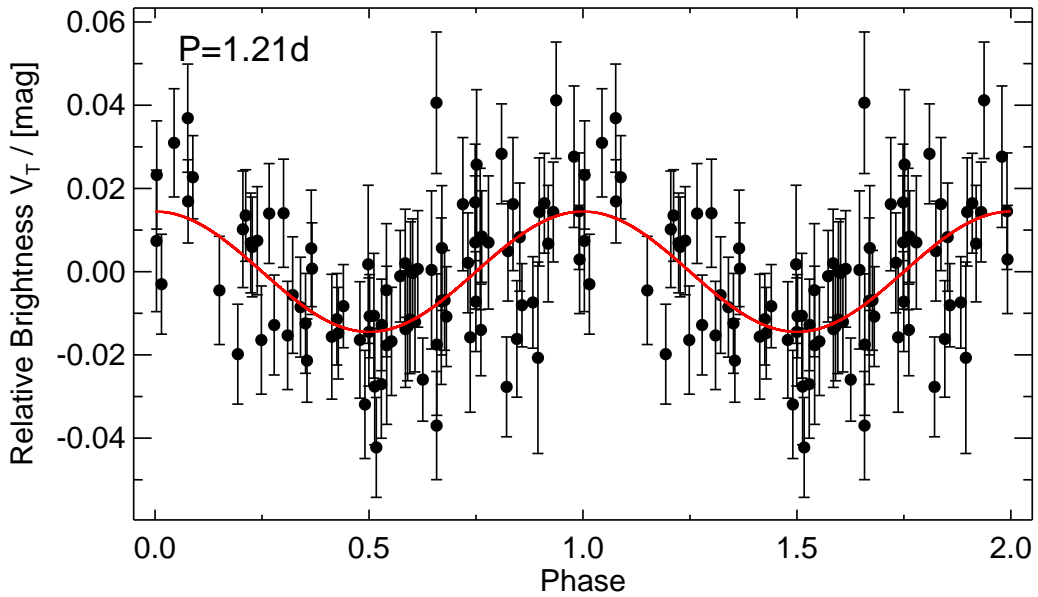


Figure 4.14: *Hipparcos* data phase-folded with a period of 1.21 days after a long term trend has been removed. The red line is a sinusoidal fit with an amplitude of 14 ± 2 mmag.

temporal line variations, periodicities, and correlations. The aim of the following analysis is not to provide a detailed explanation of the physical processes, which take place in the circumstellar environment of HD 142527, but to reliably verify that the observed *RV* are caused by a low-mass companion present inside the inner disk.

4.5.1 Line profiles and variance

In Appendix B, we plot the selected spectral lines for all our spectra in chronological order (Fig. B.1 to Fig. B.10). All spectra (shown in black) are normalized and corrected for median *RV*. A synthetic photospheric line profile, which was computed based on the derived stellar parameters for HD 142527 (Table 4.1), is over-plotted in green. The position of the line center at zero velocity is marked by the vertical dotted line. The inset numbers indicate the time of observation in days with respect to the first observation. The inset letters F and H indicate if the spectrum was observed with FEROS or HARPS. For Ca II at $\lambda 8498\text{\AA}$ and $\lambda 8662\text{\AA}$, only FEROS spectra are available (93 in total) because the spectral coverage of HARPS ends at 6910\AA .

From the plots we already can recognize complex line shapes and variations over time. The line cores are filled up by emission for all epochs. Especially for He I and Na I D we see strong red and blueshifted absorption components, indicating the presence of material in-fall (e.g. Edwards et al. 1994) towards the stellar surface and outflows, respectively. Especially the last five epochs exhibit very strong redshifted absorption features compared to the previous epochs. At the same time, the *RV* values from these epochs deviate significantly from the aver-

age variation (Fig. 4.3). We might see here indications for a variable accretion rate. Significant parts of the optical spectra, i.e. photospheric lines, have to be affected in order to produce the observed deviation. However, we do not find an indication for perturbation in the photospheric lines of the last five spectra of HD 142527.

Due to the complexity and variability of the spectral lines, a modeling approach does not seem to be reasonable for our purpose. As a first step to quantify the observed line profile variability, we computed the average line profile and the normalized variance profile (Fig. 4.15). For the computation of the normalized variance profile, we follow the approach by Johns & Basri (1995), where the variance is computed for each velocity channel and divided by the averaged line profile. The advantage of such an computation is evident: (i) all variance profiles can be compared with each other as they are normalized, (ii) regions with significant variability can be identified immediately. All lines, except $H\delta$, show higher variability on the red side than on the blue side and show variability between approximately -200 and 200 km s^{-1} on average over the line profile. The average Na I D profile shows a broad emission component with clear absorption features on the blue and red side at $\approx -50 \text{ km s}^{-1}$ and $\approx 30 \text{ km s}^{-1}$ of the line profile, respectively. The average line profile of He I shows similar features but less distinct.

4.5.2 Velocity correlation matrices

An interesting question is if the observed variations on the red and blueshifted side of the line profiles are correlated with each other. In order to quantify such an effect, we computed velocity correlation matrices. The computation is straightforward (e.g. Johns & Basri 1995): the linear Pearson correlation coefficient r is computed for all combinations of velocity channels (x, y) over the entire line profile. The resulting matrices are symmetric across the main diagonal because of $r(x, y) = r(y, x)$. In addition, if $x = y$ then $r(x, y) = 1$, i.e. each matrix will have a main diagonal with $r = 1$. The results for all our selected line sample are plotted in Fig. 4.16. In order to guide the interpretation we also simulated velocity correlation matrices for simplified cases to demonstrate various effects, which can occur over a line profile. The results can be found in Appendix D. All correlation matrices are plotted as colored contours and span the entire range of possible values for r , i.e. ranging from -1 to $+1$ in order to identify negative correlations, too. For the entire selected line sample we do not see any significant negative correlation. Areas colored light blue, yellow, and green are uncorrelated. The areas colored dark red show significant positive correlation. All lines show a relatively simple correlation profile. The correlation contours show well correlation on a local scale of the order of $\approx 100 \text{ km s}^{-1}$. Thus, the appearing and disappearing red and blueshifted absorption components observed in the line profiles do not affect the line wings far out, resulting in a slim correlation contour. That means, the entire line profile is not correlated with itself, especially the blue and redshifted absorption components show no common correlation. For $H\alpha$, a central bulge with an extension of roughly -100 to $+100 \text{ km s}^{-1}$ is observed. This is caused by a central narrow feature present in this line, which flattens out and reappears over the course of observation. Most lines show

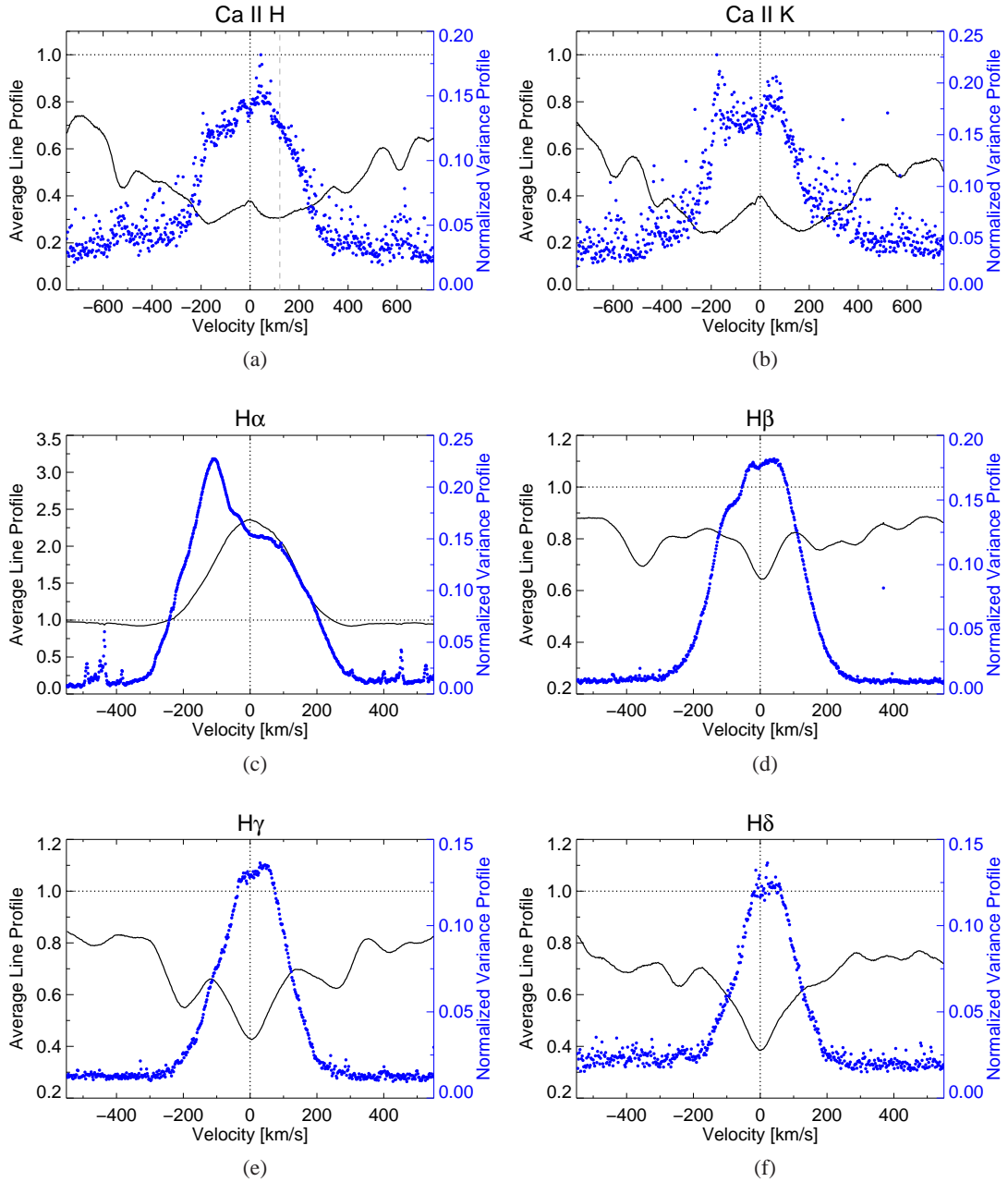


Figure 4.15: Average line profiles (black lines) and normalized variance profiles of selected spectral lines.

a bulge structure, extending from 0 to 150 km s^{-1} , in their correlation matrices. From the normalized variance profiles (Fig. 4.15) we see that the redshifted part of the line profiles show the highest variability. In addition, the variance profile shows rather a plateau like feature than a single peak. Thus, the variability of the lines in the red part between 0 and 150 km s^{-1} is similar in strength, and, therefore, causing the bulge structure in the correlation matrices. For six lines (Fig. 4.16(a)-(f)) we can already exclude the possibility of continuum variations

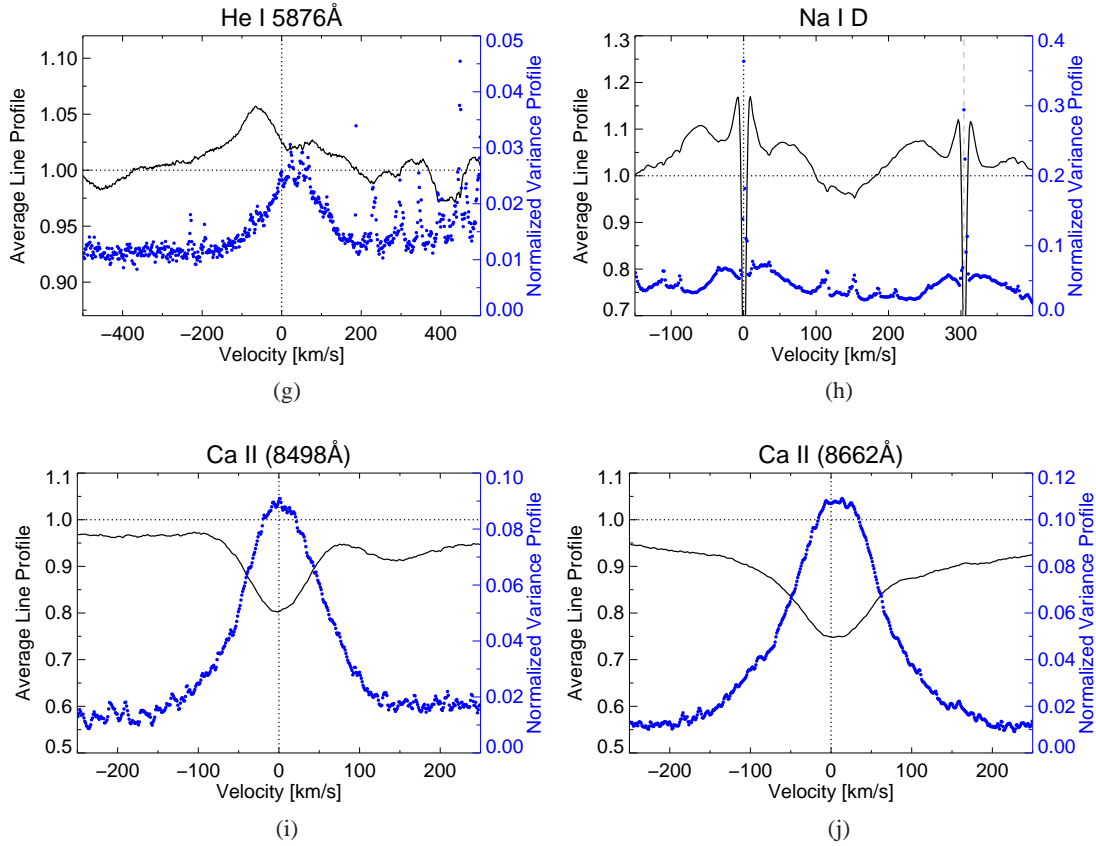


Figure 4.15: continued.

causing a strengthening and weakening of the line profile (veiling) as the entire correlation matrices would appear squarish. The lines illustrated in Fig. 4.16(g)-(j) show weak signs for veiling as the area around the main diagonal appears to be slightly squarish with $r \approx 0.7$ to 0.8 , and spans roughly $\lesssim 200 \text{ km s}^{-1}$.

4.5.3 Residual line profiles and temporal variations

We computed the residual line profiles by subtracting a synthetic photospheric spectrum, based on the found stellar parameters (Sec. 4.2.2), from the observed line profiles (in the following we refer to them as circumstellar components) for our sample. The results are presented in Fig. C.1 to Fig. C.10 in Appendix C. The effect of temporal line shape variations appear now more prominent. A visual inspection clearly indicates a correlation in line shape variations for all lines. Features, such as blue and redshifted absorption components, appear and disappear at the same time for all sample lines. This behavior indicates already a periodic like modulation of the sample lines and is a first hint for an accretion funnel flow arising from the inner disk. A main difference between $H\alpha$ and the other lines is a less prominent signature of the redshifted absorption component. A similar behavior was observed for the Balmer lines by Edwards et al.

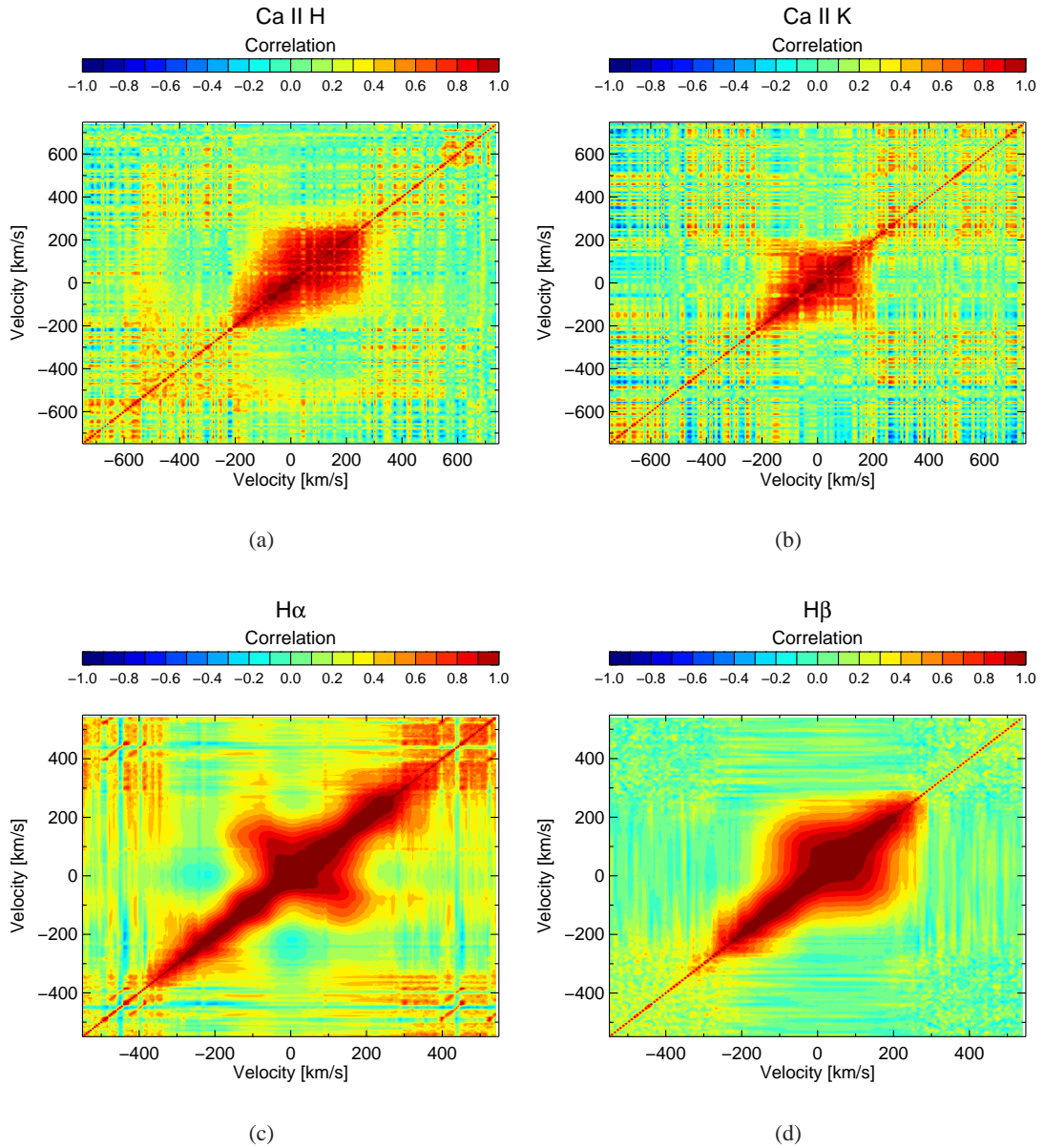


Figure 4.16: Velocity correlation matrices for the selected line sample. See text for explanation. Comment to plot (h) showing the correlation matrix for Na I D: The doublet was not split for the computation r because the D1 and D2 line show broad emission peaks, which overlap for several epochs. Therefore, the doublet cannot be separated for HD 142527. Thus, the line center of D2 is set to zero and the line center of D1 appears at $\approx 300 \text{ km s}^{-1}$. Due to symmetry reasons of the correlation matrix the doublet reoccurs at $(x, y) = (0, 300) \text{ km s}^{-1}$ and at $(x, y) = (300, 0) \text{ km s}^{-1}$. The two horizontal and two vertical line features visible in the matrix are contributions from the interstellar medium.

(1994) for a sample of T Tauri stars. A possible explanation for this might be the thermalization of H α for large accretion velocities resulting in a weaker redshifted absorption component whereas higher Balmer lines do not thermalize (Hartmann et al. 1994).

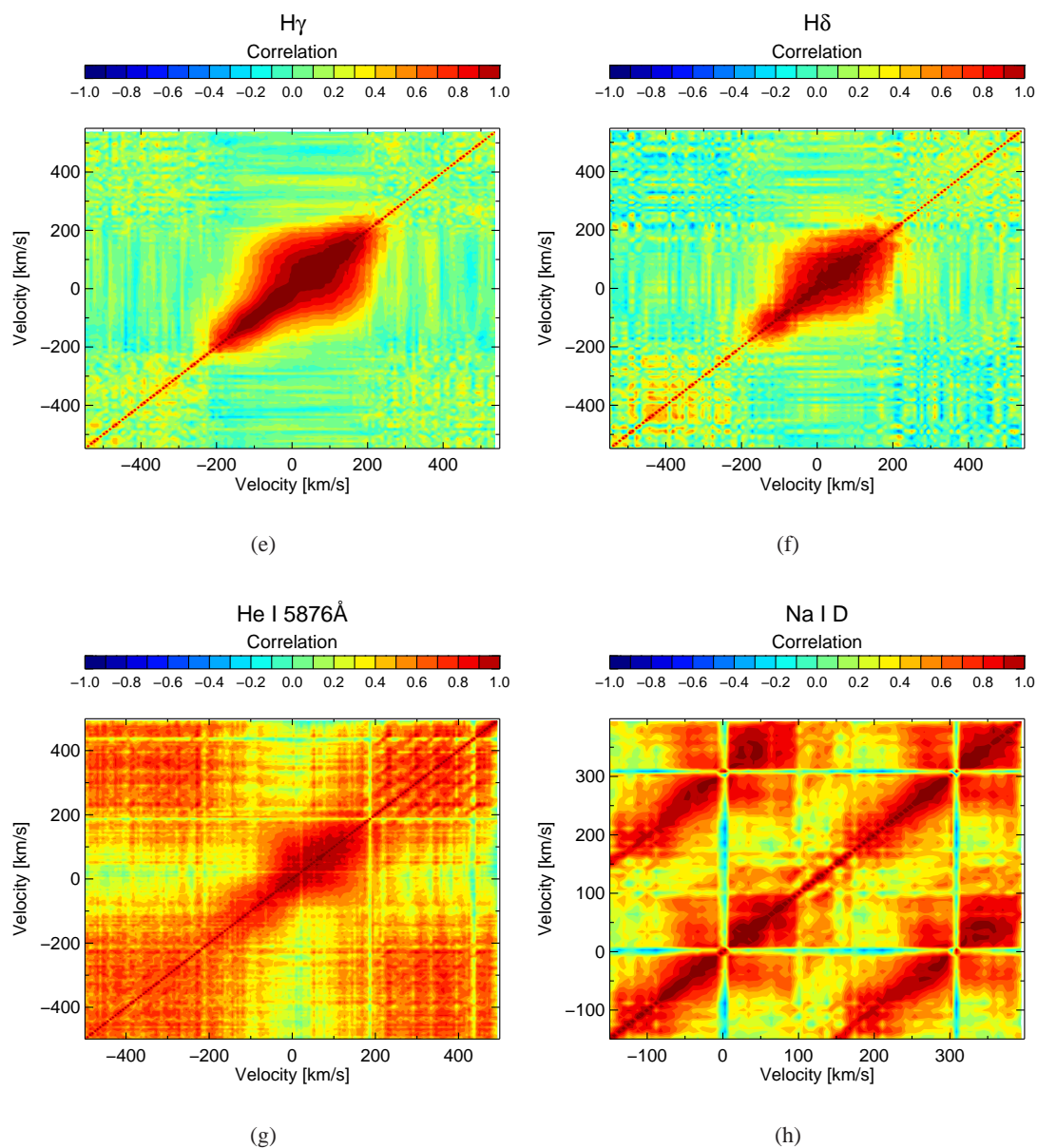


Figure 4.16: continued.

To quantify possible periodicities present in the line shapes, we measured the equivalent width for each circumstellar component, EW_{CSC} . We omitted the measurement of the Na I D doublet because it is not possible to analyze Na I D1 and Na I D2 independent from each other as the broad emission component of both lines overlap for several epochs. In addition, we cannot correct for variability of the interstellar medium (narrow line) and would result in biased values. The computed CLEANed spectrum of all EW_{CSC} measurements of the selected line sample is shown in Fig. 4.17. For six of nine lines we find a strong peak at 53.3 d. No signal is detected for the companions period of 114.5 d. However, for four lines a peak at 35 d and for three lines

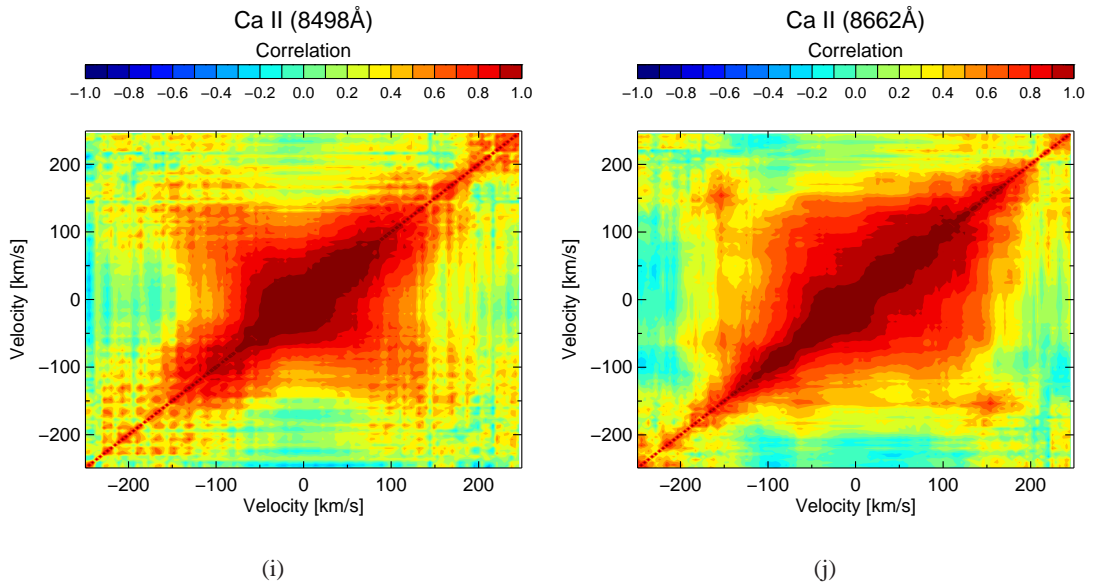


Figure 4.16: continued.

a peak at ≈ 700 d is present. To explain the behavior of the CLEANed spectrum for EW_{CSC} , we simulated our data set in the following way. For each line we used the measured values (time and EW_{CSC}) and fitted them with a sinusoid with fixed period of 53 d, but varying amplitude, phase, and offset. We added Gaussian noise to this model and computed the CLEANed spectrum. This procedure was repeated 1000 times for each line. Figure 4.18 shows the result of this simulation and plotted are the CLEANed spectra, which describe best the original ones (Fig. 4.17). With this simulation we were able to reproduce the main characteristics of the original CLEANed spectra, including the presence of the 35 d, 53.3 d, and 700 d period for the individual lines. Because the simulated data were modulated only with a single period of ≈ 53 d, we can conclude that the 53.3 d period found in the originally measured EW_{CSC} data set is the true period and the other peaks are aliases. The reason why we do not detect the 53.3 d period or have additional peaks in the CLEANed spectrum present in the measurements of EW_{CSC} of some lines, is in the nature of the used CLEAN algorithm. The window function is first centered on the highest peak of the discrete Fourier transform of the observed signal (dirty beam). After constructing the CLEAN component, the window function is rescaled and finally subtracted from the dirty beam. This process is executed iteratively. For very noisy data, the algorithm might therefore not restore the true period present in the data as it is the case for three lines of our sample and the highest peak is not necessarily the true period.

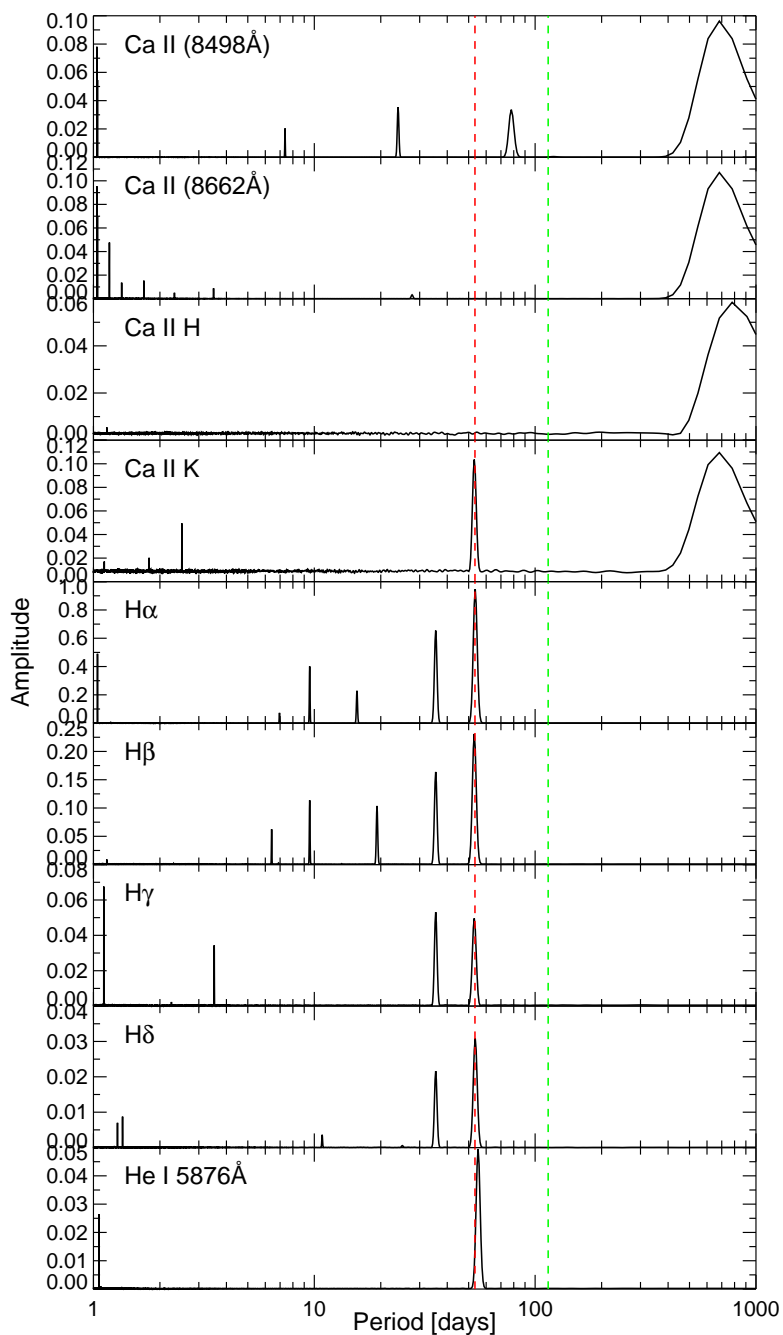


Figure 4.17: CLEANed amplitude spectrum of EW_{CSC} for the lines in our sample. The red line marks the a 53.3 d period and the period of the low-mass companion of 114.5 d is imprinted as green line.

The detected 53.3 d variation of EW_{CSC} in our selected line sample corresponds to a Keplerian radius of 0.36 AU. The dust sublimation radius, R_s , for HD 142527, assuming a dust sublimation temperature, T_s , of 1500 K can be estimated by using the equation by Tuthill et al.

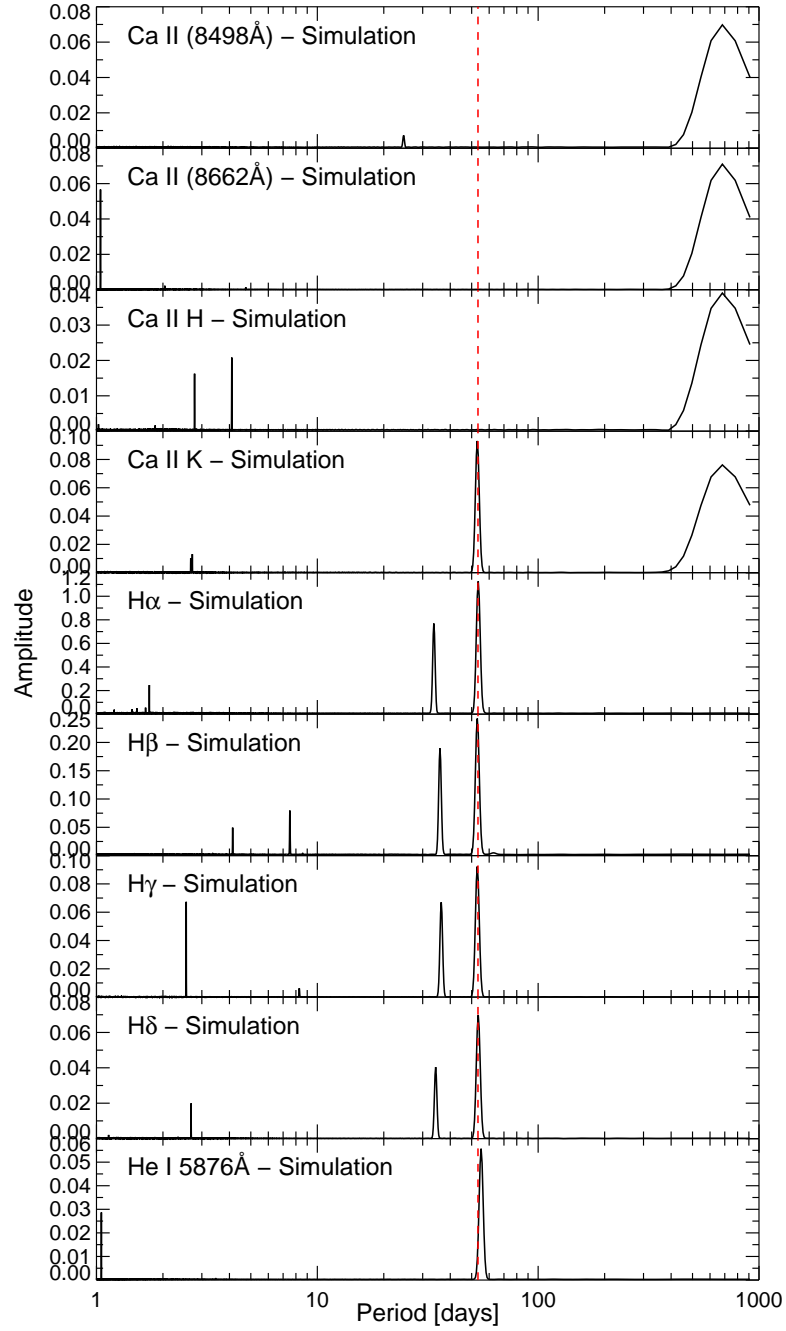


Figure 4.18: CLEANed amplitude spectrum of EW_{CSC} for the lines in our sample based on simulated data. The red line marks the a 53.3 d period. See text for explanation.

(2001):

$$R_s = 0.5 \sqrt{Q_R} \left(\frac{T_\star}{T_s} \right) R_\star, \quad (4.1)$$

where Q_R is the ratio of the dust absorption efficiencies for radiation at color temperature T of the incident and reemitted field. We used $Q_R = 5$ based on Fig. 2 of Monnier & Millan-Gabet

(2002). Using the derived stellar parameters of HD 142527 from Table 4.1 yields a dust sublimation radius of 0.34 AU. From the empirical formula by Whitney et al. (2004),

$$R_s = R_\star (T_s/T_\star)^{-2.085}, \quad (4.2)$$

we compute the same value for R_s . The observed line shape variation of 53.3 d, which corresponds to a Keplerian radius of 0.36 AU, the estimated dust sublimation radius of 0.34 AU, and the location of the inner rim of the inner disk determined to 0.3 AU by Verhoeff et al. (2011) (Sec. 4.2.1) are all comparable. This indicates a well known radial distance of the inner rim of the inner dusty disk, where a physical (but not known) process takes place causing periodic changes of the line shape.

4.6 Discussion

4.6.1 Planet or brown dwarf?

From our RV measurements we derive a *true* mass of $25 \pm 6 M_J$ for the companion around HD 142527 taking additional information from the disk inclination into account and assuming that the companion orbits in the plane of the disk. Can we call the companion a planet or is it a brown dwarf? There is already a long-lasting discussion ongoing how to define planets and where the transition to the brown dwarf regime occurs. Definitions proposed so far are very ambiguous and cannot account for all individual star-planet systems. A widely used criterion is the upper mass limit of $13 M_J$ based on the deuterium-burning limit (Burrows et al. 1997) to define a companion as planet or brown dwarf. But this limit causes several conflicts. Spiegel et al. (2011) computed the needed deuterium-burning mass for a set of models. They found masses down to $11 M_J$ where deuterium-burning can take place. Depending on the model, Spiegel et al. (2011) found out that objects even more massive than $13 M_J$ are required to establish significant deuterium burning depending on their metallicity.

Another criterion to consider is the formation process of such objects. A planet should clearly form inside the circumstellar disk, and, thus, orbiting a central star similar to our solar system. Several objects are found, which have masses down to $\approx 10 M_J$ but are not associated with a host star (“free-floating planets”). Other objects, such as CoRoT 3b with a mass of $21 M_J$ (Delplancke 2008) or multiple planet systems like HD 168443 with HD 168443 c having $17.2 M_J$ (Marcy et al. 2001), seem to have undergone clearly a planetary-like formation process. Therefore, the $13 M_J$ criterion is highly ambiguous.

The resulting cumulative distribution from a search for brown dwarf companions carried out by Sahlmann et al. (2011a,b) in the mass range between 13 to $80 M_J$ shows an absence of companions in the mass range of 25 to $45 M_J$. A similar behavior was found by Grether & Lineweaver (2006). Sahlmann et al. (2011a) proposed to use this characteristic to set a dividing line between planets and brown dwarfs, i.e. companions with masses $\leq 25 M_J$ can be still considered as plan-

ets. In addition, Schneider et al. (2011) use this threshold as well and pointed out changes in the planet radius distribution for masses around $25 M_J$. Based on this discussion, we only can argue that the $25 M_J$ companion around HD 142527 is in the transition region between planets and brown dwarfs. However, we will use the designation HD 142527 b for the low-mass companion orbiting HD 142527.

4.6.2 Properties of HD 142527 b

The low-mass companion HD 142527 b has several unusual properties. It has a true mass of $25 \pm 6 M_J$, in an eccentric orbit $e = 0.23$ around a ≈ 4 Myr young intermediate-mass star with a semimajor axis of only $a = 0.6$ AU. In addition, HD 142527 shows a complex circumstellar environment as discussed in Sec. 4.2.1. Figure 4.19, adopted from Verhoeff et al. (2011), summarizes the main properties of the star-disk system. These features set very stringent constraints

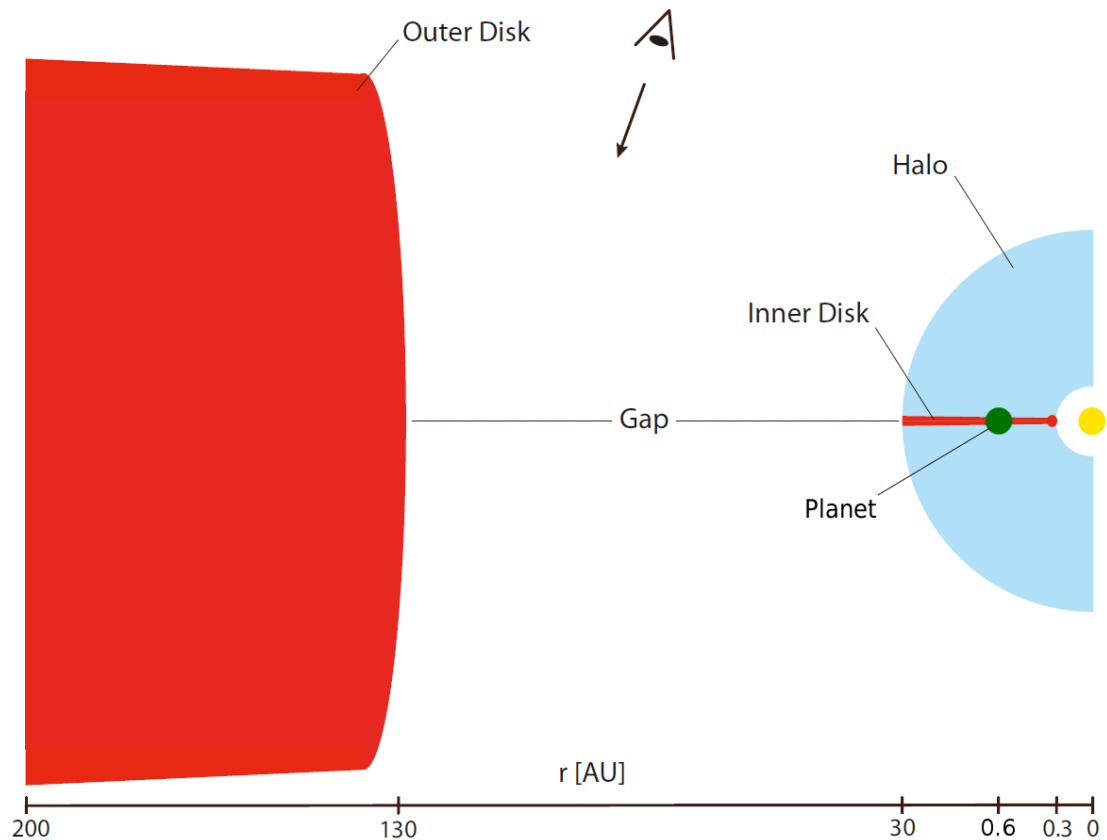


Figure 4.19: A pictographic sketch of the HD 142527 system adopted from Verhoeff et al. (2011). The position of the low-mass companion is marked by the green disk.

on planet formation models with respect to forming a massive planet and allowing for migration to a short distance in such a short time.

The rather high eccentricity of HD 142527 b is not expected because tidal circularization would lead to nearly circular orbits (e.g. Wang & Ford 2011). However, several close-in planets

being part of a planetary system show significant deviations from circular orbits due to gravitational interactions between the bodies (e.g. HD 168443, HIP 5158, HIP 57274). Mechanisms, such as planet-planet scattering and the Kozai mechanism, might explain the orbital properties of HD 142527 b, see e.g. Nagasawa et al. (2008). Previous observations of HD 142527 show several indications that more than one companion might be present: (i) the highly processed inner dusty disk, (ii) the large gap extending over 100 AU, (iii) a spiral-like structure of the outer disk (Fukagawa et al. 2006), (iv) an emission ring at 130 AU. The latter one was observed with VISIR in the Q -band by Verhoeff et al. (2011). The observed structure (see Fig. 6 in Verhoeff et al. 2011) strikingly resembles the structure of an anticyclonic vortex, which is a non-axisymmetric density perturbation, shaped like a horseshoe (Regály et al. 2012). Only stellar or substellar companions are able to form such perturbations in the disk. Therefore, it is possible that HD 142527 hosts a multi-planet (or multi-companion) system.

4.6.3 Magnetospheric accretion?

According to standard stellar evolution theory, HAeBe stars should not be able to establish strong magnetic fields of the order of several kG like they are observed in classical T Tauri stars as HAeBe stars are expected to be fully radiative. This is supported by the tentative detection of only weak magnetic fields, e.g. by Wade et al. (2007), Hubrig et al. (2007), and Hubrig et al. (2009). Wade et al. (2007) showed that their measurements of magnetic fields of HAeBe stars with strength below 0.5 kG is well in agreement with the primordial field hypothesis, where the stellar magnetic field is a remnant of the interstellar magnetic field from star formation. However, Mendigutía et al. (2011) found empirical evidence that the accretion in HAe stars is consistent with magnetospheric accretion but not for HBe stars.

We can estimate the minimum magnetic field strength required to establish magnetospheric accretion for HD 142527, under the assumption of a magnetic dipole, by applying equations provided by models by Koenigl (1991), Collier Cameron & Campbell (1993), and Shu et al. (1994) (see review by Johns-Krull et al. 1999). The derived values for the surface magnetic field are of the order of 150 G for all models using the stellar parameters provided in Table 4.1. This is a reasonable estimate for a late-type Herbig star and is in the range of detectability as already demonstrated by, e.g. Hubrig et al. (2009). Another important parameter to establish magnetospheric accretion is the ratio of the co-rotation radius, R_{cor} , and the truncation radius, R_{tr} , which has to be $R_{\text{tr}}/R_{\text{cor}} < 1$ (e.g. Bouvier et al. 2007). Using the previous result of 150 G, R_{tr} is of the order of $1.7 R_{\star}$, which corresponds to $2.8 \cdot 10^{-2}$ AU. For R_{cor} (Eqn. 4.3) we derive $1.8 R_{\star}$ or $3.0 \cdot 10^{-2}$ AU, which is larger than R_{tr} .

$$R_{\text{cor}} = \left(\frac{GM_{\star} R_{\star}^2}{v_{\star}^2} \right)^{1/3} \quad (4.3)$$

Thus, magnetospheric accretion could be present in HD 142527. Unfortunately, there is no magnetic field measurement for HD 142527 available yet, which hampers a comparison with dif-

ferent accretion processes and further interpretations. However, if we assume magnetospheric accretion processes to be present for HD 142527, there has to be a gaseous disk inside the disk truncation radius, which is with 0.36 AU one order of magnitude larger than R_{cor} . Following the interpretation by Muzerolle et al. (2004) there could be a gaseous but optically thin disk between $3 \cdot 10^{-2}$ AU and 0.3 AU present or an optically thick but geometrically thin gaseous disk inside this range. This would guarantee that the inner rim of the inner dusty disk receives still enough radiation from the central star to be puffed up.

This result does not provide an obvious interpretation of the cause of the observed 53.3 d period in the EW_{CSC} . A lock of magnetic field lines onto the inner rim of the inner dusty disk at 0.3 AU is unlikely as it requires a magnetic field strength of several kG, which is not observed for HAeBe stars. In addition, R_{tr} would fall well outside R_{cor} , preventing magnetospheric accretion anyway.

4.6.4 Gas-disk simulation

We carried out a numerical simulation of the interaction of the gas component of the inner disk with a low-mass companion in an eccentric orbit. This is done using the hydrodynamics module of the Godunov code PLUTO (Mignone et al. 2007). Time stepping is done using a second order Runge Kutta integrator, while space interpolation is performed using the second order linear TVD approximation. The HLLC approximate Riemann solver is used for computing the fluxes through cell interfaces. The geometry is polar $\mathbf{r} = (r, \phi)$. Only a segment of the disk is simulated; the computational domain is given by $r \in [0.2 \text{ AU}, 5.0 \text{ AU}]$ and $\phi \in [0, 2\pi]$. The resolution in the radial and azimuthal direction is $(N_r, N_\phi) = (256, 256)$ and the grid is uniform.

The ratio of the companion mass to stellar mass is taken to be $m_{\text{planet}}/M_\star = 10.8 \cdot 10^{-3}$. The semi-major axis of the companion is $a = 0.6 \text{ AU}$ and the eccentricity is $e = 0.23$. The disk has a uniform surface density and a scale height of $H = c_s/\Omega_k = 0.01$, where c_s is the speed of sound. The disk is assumed to cool infinitely fast, such that it is locally isothermal, i.e. sound speed is constant in time and varies only with radial distance from the central star. The equation of state is given by $p = c_s^2 \Sigma$, and $c_s \propto r^{-0.5}$. The disk has a constant and uniform mass accretion rate of $\dot{M} \approx 5 \times 10^{-9} M_\odot/\text{yr}$, chose to approximate the observed value.

For numerical reasons, the disk is only simulated up to an inner distance of 0.2 AU. The high orbital velocity of the gas at locations close to the star ($v_k \propto r^{-0.5}$), specifically the inner edge, determines the time step for the time evolution of the simulation. Extending the disk up to an inner distance of $3 \cdot 10^{-2}$ AU would increase to computational time to prohibitive values. The choice of computational domain means that the companion semi-major axis is very close to the inner boundary, therefore the location of the inner edge of the gap can be slightly artificially increased (the Hill radius of the companion at $a = 0.6 \text{ AU}$, which approximately determines the extend of the gap, is $r_h = 0.09 \text{ AU}$, which is in good agreement with our simulation). However, the broad features of the gap, and the excitation of eccentricity in the disk remain valid.

Figure 4.20 shows a snapshot of the surface density of the simulation after 255 orbital periods of the companion have elapsed. A non-axisymmetric gap has been cleared by the low-mass companion due to its orbital eccentricity. In addition, the outer rim of the gap shows a locally but not uniform increase in surface density and density waves are created along the disk. Because of the cut at 0.2 AU we are not able to identify gas, which might be locally accumulated

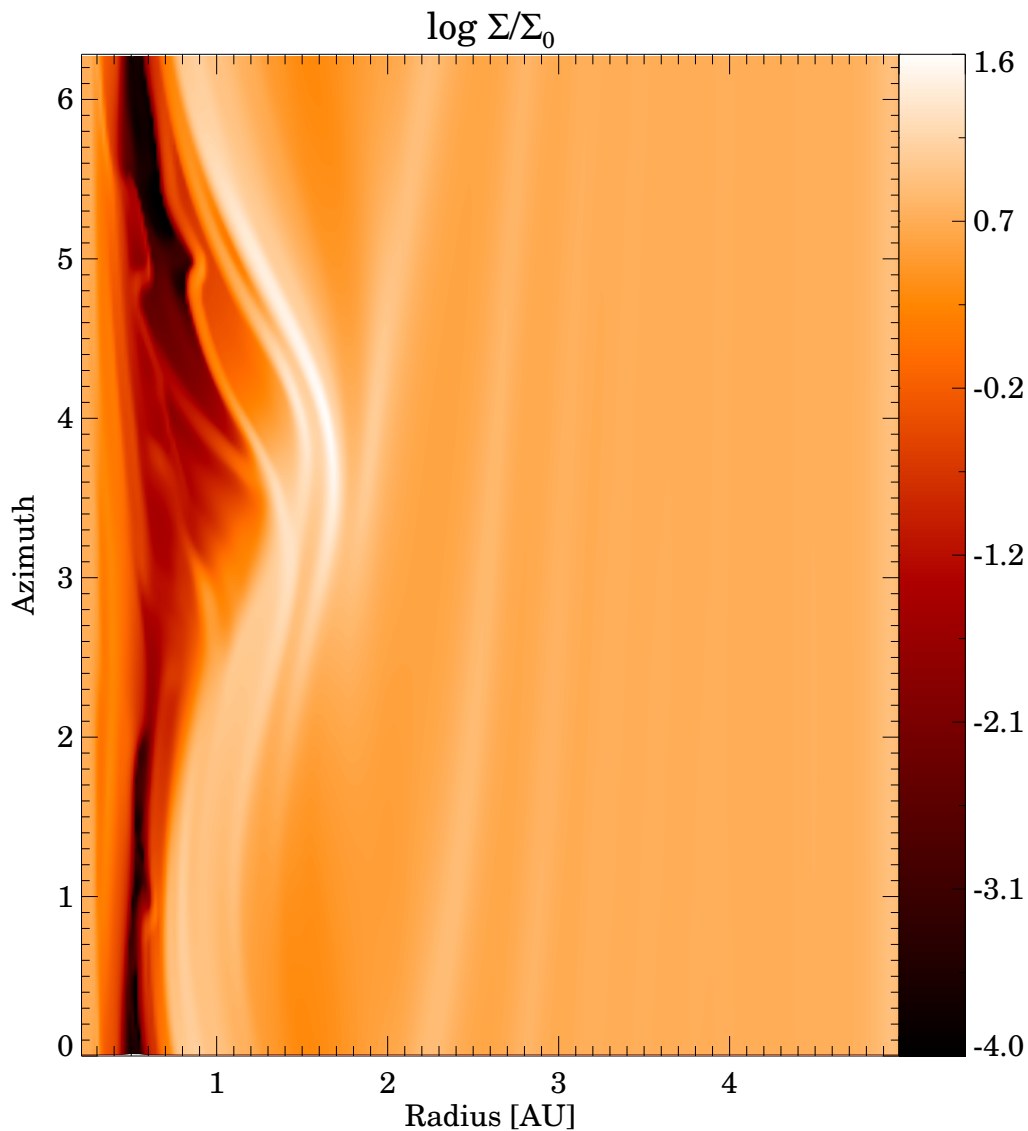


Figure 4.20: Logarithmic plot of the surface density after 255 orbital periods of a 25 M_J companion located at 0.6 AU on an eccentric orbit. See text for explanation. Computation by A. L. Uribe.

in this region due to the companion-disk interaction. Therefore, we can only speculate about the cause of the observed 53.3 d variability of the selected line sample accretion tracers (see Sec. 4.5). Under the assumption of magnetospheric accretion, we would expect a pure inner

gaseous disk ranging between $3 \cdot 10^{-2}$ and 0.3 AU (as discussed in Sec. 4.5.3). The low-mass companion may redistribute the gas along ≈ 0.3 AU, and, therefore, producing a dense and hot region. Its rotation and different visibility due to geometrical effects may cause the observed variations with a 53.3 d period in the accretion tracer lines.

However, the non-axisymmetric gap and rotating density perturbations may be a reachable target for NIR interferometry. On a 100 m baseline structures down to 1 AU at 150 pc can be detected in K -band. Multi-epoch closure phase measurements and spectroscopy of the $\text{Br}\gamma$ line makes HD 142527 an ideal target for AMBER. Detection of periodicities and co-rotational features in these measurements could lead to an independent, but indirect detection of the companion.

4.7 Conclusions

We have analyzed in total 119 optical and NIR high-resolution spectra. From RV measurements we discovered a 114.5 d period, which can be assigned to a $m \sin i = 8.5 \pm 1.0 M_J$ low-mass companion on an eccentric orbit with $e = 0.23$ and with a semi-major axis of $a = 0.60 \pm 0.01$ AU around the 4 Myr young Herbig star HD 142527. The NIR RV measurements were used to validate the observed signal in the optical measurements. From photometric measurements we found a significant period of 1.21 d, which is consistent with the measured projected rotational velocity of $v \sin i = 50 \pm 3.5 \text{ km s}^{-1}$ and i_{disk} under the assumption of perpendicular alignment of the stellar rotational axis with respect to the mid-plane of the disk. We used the measured inclination angle of $i_{disk} = 20^\circ \pm 10^\circ$ of the circumstellar disk to estimate the true mass of the companion to $m = 25 \pm 6 M_J$ making HD 142527 b to be one of the most massive planets or lowest mass brown dwarfs detected so far. In addition, we have determined a full set of stellar parameters for HD 142527, independent from previous literature values.

To verify that the 114.5 d period is not caused by any activity related feature in the disk, we analyzed Ca II K and H, $\text{H}\alpha$, $\text{H}\beta$, $\text{H}\gamma$, $\text{H}\delta$, He I at $\lambda 5876\text{\AA}$, Na I D doublet, and Ca II at $\lambda 8498\text{\AA}$ and $\lambda 8662\text{\AA}$, which are known to be accretion tracers, for changes in the line profile and periodicity. The line profiles show red and blueshifted absorption features, varying with time. These features are a clear indication of material infall and outflows, respectively. We found a 53.3 d period present in the equivalent width measurements of our line sample, which corresponds to a Keplerian radial distance of 0.3 AU from the star. The cause of this period is unclear. A simulation of the gaseous disk did not show a locally denser region at 0.3 AU but revealed the presence of a gap and density waves in the inner disk of HD 142527. We speculated about a possible magnetospheric accretion process. An accretion funnel flow might be able to form at $3 \cdot 10^{-2}$ AU if a magnetic field of at least ≈ 150 G would be present. This requires an extension of the gaseous disk down to $3 \cdot 10^{-2}$ AU. So far, no magnetic field measurements are available for HD 142527. Without magnetic field measurements and detailed modeling of the

observed line profiles the accretion process remains unclear.

HD 142527 b is the first low-mass companion discovered around a Herbig star so far and it is also by far the youngest companion detected by the RV technique (Fig. 4.21). Previous ob-

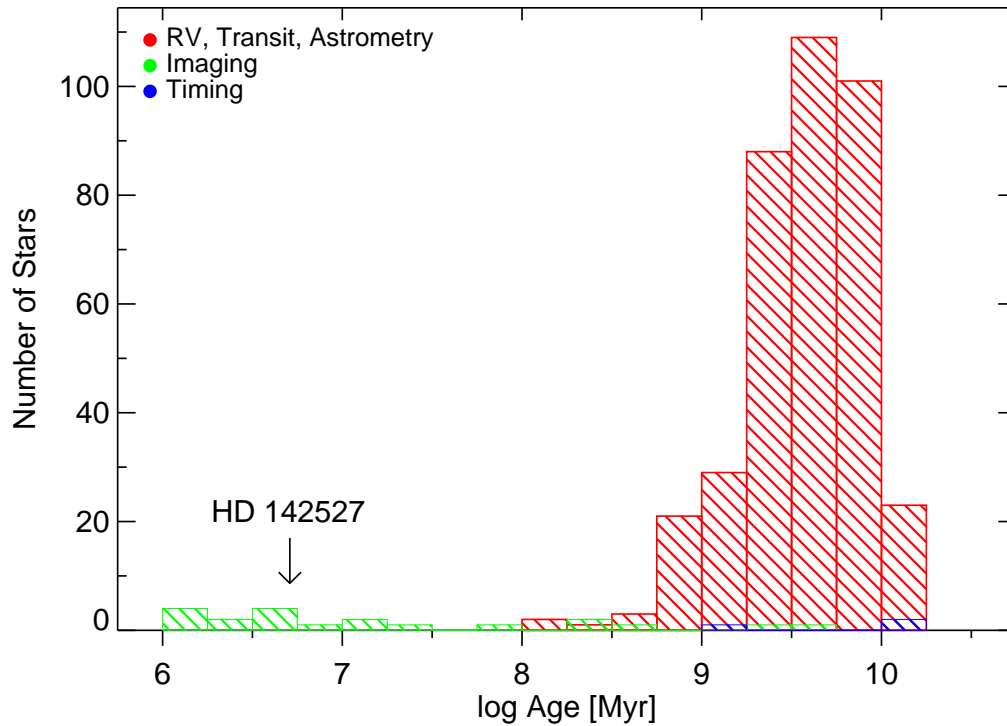


Figure 4.21: Age distribution of all exoplanet host stars (if age of host star is known) as of February 19, 2012. Controversial or rejected planets are not included. Data are extracted from the exoplanet database by Schneider et al. (2011). The position of HD 142527 is marked by an arrow.

servations and measurements by Verhoeff et al. (2011) indicate the presence of more planetary or stellar bodies around HD 142527. The age, mass, distance, and eccentricity of HD 142527 b are a test and challenge for current planet formation models.

Chapter 5

PRIMA FSU-A as a Fringe Tracker for MIDI

Abstract We report first results obtained from observations using a PRIMA FSU (Fringe Sensor Unit) as a fringe tracker for MIDI on the VLTI when operating with the 1.8-m ATs. Interferometric observations require the correction of the disturbance in the optical path induced by atmospheric turbulence (piston). The PRIMA FSU is able to compensate for such disturbances in real-time which makes it a suitable facility to stabilize the fringe signal for other VLTI instruments, like AMBER and MIDI. Currently, the atmospheric coherence time in the N -band (8 to 13 μm) observed by MIDI, as well as the thermal background in this band, require a minimum target flux of 20 Jy and a correlated flux of 10 Jy (in PRISM/HIGH_SENSE mode and using the ATs under standard conditions) to allow self-fringe-tracking and data reduction. However, we show that if the fringes are stabilized by the FSU-A, the prediction of N -band phase delay and group delay from K -band data allow a reliable data reduction even for the observation of faint targets ($F_{\text{corr},N} < 10$ Jy) with MIDI at standard detector exposure times. We were able to measure correlated fluxes down to 0.5 Jy, which pushes the current limits of MIDI down to regions where numerous new targets become accessible on ATs. The observational tests done so far and the obtained results represent a first step towards Phase Referenced Imaging with the VLTI in the mid-infrared.

Parts of this chapter were published in Müller, A., Pott, J. U., Morel, S., et al., 2010, Proceedings of SPIE, Optical and Infrared Interferometry II, Vol. 7734

5.1 Introduction

This part of the thesis covers the setup, observations, data reduction, and first results from a new observing mode available at the Very Large Telescope Interferometer (VLTI). We present observations carried out with the Mid-infrared Interferometric instrument (MIDI) in combination with PRIMA FSU-A, which is a newly available K -band fringe tracker and part of the PRIMA facility. The aim of these observations were not primarily scientific related but to demonstrate the new capabilities available with this MIDI + PRIMA FSU-A mode. Therefore, this chapter describes and presents rather technical aspects, which are important for operation for this very new observing mode at VLTI. We assume that the reader is familiar with the concept of interferometry and refer to the reviews and text books of Lawson (2000); Quirrenbach (2001); Haniff (2007); Glindemann (2011), which provide comprehensive and detailed informations with respect to optical interferometry.

This chapter is organized as follows. In Sec. 5.1.1 to 5.1.3 we describe the two used interferometers and the principle setup. The observations, including an observing sequence, is presented in Sec. 5.2. The different and new reduction procedures and their calibration is described in Sec. 5.3 and 5.4. The results of the different data reduction processes and observed correlation between several environmental parameters are presented in Sec. 5.5. Because the usage of MIDI + PRIMA FSU-A is still experimental, we provide a list of requirements for a full implementation at the VLTI in Sec. 5.6. The discussion and conclusions can be found in Sec. 5.7.

5.1.1 MIDI

MIDI (the MID-infrared Interferometric instrument, Leinert et al. (2003)) on the Very Large Telescope interferometer (VLTI), is a two beam Michelson type interferometer, i.e. the two beams are superposed coplanar. Figure 5.1 shows MIDI inside the VLTI laboratory. Its optics are mounted on a so called *warm* and *cold optical bench*. The warm optical bench consists mainly of calibration units (blackbody source, reference plates) and roof mirrors mounted on Piezo stages, which act as an internal instrumental DL and are used to scan through the interferometric signal (fringe). The cold optical bench consist of a dewar, which cools the optics and detector mounted inside, down to 5 K to 40 K in order to suppress thermal background from the instrument itself. The dewar is the metallic container visible in Fig. 5.1. Inside the dewar a filter-wheel, dispersive elements, beam-splitter, the beam combiner, and the detector are mounted. A schematic optical layout is presented in Fig. 5.2.

MIDI produces dispersed fringes in the N -band over a wavelength range from 8 to 13 μm . The mid-infrared wavelength range traces especially the dusty environment around stellar sources and makes MIDI suitable for the observation of a wide range of objects like active galactic nuclei (AGN), circumstellar and accretion disks around young stellar objects (YSO), and envelopes of

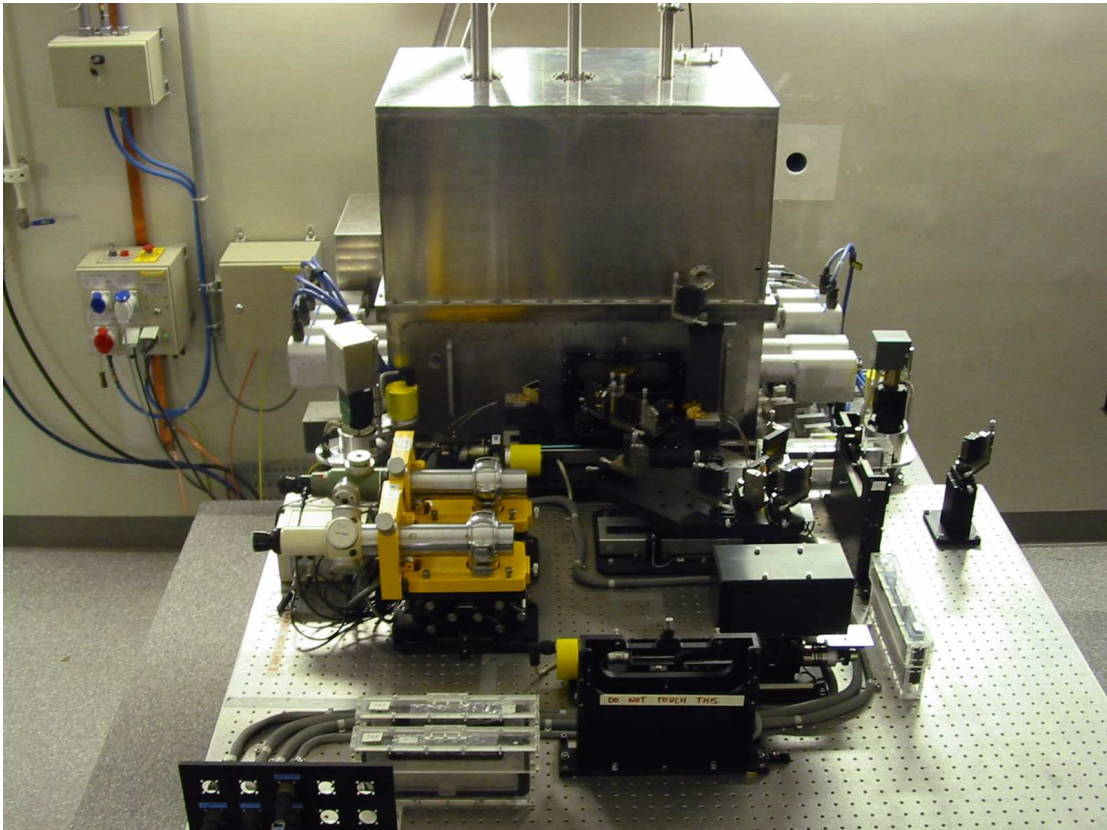


Figure 5.1: The MIDI instrument. Image courtesy ESO.

Wolf-Rayet stars, Luminous Blue variable, B[e] supergiants, AGB stars, and post-AGB stars. In addition, the study of the mineralogy, composition, and the geometrical distribution of such dusty environments are possible using the N -band. Therefore, the targets are very red, i.e. their SED peaks at infrared wavelengths. The MIDI instrument is extensively used since it was offered in 2004, resulting in more than 110 refereed journal articles so far, making it the world's most prolific interferometric instrument to date.

A prism providing a resolution of $R=30$ and a grism providing a resolution of $R=230$ at $\lambda=10.6 \mu\text{m}$ are the available dispersive elements. MIDI has two observation modes depending on two beam splitters in front of the beam combiner which reflect 30% of the incoming light into photometric beams which allows to measure the interferometric signal simultaneously to the photometric flux. This mode is called “science-photometry” (SCIPHOT) but is not of concern for MIDI + PRIMA FSU-A observations because the required “chopping”¹ will cause periodic fringe losses of FSU-A. If the beam splitters are not inserted, all incoming light is directly send to the beam combiner and is called “high-sense” mode (the mode of interest here).

¹Chopping is the is a standard method to remove background from images. The M2 mirror of the telescope is periodically tilted. Therefore, the instrument takes frames from the target source and the sky.

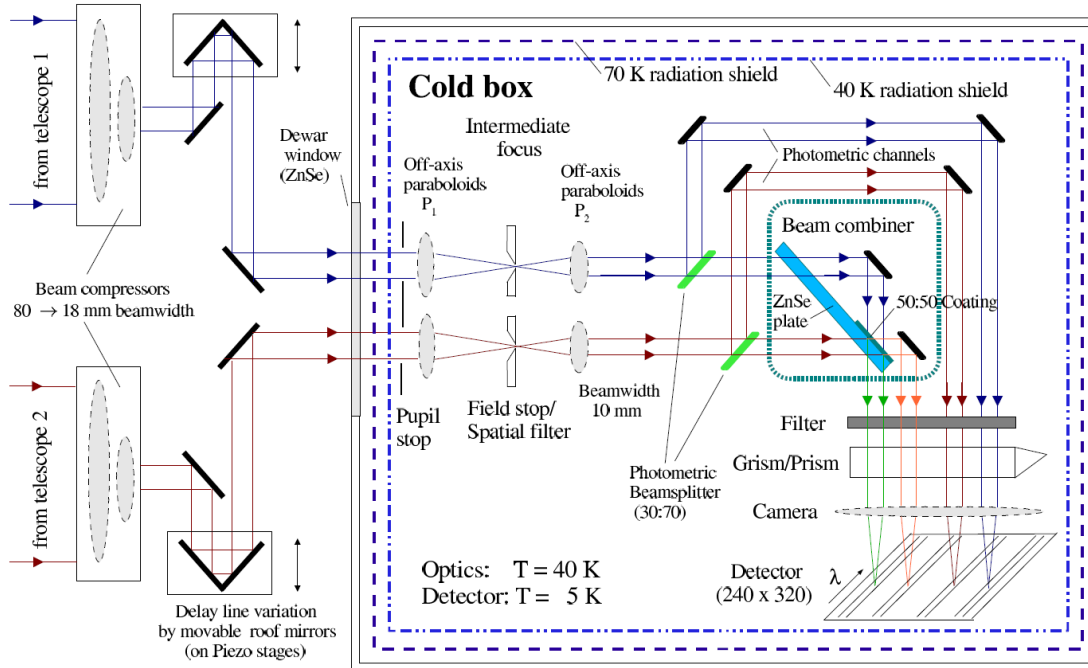


Figure 5.2: Schematic optical layout of MIDI. Image courtesy Ch. Leinert, MPIA.

The most recent (as of ESO Period 90) official required minimum target flux for MIDI in HIGH_SENSE mode when observing with the 8-m unit telescopes (UT) or 1.8-m auxiliary telescopes (AT) are:

- **UTs:** Prism: $F_{\text{tot},N} \geq 1 \text{ Jy} / F_{\text{corr},N} \geq 0.2 \text{ Jy}$, Grism: $F_{\text{tot},N} \geq 3 \text{ Jy}$
- **ATs:** Prism: $F_{\text{tot},N} \geq 20 \text{ Jy} / F_{\text{corr},N} \geq 10 \text{ Jy}$, Grism: $F_{\text{tot},N} \geq 30 \text{ Jy}$

These limits arise mainly from the thermal background in the N -band and guarantee self-fringe-tracking and data reduction. In addition, differential motion of the pupil might be a limitation as it causes a varying background on a ≈ 1 sec timescale.

5.1.2 PRIMA FSU

In 2008 the installation and commissioning of the PRIMA (Phase-Referenced Imaging and Micro-arcsecond Astrometry, Quirrenbach et al. 1998; Delplancke et al. 2006; Delplancke 2008) dual-feed facility at VLTI started and is still ongoing (Schmid et al. 2010). Once fully operational, PRIMA will be used for faint-object observations (Müller et al. 2010), phase-referenced imaging using AMBER and MIDI, and narrow-angle astrometry (Launhardt et al. 2008)².

PRIMA comes with four sub-systems: the fringe sensor unit (FSU, Sahlmann et al. 2009, 2010), the star-separator module (STS, Nijenhuis et al. 2008), differential delay lines (DDL,

²If PRIMA serves as fringe tracker for MIDI or AMBER or if its used for phase referenced imaging, PRIMA acts as a *facility* as part of the VLTI infrastructure. In the astrometric mode, PRIMA, including its subsystems, is a stand-alone *instrument* and is called PACMAN (PRIMA Astrometric Camera for Micro-arcsecond AstroNomy).

Pepe et al. 2008), and the internal laser metrology (Schuhler 2007). The latter three sub-systems do not play a any role here and will not discussed further. For a detailed description we refer to the provided references.

The PRIMA FSU consist of two identical interferometers (FSU-A and FSU-B) working in K -band. Figure 5.3 displays the schematic optical layout of one FSU with its main optical

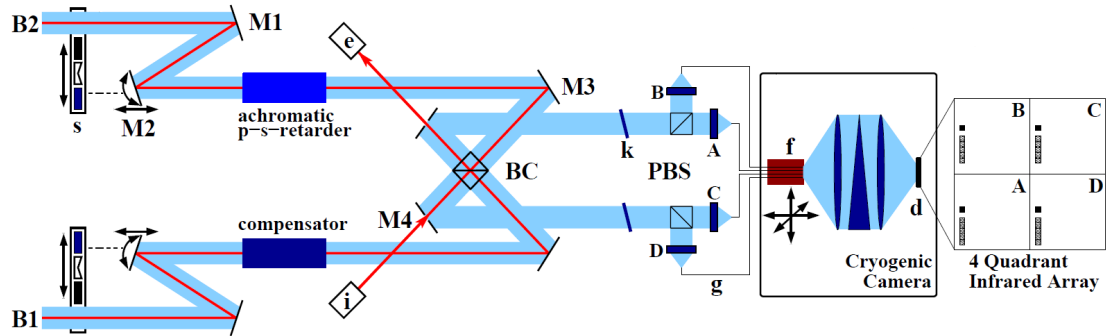


Figure 5.3: Schematic optical layout of PRIMA FSU. See text for details. Adapted from Sahlmann et al. (2009).

elements. The two telescope beams (K -band, B1 and B2) enter the FSU on the left sight in Fig. 5.3. After passing motorized stages (s), which are used to block the beams or to insert glass plates for the longitudinal atmospheric dispersion corrector into the light path, the beams going through an alignment and compensation unit (ACU). The ACU consists of flat mirrors (M2) mounted on piezo tip-tilt platforms, which are mounted on a motorized translation stage. One beam (here B2) will then go through an achromatic phase shifter (K -prism, Mottini et al. 2005) and experience a phase shift of 90° between p - and s -polarization (three reflections inside the K -prism). The second beam (here B1) is send through a silica block in order to compensate for differences in OPL between B1 and B2 caused by the retarder of B2. The beam combiner (BC), which is also a 50/50 beam splitter, superimposes both beams. The two beams (now superimposed by B1 and B2) are send to polarizing beam splitters (PBS) through the metrology dichroics (M4). The PBS separate the p and s polarization components of each beam from the BC. This results in four beams (A,B,C, and D), which are now separated by 90° in phase with respect to each other. Each beam is now injected into single mode fibres (g), which enter a cryostat containing dispersive elements and a four-quadrant (ABCD channel) infrared detector (d). Each channel consists of five pixel over where the entire K -band gets spectrally dispersed, which allows the measurement of the group delay. For a more detailed description of the individual FSU components and its current performance we refer to Mottini et al. (2005); Sahlmann et al. (2009, 2010); Schmid et al. (2010).

For clarity, the so called ABCD principle (spatial phase shifting) is presented in Fig. 5.4. Before the two beams enter the BC, the spatial component of the electromagnetic field can be written

as

$$\begin{aligned}
 \vec{E}_{p1}(\vec{x}) &\sim e^{-i\vec{k}\vec{x}} \\
 \vec{E}_{s1}(\vec{x}) &\sim e^{-i\vec{k}\vec{x}} \\
 \vec{E}_{p2}(\vec{x}) &\sim e^{-i\vec{k}\vec{x}} \\
 \vec{E}_{s2}(\vec{x}) &\sim e^{-i(\vec{k}\vec{x}+\pi/2)},
 \end{aligned} \tag{5.1}$$

where p and s denote the polarization of beam 1 and 2. After passing the BC and the PBS each of the four beams can be expressed as linear superposition of the initial signals of Eqn. 5.1. Additional phase shifts of the beams of 90° occur at the reflections inside the BC and PBS and have to be taken into account. From Figure. 5.4 we see that channel A is a superposition of the transmitted p -polarized beam 1 and the reflected p -polarized beam 2, which has an additional phase shift of 90° . Channel B is a superposition of the transmitted s -polarized beam 1 and the reflected s -polarized beam 2 and so on. We can write the resulting superposed signals as:

$$\begin{aligned}
 \vec{E}_A(\vec{x}) &\sim \vec{E}_{p1}(\vec{x}) + \vec{E}_{p2}(\vec{x})e^{-i\pi/2} \sim e^{-i\vec{k}\vec{x}} + e^{-i\vec{k}\vec{x}+\pi/2} \\
 \vec{E}_B(\vec{x}) &\sim \vec{E}_{s1}(\vec{x}) + \vec{E}_{s2}(\vec{x})e^{-i\pi/2} \sim e^{-i\vec{k}\vec{x}} + e^{-i\vec{k}\vec{x}+\pi} \\
 &\vdots
 \end{aligned} \tag{5.2}$$

The detected intensity I per channel is then:

$$\begin{aligned}
 I_A &\sim |\vec{E}_A(\vec{x})|^2 \sim 2 \left(1 + \cos \frac{\pi}{2}\right) \\
 I_B &\sim |\vec{E}_B(\vec{x})|^2 \sim 2(1 + \cos \pi) \\
 &\vdots
 \end{aligned} \tag{5.3}$$

Thus, the detected intensity per channel is shifted by 90° .

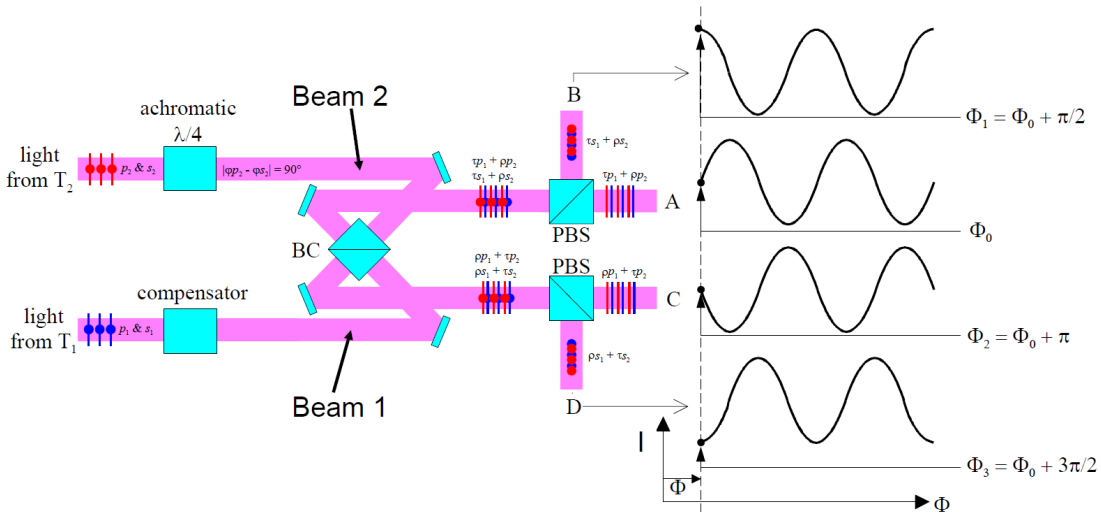


Figure 5.4: Working principle of the ABCD algorithm and its implementation in the PRIMA FSU. See text for explanation. Adapted from Sahlmann (2007).

5.1.3 MIDI + PRIMA FSU-A

The design and sensitivity of the PRIMA FSUs allow to estimate of phase delay and group delay in real time in order to correct for atmospheric turbulence effects (“piston”) which causes random variations of the optical path difference (OPD). The operation and sensitivity in the K -band makes the FSU an especially suitable fringe tracker for MIDI compared to FINITO (Le Bouquin et al. 2008) which is an H -band fringe tracker at VLTI. FINITO has a point source sensitivity of $H = 5$ mag on ATs which typically delivers enough photons in N -band for standard MIDI self-fringe-tracking operation. Also, the problem of MIDI+FINITO is the usually over-resolved diameter in H -band compared to N -band. Using PRIMA FSU with MIDI alleviates this problem.

Figure 5.5 shows a schematic view of the VLTI laboratory as it is configured when MIDI is used with PRIMA FSU-A in single-feed, on-axis mode. The telescopes, here the 1.8m auxiliary telescopes AT1 and AT2, send the light to the main delay lines. The M12 mirrors send the light beams into the interferometric laboratory where they pass the switchyard which brings it on the designated beam paths. A dichroic mirror in the light path sends the N -band to MIDI while the near infrared part of the light passes the dichroic mirror. Another dichroic mirror on the PRIMA bench send the H -band to the IRIS tip-tilt corrector (Gitton et al. 2004) while the K -band goes to FSU-A.

During several PRIMA commissioning runs several nights (in total 10 full nights) were dedicated to test the MIDI + PRIMA FSU-A single-feed observing mode (on a back-up basis without impacting the higher priority commissioning tasks) where PRIMA FSU-A is used as a fringe tracker for MIDI at the ATs³. “First light” of the MIDI + PRIMA FSU-A mode was obtained in the night of July 23rd, 2009 (Fig. 5.6). Figure 5.6 shows a part of the MIDI real time display visible during observations. Each vertical line corresponds to the average Fourier transform of the frames of the same scan of the channeled spectrum and the horizontal axis of the plot can be interpreted as a time axis. Therefore, one can follow by eye the change in OPD (and therefore of the change in group delay, too) with time. Figure 5.6a) shows the signal of a typical observation when MIDI is operated without an external fringe tracker. The scatter in time caused by the atmospheric piston turbulence is clearly visible. The situation changes dramatically when FSU-A as a fringe tracker is used and the fringe signal gets stabilized by FSU-A (see Fig. 5.6b)) where a more substantial portion of the atmospheric piston turbulence get corrected. Typical group delay variations for MIDI “alone” are $\approx 30 - 35 \mu\text{m}$, which have to

³The data recorded during the commissioning of PRIMA have several drawbacks. A regular laboratory calibration of FSU-A was not carried out, which results in unknown phase shifts and wavelength calibration. Therefore, a post processing of the FSU-A data with respect to GD and PD is not possible. Hence, a proper reduction of MIDI+PRIMA data is not possible. In addition, a fibre of FSU-A inside the FSU cryostat was broken, causing significant flux losses. The intervention to fix this problem took place in March 2011. All these reasons make a homogeneous reduction and comparison of MIDI + PRIMA FSU-A data not possible. Therefore, we only present data from the official MIDI + PRIMA FSU-A run (ID: 087.C-0824).

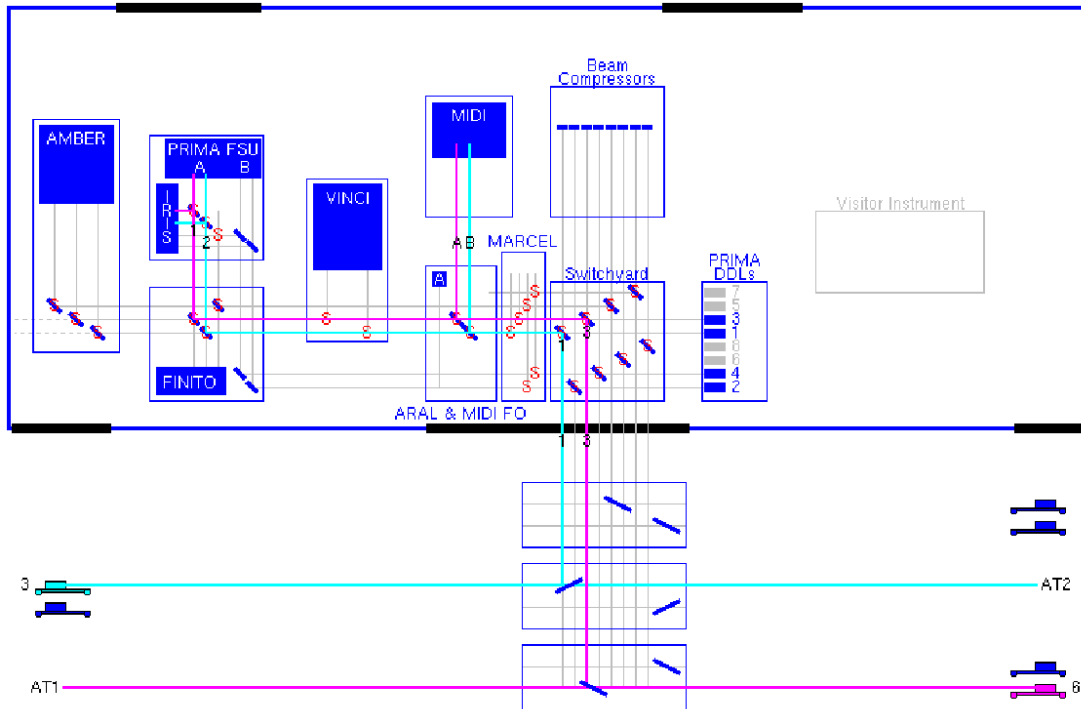


Figure 5.5: Schematic view of the VLTI laboratory configuration when MIDI is used with PRIMA FSU-A in single-feed, on-axis mode. The light path for the two beams are colored in blue and pink.

be corrected when reducing the data. Using FSU-A as a fringe tracker the group delay residuals in N band can go down to $1 \mu\text{m}$.

The observations aimed to test the current VLTI environment (including hard- and software,

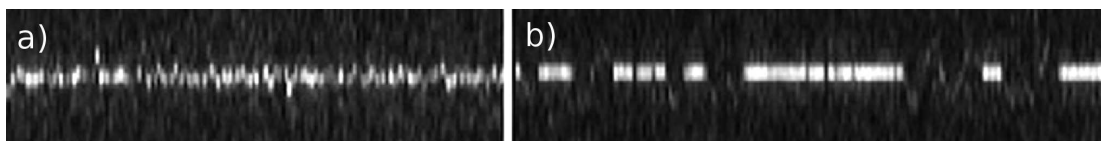


Figure 5.6: First light of the MIDI + PRIMA FSU-A mode on HD 187642 (Altair) in the night of July 23rd, 2009. Snapshot of the MIDI real time display visible during observation showing the average Fourier transform of the frames of the same scan of the channeled spectrum for MIDI without (a) and with (b) fringe tracker. The gaps visible in the right plot (b) are periods where FSU-A lost the fringe.

VLTI setup, observing templates, overall functionality, ...) when PRIMA and MIDI are used together. In addition, it was tried to retrieve estimations for the limiting magnitudes (IRIS in H -band, PRIMA in K -band, MIDI in N -band).

Results from these observations were partly published during the SPIE conference “Optical

and infrared Interferometry II” (Müller et al. 2010). The success of this mode with respect of higher sensitivity and overall improved data quality for MIDI resulted in a “technical” proposal where three full nights on the ATs were approved. The run was very successful concerning the observations. Sophisticated data reduction and analysis is still ongoing and can only partly presented in this document (Sec. 5.2 to Sec. 5.5).

5.2 Observations

The observations were carried out under the observing ID 087.C-0824. The nights were provided by the MIDI science group in the course of the MIDI GTO program. Originally, the observations were scheduled for September 17 to September 19. Due to failures of IRIS related hardware at the beginning of the first night, which could not be repaired, the run resulted in a 100% loss. The observations were rescheduled November 27 to November 30, 2011. Our target list included 18 objects. The sample consists of various objects ranging from simple calibrator stars to binary stars, Herbig Ae/Be stars, and an AGN. The *total N*-band fluxes ranging from 111 Jy down to 2.36 Jy. Table 5.1 lists all objects with their main properties. In addition, we list for each science target the corresponding calibrator star used in this observing run. For clarification: we denote the designation “science” for targets, which are not a MIDI calibrator star and are used to demonstrate effects on, e.g. correlated flux measurements.

The used instrumental setup of MIDI was a standard one, i.e. there were no extra modifications on the software side. Only the keyword `DEL.FT.SENSOR`, which defines the used fringe tracker for MIDI, was changed to the value `FSUA` in the template. This is a necessary step to prevent MIDI sending offset commands to the main DL. All observations were carried out using MIDI with the prism in the so called `HIGH_SENSE` mode. For bright objects, i.e. $F_{\text{corr}} > 10$ Jy, 8 000 frames were recorded for each observations. For faint objects with expected correlated fluxes $F_{\text{corr}} \lesssim 10$ Jy we used up to 32 000 frames.

A calibration of FSU-A during day time was carried out during the first two days. The calibration is needed to define the wavelengths and phase shifts of each pixel and each quadrant, respectively. Due to technical tests till sunset by the day time staff it was not possible to execute a calibration for the third night. From previous commissioning runs it is known that the calibration values do not change on a timescale of several days. Therefore, we used the calibration values derived on the second day for the reduction of the data obtained in the third night.

After each preset of the telescopes we executed a sky calibration of FSU-A and beam optimization. The sky calibration consists of recording flat fields and background images, which are necessary for the later reduction process. It depends on the *K*-band brightness of the star and the used DIT of the FSU. By default, the used DIT is set to 1 ms (or 1 kHz). This value has to be adjusted for fainter *K*-band targets. For $K \gtrsim 6$ mag on the ATs, the DIT has to be increased.

For faint science sources and when the weather conditions (seeing and coherence time) allowed it, we increased the DIT to 10 ms (or 100 Hz). The corresponding calibrator observations were then also carried out with the same DIT to ensure same conditions and comparability. For all science observation we observed at least one calibrator star. The observing log is presented in Table 5.2, including baseline properties and environmental conditions.

Table 5.1: Targets observed during the MIDI + PRIMA FSU-A observing run.

(1)	(2)	(3)	(4)	(5)	(6)	(7)	(8)	(9)	(10)	(11)
Target	Type	RA (J2000)	Dec (J2000)	V^a	H^a	K^a	$F_{\text{tot}}(9\mu\text{m})$	ϕ^a	Calibrator	Remarks
		[h m s]	[$^{\circ}$ ' '']	[mag]	[mag]	[mag]	[Jy]	[mas]		
HD 1014	Cal	00:14:27.6	-07:46:49.9	5.2	0.8	0.6	42.35	4.619	–	–
HD 1522	Cal	00:19:25.6	-08:49:26.5	3.6	1.1	1.0	27.32	3.272	–	–
HD 16212	Cal	02:36:00.1	-07:49:53.6	5.6	1.4	1.2	19.43	3.110	–	–
NGC 1068	Sci	02:42:40.7	-00:00:47.8	8.9	6.3	$\approx 9^b$	16.5^c	–	HD 16212	Seyfert 2 galaxy
RY Tau	Sci	04:21:57.4	+28:26:35.6	10.2	6.1	5.4	12.28	–	HD 27639	classical TTS
HD 27639	Cal	04:22:22.7	+20:49:16.9	5.9	1.5	1.4	19.50	3.080	–	–
HD 28305	Cal	04:28:37.0	+19:10:49.5	3.5	1.3	1.4	17.90	2.610	–	–
HD 36167	Cal	05:29:44.0	-01:05:32.1	4.7	1.0	0.8	27.31	3.660	–	–
δ Ori A	Sci	05:32:00.4	-00:17:56.7	2.2	3.0	3.9	3.05	–	HD 36167	binary ^d , $\rho = 325$ mas, PA=133 $^{\circ}$
β Pic	Sci	05:47:17.1	-51:03:59.4	3.9	3.5	3.5	3.22	–	HD 53047, HD 50310	planet-hosting star
HD 50310	Cal	06:49:56.2	-50:36:52.4	2.9	0.5	0.3	47.60	4.490	–	–
HD 50778	Cal	06:54:11.4	-12:02:18.9	4.1	0.8	0.6	34.85	3.907	–	–
HD 53047	Cal	07:00:51.5	-51:24:09.2	5.2	1.1	0.8	31.27	3.940	–	–
HD 53179	Sci	07:03:43.2	-11:33:06.2	9.9	5.2	3.8	111.00	–	HD 50778	Z CMa, HAeBe star, binary ^e
HD 83618	Cal	09:39:51.4	-01:08:34.1	3.9	1.0	0.9	27.79	3.362	–	–
HD 92305	Cal	10:35:28.1	-78:36:28.0	4.1	0.6	0.4	49.35	4.860	–	–
HD 100546	Sci	11:33:25.4	-70:11:41.2	6.8	6.0	5.4	38.47	–	HD 92305	HAeBe star
24 Psc	Sci	23:52:55.5	-03:09:19.7	5.9	3.8	3.7	2.36	–	HD 1014, HD 1522	binary ^f , $\rho = 43$ mas, PA=241 $^{\circ}$

Notes. The columns are: (1) the name of the target; (2) calibrator or science observation; (3) right ascension; (4) declination; (5) V -band magnitude; (6) H -band magnitude; (7) K -band magnitude; (8) $AKARI$ photometry at $9\mu\text{m}$ (Ishihara et al. 2010); (9) diameter of the stellar disk of the calibrator star; (10) corresponding calibrator star for the science target; (11) remarks.

^(a) Values taken from the database provided by Roy van Boekel. The database is distributed together with the MIA+EWS software package.

^(b) Estimated K -band magnitude as we only track on the core of the galaxy, see Wittkowski et al. (2004); Weigelt et al. (2004). ^(c) Photometry at $\lambda = 12 \mu\text{m}$ from Tristram et al. (2009). ^(d) Values for separation and position angle from Maíz Apellániz (2010). ^(e) See Koresko et al. (1991).

^(f) Values for separation and position angle from Mason et al. (2010).

Table 5.2: Overview of the observations of the MIDI + PRIMA FSU-A run.

(1)	(2)	(3)	(4)	(5)	(6)	(7)	(8)	(9)	(10)	(11)	(12)	(13)	(14)	(15)	(16)	(17)
#	Target	Date	UT [h m]	Station	u [m]	v [m]	BL [m]	PA [$^{\circ}$]	V_{model}^a at $2.2\mu\text{m}$	V_{model}^a at $10\mu\text{m}$	f_{FSU} [Hz]	DIT_{IRIS} [ms]	Airmass	Seeing [$''$]	τ_0 [ms]	RH [%]
1	HD 1014	2011-11-28	00:59	A1-B2	-9.80	4.92	10.97	296.7	0.98	1.00	1000	2	1.054	0.71	5.91	11
2	24 Psc	2011-11-28	01:18	A1-B2	-9.02	4.77	10.20	297.9	0.11	0.93	1000	10	1.126	1.03	4.07	12
3	HD 16212	2011-11-28	02:21	A1-B2	-10.35	4.57	11.31	293.8	0.99	1.00	1000	2	1.052	0.85	4.84	21
4	NGC 1068	2011-11-28	02:44	A1-B2	-10.26	4.50	11.20	293.7	–	–	100	2000	1.102	1.08	5.39	21
5	HD 16212	2011-11-28	03:06	A1-B2	-10.00	4.84	11.10	295.8	0.99	1.00	100	2	1.047	1.08	3.56	21
6	HD 1014	2011-11-28	03:30	A1-B2	-5.57	5.64	7.93	315.4	0.99	1.00	1000	2	1.451	1.64	2.35	22
7	24 Psc	2011-11-28	04:04	A1-B2	-3.32	5.03	6.03	326.6	0.99	1.00	1000	10	2.046	1.46	2.65	22
8	HD 28305	2011-11-28	04:33	A1-B2	-10.24	3.69	10.89	289.8	1.00	1.00	1000	3	1.386	1.39	2.83	20
9	HD 16212	2011-11-28	05:18	A1-B2	-6.84	5.52	8.79	308.9	1.00	1.00	100	3	1.288	0.81	4.80	20
10	HD 36167	2011-11-28	06:25	A1-B2	-9.61	4.57	10.64	295.4	0.99	1.00	1000	6	1.109	0.69	5.69	22
11	δ Ori A	2011-11-28	06:44	A1-B2	-9.26	4.52	10.31	296.0	0.98	0.57	1000	7	1.134	0.80	4.84	22
12	HD 36167	2011-11-28	07:05	A1-B2	-8.77	4.60	9.91	297.7	0.99	1.00	1000	2	1.163	0.96	3.98	21
13	δ Ori A	2011-11-28	07:16	A1-B2	-8.53	4.53	9.66	298.0	0.73	0.56	1000	7	1.188	1.10	3.49	21
14	HD 50778	2011-11-28	07:31	A1-B2	-9.89	5.06	11.11	297.1	0.99	1.00	1000	2	1.030	1.01	3.77	20
15	HD 53179	2011-11-28	07:58	A1-B2	-9.61	5.19	10.92	298.4	–	–	1000	100	1.042	1.81	2.72	22
16	24 Psc	2011-11-29	02:31	A1-D0	-26.36	-22.81	34.86	229.1	0.75	0.62	1000	10	1.335	1.19	3.21	20
17	HD 1014	2011-11-29	02:51	A1-D0	-26.44	-22.13	34.48	230.1	0.86	0.99	1000	3	1.281	1.09	3.15	26
18	HD 16212	2011-11-29	03:12	A1-D0	-26.13	-24.04	35.51	227.4	0.93	1.00	100	4	1.051	1.21	2.83	19
19	HD 27639	2011-11-29	03:53	A1-D0	-23.04	-16.55	28.37	234.3	0.95	1.00	1000	4	1.450	1.38	2.45	18
20	HD 27639	2011-11-29	04:12	A1-D0	-24.09	-17.19	29.59	234.5	0.95	1.00	1000	4	1.431	1.25	2.69	17
21	RY Tau	2011-11-29	04:55	A1-D0	-26.10	-16.73	31.00	237.4	–	–	1000	100	1.673	1.12	2.95	17
22	HD 50778	2011-11-29	05:36	A1-D0	-19.31	-26.71	32.96	215.9	0.90	1.00	1000	4	1.098	1.11	2.93	18
23	HD 53179	2011-11-29	05:57	A1-D0	-20.35	-26.37	33.31	217.7	–	–	1000	100	1.082	0.68	4.83	18
24	HD 50310	2011-11-29	06:17	A1-D0	-22.72	-26.32	34.77	220.8	0.86	0.99	1000	4	1.125	0.95	3.37	18
25	β Pic	2011-11-29	06:30	A1-D0	-26.43	-19.67	32.95	233.4	–	–	1000	10	1.123	0.80	4.00	18
26	HD 50310	2011-11-29	06:46	A1-D0	-24.44	-24.00	34.26	225.5	0.86	0.99	1000	4	1.114	0.77	4.10	18

Table 5.2: continued.

(1)	(2)	(3)	(4)	(5)	(6)	(7)	(8)	(9)	(10)	(11)	(12)	(13)	(14)	(15)	(16)	(17)
#	Target	Date	UT	Station	u	v	BL	PA	V_{model}^a	V_{model}^a	f_{FSU}	DIT_{IRIS}	Airmass	Seeing	τ_0	RH
			[h m]		[m]	[m]	[m]	[$^\circ$]	at $2.2\mu\text{m}$	at $10\mu\text{m}$	[Hz]	[ms]		[$''$]	[ms]	[%]
27	HD 53047	2011-11-29	07:01	A1-D0	-24.65	-23.51	34.07	226.4	0.90	0.99	1000	4	1.121	0.96	3.30	19
28	HD 83618	2011-11-29	07:44	A1-D0	-15.99	-23.65	28.55	214.1	0.95	1.00	100	3	1.273	0.83	3.73	19
29	HD 92305	2011-11-29	08:28	A1-D0	-14.82	-26.97	30.78	208.8	0.87	0.99	1000	4	1.793	1.04	2.95	24
30	HD 1014	2011-11-30	00:46	B2-D0	-16.25	-28.94	33.19	209.3	0.87	0.99	1000	2	1.051	2.02	1.84	17
31	HD 1522	2011-11-30	01:26	B2-D0	-17.72	-28.66	33.70	211.7	0.93	1.00	1000	3	1.074	1.53	2.50	18
32	24 Psc	2011-11-30	01:46	B2-D0	-19.05	-27.92	33.80	214.3	0.90	0.40	1000	10	1.198	1.78	2.10	20
33	HD 1014	2011-11-30	02:03	B2-D0	-18.94	-28.13	33.91	214.0	0.86	0.99	1000	2	1.151	1.28	2.95	20
34	24 Psc	2011-11-30	02:24	B2-D0	-19.53	-27.75	33.93	215.1	0.94	0.42	1000	10	1.321	1.11	3.40	18
35	HD 1522	2011-11-30	02:46	B2-D0	-19.49	-27.66	33.84	215.2	0.93	1.00	1000	3	1.250	1.12	4.23	21
36	24 Psc	2011-11-30	03:04	B2-D0	-19.45	-27.56	33.73	215.2	0.92	0.41	1000	10	1.535	1.37	3.41	20
37	HD 27639	2011-11-30	03:43	B2-D0	-12.14	-20.45	23.78	210.7	0.97	1.00	1000	4	1.460	0.93	4.93	20
38	RY Tau	2011-11-30	04:03	B2-D0	-13.48	-17.61	22.18	217.4	–	–	1000	100	1.676	0.73	6.19	20
39	HD 16212	2011-11-30	04:21	B2-D0	-18.86	-28.17	33.90	213.8	0.93	1.00	100	3	1.143	0.73	6.00	20
40	HD 50778	2011-11-30	06:39	B2-D0	-13.82	-30.00	33.03	204.7	0.90	1.00	1000	2	1.028	0.90	4.69	14
41	HD 53179	2011-11-30	07:11	B2-D0	-15.10	-29.65	33.27	207.0	–	–	1000	40	1.026	0.72	5.78	12
42	HD 92305	2011-11-30	08:11	A1-D0	-13.51	-27.76	30.87	206.0	0.87	0.99	1000	2	1.812	0.89	4.72	12
43	HD 100546	2011-11-30	08:48	A1-D0	-12.25	-30.73	33.09	201.8	–	–	1000	100	1.600	0.98	4.36	13

Notes. The columns are: (1) index number by which an observation can be identified in tables and figures; (2) the name of the observed object; (3) date; (4) time; (5) telescope stations; (6) and (7) u, v -coordinates; (8) length of the projected baseline; (9) position angle of the projected baseline; (10) and (11) model visibility in K -band for FSU-A and in N -band for MIDI, respectively; (12) FSU-A operation frequency; (13) IRIS DIT; (14) airmass; (15) seeing; (16) coherence time; (17) relative humidity.

^(a) See Sec. 5.2.2 for explanation.

5.2.1 Observing sequence

Till this day, MIDI + PRIMA FSU-A observations are still carried out in an experimental or engineering like fashion and requires several steps with manual setup of the system. In addition, it was our responsibility to configure and use VLTI in a proper way. Therefore, we list the major steps of a typical observing sequence in the following. Calibrations of MIDI and FSU-A executed during daytime are carried out using standardized templates and will not discussed here.

Preparation

Besides a proper configuration of the VLTI from ISS level, there are following steps which have to be applied prior to the observation.

- Determination of the offset value, which has to be applied to LMOT1 of FSU-A in order to compensate for instrumental OPD between MIDI and FSU-A. The current value is $-9.5 \cdot 10^{-4}$ m and could in principle only change after realignment of the instrument.
- Because of dichroics and their mounts in front of IRIS, which are transparent for K -band (to FSU-A) but reflective for H -band (to IRIS), the position of the MIDI reference pixel ($x = 64, y = 64$) on IRIS has to be changed from ISS level. As a rule of thumb its minus six pixels in x -direction and -12 pixels in y -direction.
- The keyword `DEL.FT.SENSOR` of the MIDI template has to be changed to `FSUA` to guarantee that only FSU-A can send offsets to the main DL.
- The IRIS filter is set to K -band by default if the preset is executed from MIDI. Therefore, it has to be ensured that the H -band filter is set for IRIS otherwise FSU-A will not receive any light.

Observation

After a successful setup the actual observation is carried out by the following steps (in chronological order).

1. Preset of VLTI including telescopes and DLs, which has to be executed from MIDI.
2. Start of acquisition, telescope tracking and guiding (close of STRAP loop).
3. Optimization of the telescope focus and initialization of “lab guiding” with IRIS.
4. Optional: check of MIDI pupil alignment, record of acquisition images.
5. Optional: FSU-A: beam optimization (spiral search, beam tracking)
6. Execution of FSU-A sky calibration.

7. FSU-A: fringe scan and its evaluation, optimization of OPDC parameters (zero OPD and SNR thresholds). Standard values for the three SNR levels are 5 (detection level), 2 (close level), 1 (open level).
8. Start fringe tracking of FSU-A.
9. Data recording of MIDI and FSU-A.

Fringe scan with FSU-A

Depending on the accuracy of the OPD model for a certain pair of telescope station the position of zero OPD can change with time and telescope pointing. To find fringes on FSU-A two possibilities are available. The first method is running a ZPD search where an increasing sawtooth pattern (or one dimensional spiral) is performed by the tracking DL until the fringe is detected. This is relatively time consuming if the position of zero OPD is unknown. A more efficient way is to perform a so called fringe scan. Therefore the tracking DL drives a ramp of a previously defined range. The detection of the fringe is carried out by an online evaluation of this scan. Currently, we simply compute the flux difference of the white-light channels A-C and B-D. The fringe signal between the channels A and C, and B and D, respectively, have opposite phases because of 180° phase-shifts from channel to channel. Therefore, the difference between two opposite channels results in a fringe signal with doubled amplitude. Outside of the fringe only residual noise is left because the two beams are uncorrelated (Fig. 5.7). An estimation of the

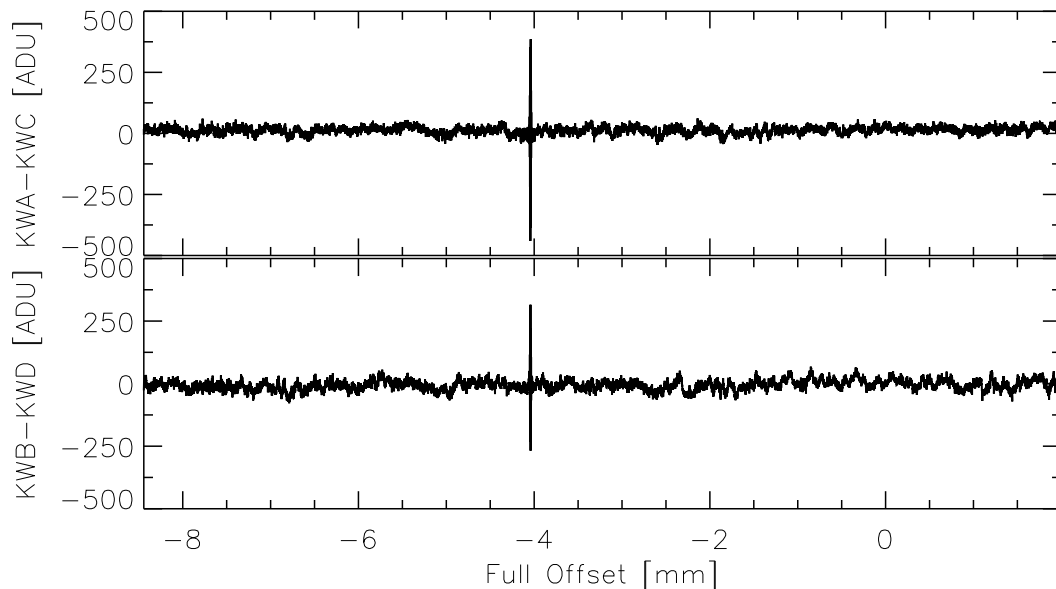


Figure 5.7: Fringe scan of β Pic. A ramp of ≈ 10 mm was driven by the racking DL and is called “Full Offset” here. The plots show the subtracted white-light channels A-C and B-D, respectively. The fringe, visible as a peak like feature in both plots, is clearly detected at a position of ≈ 4 mm.

central fringe position is derived by finding the maximum of the SNR of the PD measurements, which is located at $4.04 \cdot 10^{-3}$ m in this case. Figure 5.8 shows a close-up view of Fig. 5.7 around the fringe position. The last step of the evaluation is a fit of a function to the measured

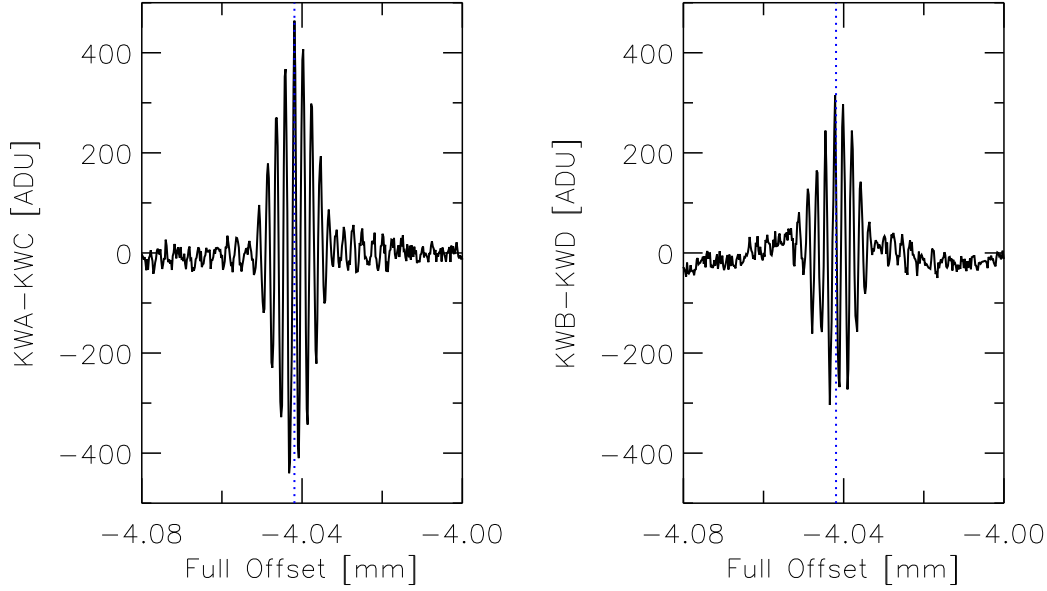


Figure 5.8: Close-up view of the detected fringe from the scan. The vertical blue line marks the estimated position of the fringe center based on SNR measurements of the PD.

PD SNR values around the fringe. The function (C. Schmid, private communication) consists of two Gaussians and one of them is modulated by a sinus (Eqn. 5.4), which is an approximate description of the measured PD SNR:

$$SNR_{\text{fit}} = P_1 \left\{ \exp \left[-0.5 \left(\frac{x - P_2}{P_3} \right)^2 \right] + P_4 \exp \left[-0.5 \left(\frac{x - P_5}{P_6} \right)^2 \right] \sin(x \cdot P_7 - P_8) \right\} + P_9, \quad (5.4)$$

where x is the current offset position of the tracking DL, P_1 and P_4 are the amplitudes, P_2 and P_3 are the centers, and P_3 and P_6 are the widths of the two Gaussians, respectively. P_7 and P_8 are the frequency and phase of the sinusoidal signal, respectively. P_9 is an offset parameter. This enables us to derive estimates for the central fringe position as well as reasonable SNR thresholds for the OPDC. The open level, SNR_{open} , is simply defined by P_8 . The close level, SNR_{close} , is approximately defined by

$$SNR_{\text{close}} \approx SNR_{\text{fit}}(x = P_2 - 2P_3) \quad (5.5)$$

and the detection level, SNR_{detect} , is approximately defined by

$$SNR_{\text{detect}} \approx SNR_{\text{fit}}(x = P_2 - P_3). \quad (5.6)$$

The result of such a fit is presented in Fig. 5.9. By default, the thresholds for the OPDC are set to $SNR_{\text{open}} = 1$, $SNR_{\text{close}} = 2$, and $SNR_{\text{detect}} = 5$. This fit gives us optimized values for the SNR thresholds: $SNR_{\text{open}} = 0.7$, $SNR_{\text{close}} = 1.9$, and $SNR_{\text{detect}} = 6.4$. The execution of

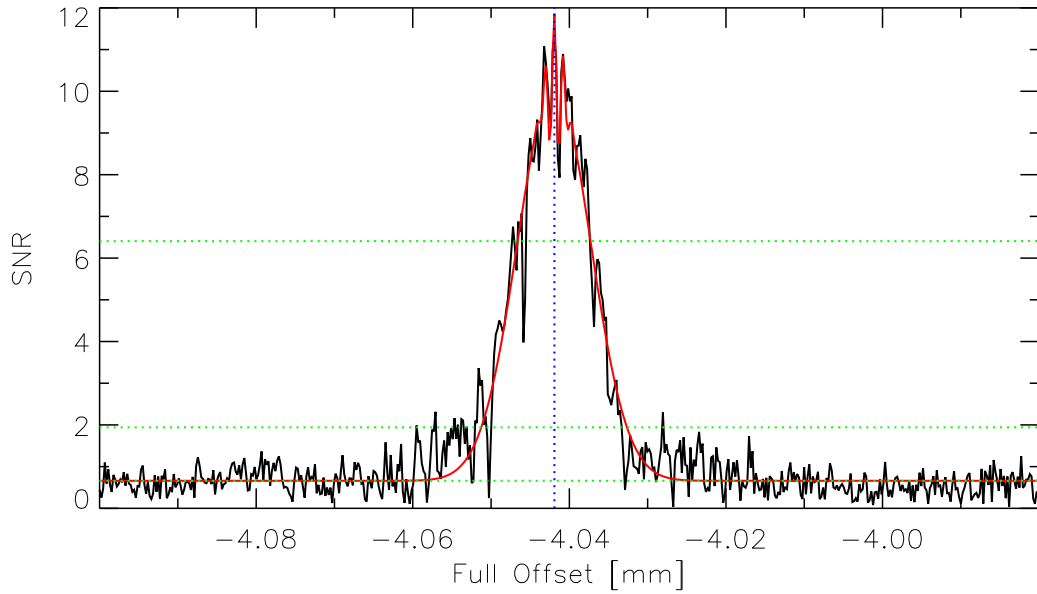


Figure 5.9: Fit (red) of the measured PD SNR (black). The vertical blue line marks the estimated position of the fringe center. The three horizontal green lines mark the estimated SNR thresholds for the OPDC of this particular fringe scan, where SNR_{open} is the lowest, SNR_{close} is the middle, and SNR_{detect} is the upper line.

a fringe scan and its evaluation provides us therefore with optimized OPDC parameters, which guarantee an efficient and optimal fringe track. The SNR thresholds depend mainly on the K -band visibility of the star and the current weather conditions during observation. The contrast for objects with visibilities significantly lower than 1 will have by definition a lower contrast ratio. Thus, the fringe will appear less prominent with respect to the flux residuals (see Fig. 5.7). In case of unfavorable seeing conditions, $seeing \gtrsim 1.5$ arcsec, the injection of the flux into the fibres of FSU-A will be degraded because of the limited bandwidth of tip-tilt corrections send by IRIS.

5.2.2 Estimation of visibility

In Table 5.2 we list the expected K - and N -band visibility for simple sources (calibrator stars, binaries) for a given BL and PA during observation. MIDI calibrator stars are usually giant stars with spectral types K or M because they have to be bright and red sources. Therefore, the

apparent stellar diameter of these stars reaches values where K -band visibilities $V_K < 1$ are expected. Thus, a trivial point source model cannot be applied here but a uniform disk model, which is the simplest model to describe photospheric emission from a star as it does not account for limb-darkening effects. It is defined by

$$V = \left| 2 \frac{J_1(\pi\theta f_s)}{\pi\theta f_s} \right|, \quad (5.7)$$

where θ is the apparent stellar diameter in arcsec and $f_s = BL/\lambda$ is the spatial frequency in fringe cycles / rad. The expected visibility of a binary star (24 Psc and δ Ori A) was modeled by assuming two point sources, which have a separation and orientation given by the values provided in Table 5.2 (Eqn. 5.8).

$$V = \sqrt{\frac{1 + F^2 + 2F \cos\left((2\pi/\lambda)\vec{B} \cdot \vec{\rho}\right)}{1 + F}}, \quad (5.8)$$

where $F = F_2/F_1$ is the flux ratio between the two stars, \vec{B} is the baseline vector, and $\vec{\rho}$ is the separation vector of the two stars.

5.3 Data reduction

The MIDI data reduction of the MIDI + PRIMA FSU-A observations was performed using two different approaches, which will be described in the following sections.

5.3.1 Reduction using EWS

The first method we used is a coherent data reduction and is performed using the standard EWS software package⁴ (Jaffe 2004). We will subsequently refer to this reduction procedure as the *EWS* method. The reduction process is already described in great detail by Tristram (2007) and Burtscher (2011). Therefore, we will briefly list the main steps performed by this reduction package. FSU-A data are not taken into account here.

a) Creating masks Computation of custom masks for observed MIDI calibrator stars by constructing an image of the correlated flux as a function of wavelength and slit position on the detector and fitting a set of smoothed Gaussian to this image. This step makes use of the `midimakeMask` command of EWS. An observed science target, which is supposed to be faint here, will use the mask of its corresponding calibrator.

⁴EWS is part of the software package MIA+EWS (MIDI Interactive Analysis + Expert Work Station) and is available for download at <http://www.strw.leidenuniv.nl/~nevec/MIDI/index.html>

- b) Compression** Compress MIDI data using customized masks to obtain a 1-dimensional spectrum using the `oir1dCompressData` command from EWS.
- c) Form fringes** Form spectrally dispersed fringes by subtraction of the two interferometric channels and suppression of background using the `oirFormFringes` command from EWS.
- d) Instrumental OPD** Remove the known instrumental OPD components from the fringe spectra using the `oirRotateInsOpd` command from EWS.
- e) Group delay** Computation of MIDI group delay, GD_{MIDI} , using the `oirGroupDelay` command from EWS.
- f) Remove GD** Remove GD_{MIDI} and instrumental OPD from the fringe data using the `oirRotateGroupDelay` command from EWS.
- g) Flag bad data** Data, which do not meet certain criteria, especially if there were jumps in OPD detected, are flagged as bad frames and will not be processed further. This step is executed by the `oirRotateGroupDelay` command from EWS.
- h) Averaging good frames** In the final step, all unflagged but phase rotated frames are averaged to derive a raw correlated flux, $F_{\text{corr, raw}}$, using the `oirAverageVis` command from EWS.

5.3.2 Reduction of MIDI + PRIMA FSU-A data

This reduction method is more complex as it takes the interferometric K -band data into account. The aim of this reduction is to predict the N -band GD, PD, and dispersion from the K -band measurements by FSU-A. This is in particular a powerful method for faint or resolved N -band targets where standard reduction methods, such as *EWS*, can not be successful because of very low SNR data. Because we make use of the analytical findings by Koresko et al. (2006) we will subsequently refer to this reduction procedure as the *Koresko* method. The reduction steps presented in the following are implemented in a pipeline written in IDL, which also makes use of the routines provided by EWS.

Preparation

The following steps apply to all observations, i.e. they are executed on both bright calibrator stars and faint science targets.

Table 5.3: MIDI files with NULL values.

#	Target	Date	Time	Null at Frame
1	HD 1014	2011-11-28	00:59	7173
2	24 Psc	2011-11-28	01:18	3922
3	HD 16212	2011-11-28	02:21	6551
4	NGC 1068	2011-11-28	02:44	5690
7	24 Psc	2011-11-28	04:04	4878
14	HD 50778	2011-11-28	07:31	6360
21	RY Tau	2011-11-29	04:55	1531
33	HD 1014	2011-11-30	02:03	2966
36	24 Psc	2011-11-30	03:04	3970
40	HD 50778	2011-11-30	06:39	13674
43	HD 100546	2011-11-30	08:48	18440

Notes. For comparison the index number in the first columns refers to the index number of Table 5.2.

NULL time stamps A known problem of the MIDI data are the sporadic appearing NULL values in the timestamps, which are identified to be of electronic origin of a timing board. This is problematic for the later synchronization in time of the MIDI data with the FSU-A data if not corrected. This affects also the values “localOPD”, “stepping phase”, and “integration time” present in the MIDI fits files. In addition, the OPD values are arbitrary values and therefore wrong because MIDI has no longer control about the delay lines when PRIMA FSU-A is used as a fringe tracker. Therefore, we replace the OPD values with zero and correct for NULL timestamps. Table 5.3 lists the found NULL values present in our data set.

FSU-A Laboratory Calibration The “Lab Calibration” files of FSU-A are reduced and analyzed to get the wavelength and phase-shift values of each channel, which are needed later in the reduction process. The reduction is carried out by a set of MATLAB routines, which are also used at the telescope, provided by R. Abuter (private communication).

MIDI Masks Computation of custom masks similar to Sec. 5.3.1 a).

K-band GD and PD Computation of the group and phase delay of each PRIMA FSU-A fringe track. We use the algorithm described in Sahlmann et al. (2009) (especially Eqns. 1 to 10.)

Prediction of N-band GD and PD Computation of group delay ($GD_{\text{comp},N}$), phase delay ($PD_{\text{comp},N}$), and dispersion ($DISP_{\text{comp},N}$) for the N-band using K-band GD and PD from PRIMA FSU-A. We use the approach from Koresko et al. (2006) and do not present a detailed description here because the computation itself is straightforward, see Eqn. 9 to 14 in Koresko et al. (2006).

The K -band GD from FSU-A is filtered by a low-pass Butterworth filter because the FSU-A GD tracking happens at ≈ 1 Hz frequency only. The crucial part for the computation is to reliably unwrap the K -band phase delay measured by PRIMA FSU-A. J. U. Pott developed a sophisticated routine, which is able to identify phase jumps and reliably correct for them. The basic strategy, which consists of four steps, is briefly described in the following:

- “intra-data unwrap”: define and clean-up areas with half of the phases around $-\pi$ and π , which belong together. This is realized by comparing the median filtered and smoothed PD values. The filter window is defined by a certain box size.
- unwrapping of individual pixel, where a phase-jump around the local median is detected
- “inter-pixel unwrap”: unwrap where the local median jumps by more than $\lambda/2$
- The previous steps might produce blocks of PD values, which are wrapped with respect to each other. In a last step, the routine applies an “inter-block unwrap”.

Figure 5.10 and Fig. 5.11 show exemplarily the intermediate steps and the final result of the unwrapping algorithm. In case of a perfect fringe track (Fig. 5.10), i.e. FSU-A was locked on the fringe during the entire observation, the K -band phase delay is a constant value without any phase jumps. If FSU-A lost the fringe occasionally during the observation (this depends on various parameters such as target brightness and visibility, airmass, seeing, coherence time, used OPDC SNR thresholds), the computed phase delay is a random value as it is computed from the flux of the uncorrelated beams during this time. Figure 5.11 shows the intermediate and final unwrapped phase delay for an observation with a lock ratio of 90%.

Reduction steps for calibrator stars

To reduce data recorded in the MIDI + PRIMA FSU-A mode, we have to distinguish between observations of calibrator stars and science targets. We assume that the calibrator stars have correlated N -band fluxes $F_{\text{corr},N} > 10$ Jy, which is the case for our sample. This lower flux limit guarantees a reduction of the MIDI data independent from FSU-A data obtained with the ATs, which is important for the reduction of science targets with $F_{\text{corr},N} < 10$ Jy. This issue will be discussed in the next section. For bright calibrator stars we perform following reduction steps:

- The reduction steps a) to e) described in Sec. 5.3.1 are performed in a similar way.
- Synchronization of MIDI and PRIMA FSU-A data. The typical sub-integration time of MIDI is usually 18 ms in PRISM HIGH_SENSE mode. PRIMA FSU-A is operated usually with 1 ms and up to 10 ms for faint K -band targets. In addition, the timestamps of MIDI are in MJD, the timestamps of PRIMA FSU-A are in micro seconds. Therefore, we have to express the MIDI timestamps in microseconds with respect of

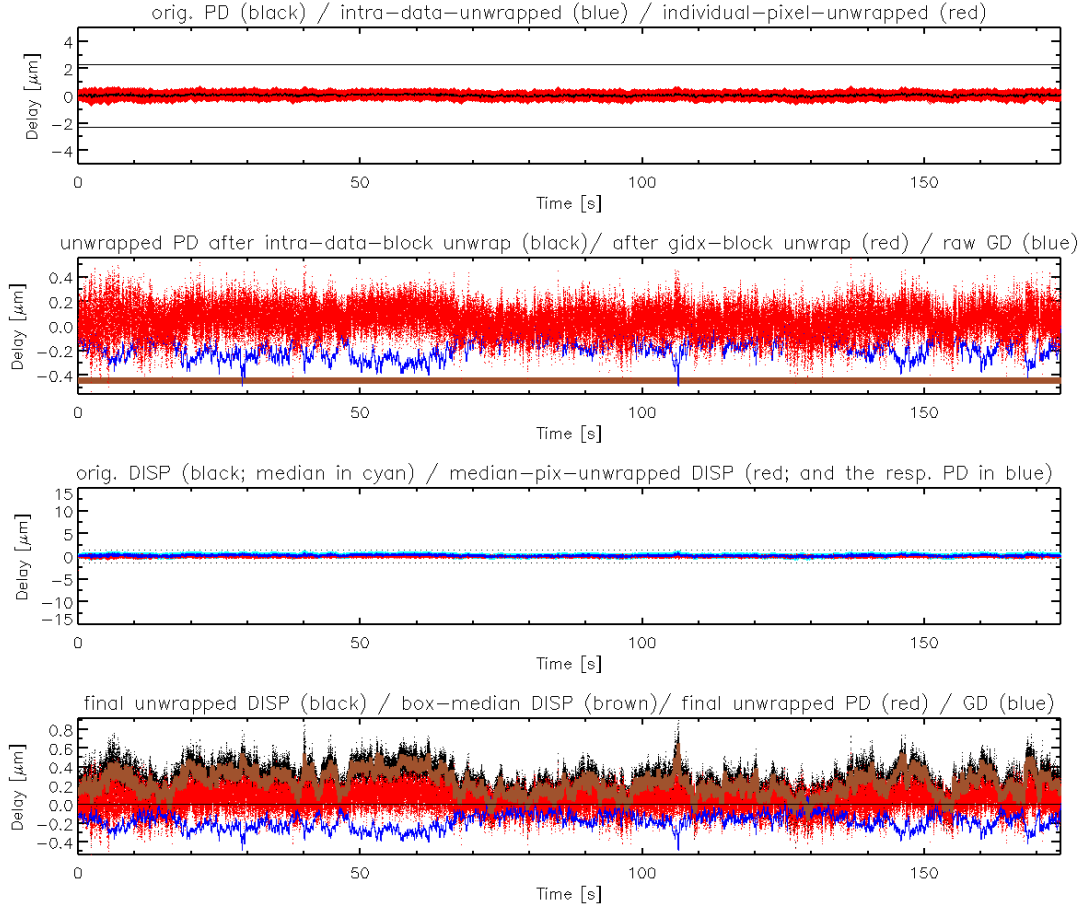


Figure 5.10: FSU-A observation of HD1014 (#1). The lock ratio is 100%. The phase delay appears as a smooth constant line without any jumps.

the start of file recording of PRIMA FSU-A. In addition, ≈ 20 PRIMA FSU-A frames were recorded during one MIDI exposure. These frames are identified and the values ($PD_{\text{comp},N}$, $GD_{\text{comp},N}$, and $DISP_{\text{comp},N}$) averaged. This depends also on the OPDC state of PRIMA FSU-A, i.e. if FSU-A locked on the fringe during a MIDI integration or not. We use the information of the OPDC state to flag the MIDI data.

- The offset of $GD_{\text{comp},N}$ is then fitted to GD_{MIDI} , which was measured in step e). This information is needed later for faint science targets.
- Remove the group delay $GD_{\text{comp},N}$ derived from K -band data using the `oirRotateGroupDelay` command from EWS. In addition, we provide the routine a phase file containing the previous determined $DISP_{\text{comp},N}$ from the K -band data. This corrects for changes of the water vapor dispersion phase in the N -band.
- In the final step we average all unflagged but phase rotated frames together to derive a raw correlated flux, $F_{\text{corr, raw}}$, using the `oirAverageVis` command from EWS.

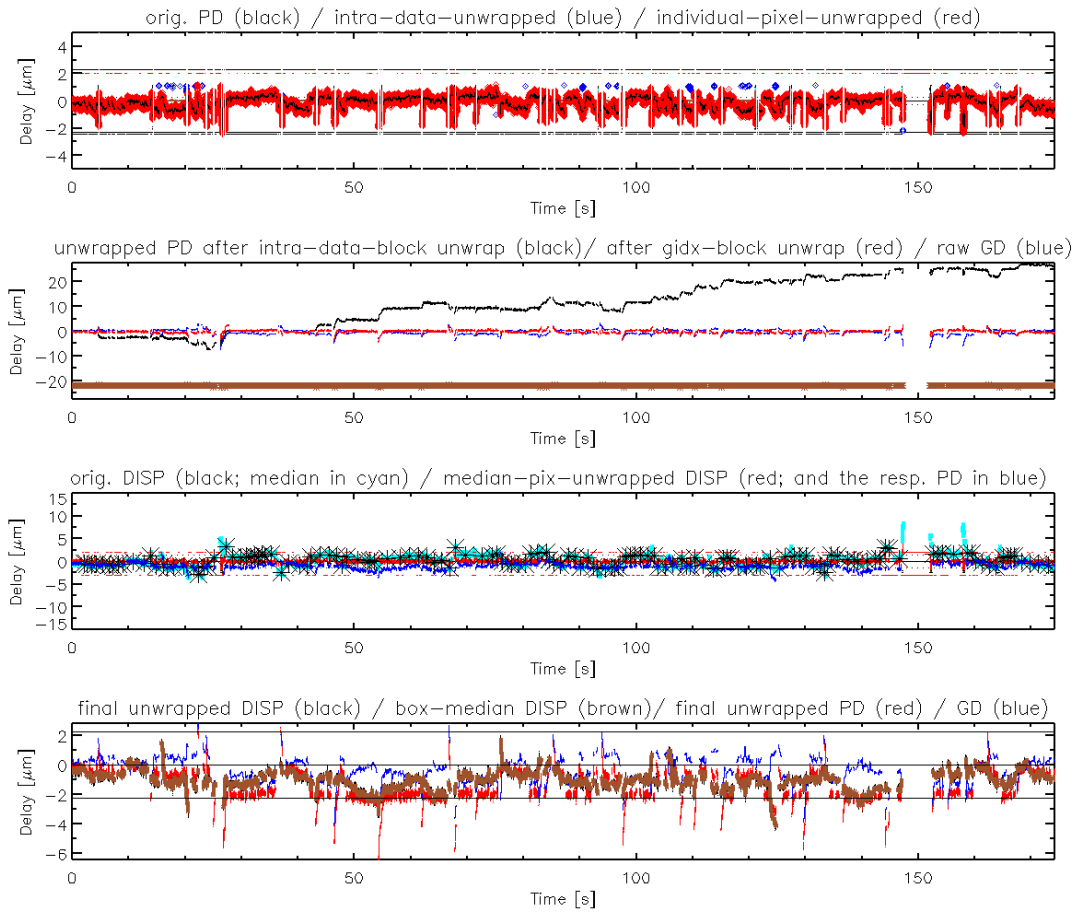


Figure 5.11: FSU-A observation of HD1014 (#30). The lock ratio is 90%. The phase delay measurement shows several jumps and drifts, which are properly handled by the unwrapping algorithm. Data where the OPDC state of FSU-A was not in state 7 are removed and appear as gaps in the plot.

Reduction steps for faint science targets

- The first four steps are identical to that of Sec. 5.3.2. The only difference is that we use the custom made masks from the calibrator stars for the corresponding science source.
- If the science source has a correlated flux $F_{\text{tot},N} \lesssim 10$ Jy we cannot determine the N -band group delay using standard methods and therefore, we cannot determine a mean position of GD_{MIDI} . We use $PD_{\text{comp},N}$, $GD_{\text{comp},N}$, $DISP_{\text{comp},N}$, and apply the determined offset from the corresponding calibrator observation to $GD_{\text{comp},N}$.
- Remove the group delay $GD_{\text{comp},N}$ derived from K -band data using the `oirRotateGroupDelay` command from EWS. In addition, we provide the routine a phase file containing the previously determined $DISP_{\text{comp},N}$ from the K -band data. This corrects for changes of the water vapor dispersion phase in the N -band.

- In the final step we average all unflagged but phase rotated frames together to derive a raw correlated flux, $F_{\text{corr, raw}}$, using the `oirAverageVis` command from EWS.

5.4 Calibration

After describing the reduction process of calibrator and science data, we will now describe the necessary steps to derive calibrated correlated N -band fluxes, $F_{\text{corr, cal}}$ **without** any photometry taken during the observation. From the previous reduction process we obtained the raw correlated amplitude of the calibrator stars and science targets, $F_{\text{corr, raw}}$.

5.4.1 Construction of the Transfer Function

From a calibrator database (“vanBoekel database” available in EWS provided by Roy van Boekel, it contains data to 789 calibrator stars) we know the apparent stellar diameter, θ , and the N -band spectrophotometry of the calibrator source, F_{tot} . In addition, the projected baseline, BL , can be computed from the coordinates of the used telescope stations and observing time. From these values we can compute a theoretical visibility, V_{model} , using a uniform disk model (see Sec. 5.2.2). The theoretical correlated flux that can be expected from the calibrator star is computed by $F_{\text{corr, model}} = V_{\text{model}} \cdot F_{\text{tot}}$. The transfer function of each night, TF , can be know computed by $TF = F_{\text{corr, raw}}/F_{\text{corr, model}}$. Figure 5.12 shows the TF s for all calibrators (lines in light blue (*Koresko*) and light green *EWS*) observed during the three nights of the MIDI + PRIMA FSU-A observing run. We constructed a mean TF by averaging the individual TF s, which is valid during a “stable” (with respect to weather conditions) night. The error bars are derived by computing the standard deviation of all TF s for each individual night.

5.4.2 Calibration of $F_{\text{corr, raw}}$

To obtain calibrated correlated fluxes we finally only need to compute $F_{\text{corr, cal}} = F_{\text{corr, raw}}/TF$. This applies to calibrator stars and science targets. To obtain calibrated visibilities (which is not strictly required for most science cases) one need photometric information of the science source. Because the quality of the photometric MIDI N -band data from the ATs is generally poor (small FoV, limited sensitivity due to small light collection area), one could use data from other sources, such as TIMMI2, *Spitzer*, VISIR, amongst other sources (successfully applied in Müller et al. (2010)). However, this assumes that the science source is photometrically stable between the time where the interferometric and photometric data were recorded.

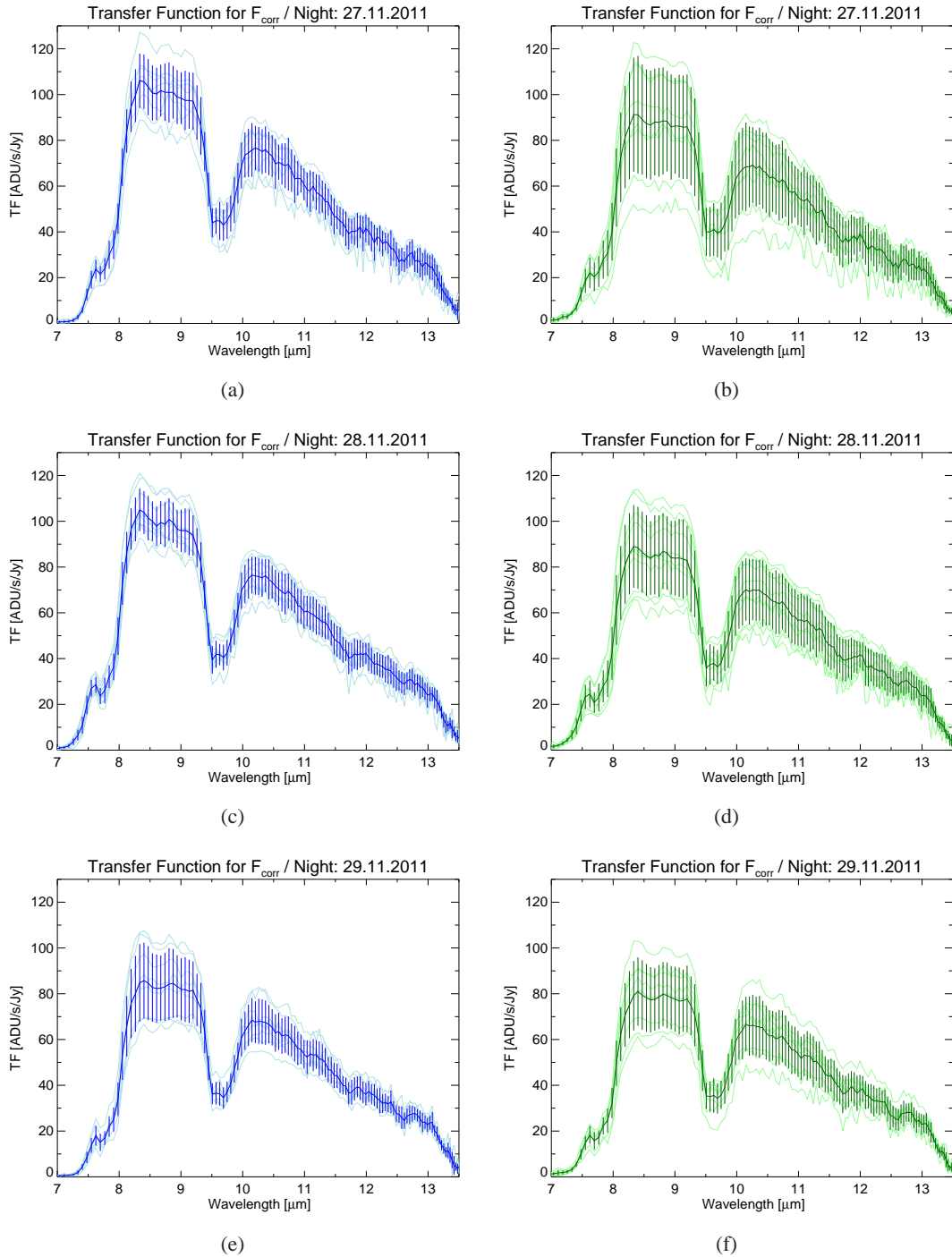


Figure 5.12: Transfer functions for the correlated flux for all calibrator stars observed during the three nights. The lines in blue in the left column (plots (a), (c), and (e)) are the mean TF s constructed by averaging the individual TF s derived by the *Koresko* reduction method. The plots in green in the right column (plots (b), (d), and (f)) show the same results but for the *EWS* reduction method. The calibrator star HD1014 (index number 6 in Table 5.2) observed on the night of November 27 is not taken into account because its resulting TF deviates significantly from the sample of this night. The strong absorption feature around 9.7 μm is caused by atmospheric Ozone.

5.5 Results

5.5.1 Comparison between *EWS* and *Koresko*

Table 5.4 lists the FSU-A lock ratio and the K -band GD and PD residuals of each observation. In addition, the total number of recorded MIDI frames and the number of used MIDI frames for the reduction using the *EWS* and *Koresko* reduction method are presented. For brighter N -band objects, the standard *ews* reduction method tends to use slightly more frames than *Koresko*. This is simply related to the fact that the *Koresko* method takes the FSU-A data into account in order to flag a MIDI frame as “good” or “bad”. Thus, the constraints that a MIDI frame is considered as “good” are much more stringent. As described in Sec. 5.3.2, FSU-A must be locked on the fringe (OPDC state 7) during one MIDI frame. In addition, using *EWS* OPD jumps of $10 \mu\text{m}$ are allowed between two successive frames before the frame is flagged as “bad”. This value represents five times the wavelength of the K -band and such jumps can only occur with a loss of the fringe by FSU-A.

The number of used frames changes drastically for faint N -band targets with $F_{\text{corr},N} < 10 \text{ Jy}$, i.e. for faint and/or resolved targets. At such flux levels an efficient reduction using *EWS* is no longer possible because the faint interferometric signal is on the level of the residual N -band background. However, the additional informations provided by FSU-A (we know if FSU-A was tracking on the fringe and we know the K -band GD and PD) allow us to predict the group delay and dispersion for the N -band at the point of observation as described in Sec. 5.3.2. Figure 5.13 displays exemplarily the measured (by *EWS*) and predicted (by *Koresko*) N -band GD and DISP. All characteristics and drifts can be predicted by the K -band data. This comparison is of course only applicable to bright sources with $F_{\text{corr},N} \gtrsim 10 \text{ Jy}$ where the N -band GD can be determined by *EWS*.

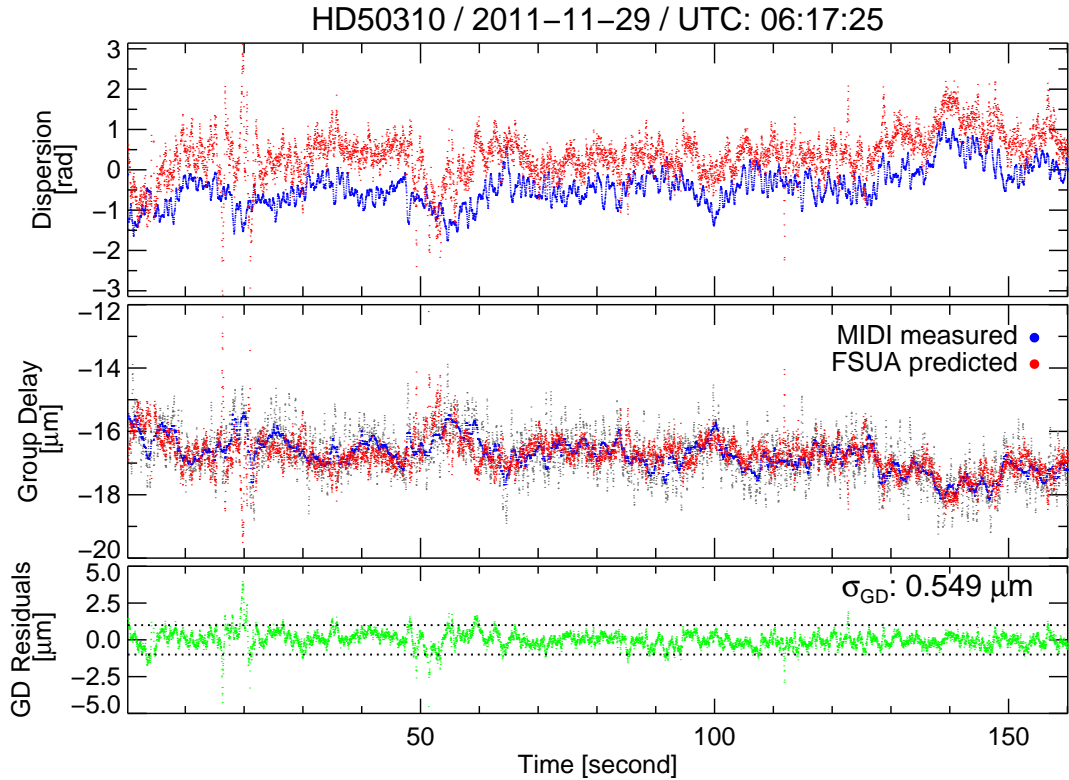


Figure 5.13: This plot shows the measured (blue dots) and predicted (red dots) DISP (upper plot) and GD (middle plot) values for the bright calibrator HD 50310 (#24). In our context “measured” means that the star was bright enough to reduce the data using standard *EWS* method. The red dots are the computed *N*-band DISP and GD values from the PRIMA FSU-A data. Flagged data are not plotted. The lower plot shows the GD residuals (green dots) between the measured and predicted GD values. The standard deviation is only $0.5 \mu\text{m}$ and demonstrates the high potential of the MIDI + PRIMA FSU-A mode. This plot cannot be produced for a faint target as the standard reduction method does not allow to reach this sensitivity.

Table 5.4: Fringe track performance and used MIDI frames.

(1)	(2)	(3)	(4)	(5)	(6)	(7)	(8)	(9)
#	Target	LR7	LR57	σ_{GD}	σ_{PD}	Total	Used Frames	
		[%]	[%]	[nm]	[nm]	Frames	<i>EWS</i>	<i>Koresko</i>
1	HD 1014	100.0	100.0	85	110	8000	7990	7605
2	24 Psc	97.2	97.5	749	774	16000	4	15392
3	HD 16212	100.0	100.0	71	167	8000	7991	7831
4	NGC 1068	28.6	31.7	51	232	16000	19	1862
5	HD 16212	65.0	65.3	580	763	8000	6779	4892
6	HD 1014	43.1	45.1	1040	1507	16000	13413	6527
7	24 Psc	30.3	33.3	1295	1774	16000	4	3406

Table 5.4: continued.

(1)	(2)	(3)	(4)	(5)	(6)	(7)	(8)	(9)
#	Target	LR7	LR57	σ_{GD}	σ_{PD}	Total	Used Frames	
		[%]	[%]	[nm]	[nm]	Frames	<i>EWS</i>	<i>Koresko</i>
8	HD 28305	26.7	27.7	753	845	8000	2386	1840
9	HD 16212	96.8	97.0	241	326	8000	7709	7564
10	HD 36167	100.0	100.0	52	115	8000	7985	7832
11	δ Ori A	100.0	100.0	94	116	16000	3	15960
12	HD 36167	100.0	100.0	128	88	8000	7997	7907
13	δ Ori A	98.4	98.5	295	299	16000	4	15685
14	HD 50778	100.0	100.0	82	82	8000	7984	7982
15	HD 53179	87.7	88.9	504	468	16000	14442	12639
16	24 Psc	99.1	99.9	770	824	14240	5	12905
17	HD 1014	93.6	94.2	450	500	8000	7993	7364
18	HD 16212	72.2	72.7	493	610	8000	6489	5085
19	HD 27639	19.7	20.4	680	854	16000	3626	2729
20	HD 27639	91.5	92.7	445	433	8000	7793	6263
21	RY Tau	71.4	76.3	907	800	16000	2142	7315
22	HD 50778	65.3	65.9	516	541	8000	7996	5018
23	HD 53179	100.0	100.0	165	134	16000	15998	15970
24	HD 50310	99.6	99.8	115	144	8000	7990	7601
25	β Pic	99.8	100.0	405	733	24000	5	23725
26	HD 50310	87.9	88.3	363	437	8000	7950	6775
27	HD 53047	78.3	79.1	490	427	8000	7542	6028
28	HD 83618	88.8	89.0	573	668	8000	7731	6541
29	HD 92305	76.2	76.9	607	641	8000	7816	5477
30	HD 1014	90.2	93.2	835	1045	8000	7716	3781
31	HD 1522	84.8	86.6	705	1143	8000	7998	6148
32	24 Psc	24.8	28.1	1618	3192	16000	7	2458
33	HD 1014	95.9	96.9	509	644	8000	7995	6976
34	24 Psc	92.1	93.2	1187	1369	16000	5	13635
35	HD 1522	72.5	74.1	738	1209	8000	7770	5360
36	24 Psc	37.0	39.5	1416	2853	16000	5	4460
37	HD 27639	99.8	100.0	141	263	8000	7704	7880
38	RY Tau	90.3	95.0	730	801	8000	1829	5906
39	HD 16212	100.0	100.0	139	261	8000	7990	7854
40	HD 50778	98.5	98.6	532	798	16000	15986	15537
41	HD 53179	99.7	100.0	518	524	16000	15991	15756

Table 5.4: continued.

(1)	(2)	(3)	(4)	(5)	(6)	(7)	(8)	(9)
#	Target	LR7	LR57	σ_{GD}	σ_{PD}	Total	Used Frames	
		[%]	[%]	[nm]	[nm]	Frames	<i>EWS</i>	<i>Koresko</i>
42	HD 92305	91.0	91.5	334	239	8000	7214	7065
43	HD 100546	31.6	40.1	966	1227	32000	3	2018

Notes. The columns are: (1) index number; (2) observed object; (3) lock ratio for an OPDC state of 7; (4) lock ratio for an OPDC state of 5 and 7; (5) and (6) K -band group delay and phase delay residuals of FSU-A over the entire observation but only data where OPDC state was 7 were considered; (7) total number of recorded MIDI frames; (8) and (9) the number of “good” frames of the individual data reduction methods.

5.5.2 Calibrated correlated N -band fluxes

In Sec. 5.4.1 we described the construction of the TF s using the *EWS* and *Koresko* method and displayed them for each night. From these plots (Fig. 5.12 a) to f)) we can already see a significant difference: the TF s obtained from the reduction of the MIDI data taken the K -band FSU-A data into account (*Koresko*) show significant lower scatter with respect to each other, which results in smoother averaged TF s with smaller error bars. This has impact on the calibration of the raw correlated N -band fluxes. In addition, the *Koresko* TF s are higher than the TF s constructed by the *EWS* method. This implies that the *Koresko* method is more sensitive, i.e. we are able to detect more photons from an observations compared to the *EWS* method. Thus, we will be more sensitive for fainter targets. In Figure 5.14.1 to Fig. 5.14.43 the final calibrated correlated N -band fluxes, $F_{\text{corr},N}$, of all observations are plotted. $F_{\text{corr},N}$ is plotted for *EWS* and *Koresko* for comparison. From these plots, we can already see differences between the reduction methods: (i) the error on $F_{\text{corr},N}$ derived from *Koresko* is significantly lower and (ii) for faint N -band targets we are only able to measure $F_{\text{corr},N}$ using *Koresko*. In addition, our faintest $F_{\text{corr},N}$ measurements in this run are at the 0.5 Jy level using the ATs, which is almost a factor 20 better what can be expected if MIDI is used without PRIMA FSU-A as a fringe tracker (with respect to the official limits provided in Sec. 5.1.1).

Differences in $F_{\text{corr},N}$ between the results obtained with *EWS* and *Koresko* with respect to slope and flux differences, which can be observed in, e.g. Fig. 5.14.6 are unclear and still part of investigations. In general, $F_{\text{corr},N}$ obtained with the *EWS* method is not always higher or always lower than $F_{\text{corr},N}$ measurements obtained with the *Koresko* method. This might be an indication that the accuracy of *Koresko* is higher than that of *EWS*.

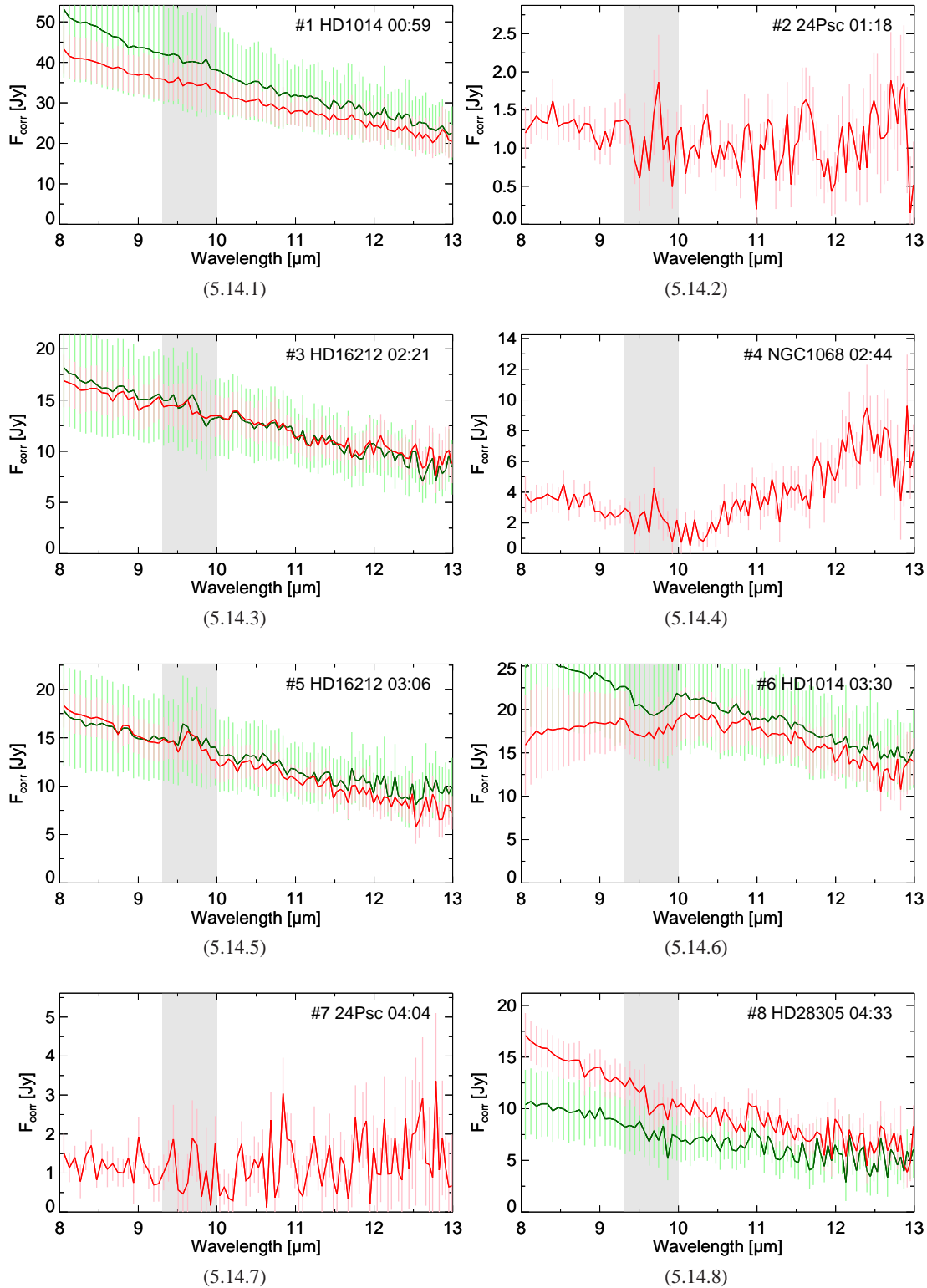


Figure 5.14: Calibrated correlated N -band fluxes obtained after the reduction with the *EWS* (in green) and *Koresko* (in red) method. The vertical gray region between 9.3 and 10 μm is characterized by the strong telluric ozone absorption band. For faint targets with $F_{\text{corr}} \lesssim 5$ Jy, a useful result cannot be produced by the *EWS* method and is not shown. The index number, which is identical to the index number of Table 5.2, the object name, and the time stamp of observation is displayed in the upper right corner of each plot.

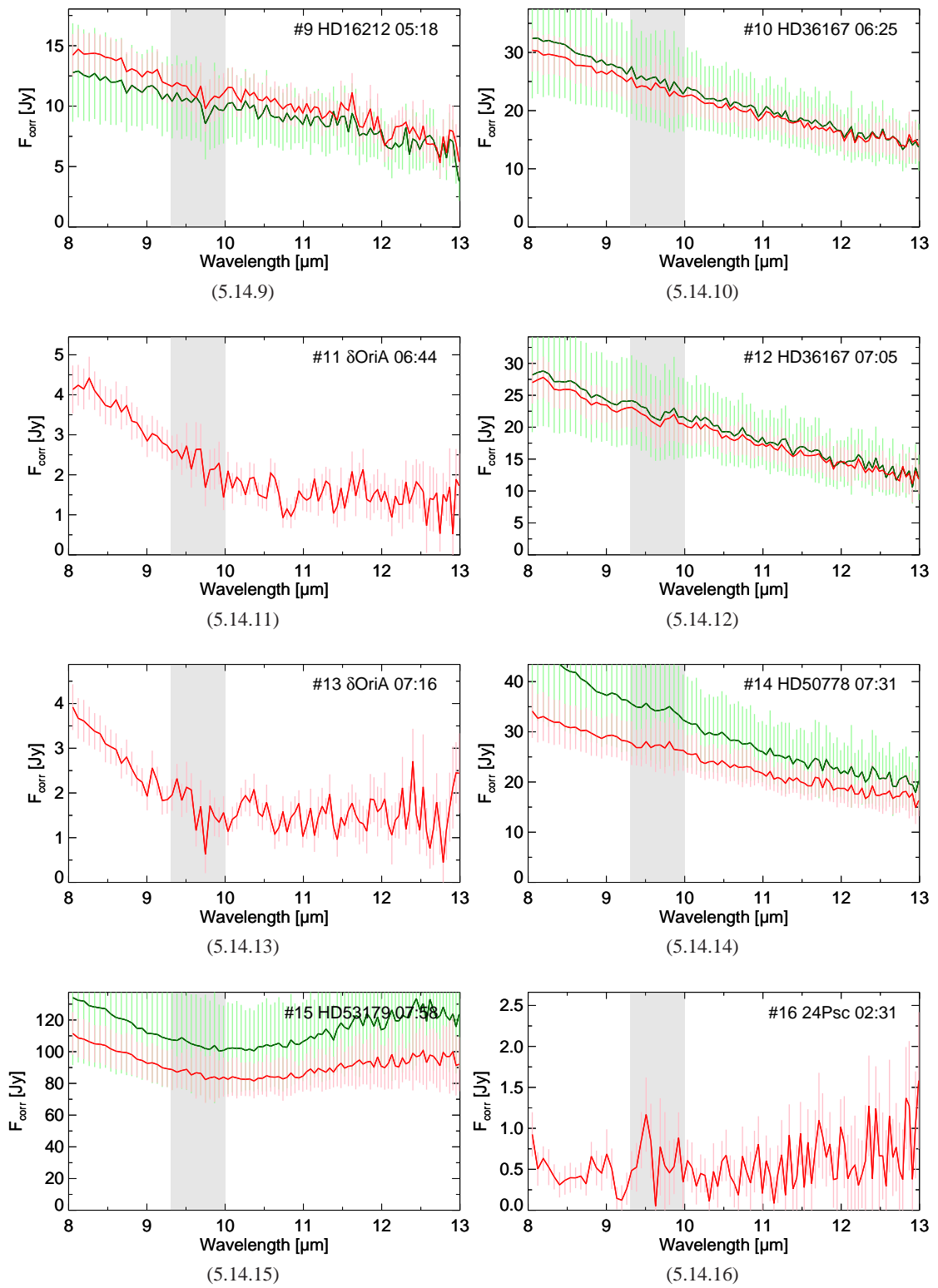


Figure 5.14: continued.

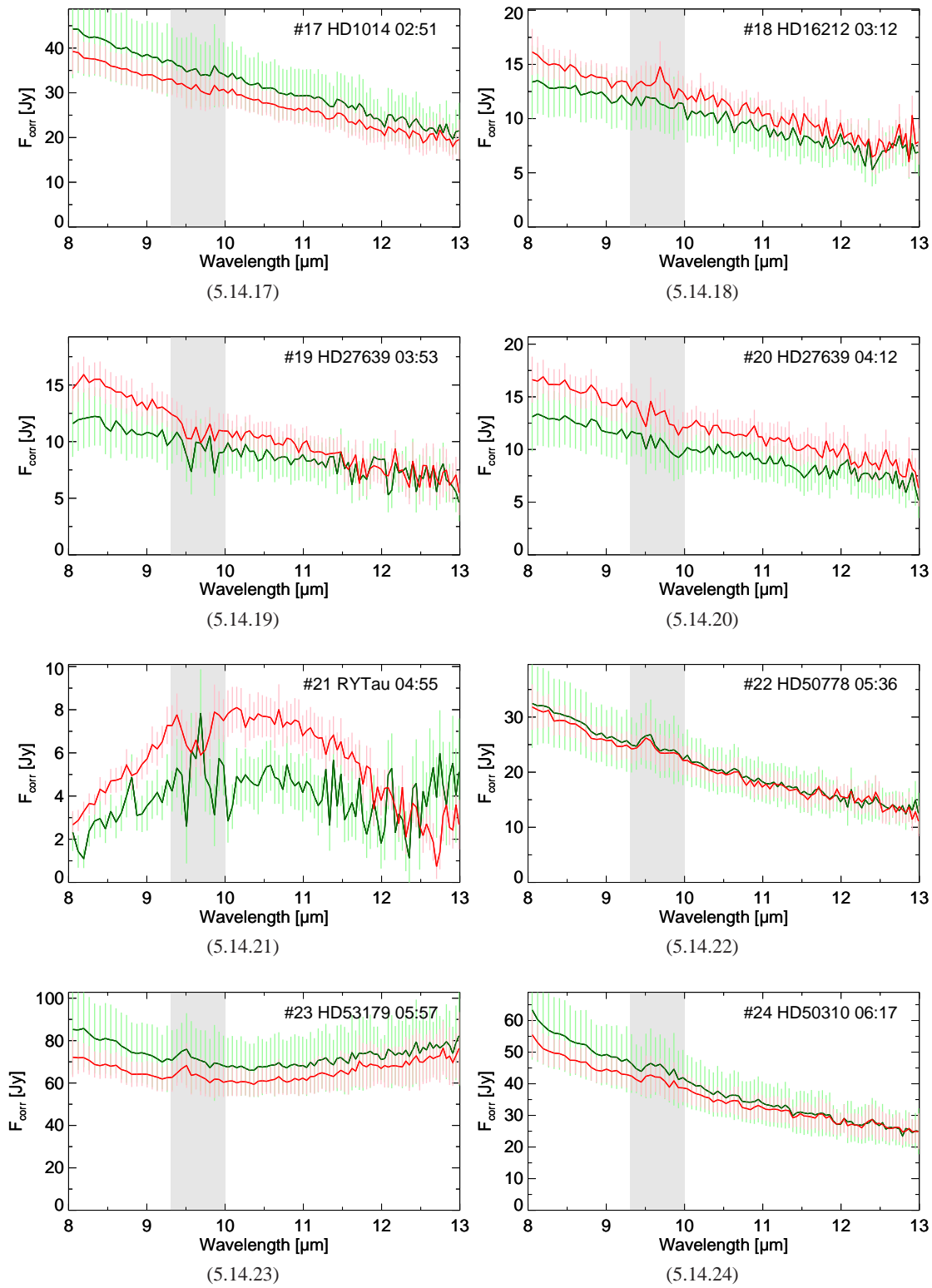


Figure 5.14: continued.

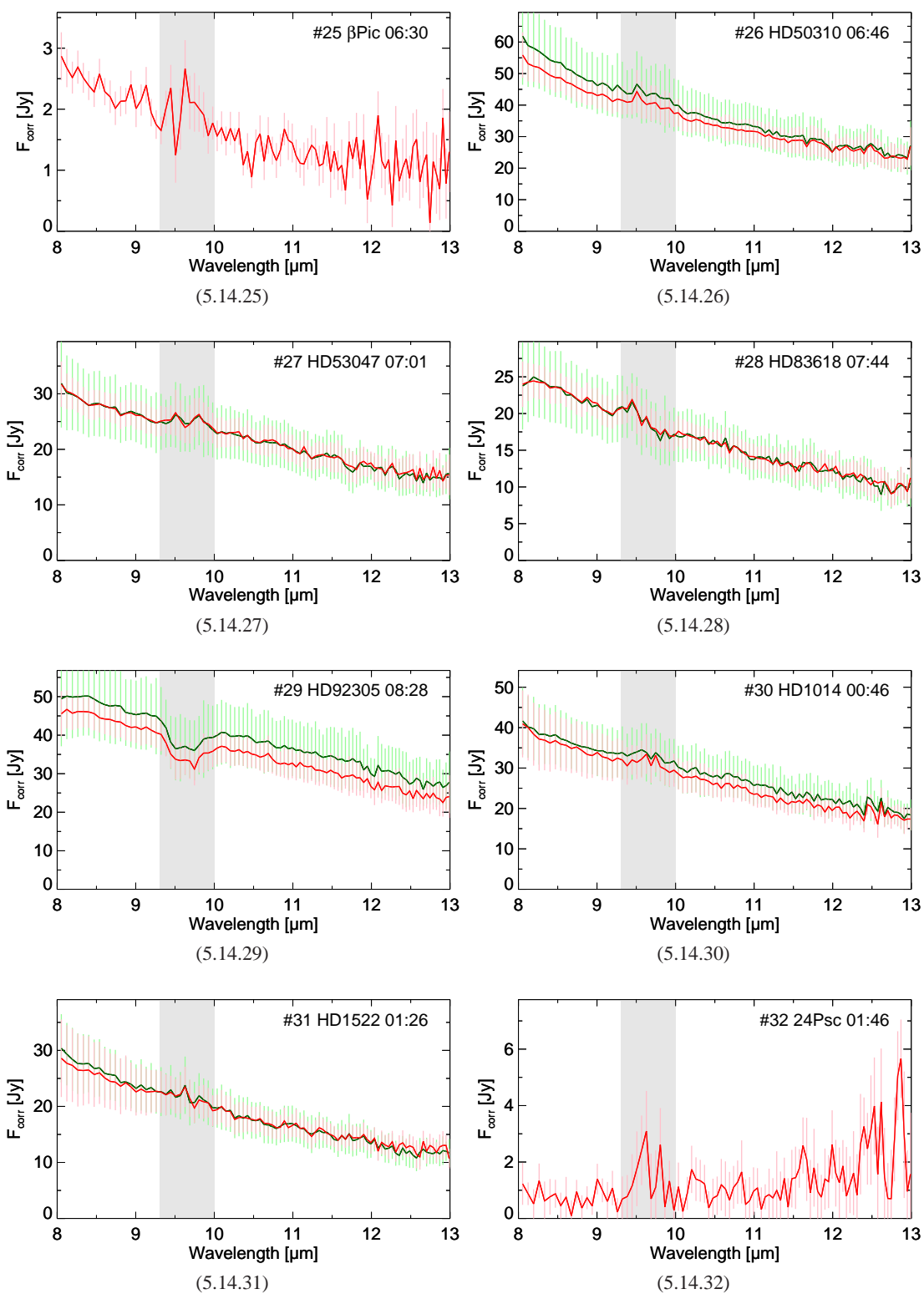


Figure 5.14: continued.

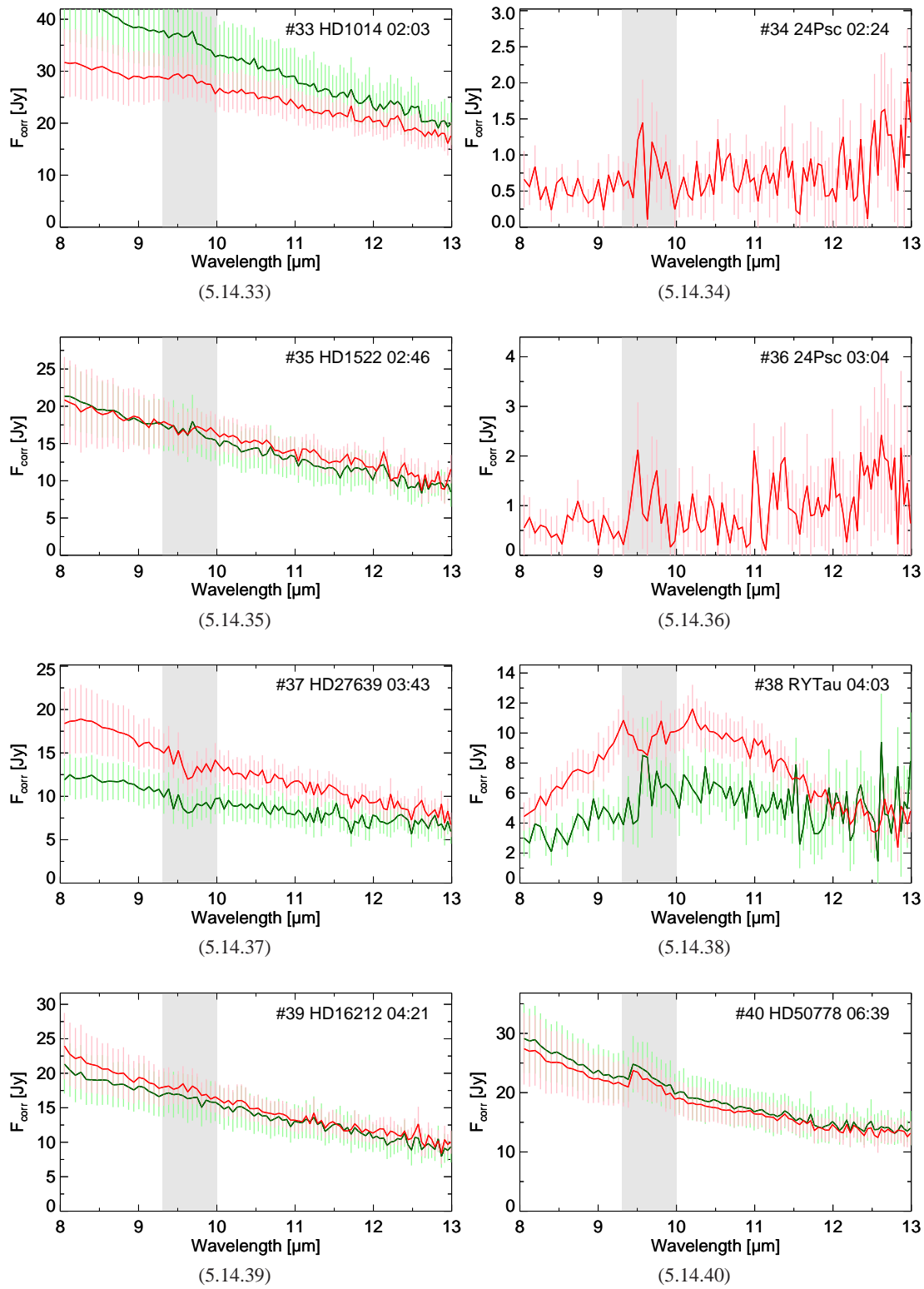


Figure 5.14: continued.

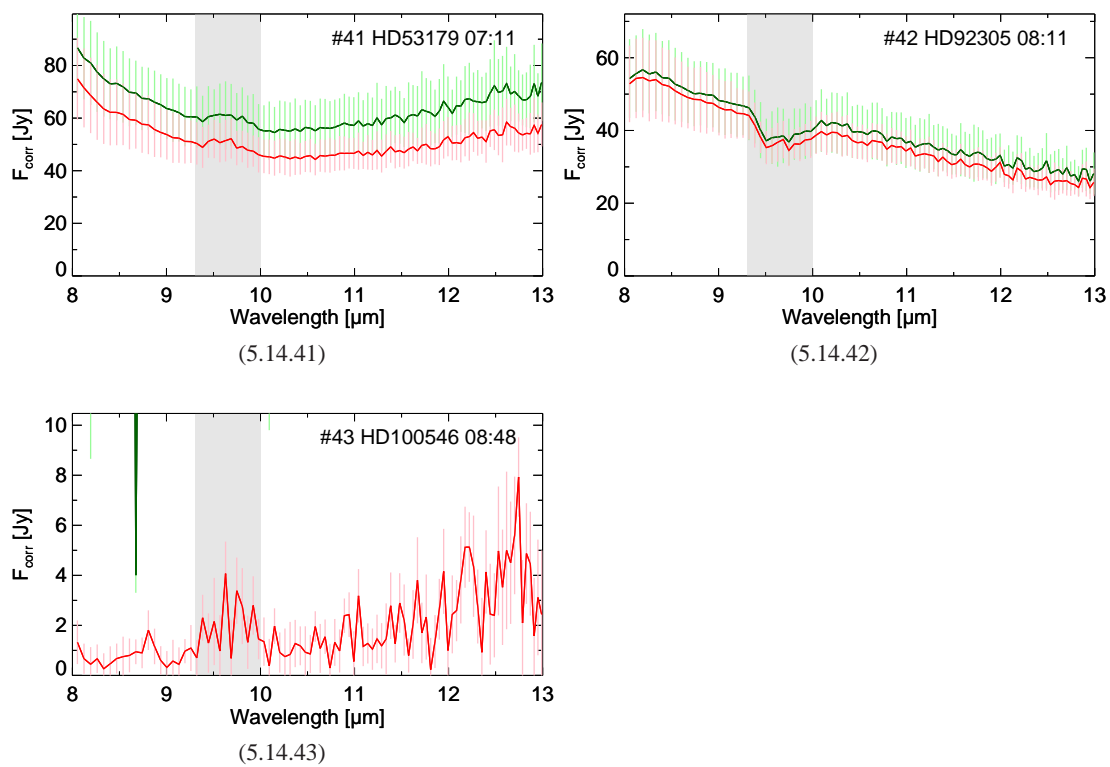


Figure 5.14: continued.

5.5.3 Correlations

To characterize the fringe track performance under different conditions we correlated various parameters and measurements from the observation with each other. This allows the estimation of environmental requirements and target properties, too, in order to guarantee a successful observation using the MIDI + PRIMA FSU-A mode. Figure 5.15 to Fig. 5.17 show several correlation plots for the FSU-A group delay and phase delay residuals as well as for the measured lock ratio. All data are derived from our MIDI + PRIMA FSU-A observation run in November 2011. The group delay and phase delay residuals are computed from the respective values where the OPDC state was at least in level 7 (detection level). For each correlation plot, the linear Pearson correlation coefficient, r , and the probability p that the data are linearly uncorrelated are computed (Bevington & Robinson 2003). Bright calibrator stars and (faint) science targets are treated separately in order to detect differences with respect to the calibrator observations caused by the brightness difference. However, there is no such bias present in the data set.

From the correlation plots we see strong correlations for seeing and coherence time, which is expected because The ABCD fibres are vulnerable for differential injection of the light under degraded weather conditions. This results in flux dropouts and lower SNR or even loss of the fringe.

At least a trend is visible for the airmass. With higher airmass the light path through the atmosphere increases. In addition, longitudinal dispersion, caused by different OPLs of the two beams, leads to lower contrast of the fringe signal. The PRIMA FSU-A possess a longitudinal atmospheric dispersion compensator to correct for this effect. However, a complete test or analysis is still missing.

The length of the IRIS DIT does not seem to have an effect on the fringe tracking performance of PRIMA FSU-A. This is an advantage for science targets, which are faint in H -band.

From this correlation plots we can provide a first estimate of environmental requirements and target properties which have to be met. The K -band visibility of the target should be higher than ≈ 0.25 for a given baseline. The seeing conditions should be better than < 1.5 arcsec, the airmass of the object should be higher than 2, and the coherence time must be $\tau_0 > 1.5$ ms. To obtain analyzable data for MIDI the correlated N -band flux of the target must be $\gtrsim 0.5$ Jy. These estimations apply to the observation with ATs only and should provide an acceptable lock ratio of FSU-A of at least 30%. A comparable MIDI + PRIMA FSU-A data set for the UTs is not available, yet.

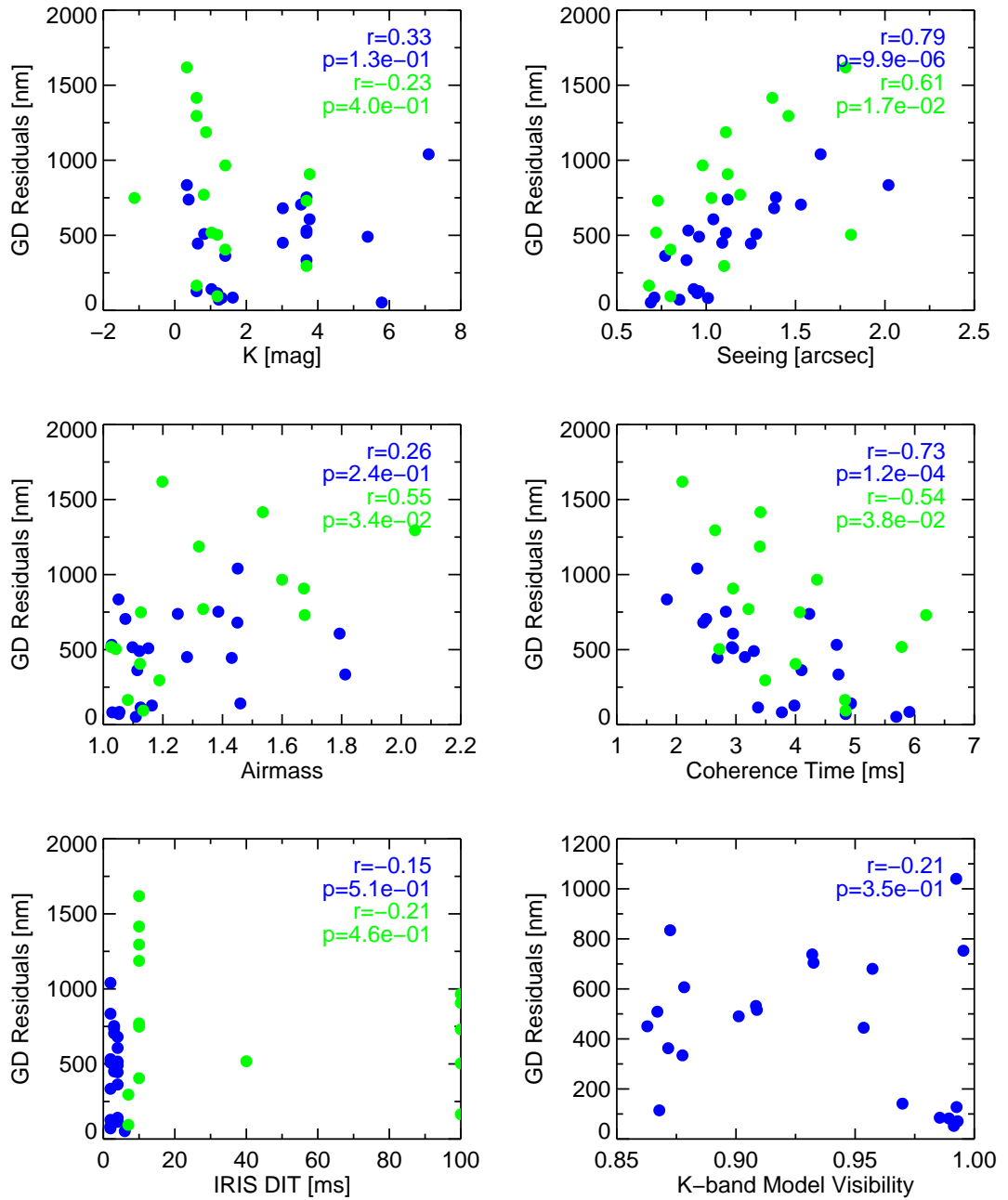


Figure 5.15: Correlation plots for FSU-A group delay residuals (in nano meter). Blue points mark the observation of bright calibrator stars, green points mark the observation of science targets. The corresponding correlation factor r and the probability p are imprinted for the calibrator and science observations, respectively. The last plot does not show science targets because we did not measure the visibility for our observed science targets. Only data are taken into account where PRIMA FSU-A was operated with 1 kHz.

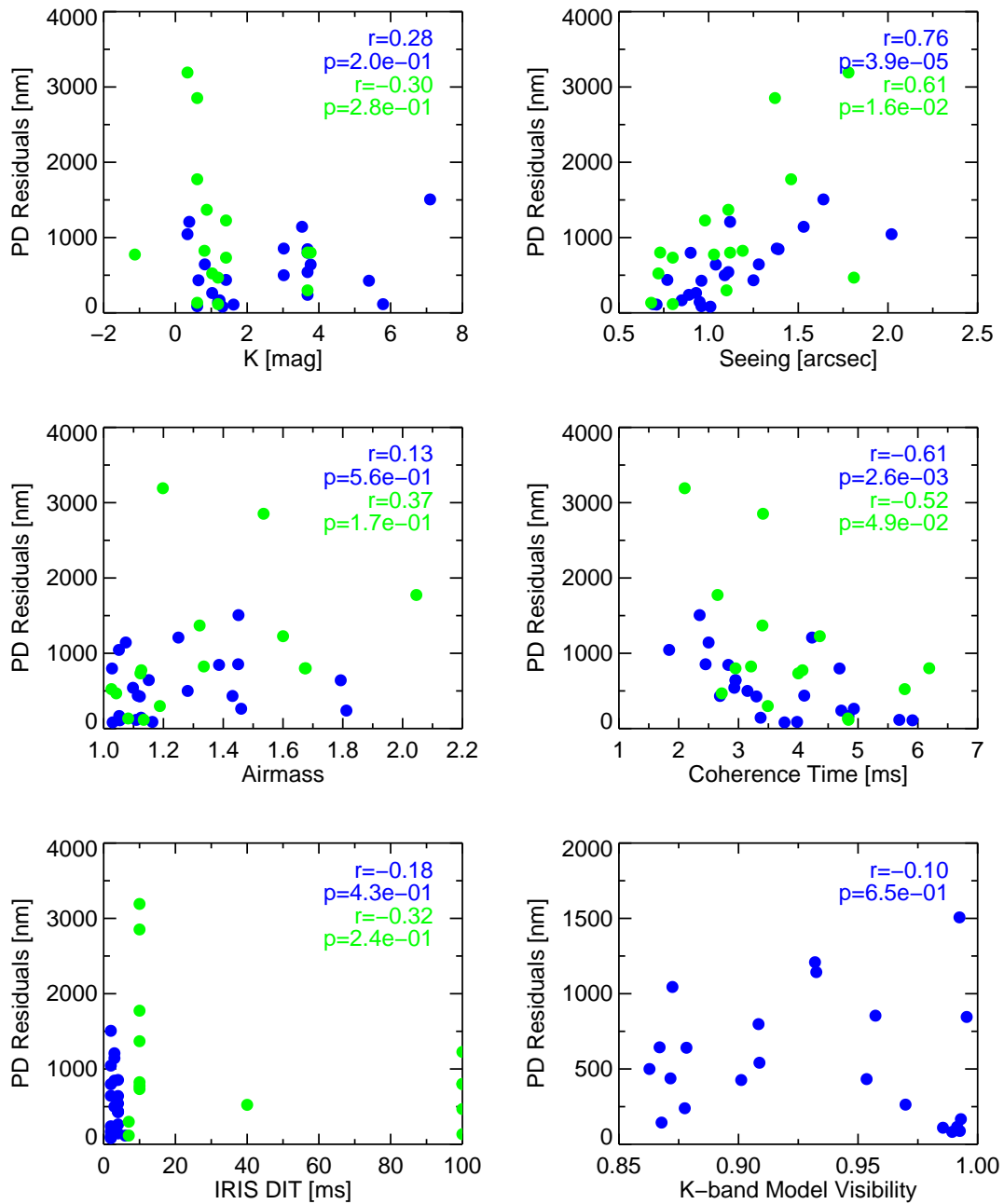


Figure 5.16: Same as Fig. 5.15 but for FSU-A phase delay.

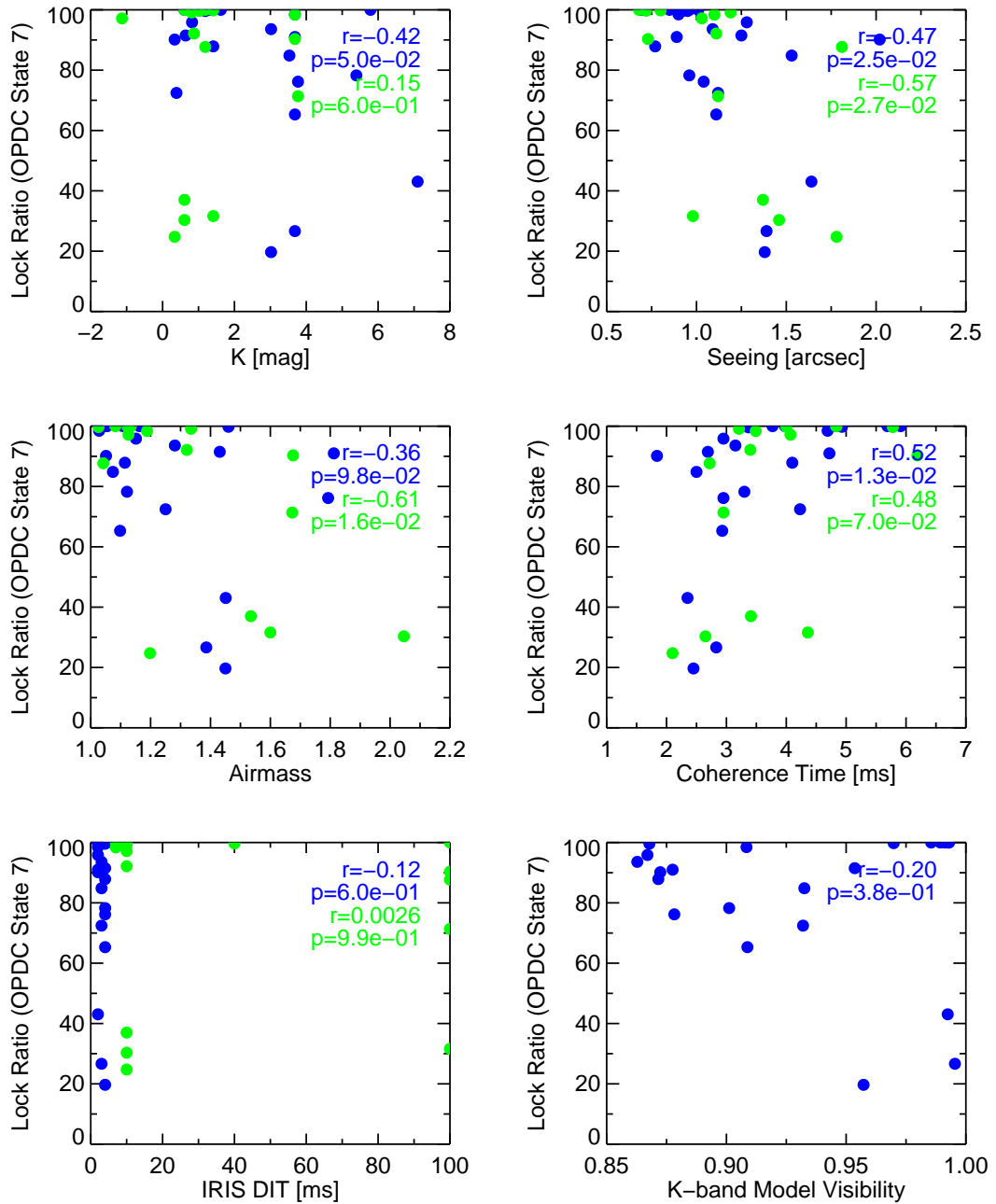


Figure 5.17: Same as Fig. 5.15 but for FSU-A lock ratio.

5.6 Requirements for implementation at VLTI

From the observations and data reduction process described above we proofed the functionality of the MIDI + PRIMA FSU-A and that we are able to make fully make use of the K - and N -band data. However, the observations were still carried out in an experimental or engineering fashion. In the following sections we list modifications and requirements, which are necessary to implement the MIDI + PRIMA FSU-A “on-axis” mode in order to guarantee “smooth” and efficient operation.

Concerning the present hardware in the VLTI laboratory no additional modifications are necessary for MIDI + PRIMA FSU-A single-feed.

From operations point of view several modifications in the templates and software are necessary and are listed and described in the following.

5.6.1 IRIS

- At each preset the IRIS filter changes back to K -band. When FSU-A is used as fringe tracker for MIDI it has to be set to H -band (PRIMA FSUs are operating in K -band).
- The reference pixels for MIDI on IRIS have to be determined and stored in a database. They change because of dual-feed optics in front of IRIS. At the moment we have to set the previous found reference pixels manually at the beginning of each night.

5.6.2 MIDI

- The current MIDI real time display (RTD) is not able to show the *delay function* for faint N -band targets. A workaround can be the implementation of a smoothing parameter when FSU-A is used as a fringe tracker. A proper smoothing value could be derived by the expected N -band correlated flux provided by the observing template. We demonstrated in Fig. 5.18 the feasibility of this modification by a home written routine where we plot the *delay function* for a $F_{\text{corr},N} = 0.5$ Jy source observed with the ATs.
- For very faint N -band ($F_{\text{corr}} \lesssim 5$ Jy) sources a quick-look tool could be provided to check if the observation was successful. Such a tool already exists for MIDI stand-alone operation (*Oyster*).
- The FITS header of MIDI has to be adjusted to provide information similar to AMBER+FINITO. In Table 5.5 we list important keywords that should be present in the primary FITS header of MIDI, when FSU-A is set as a fringe tracker.

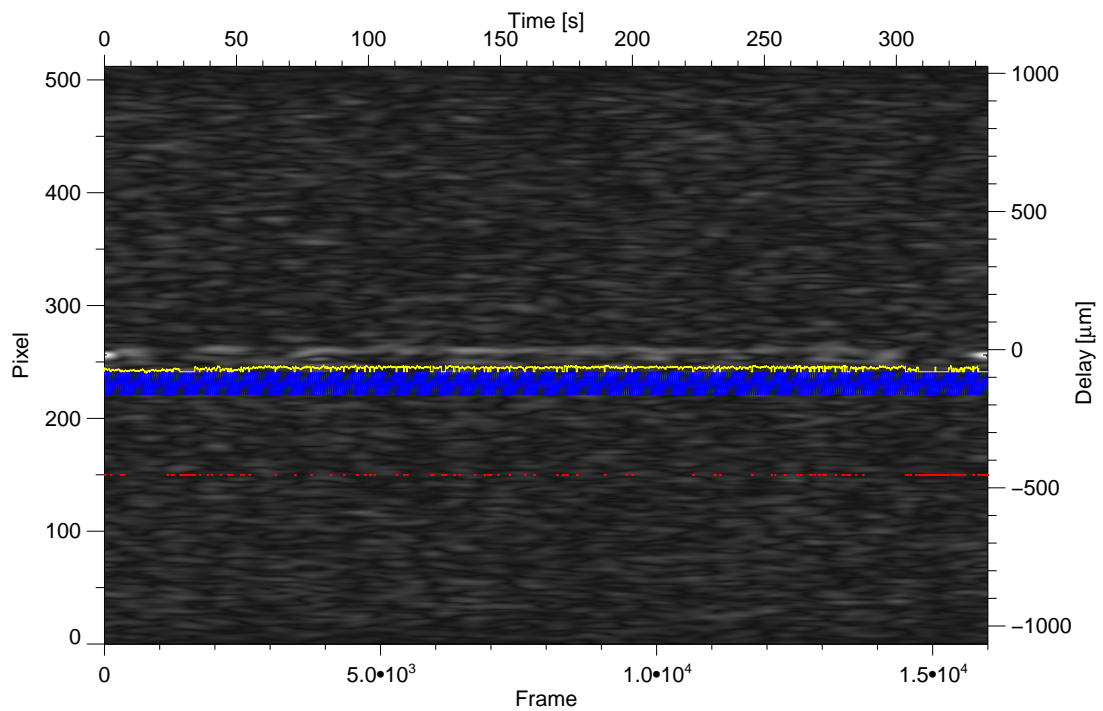


Figure 5.18: 24 Psc (#34), $F_{\text{corr},N} = 0.5$ Jy. This plot shows the Fourier transformation of the complex “de-rotated” (in terms of instrumental delay) MIDI data, which is the *delay function* and is used to determine the atmospheric delay (this plot is similar to the MIDI RTD at the telescope during observation). Because PRIMA FSU-A was used as a fringe tracker the MIDI data are already corrected for changes caused by the atmospheric OPD, which results in this straight and smooth delay function. The yellow line is the computed GD (displayed with an offset), the blue line shows the instrumental delay function, and the red points indicate bad flagged MIDI frames. To make the delay function visible, we smoothed the data over 200 frames. The lock ratio (OPDC state 7) of FSU-A was 92.1%.

Table 5.5: Important keyword parameters to be used in the (primary) MIDI FITS header.

Keyword	Value	Description
MIDI		
HIERARCH ESO DEL PRI FSU1 LOCKR =	1.00	/ Lock ratio for FSU-A.
HIERARCH ESO DEL FNT PRI PHA_RMS =	0.628801737	/ RMS value of phase in FSU-A.
HIERARCH ESO DEL FT SENSOR =	'FSU-A'	/ Fringe Tracker Sensor Name.
HIERARCH ESO DEL FT STATUS =	'ON'	/ Fringe Tracker Status.
from FSU-A		
HIERARCH ESO ISS PRI FSU1 ACU1 NAME=	'TTP1/LMOT1'	/ Name of the Alignment Compent.
HIERARCH ESO ISS PRI FSU1 ACU1 OPL=	-0.0000404	/ OPL Z position of ACU j [m].
HIERARCH ESO ISS PRI FSU1 ACU1 TILTX=	-0.0000639	/ Tilt X position of ACU j [deg].
HIERARCH ESO ISS PRI FSU1 ACU1 TIPY=	-0.0001103	/ Tip Y position of ACU j [deg].
HIERARCH ESO ISS PRI FSU1 ACU2 NAME=	'TTP2/LMOT2'	/ Name of the Alignment Compent.
HIERARCH ESO ISS PRI FSU1 ACU2 OPL=	0.0010611	/ OPL Z position of ACU j [m].
HIERARCH ESO ISS PRI FSU1 ACU2 TILTX=	-0.0006724	/ Tilt X position of ACU j [deg].
HIERARCH ESO ISS PRI FSU1 ACU2 TIPY=	0.0005442	/ Tip Y position of ACU j [deg].
HIERARCH ESO ISS PRI FSU1 DIT=	0.0006558	/ Duration of a sub-integration [s].
HIERARCH ESO ISS PRI FSU1 DUOF=	1	/ NDRO parameter.
HIERARCH ESO ISS PRI FSU1 EXPNO=	0	/ Unique exposure ID number.
HIERARCH ESO ISS PRI FSU1 FREQ=	1000.0000000	/ FSU frequency [Hz].
HIERARCH ESO ISS PRI FSU1 GDFAC=	14	/ Number of sub-integrations per GD.
HIERARCH ESO ISS PRI FSU1 GDR=	1	/ Group delay rate [Hz].
HIERARCH ESO ISS PRI FSU1 ID =	'FSU-A '	/ Unique identifier bound to hardware.
HIERARCH ESO ISS PRI FSU1 NAME=	'FSU-A '	/ Name of the FSU (FSU-A, or FSUB).
HIERARCH ESO ISS PRI FSU1 NDIT=	3	/ Number of subintegration before readout.
HIERARCH ESO ISS PRI FSU1 NSAMPIX=	14	/ Number of samples per pixel.
HIERARCH ESO ISS PRI FSU1 RM =	'NDRO '	/ Read-out mode [list_item].
HIERARCH ESO ISS PRI FSU1 SHUT1 NAME=	'SHT1 '	/ Name of shutter j of FSU-A.
HIERARCH ESO ISS PRI FSU1 SHUT1 VALUE=	'open '	/ Value of shutter j of FSU-A.
HIERARCH ESO ISS PRI FSU1 SHUT2 NAME=	'SHT2 '	/ Name of shutter j of FSU-A.
HIERARCH ESO ISS PRI FSU1 SHUT2 VALUE=	'open '	/ Value of shutter j of FSU-A.

In addition, in `array description` (3rd extension in the MIDI FITS files) and `array geometry` (4th extension in the MIDI FITS files) the PRIMA FSUs have to be listed, which is not the case at the moment.

5.6.3 PRIMA FSU-A

- A procedure has to be implemented to automatically adjust the FSU-A LMOT1 position (relative change currently $\approx -9.5 \cdot 10^{-4}$ m) to compensate for the difference in instrumental OPD between MIDI and FSU-A in order to have fringes on both instruments simultaneously. In principle, this value should not change if the saved LMOT positions of FSU-A are not changed. If these values would change an analytical approach can be found to adjust the LMOT1 offset. This value is set manually at the moment.

5.6.4 Observing Template and Observing Sequence

The MIDI + PRIMA FSU-A mode is currently operated in an experimental fashion. During operation at least two “Bob” panels are open (one for MIDI, one for FSU-A). Before each preset, breakpoints and values have to be set manually for both observing templates. In the ideal case there will be a single template containing the observing sequence for both, MIDI and FSU-A.

As of period 89 the estimated execution time per OB is set to 25 min. From our experience the observing sequence presented in Sec. 5.2.1 can be executed in 20 min, i.e. a calibrated point executing a Cal-Sci sequence can be obtained in 40 min. For faint or slightly resolved targets in *K*-band this time should be increased as the FSU-A needs more optimization with respect to fringe detection and OPDC SNR thresholds.

Ideally all steps from the observing sequence listed above would be executed using a single observing template. Besides the merging of the individual templates of MIDI and PRIMA FSU-A additional requirements have to be implemented:

- If FSU-A is set as fringe tracker pop-up windows asking for a fringe search with MIDI and where to move the delay line should be avoided as MIDI has no control over the delay lines.
- The DIT list in the FSU-A sky calibration template should be removed. Instead the DIT provided by the OB should be automatically set.
- Providing the possibility to enter FSU-A as a fringe tracker for MIDI in, e.g. p2pp.
- Include templates for fringe scans and their automated evaluation. The results (zero OPD, SNR thresholds for the OPDC) should be directly send to the OPDC.
- The record length of the FSU-A data should automatically determined and set depending on the sub-integration time and NSCANS value of MIDI.

- The data recording for FSU-A and MIDI should start and end more or less simultaneously.
- Pop-up windows asking for the execution of FSU-A beam optimization (spiral search, beam tracking), fringe scan, start of FSU-A fringe tracking, ... should be implemented.
- The operating frequency of the FSU-A should set automatically (or with the option to enter it manually) depending on the K -band magnitude of the target. This affects the sky calibration and fringe scanning template.
- Depending of the current OPL it might be necessary to set the LADC of PRIMA FSU-A. (If the usage of the LADC improves the data quality is still under investigation.)

5.6.5 Generated Files

The files generated by MIDI and PRIMA FSU-A need some modifications, too.

- The implementation of the PRIMA FSU-A data into the MIDI files, which is the current strategy when FINITO is used as fringe tracker, may not be efficient. The file sizes of the FSU-A data are comparable to the MIDI file sizes. An implementation of the PRIMA FSU-A data into the MIDI files would generate files twice as large as now. The number of splitted files doubles as well. In addition, PRIMA FSU-A is usually operated 20 times faster, which makes a merging of the two data sets even more difficult.
- The files produced by PRIMA FSU-A (calibration files and fringe track files) should have a comparable file name of the format PACMAN.YYYY-MM-DDTHH:MM:SS.fits.
- The OPD values written in the MIDI files are wrong as MIDI has no control over the delay lines. If this cannot be fixed, the OPD values should be set to zero.
- Important values to be stored from PRIMA FSU-A fringe tracking (already present in the current FITS files): Time, GD, PD, OPD, OPDSNR, GDSNR, raw data, RTOFFSET, STATE, FUOFFSET, DL(1-6) positions.

5.7 Discussion and conclusions

We gave an overview about the MIDI + PRIMA FSU-A single-feed mode and presented a list of requirements and changes, which should be implemented/applied to the current software environment. In addition, we presented the reduction strategy of the data obtained in this new observing mode with first very promising results. We demonstrated that K -band PRIMA FSU-A data can be used to reduce the MIDI N -band data as they contain important measurements (PD , GD , $Dispersion$), which are not accessible from faint N -band targets.

We demonstrated that

- faint K -band targets with PRIMA FSU-A (down to 9 mag) and faint N -band (down to 0.5 Jy) targets with MIDI are accessible, which were out of reach for the ATs with MIDI stand-alone,
- the MIDI + PRIMA FSU-A mode pushes the limiting N -band flux down by a factor of ≈ 20 on the ATs,
- we reach significant gain in sensitivity for MIDI when PRIMA FSU-A is used as fringe tracker,
- we can reduce and calibrate the MIDI data making use of the K -band data.

The advantages of the usage of the ATs with the MIDI + PRIMA FSU-A mode are obvious. The ATs are dedicated to pure interferometric observations. Therefore, it can reduce the overbooking pressure on the UTs, i.e. more observations (interferometric and non-interferometric) are possible. Due to the 30 dedicated stations for the ATs, dozens of baselines ranging from 8 to 200 m at different position angles are available, though not all of them at the same time (for comparison: the four UTs can only provide six fixed baselines ranging from 46 to 130 m).

To be able to extract all necessary information for a successful observation the observer has to provide several magnitudes of the object he wants to observe: V -band magnitude (STRAP), H -band (IRIS), K -band (PRIMA), and the N -band values.

To guarantee good data quality for both, MIDI and PRIMA FSU-A, following environmental requirements and target properties have to be met:

- The lock ratio of FSU-A (OPDC state 7) should be at least 30%.
- The K -band visibility should be higher than ≈ 0.25 .
- Seeing < 1.5 arcsec, airmass < 2 , $\tau_0 > 1.5$ ms
- $F_{\text{corr},N} \gtrsim 0.5$ Jy using ATs

The MIDI + PRIMA FSU-A single-feed mode is the easiest accessible mode with respect to necessary software and hardware modifications. An advanced usage of PRIMA and MIDI is the off-axis mode, which uses the PRIMA STSs to split the FoV into two equal part. This would be useful in particular for N -band science targets, which are too faint in K -band and require a bright star (in K -band) where PRIMA FSU is able to track the fringe. The drawback of this mode is the additional flux loss of 20% to 30% due to the additional reflections inside the STS.

Even if the data presented here show already groundbreaking results on the ATs, there is still a

lot of room for optimizing the reduction process. Understanding these single-feed data are an important step towards phase referenced imaging when MIDI and PRIMA are used with additional subsystem, such as the star separators. In addition, these data, unique of its kind, are a first reference for the implementation of future N -band interferometric instruments, which are using external K -band fringe tracker, like MATISSE.

Chapter 6

Outlook

In this work we demonstrated the feasibility of detailed characterization of Herbig Ae/Be stars with respect to stellar parameters, stellar activity, multiplicity, and planetary companions. In contrast to T Tauri stars several fundamental questions have to be still answered for Herbig Ae/Be stars:

- Can HAeBe stars develop their own magnetic field or are current weak detections left-overs of a primordial magnetic field of the molecular cloud they were formed of?
- Are the detection of X-rays related to such magnetic fields or do they originate always from stellar low-mass companions?
- How does the rotational velocity of HAeBes evolve? Will they rotate always with a significant fraction of their break-up velocity?
- What accretion mechanism is present? Magnetospheric accretion or disk accretion? Is there a mass range where a transition between both mechanisms occur?
- Is the evolution and mineralogy of the circumstellar disks of HAeBe stars similar to the one of T Tauri stars?
- Can planetary companions lower than $1 M_J$ form?

These results should encourage further observations using high-angular and high-temporal resolution techniques such as spectroscopy and interferometry. Especially the second generation instruments arriving at the VLT soon, will significantly help to answer these questions. With MATISSE (mid-infrared) and GRAVITY (near-infrared) two four-beam combiner will be available in the next two to three years. Their imaging capabilities on a milli-arcsecond scale will provide unprecedented insights in the contribution of warm dust and hot gas insight circumstellar disks with possible detections of planets during their formation process. SPHERE, an instrument dedicated to exoplanet search, will probe the circumstellar environment of young stars for exoplanets down to the 1 AU scale. The distribution of dust and gas in circumstellar

disks will be traced and imaged with ALMA in the future. All these new data arriving in the future will help to better understand the formation and evolution of Herbig Ae/Be stars and their stellar and sub-stellar companions.

Abbreviations

ACU	Alignment and Compensation Unit
ADU	Analogue-to-Digital Unit
AGN	Active Galactic Nuclei
AMBER	Astronomical Multi-BEam CombineR
AO	Adaptive Optics
AT	Auxiliary Telescope
BL	Base Line
BOB	Broker for Observation Blocks
DDL	Differential Delay Line
DIT	Detector Integration Time
DL	Delay Line
ESO	European Southern Observatory
FEROS	Fiber-fed Extended Range Optical Spectrograph
FITS	Flexible Image Transport System
FSU	Fringe Sensor Unit
GD	Group Delay
GLS	Generalized Lomb-Scargle Periodogram
GTO	Guaranteed Time Observation
HAeBe	Herbig Ae/Be
HRD	HertzsprungRussell Diagram
IDL	Interactive Data Language
IRIS	Infrared Image Sensor
JD	Julian Date
LADC	Longitudinal Atmospheric Dispersion Compensator
LMOT	Linear MOTor
LR	Lock Ratio
MATISSE	Multi-AperTure mid-Infrared SpectroScopic Experiment
MIDI	MID-infrared Interferometric instrument
NACO	NAOS-CONICA Nasmyth Adaptive Optics System (NAOS) Near-Infrared Imager and Spectrograph (CONICA)

OB	Observation Block
OPD	Optical Path Difference
OPDC	Optical Path Difference Controller
P2PP	Phase II Proposal Preparation
PA	Position Angle
PACMAN	PRIMA Astrometric Camera for Micro-arcsecond AstroNomy
PD	Phase Delay
PRIMA	Phase Referenced Imaging and Micro-arcsecond Astrometry
RTD Scope	Real Time Display SCOPe GUI
RV	Radial Velocity
SNR	Signal to Noise Ratio
SPHERE	Spectro-Polarimetric High-contrast Exoplanet REsearch
STRAP	System for Tip-tilt Removal with Avalanche Photodiodes
STS	Star-Separator
TTS	T Tauri Star
UT	Unit Telescope
VLT	Very Large Telescope
VLTI	Very Large Telescope Interferometer

Bibliography

- Acke, B. & van den Ancker, M. E. 2004, *A&A*, 426, 151
- Appenzeller, I. 1994, in *Astronomical Society of the Pacific Conference Series*, Vol. 62, *The Nature and Evolutionary Status of Herbig Ae/Be Stars*, ed. P. S. The, M. R. Perez, & E. P. J. van den Heuvel, 12–+
- Aufdenberg, J. P., Mérand, A., Coudé du Foresto, V., et al. 2006, *ApJ*, 645, 664
- Augereau, J. C., Lagrange, A. M., Mouillet, D., & Ménard, F. 2001, *A&A*, 365, 78
- Barnes, III, T. G., Jeffery, E. J., Montemayor, T. J., & Skillen, I. 2005, *ApJS*, 156, 227
- Bean, J. L., Seifahrt, A., Hartman, H., et al. 2010, *ApJ*, 713, 410
- Bevington, P. R. & Robinson, D. K. 2003, *Data reduction and error analysis for the physical sciences*, ed. Bevington, P. R. & Robinson, D. K.
- Blondel, P. F. C. & Djie, H. R. E. T. A. 2006, *A&A*, 456, 1045
- Boehm, T. & Catala, C. 1995, *A&A*, 301, 155
- Boss, A. P. 1997, *Science*, 276, 1836
- Boss, A. P. 2001, *ApJ*, 563, 367
- Bouvier, J., Alencar, S. H. P., Harries, T. J., Johns-Krull, C. M., & Romanova, M. M. 2007, *Protostars and Planets V*, 479
- Bouwman, J., Lawson, W. A., Dominik, C., et al. 2006, *ApJ*, 653, L57
- Brown, J. M., Blake, G. A., Dullemond, C. P., et al. 2007, *ApJ*, 664, L107
- Burrows, A., Marley, M., Hubbard, W. B., et al. 1997, *ApJ*, 491, 856
- Burtscher, L. 2011, PhD thesis, Max-Planck-Institut für Astronomie, Königstuhl 17, 69117 Heidelberg, Germany
- Carmona, A., van den Ancker, M. E., & Henning, T. 2007, *A&A*, 464, 687

- Carpenter, J. M., Mamajek, E. E., Hillenbrand, L. A., & Meyer, M. R. 2006, *ApJ*, 651, L49
- Castelli, F. & Kurucz, R. L. 2004, *ArXiv Astrophysics e-prints*
- Catala, C., Felenbok, P., Czarny, J., Talavera, A., & Boesgaard, A. M. 1986, *ApJ*, 308, 791
- Chauvin, G., Lagrange, A.-M., Bonavita, M., et al. 2010, *A&A*, 509, A52+
- Claret, A. 2000, *A&A*, 359, 289
- Claret, A. & Hauschildt, P. H. 2003, *A&A*, 412, 241
- Collier Cameron, A. & Campbell, C. G. 1993, *A&A*, 274, 309
- Corporon, P. 1998, PhD thesis, Université de Montréal, C. P. 6128 Succ A, Montréal, QC H3C 3J7, Canada
- Coulson, I. M. & Walther, D. M. 1995, *MNRAS*, 274, 977
- Cutri, R. M., Skrutskie, M. F., van Dyk, S., et al. 2003, *VizieR Online Data Catalog*, 2246, 0
- Davis, R., Strom, K. M., & Strom, S. E. 1983, *AJ*, 88, 1644
- de Geus, E. J., Lub, J., & van de Grift, E. 1990, *A&AS*, 85, 915
- de Zeeuw, P. T., Hoogerwerf, R., de Bruijne, J. H. J., Brown, A. G. A., & Blaauw, A. 1999, *AJ*, 117, 354
- Delplancke, F. 2008, *New A Rev.*, 52, 199
- Delplancke, F., Derie, F., Lévêque, S., et al. 2006, in *Society of Photo-Optical Instrumentation Engineers (SPIE) Conference Series*, Vol. 6268
- Dent, W. R. F., Greaves, J. S., & Coulson, I. M. 2005, *MNRAS*, 359, 663
- Desort, M., Lagrange, A., Galland, F., Udry, S., & Mayor, M. 2007, *A&A*, 473, 983
- Diolaiti, E., Bendinelli, O., Bonaccini, D., et al. 2000, *A&AS*, 147, 335
- Donehew, B. & Brittain, S. 2011, *AJ*, 141, 46
- Doucet, C., Pantin, E., Lagage, P. O., & Dullemond, C. P. 2006, *A&A*, 460, 117
- Dunkin, S. K., Barlow, M. J., & Ryan, S. G. 1997, *MNRAS*, 286, 604
- Edwards, S., Hartigan, P., Ghandour, L., & Andrulis, C. 1994, *AJ*, 108, 1056
- Fedele, D., van den Ancker, M. E., Acke, B., et al. 2008, *A&A*, 491, 809
- Fedele, D., van den Ancker, M. E., Henning, T., Jayawardhana, R., & Oliveira, J. M. 2010, *A&A*, 510, A72+

- Finkenzeller, U. 1985, *A&A*, 151, 340
- Finkenzeller, U. & Mundt, R. 1984, *A&AS*, 55, 109
- Fukagawa, M., Tamura, M., Itoh, Y., et al. 2006, *ApJ*, 636, L153
- Garcia Lopez, R., Natta, A., Testi, L., & Habart, E. 2006, *A&A*, 459, 837
- Gitton, P. B., Leveque, S. A., Avila, G., & Phan Duc, T. 2004, in *Society of Photo-Optical Instrumentation Engineers (SPIE) Conference Series*, ed. W. A. Traub, Vol. 5491, 944
- Glindemann, A. 2011, *Principles of Stellar Interferometry*, ed. Glindemann, A.
- Grady, C. A., Schneider, G., Sitko, M. L., et al. 2009, *ApJ*, 699, 1822
- Gray, R. O. & Corbally, C. J. 1994, *AJ*, 107, 742
- Grether, D. & Lineweaver, C. H. 2006, *ApJ*, 640, 1051
- Guimarães, M. M., Alencar, S. H. P., Corradi, W. J. B., & Vieira, S. L. A. 2006, *A&A*, 457, 581
- Gustafsson, B., Edvardsson, B., Eriksson, K., et al. 2008, *A&A*, 486, 951
- Haisch, Jr., K. E., Lada, E. A., & Lada, C. J. 2001, *ApJ*, 553, L153
- Haniff, C. 2007, *New A Rev.*, 51, 565
- Hartmann, L., Hewett, R., & Calvet, N. 1994, *ApJ*, 426, 669
- Henning, T. 2008, *Physica Scripta Volume T*, 130, 014019
- Herbig, G. H. 1960, *ApJS*, 4, 337
- Hillenbrand, L. A. 2008, *Physica Scripta Volume T*, 130, 014024
- Hogeveen, S. J. 1992, *Ap&SS*, 193, 29
- Houk, N. 1978, *Michigan catalogue of two-dimensional spectral types for the HD stars*, ed. Houk, N.
- Howard, A. W., Marcy, G. W., Bryson, S. T., et al. 2011, *ArXiv e-prints*
- Hubrig, S., Mikulášek, Z., González, J. F., et al. 2011, *A&A*, 525, L4+
- Hubrig, S., Pogodin, M. A., Yudin, R. V., Schöller, M., & Schnerr, R. S. 2007, *A&A*, 463, 1039
- Hubrig, S., Schöller, M., & Yudin, R. V. 2004, *A&A*, 428, L1
- Hubrig, S., Stelzer, B., Schöller, M., et al. 2009, *A&A*, 502, 283
- Hubrig, S., Yudin, R. V., Schöller, M., & Pogodin, M. A. 2006, *A&A*, 446, 1089

- Huélamo, N., Lacour, S., Tuthill, P., et al. 2011, *A&A*, 528, L7
- Huerta, M., Johns-Krull, C. M., Prato, L., Hartigan, P., & Jaffe, D. T. 2008, *ApJ*, 678, 472
- Ishihara, D., Onaka, T., Kataza, H., et al. 2010, *A&A*, 514, A1
- Jaffe, W. J. 2004, in *Society of Photo-Optical Instrumentation Engineers (SPIE) Conference Series*, ed. W. A. Traub, Vol. 5491, 715
- Jayawardhana, R., Coffey, J., Scholz, A., Brandeker, A., & van Kerkwijk, M. H. 2006, *ApJ*, 648, 1206
- Jeffery, E. J., Barnes, III, T. G., Skillen, I., & Montemayor, T. J. 2007, *ApJS*, 171, 512
- Johns, C. M. & Basri, G. 1995, *AJ*, 109, 2800
- Johns-Krull, C. M., Valenti, J. A., & Koresko, C. 1999, *ApJ*, 516, 900
- Kaeuffl, H.-U., Ballester, P., Biereichel, P., et al. 2004, in *Society of Photo-Optical Instrumentation Engineers (SPIE) Conference Series*, ed. A. F. M. Moorwood & M. Iye, Vol. 5492, 1218–1227
- Kaufer, A., Stahl, O., Tubbesing, S., et al. 1999, *The Messenger*, 95, 8
- Koenigl, A. 1991, *ApJ*, 370, L39
- Koresko, C., Colavita, M. M., Serabyn, E., Booth, A., & Garcia, J. 2006, in *Society of Photo-Optical Instrumentation Engineers (SPIE) Conference Series*, Vol. 6268
- Koresko, C. D., Beckwith, S. V. W., Ghez, A. M., Matthews, K., & Neugebauer, G. 1991, *AJ*, 102, 2073
- Kouwenhoven, M. B. N., Brown, A. G. A., Zinnecker, H., Kaper, L., & Portegies Zwart, S. F. 2005, *A&A*, 430, 137
- Kraus, A. L. & Ireland, M. J. 2012, *ApJ*, 745, 5
- Launhardt, R., Queloz, D., Henning, T., et al. 2008, in *Society of Photo-Optical Instrumentation Engineers (SPIE) Conference Series*, Vol. 7013
- Lawson, P. R., ed. 2000, *Principles of Long Baseline Stellar Interferometry*
- Le Bouquin, J.-B., Abuter, R., Bauvir, B., et al. 2008, in *Society of Photo-Optical Instrumentation Engineers (SPIE) Conference Series*, Vol. 7013
- Leinert, C., Graser, U., Przygodda, F., et al. 2003, *Ap&SS*, 286, 73
- Leinert, C., Richichi, A., & Haas, M. 1997, *A&A*, 318, 472

- Lenzen, R., Hartung, M., Brandner, W., et al. 2003, in SPIE, Vol. 4841, 944–952
- Mahmud, N. I., Crockett, C. J., Johns-Krull, C. M., et al. 2011, *ApJ*, 736, 123
- Maíz Apellániz, J. 2010, *A&A*, 518, A1
- Malfait, K., Bogaert, E., & Waelkens, C. 1998, *A&A*, 331, 211
- Manoj, P., Bhatt, H. C., Maheswar, G., & Muneer, S. 2006, *ApJ*, 653, 657
- Marcy, G. W., Butler, R. P., Vogt, S. S., et al. 2001, *ApJ*, 555, 418
- Mason, B. D., Hartkopf, W. I., & Tokovinin, A. 2010, *AJ*, 140, 735
- Mason, B. D., Wycoff, G. L., Hartkopf, W. I., Douglass, G. G., & Worley, C. E. 2001, *AJ*, 122, 3466
- Mayor, M., Marmier, M., Lovis, C., et al. 2011, ArXiv e-prints
- Mayor, M., Pepe, F., Queloz, D., et al. 2003, *The Messenger*, 114, 20
- Mayor, M. & Queloz, D. 1995, *Nature*, 378, 355
- Meeus, G., Waters, L. B. F. M., Bouwman, J., et al. 2001, *A&A*, 365, 476
- Mendigutía, I., Calvet, N., Montesinos, B., et al. 2011, *A&A*, 535, A99
- Mignone, A., Bodo, G., Massaglia, S., et al. 2007, *ApJS*, 170, 228
- Monnier, J. D. & Millan-Gabet, R. 2002, *ApJ*, 579, 694
- Mottini, S., Cesare, S., & Nicolini, G. 2005, in Society of Photo-Optical Instrumentation Engineers (SPIE) Conference Series, Vol. 5962
- Müller, A., Pott, J.-U., Morel, S., et al. 2010, in Society of Photo-Optical Instrumentation Engineers (SPIE) Conference Series, Vol. 7734
- Muzerolle, J., D’Alessio, P., Calvet, N., & Hartmann, L. 2004, *ApJ*, 617, 406
- Nagasawa, M., Ida, S., & Bessho, T. 2008, *ApJ*, 678, 498
- Natta, A., Testi, L., Muzerolle, J., et al. 2004, *A&A*, 424, 603
- Nijenhuis, J., Visser, H., de Man, H., et al. 2008, in Society of Photo-Optical Instrumentation Engineers (SPIE) Conference Series, Vol. 7013
- Pepe, F., Queloz, D., Henning, T., et al. 2008, in Society of Photo-Optical Instrumentation Engineers (SPIE) Conference Series, Vol. 7013
- Pérez, M. R., van den Ancker, M. E., de Winter, D., & Bopp, B. W. 2004, *A&A*, 416, 647

- Perryman, M. A. C. & ESA, eds. 1997, ESA Special Publication, Vol. 1200, The HIPPARCOS and TYCHO catalogues. Astrometric and photometric star catalogues derived from the ESA HIPPARCOS Space Astrometry Mission
- Pirzkal, N., Spillar, E. J., & Dyck, H. M. 1997, *ApJ*, 481, 392
- Pollack, J. B., Hubickyj, O., Bodenheimer, P., et al. 1996, *Icarus*, 124, 62
- Pontoppidan, K. M., Blake, G. A., van Dishoeck, E. F., et al. 2008, *ApJ*, 684, 1323
- Pott, J., Perrin, M. D., Furlan, E., et al. 2010, *ApJ*, 710, 265
- Povich, M. S., Giampapa, M. S., Valenti, J. A., et al. 2001, *AJ*, 121, 1136
- Praderie, F., Catala, C., Simon, T., & Boesgaard, A. M. 1986, *ApJ*, 303, 311
- Prato, L., Huerta, M., Johns-Krull, C. M., et al. 2008, *ApJ*, 687, L103
- Preibisch, T. & Mamajek, E. 2008, The Nearest OB Association: Scorpius-Centaurus (Sco OB2), ed. Reipurth, B., 235–+
- Queloz, D., Henry, G. W., Sivan, J. P., et al. 2001, *A&A*, 379, 279
- Quirrenbach, A. 2001, *ARA&A*, 39, 353
- Quirrenbach, A., Coudé du Foresto, V., Daigne, G., et al. 1998, in Society of Photo-Optical Instrumentation Engineers (SPIE) Conference Series, ed. R. D. Reasenberg, Vol. 3350, 807–817
- Regály, Z., Juhász, A., Sándor, Z., & Dullemond, C. P. 2012, *MNRAS*, 419, 1701
- Roberts, D. H., Lehar, J., & Dreher, J. W. 1987, *AJ*, 93, 968
- Rousset, G., Lacombe, F., Puget, P., et al. 2003, in SPIE, ed. P. L. Wizinowich & D. Bonaccini, Vol. 4839, 140–149
- Saar, S. H. & Donahue, R. A. 1997, *ApJ*, 485, 319
- Sahlmann, J. 2007, Master's thesis, Albert-Ludwigs-Universitaet, Freiburg im Breisgau, 2007.
- Sahlmann, J., Abuter, R., Ménardi, S., et al. 2010, in Society of Photo-Optical Instrumentation Engineers (SPIE) Conference Series, Vol. 7734
- Sahlmann, J., Ménardi, S., Abuter, R., et al. 2009, *A&A*, 507, 1739
- Sahlmann, J., Ségransan, D., Queloz, D., & Udry, S. 2011a, in IAU Symposium, Vol. 276, IAU Symposium, ed. A. Sozzetti, M. G. Lattanzi, & A. P. Boss, 117–120
- Sahlmann, J., Ségransan, D., Queloz, D., et al. 2011b, *A&A*, 525, A95

- Schmid, C., Abuter, R., Ménardi, S., et al. 2010, in Society of Photo-Optical Instrumentation Engineers (SPIE) Conference Series, Vol. 7734
- Schneider, J., Dedieu, C., Le Sidaner, P., Savalle, R., & Zolotukhin, I. 2011, *A&A*, 532, A79+
- Schuhler, N. 2007, PhD thesis, Université de Strasbourg
- Seifahrt, A., Käuffl, H. U., Zängl, G., et al. 2010, *A&A*, 524, A11+
- Setiawan, J., Henning, T., Launhardt, R., et al. 2008, *Nature*, 451, 38
- Shu, F., Najita, J., Ostriker, E., et al. 1994, *ApJ*, 429, 781
- Sicilia-Aguilar, A., Hartmann, L., Calvet, N., et al. 2006, *ApJ*, 638, 897
- Sicilia-Aguilar, A., Hartmann, L. W., Watson, D., et al. 2007, *ApJ*, 659, 1637
- Siess, L., Dufour, E., & Forestini, M. 2000, *A&A*, 358, 593
- Smith, R. C. & Worley, R. 1974, *MNRAS*, 167, 199
- Spiegel, D. S., Burrows, A., & Milsom, J. A. 2011, *ApJ*, 727, 57
- Stelzer, B., Robrade, J., Schmitt, J. H. M. M., & Bouvier, J. 2009, *A&A*, 493, 1109
- Sylvester, R. J., Skinner, C. J., Barlow, M. J., & Mannings, V. 1996, *MNRAS*, 279, 915
- Thé, P. S., de Winter, D., & Perez, M. R. 1994, *A&AS*, 104, 315
- Thi, W. F., van Dishoeck, E. F., Blake, G. A., et al. 2001, *ApJ*, 561, 1074
- Tognelli, E., Prada Moroni, P. G., & Degl'Innocenti, S. 2011, ArXiv e-prints
- Tokovinin, A. 2008, *MNRAS*, 389, 925
- Tristram, K. R. W. 2007, PhD thesis, Max-Planck-Institut für Astronomie, Königstuhl 17, 69117 Heidelberg, Germany
- Tristram, K. R. W., Raban, D., Meisenheimer, K., et al. 2009, *A&A*, 502, 67
- Tuthill, P. G., Monnier, J. D., & Danchi, W. C. 2001, *Nature*, 409, 1012
- van Boekel, R., Min, M., Waters, L. B. F. M., et al. 2005, *A&A*, 437, 189
- van den Ancker, M. E., de Winter, D., & Tjin A Djie, H. R. E. 1998, *A&A*, 330, 145
- van der Plas, G., van den Ancker, M. E., Fedele, D., et al. 2008, *A&A*, 485, 487
- van Leeuwen, F. 2007, *A&A*, 474, 653
- Verhoeff, A. P., Min, M., Pantin, E., et al. 2011, *A&A*, 528, A91+

- Verhoeff, A. P., Waters, L. B. F. M., Veerman, H., et al. 2010, submitted
- von Zeipel, H. 1924, MNRAS, 84, 665
- Vrba, F. J., Rydgren, A. E., Chugainov, P. F., Shakovskaia, N. I., & Zak, D. S. 1986, ApJ, 306, 199
- Wade, G. A., Bagnulo, S., Drouin, D., Landstreet, J. D., & Monin, D. 2007, MNRAS, 376, 1145
- Wang, J. & Ford, E. B. 2011, MNRAS, 418, 1822
- Waters, L. B. F. M. & Waelkens, C. 1998, ARA&A, 36, 233
- Weigelt, G., Wittkowski, M., Balega, Y. Y., et al. 2004, A&A, 425, 77
- Weise, P., Launhardt, R., Setiawan, J., & Henning, T. 2010, A&A, 517, A88+
- White, R. J. & Basri, G. 2003, ApJ, 582, 1109
- Whitney, B. A., Indebetouw, R., Bjorkman, J. E., & Wood, K. 2004, ApJ, 617, 1177
- Wittkowski, M., Kervella, P., Arsenault, R., et al. 2004, A&A, 418, L39
- Zechmeister, M. & Kürster, M. 2009, A&A, 496, 577

Appendix A

HD 142527 - Radial velocity measurements

Table A.1: Measured RV s and their corresponding uncertainties for all used spectrographs. The radial velocity shifts between the different spectrographs are not included.

Instrument	Time [JD-2 400 000 d]	RV [m s ⁻¹]	σ_{RV} [m s ⁻¹]	Instrument	Time [JD-2 400 000 d]	RV [m s ⁻¹]	σ_{RV} [m s ⁻¹]
FEROS	54309.56249	-1040	161	FEROS	54579.75266	-1044	178
FEROS	54309.69843	-1260	194	FEROS	54580.81909	-1209	171
FEROS	54310.63076	-1307	166	FEROS	54581.63191	-872	153
FEROS	54310.68073	-1319	168	FEROS	54581.81556	-925	168
FEROS	54311.67479	-1213	191	FEROS	54582.72243	-1091	189
FEROS	54311.72336	-1176	195	FEROS	54582.81447	-967	179
FEROS	54312.57737	-1398	161	FEROS	54583.63305	-941	163
FEROS	54312.65436	-1467	171	FEROS	54587.63065	-1000	182
FEROS	54313.56831	-1409	214	FEROS	54587.74255	-1186	169
FEROS	54313.64131	-2335	292	FEROS	54588.75565	-1341	165
FEROS	54314.67948	-1105	191	FEROS	54588.86183	-1160	172
FEROS	54497.88511	-1294	165	FEROS	54591.83584	-1144	181
FEROS	54498.88743	-1101	161	FEROS	54591.91729	-988	186
FEROS	54499.87845	-1024	219	HARPS	54594.85144	-675	147
HARPS	54560.88823	-902	135	HARPS	54595.57615	-813	128
HARPS	54561.8896	-522	177	HARPS	54595.71268	-422	140
FEROS	54572.68089	-1087	190	HARPS	54595.88751	-586	138
FEROS	54572.77036	-941	167	HARPS	54596.57009	-635	132
FEROS	54574.70829	-979	186	HARPS	54596.75424	-439	169
FEROS	54574.73713	-978	165	HARPS	54596.85669	-764	125
FEROS	54574.8617	-973	184	FEROS	54633.6206	-1350	170
FEROS	54575.78341	-1114	177	FEROS	54638.77732	-1082	172
FEROS	54576.68279	-1329	168	FEROS	54639.77366	-1424	177
FEROS	54577.67343	-949	182	FEROS	54642.81139	-1185	185
FEROS	54577.86587	-1158	194	HARPS	54874.82807	-1277	166
FEROS	54578.70076	-1337	162	HARPS	54875.8432	-1026	139

Table A.1: continued.

Instrument	Time [JD-2 400 000 d]	RV [m s ⁻¹]	σ_{RV} [m s ⁻¹]	Instrument	Time [JD-2 400 000 d]	RV [m s ⁻¹]	σ_{RV} [m s ⁻¹]
HARPS	54876.80006	-944	149	FEROS	55073.66253	-983	216
HARPS	54877.82487	-891	157	FEROS	55074.58756	-1183	172
HARPS	54891.79063	-883	134	CRIRES	55075.52116	-312	223
HARPS	54892.83191	-615	129	CRIRES	55086.5086	-209	90
HARPS	54894.89721	-834	146	CRIRES	55094.50143	-220	131
FEROS	54943.84106	-1451	169	FEROS	55257.79841	-970	171
FEROS	54944.90529	-1567	170	FEROS	55258.81917	-1092	189
FEROS	54945.78584	-1332	177	FEROS	55258.87529	-1245	175
FEROS	54945.86997	-1562	175	FEROS	55260.85557	-968	176
FEROS	54946.90433	-1411	153	FEROS	55262.7821	-894	172
FEROS	54947.8537	-1300	182	FEROS	55263.83414	-1017	161
FEROS	54947.91708	-1263	166	FEROS	55338.77617	-1211	164
FEROS	54948.83204	-1278	169	FEROS	55343.70663	-1238	188
FEROS	54949.85164	-999	183	FEROS	55346.73162	-1566	168
FEROS	54950.89833	-1305	187	FEROS	55347.66264	-1158	211
FEROS	54951.89843	-1616	167	FEROS	55348.70992	-1395	175
FEROS	54985.64716	-1170	171	FEROS	55349.71695	-1175	197
FEROS	54986.70095	-1487	179	FEROS	55351.71407	-1313	182
FEROS	54989.57055	-1503	169	FEROS	55358.6555	-1159	215
FEROS	54990.74763	-1348	195	FEROS	55628.87124	-1168	177
FEROS	54993.76572	-1347	175	FEROS	55628.88586	-1257	178
FEROS	54994.64674	-1428	196	FEROS	55630.80276	-1325	202
CRIRES	55032.49898	412	262	FEROS	55630.84562	-1272	194
CRIRES	55037.64491	756	175	FEROS	55634.88038	-1190	211
CRIRES	55041.55951	399	151	FEROS	55635.77146	-1226	194
CRIRES	55046.54745	-103	166	FEROS	55635.79019	-1432	182
FEROS	55053.51561	-1442	170	FEROS	55637.85554	-1099	204
FEROS	55058.56658	-1250	186	FEROS	55639.72227	-1260	169
FEROS	55060.54462	-1293	261	FEROS	55671.68511	-984	194
CRIRES	55062.54014	-197	153	FEROS	55671.84404	-2227	227
CRIRES	55063.49124	-146	139	FEROS	55672.85654	-2597	186
CRIRES	55064.49222	-235	174	FEROS	55673.83551	-1712	194
FEROS	55070.61077	-1437	158	FEROS	55674.81147	-1932	173
FEROS	55072.46652	-1299	166				

Appendix B

HD 142527 - Line profiles

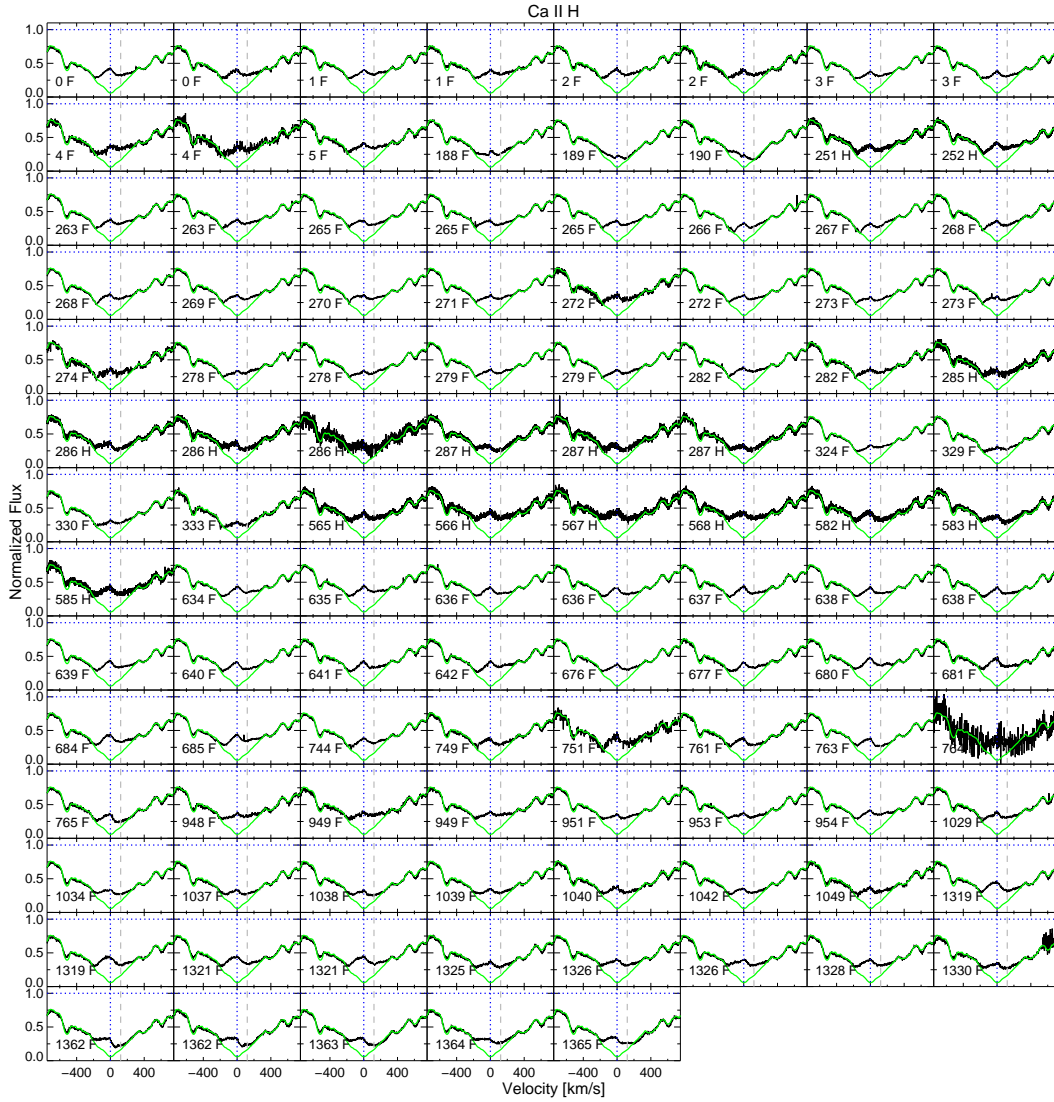


Figure B.1: Normalized and median RV corrected line profiles for Ca II H plotted over velocity space in chronological order. The synthetic photospheric line profile based on the stellar parameters (Table 4.1) is shown as green line. The position of the line center at zero velocity is marked by the vertical dotted line. The inset numbers indicate the time of observation in days with respect to the first observation. The inset letters F and H indicate if the spectrum was observed with FEROS or HARPS. The vertical dashed line marks the position of $H\epsilon$, which might contaminate the line profile of Ca II H.

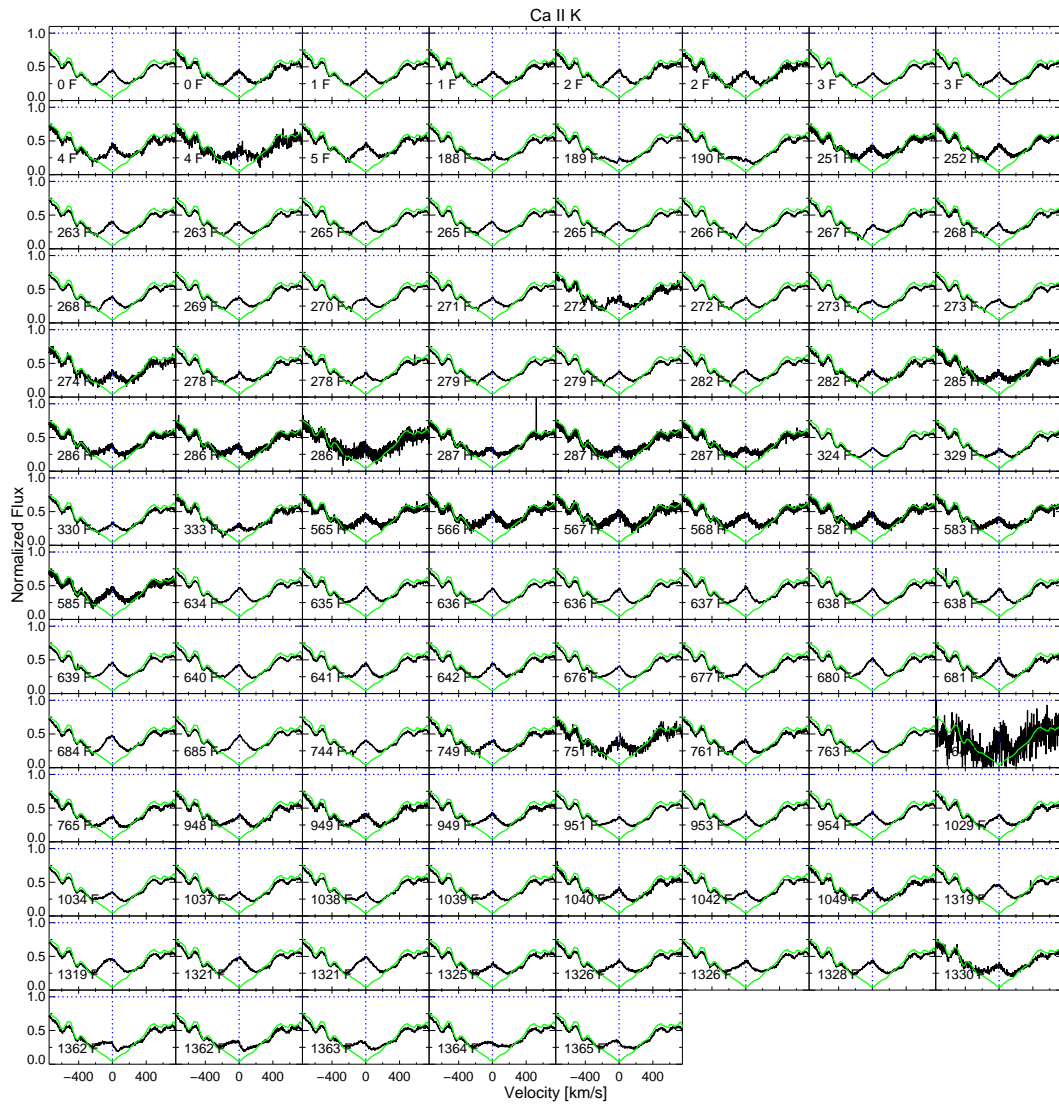
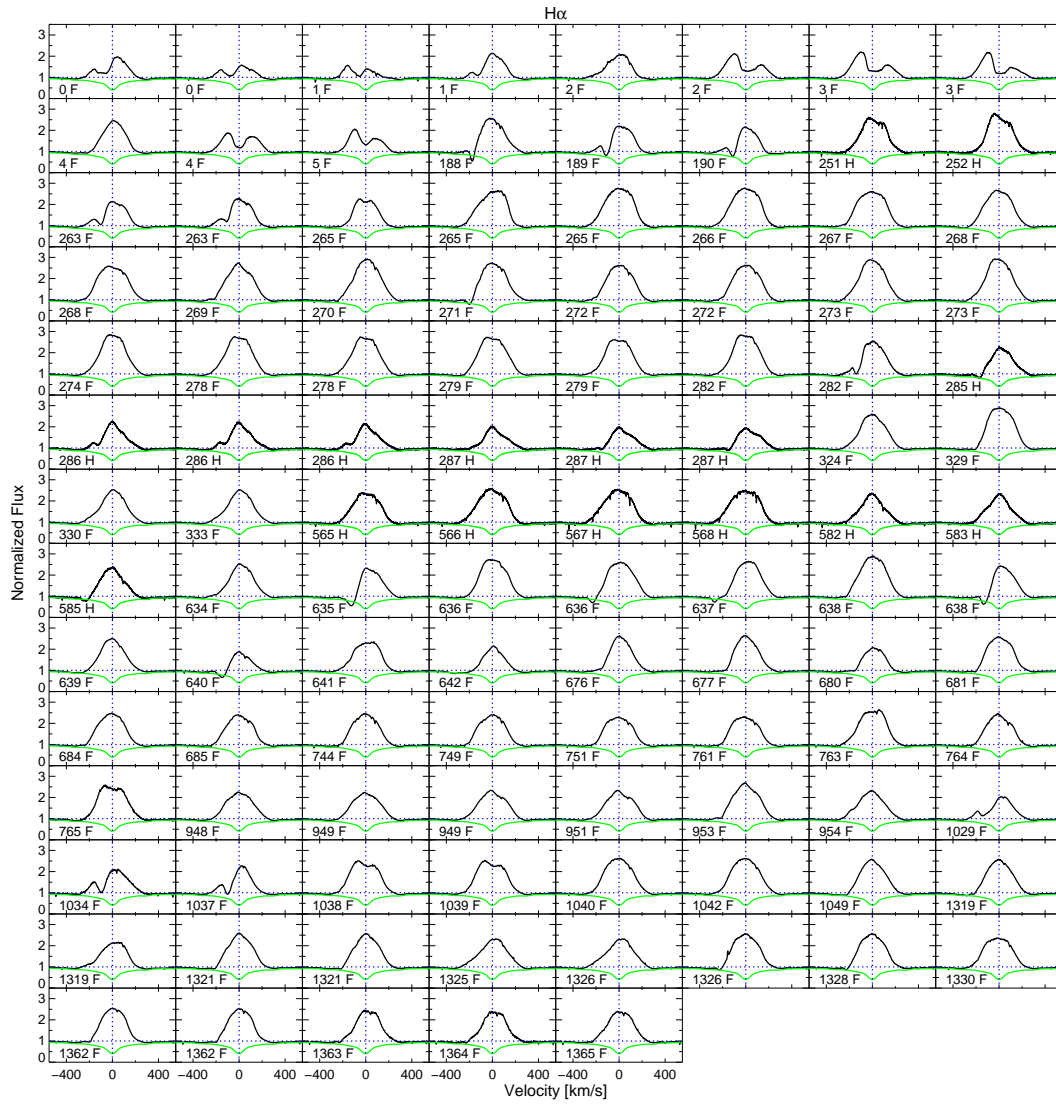
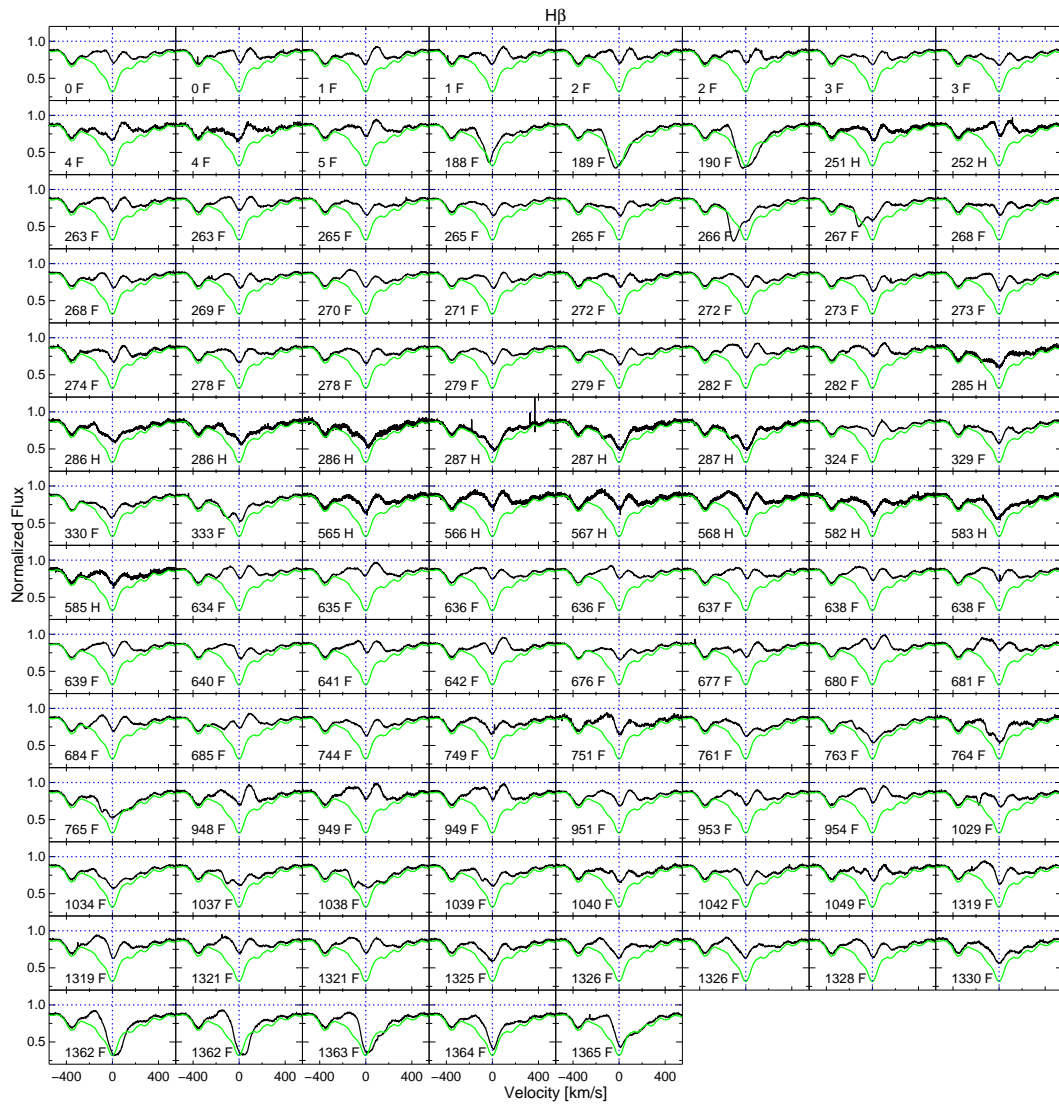
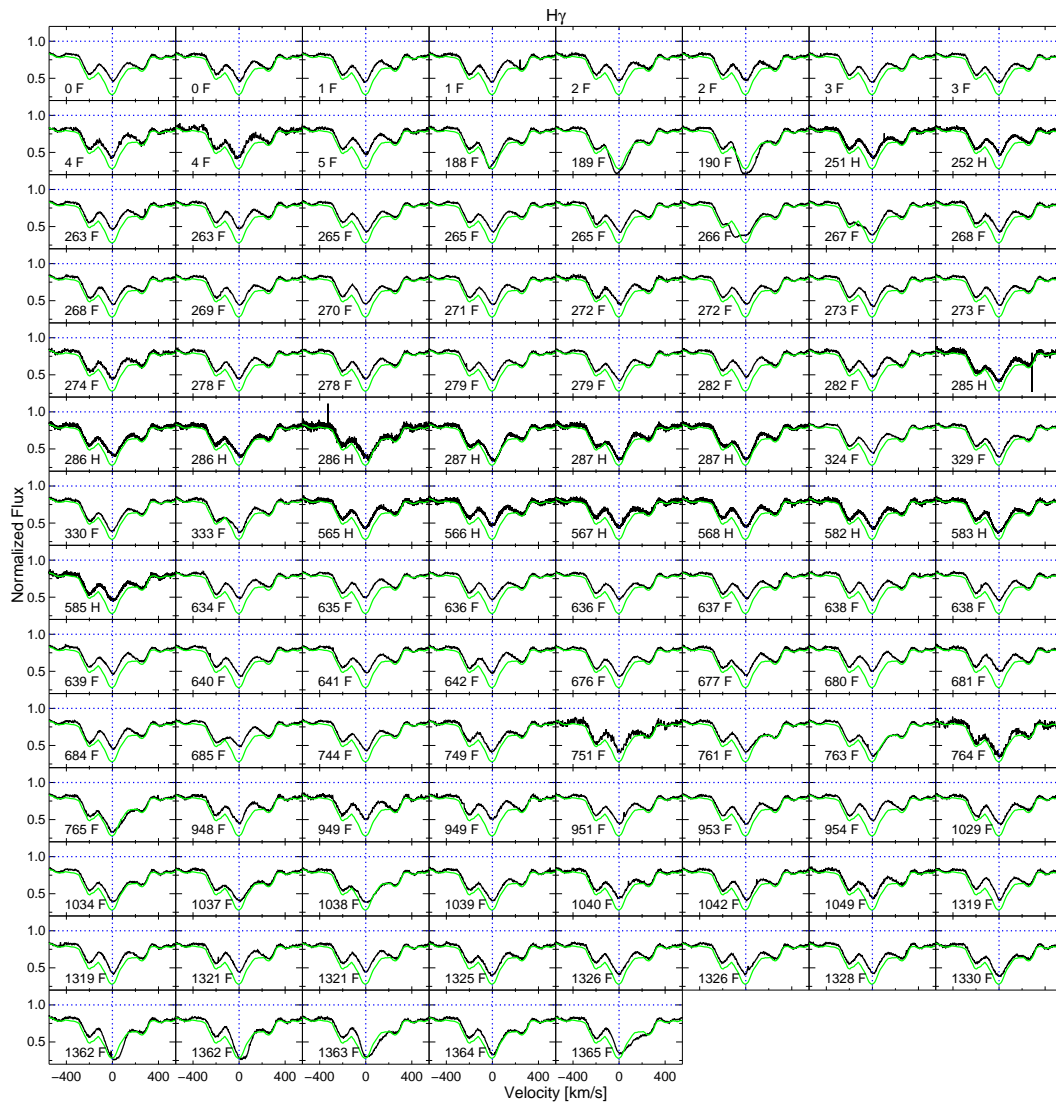


Figure B.2: Same as Fig. B.1 but for Ca II K.

Figure B.3: Same as Fig. B.1 but for H α .

Figure B.4: Same as Fig. B.1 but for $H\beta$.

Figure B.5: Same as Fig. B.1 but for H γ .

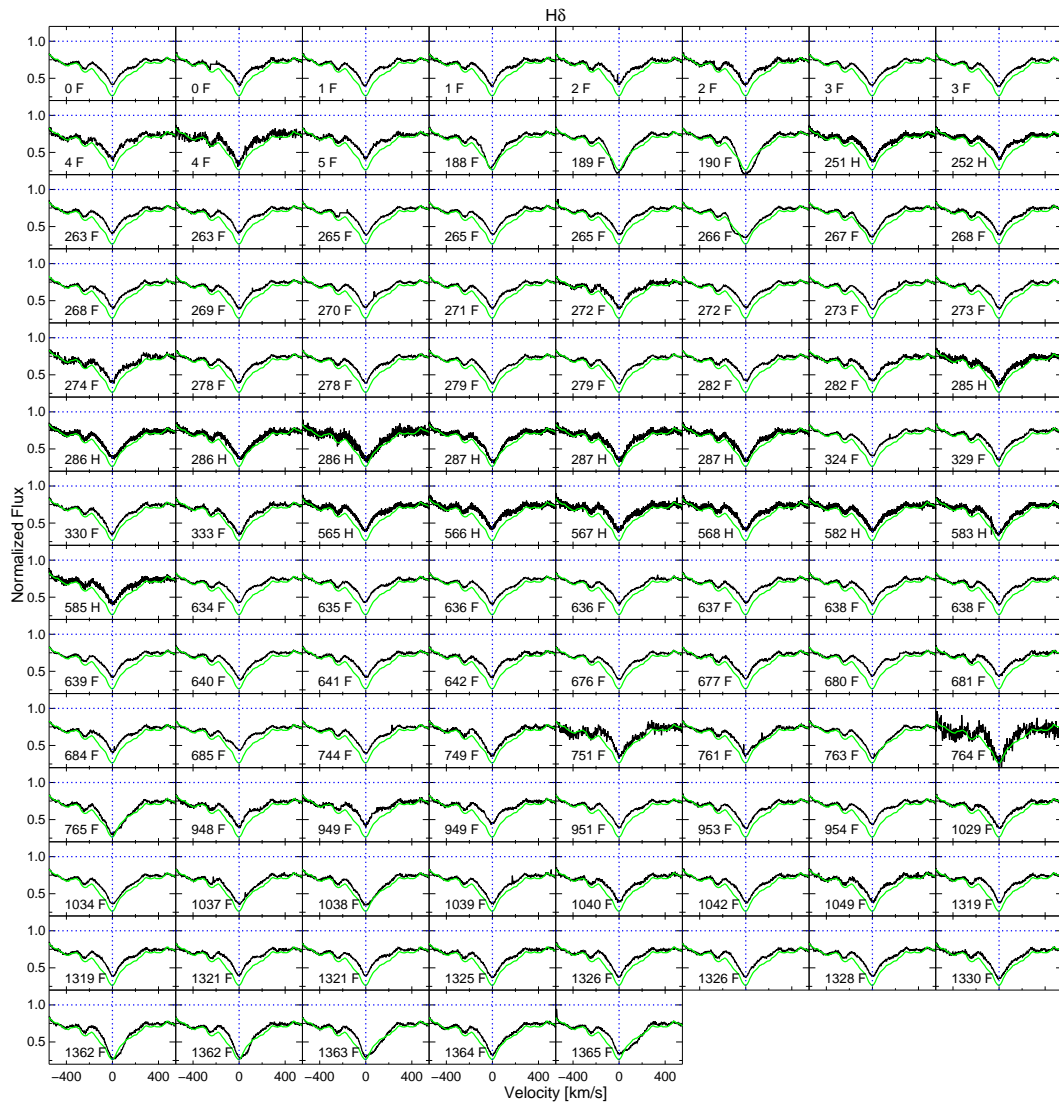
Figure B.6: Same as Fig. B.1 but for H δ .



Figure B.7: Same as Fig. B.1 but for He I.

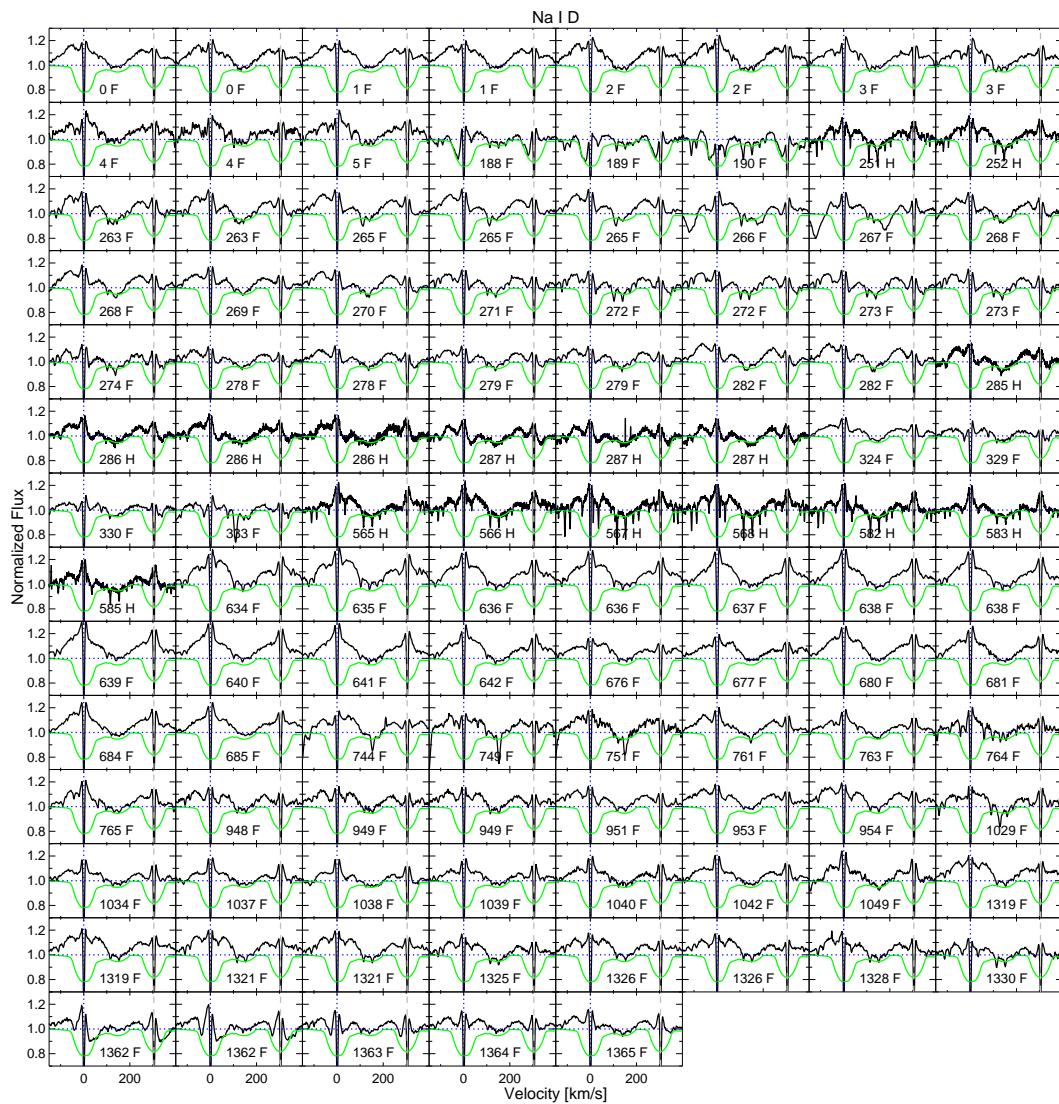


Figure B.8: Same as Fig. B.1 but for the Na I D doublet. The narrow and strong absorption lines are the contribution by the interstellar medium. We arbitrarily choose the line center of Na I D2 to set the zero velocity point.

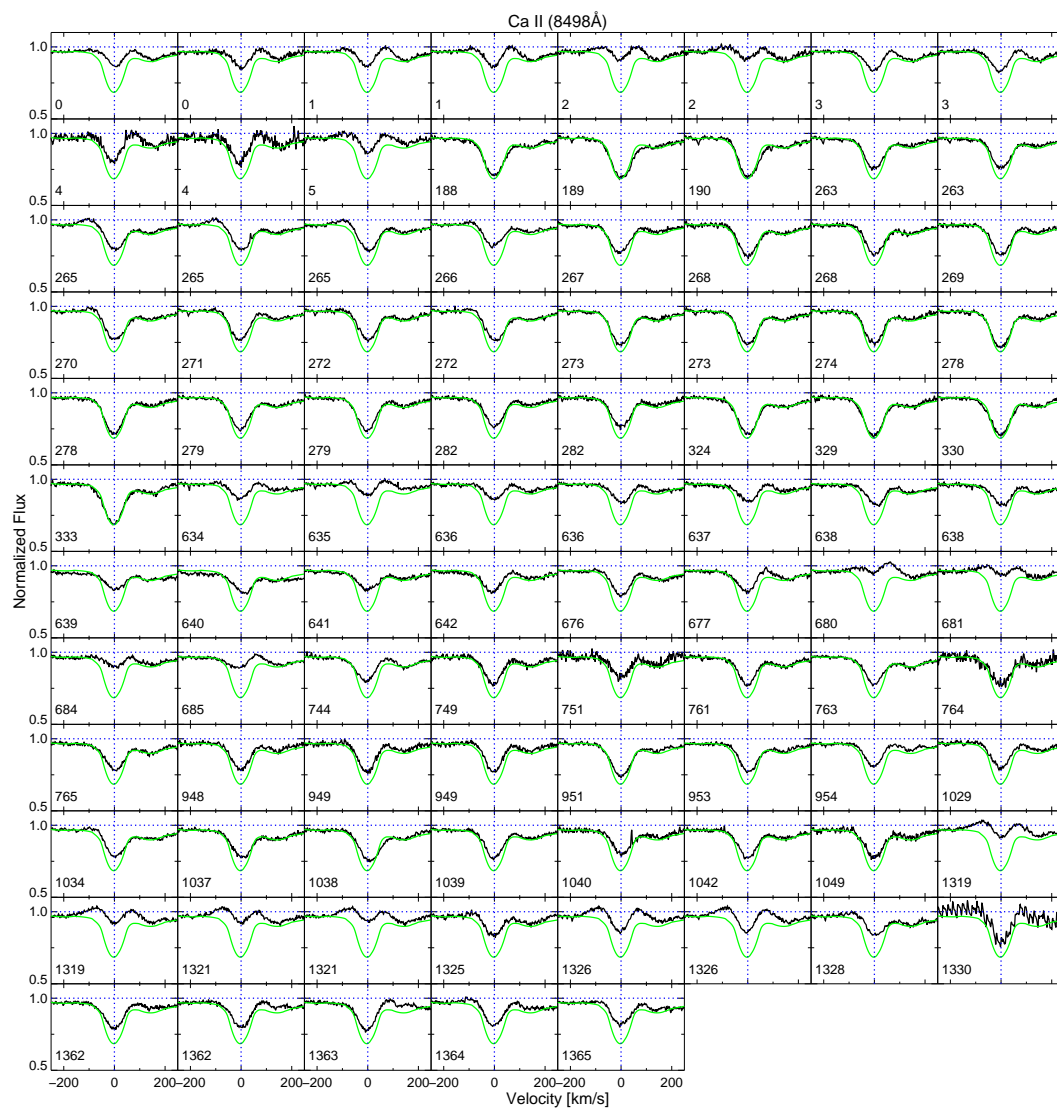


Figure B.9: Same as Fig. B.1 but for Ca II at $\lambda 8498\text{\AA}$. Because the spectral coverage of HARPS ends at 6910\AA , only FEROS data can be shown for this line (93 in total).

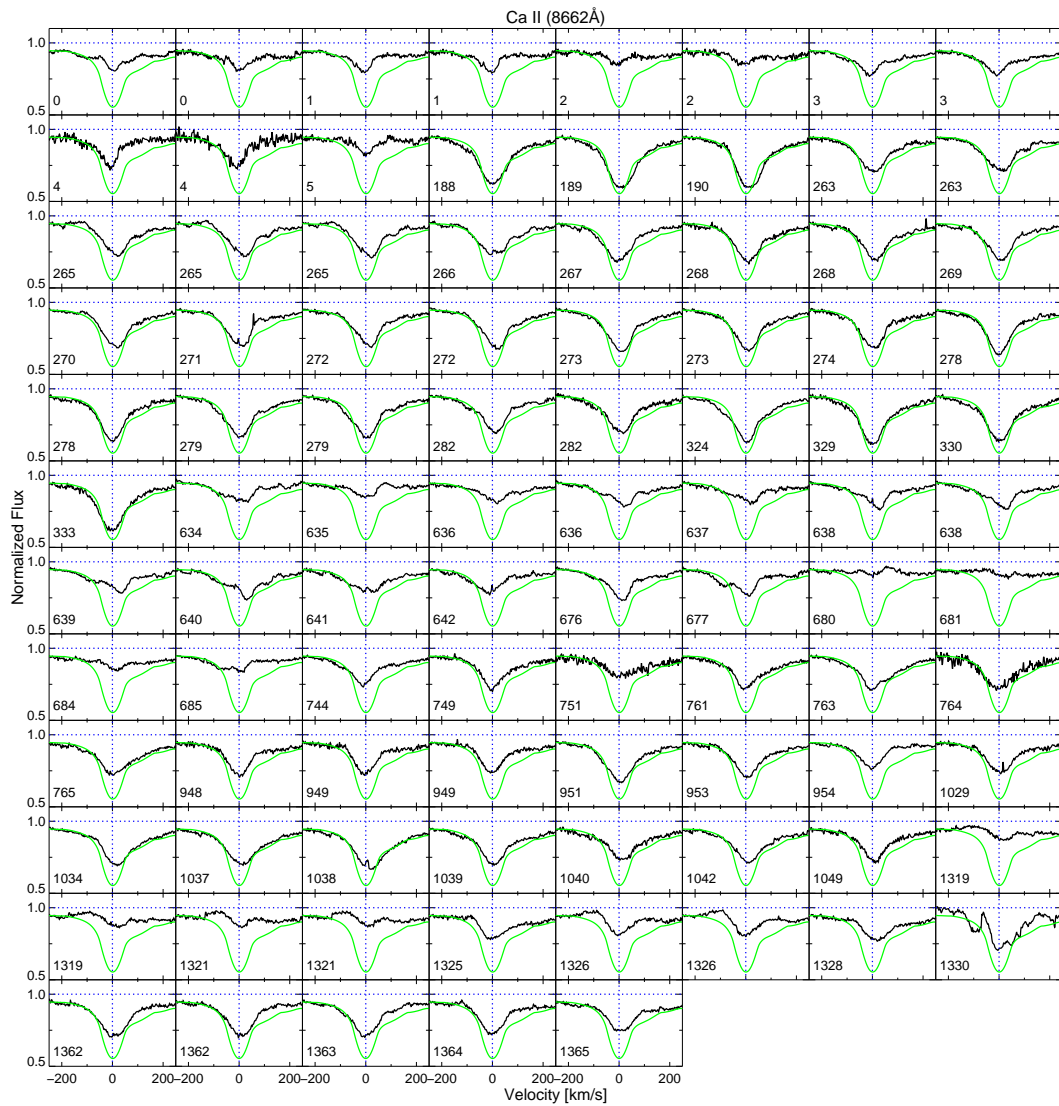


Figure B.10: Same as Fig. B.1 but for Ca II at $\lambda 8662\text{\AA}$. Because the spectral coverage of HARPS ends at 6910\AA , only FEROS data can be shown for this line (93 in total).

Appendix C

HD 142527 - Circumstellar components

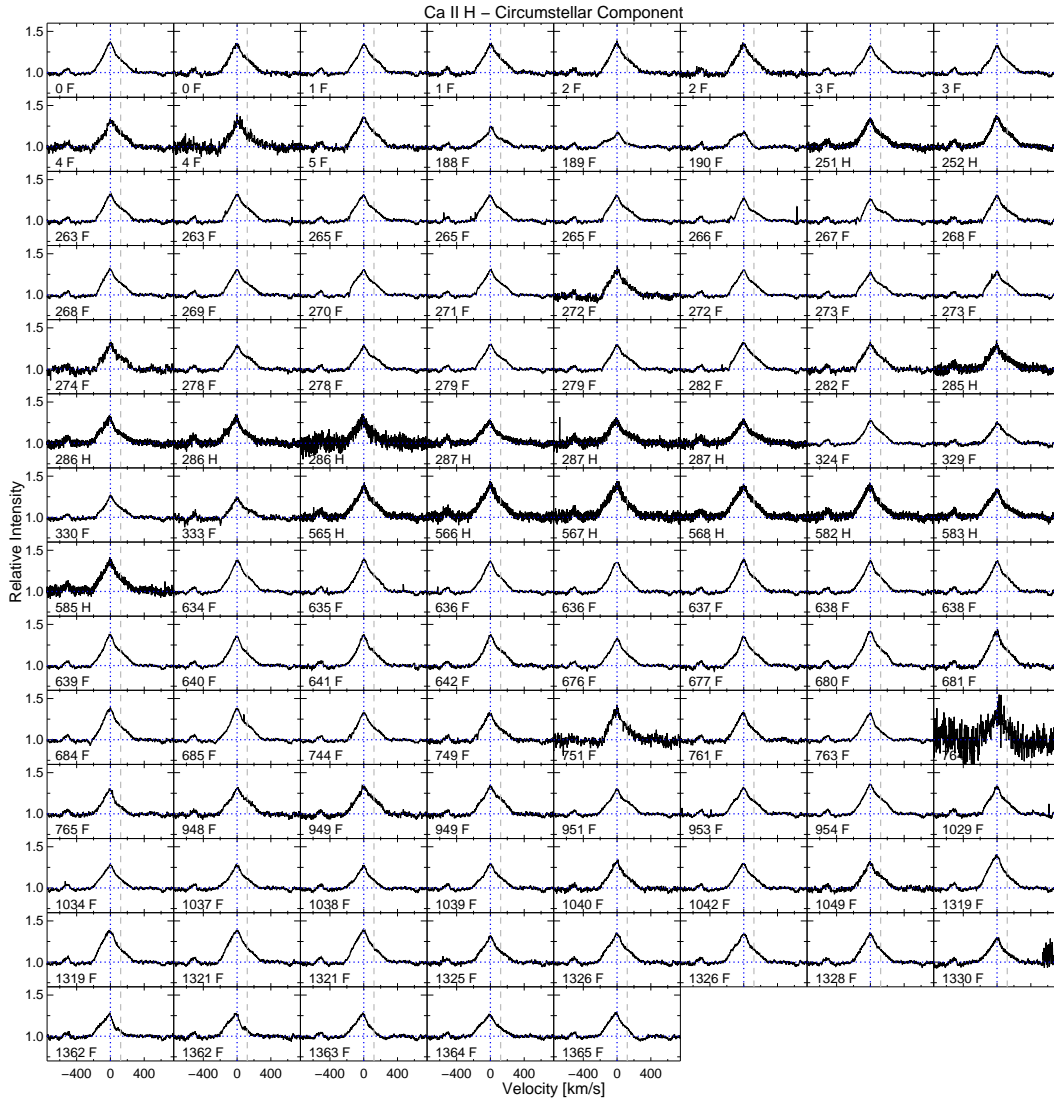


Figure C.1: Circumstellar component profiles for Ca II H plotted over velocity space in chronological order. The position of the line center at zero velocity is marked by the vertical dotted line. The inset numbers indicate the time of observation in days with respect to the first observation. The inset letters F and H indicate if the spectrum was observed with FEROS or HARPS. The vertical dashed line marks the position of He ϵ , which might contaminate the line profile of Ca II H.

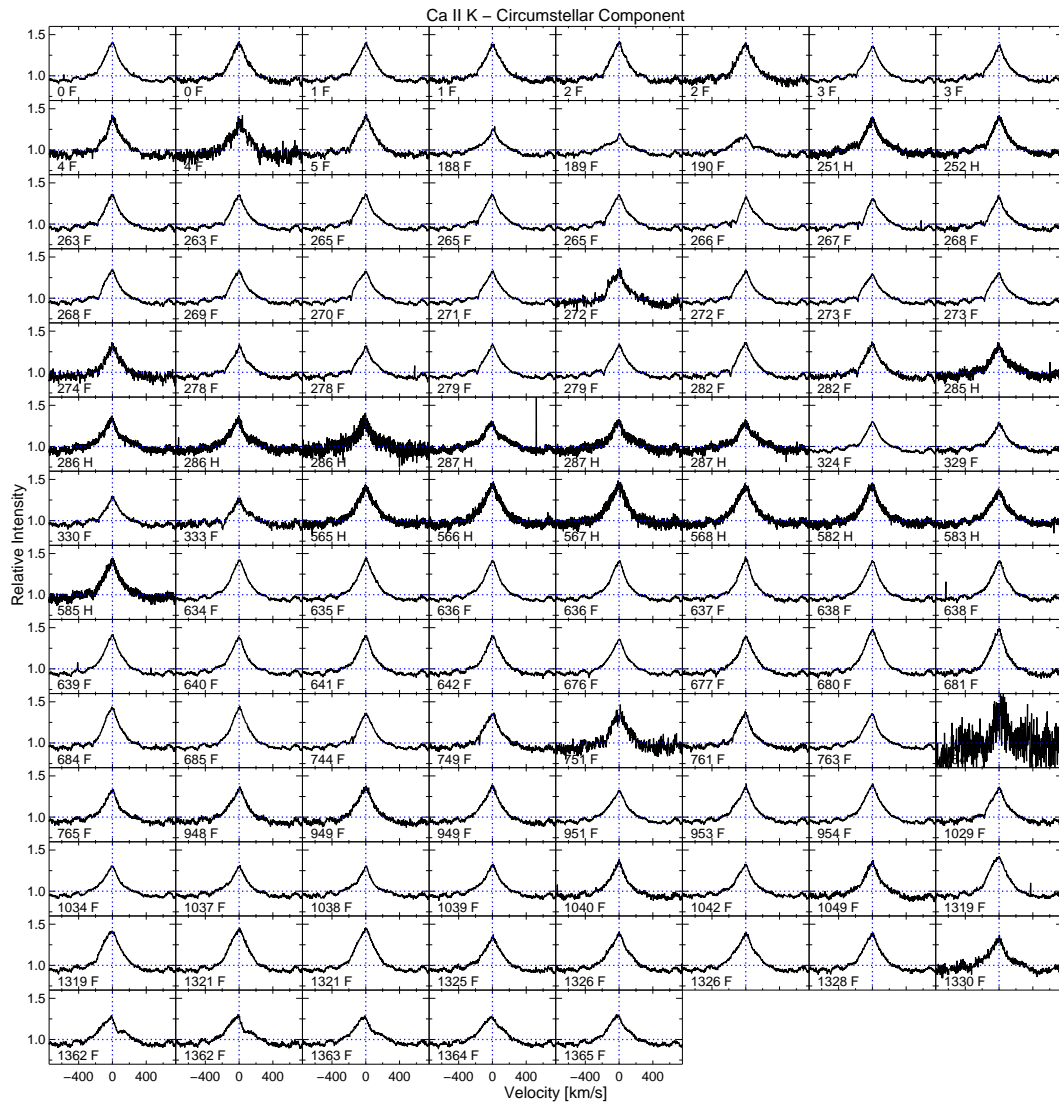
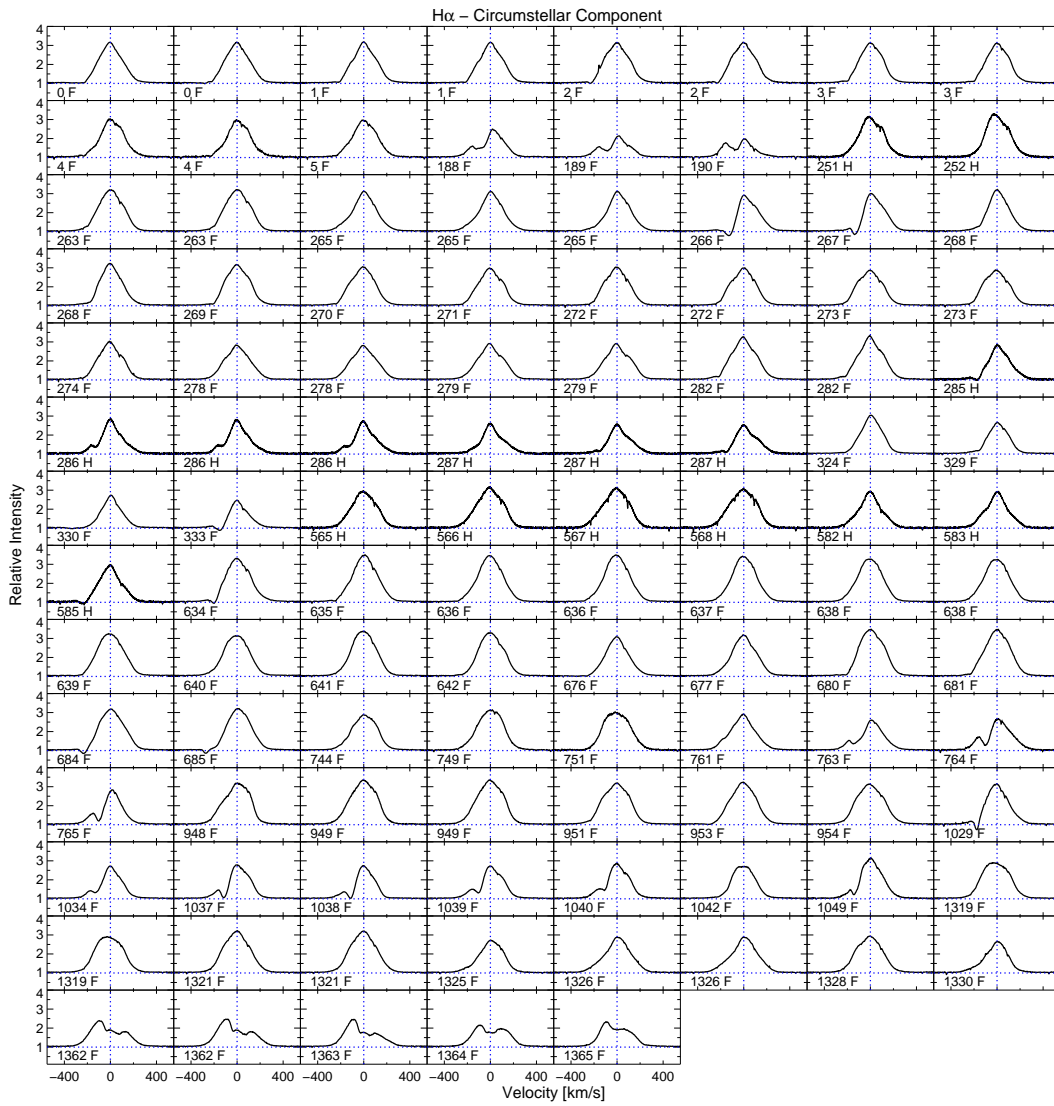
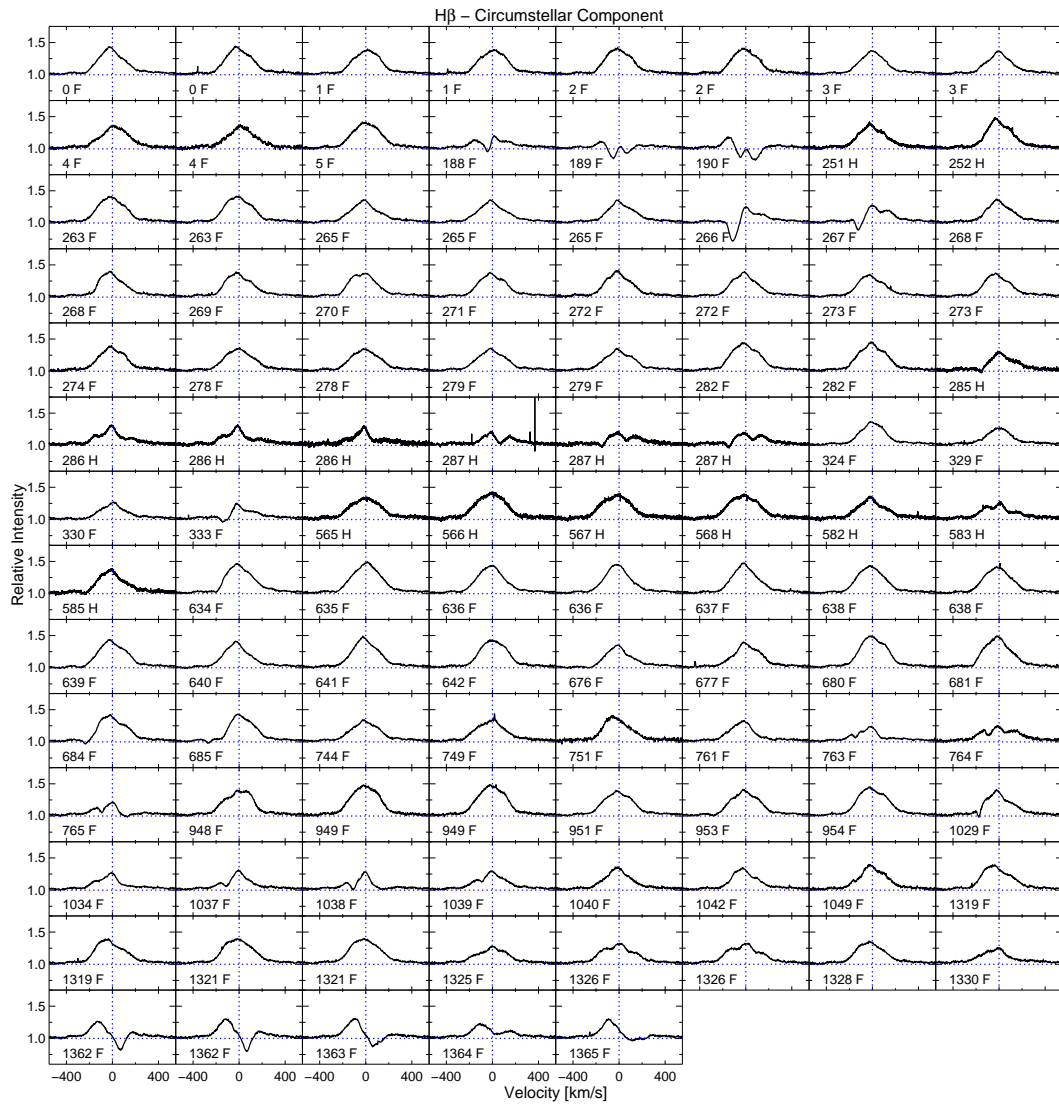
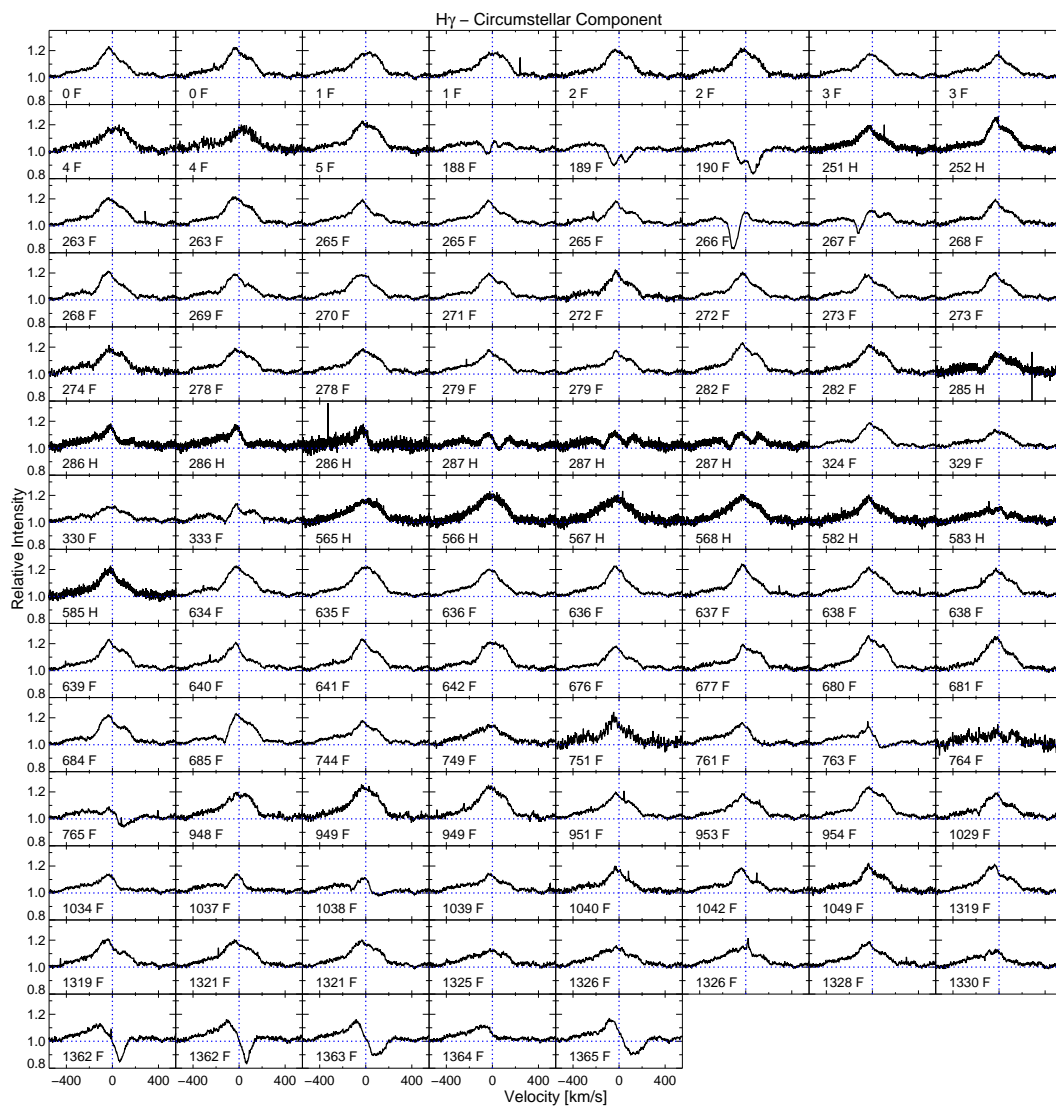
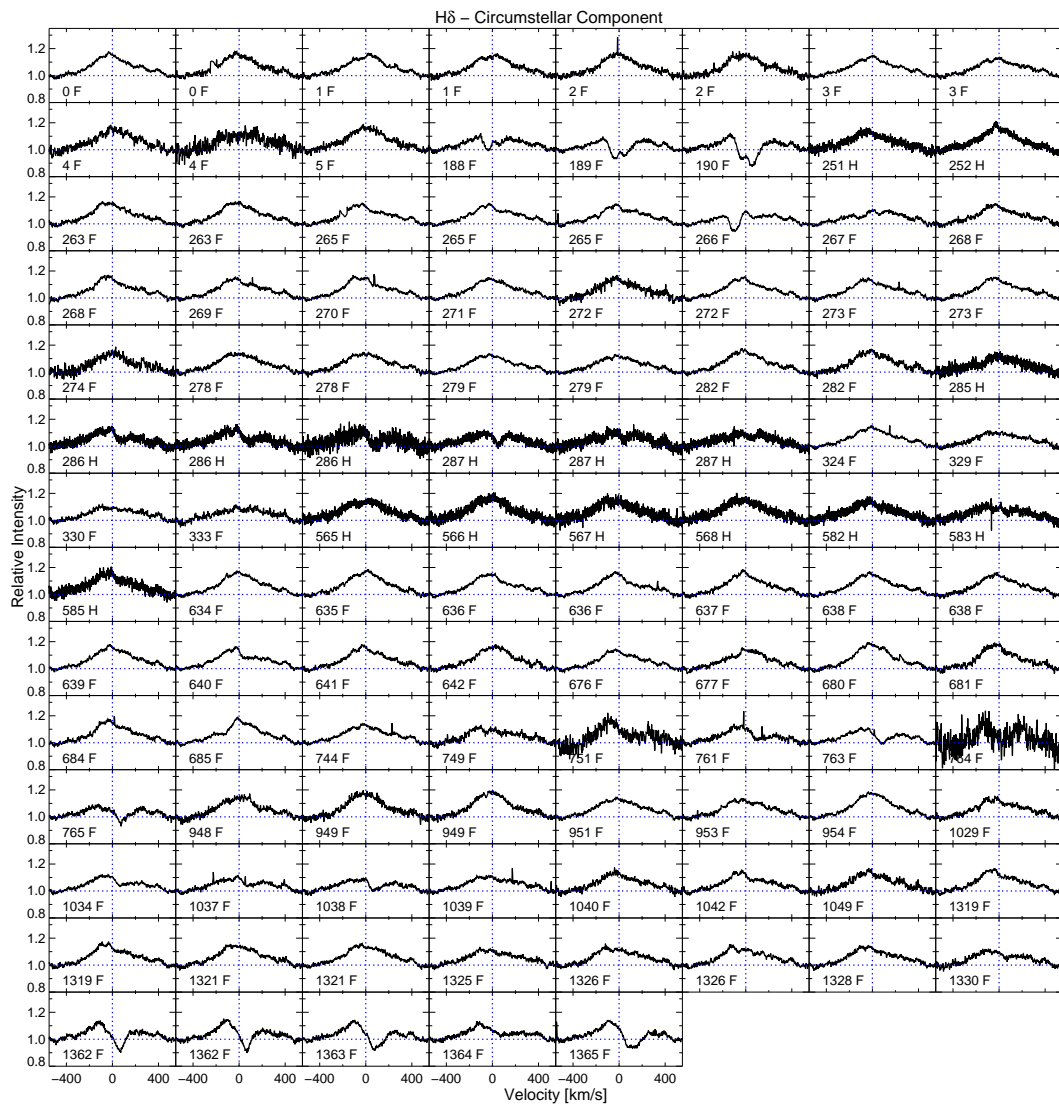


Figure C.2: Same as Fig. C.1 but for Ca II K.

Figure C.3: Same as Fig. C.1 but for H α .

Figure C.4: Same as Fig. C.1 but for H β .

Figure C.5: Same as Fig. C.1 but for H γ .

Figure C.6: Same as Fig. C.1 but for H δ .

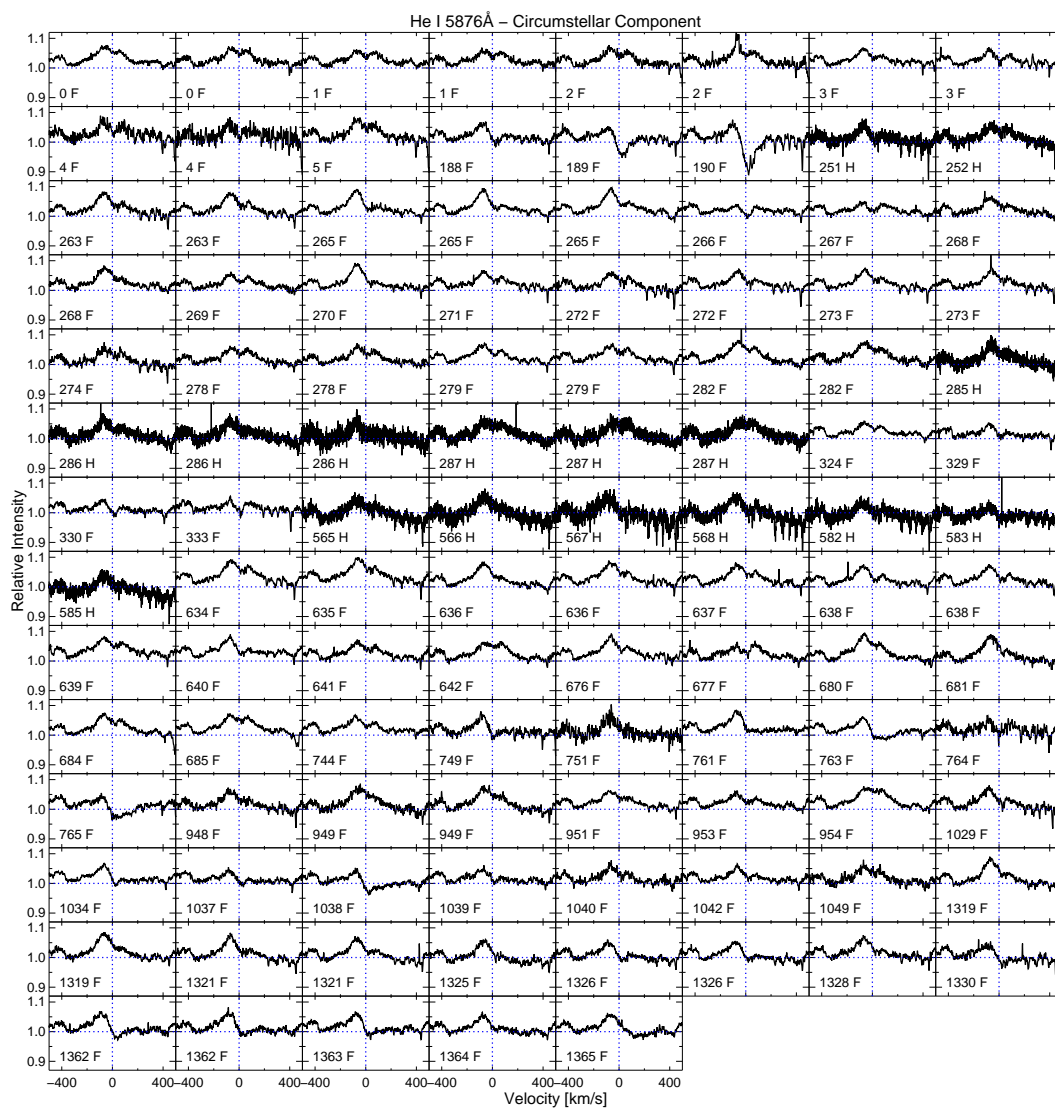


Figure C.7: Same as Fig. C.1 but for He I.

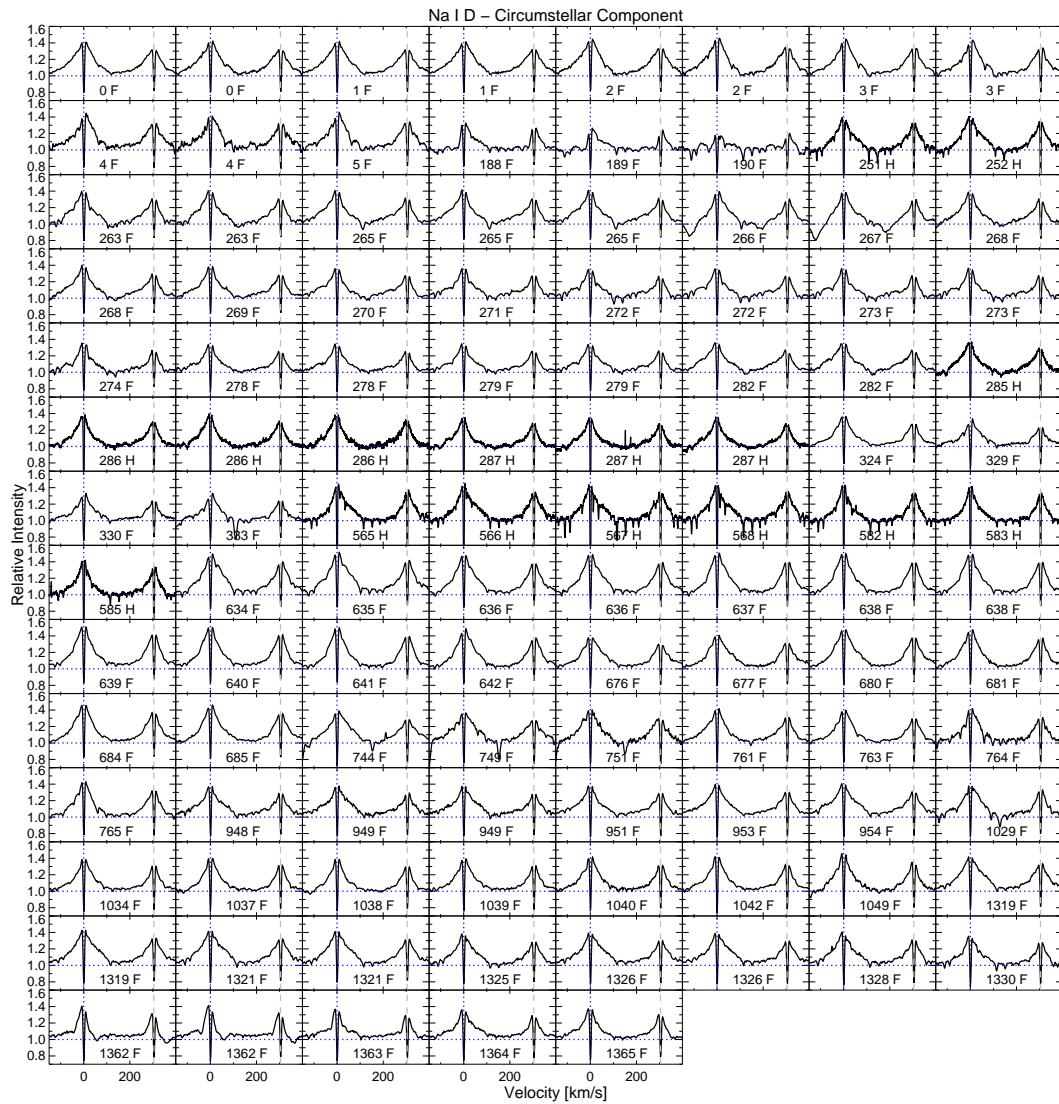


Figure C.8: Same as Fig. C.1 but for the Na I D doublet.



Figure C.9: Same as Fig. C.1 but for Ca II at $\lambda 8498\text{\AA}$.

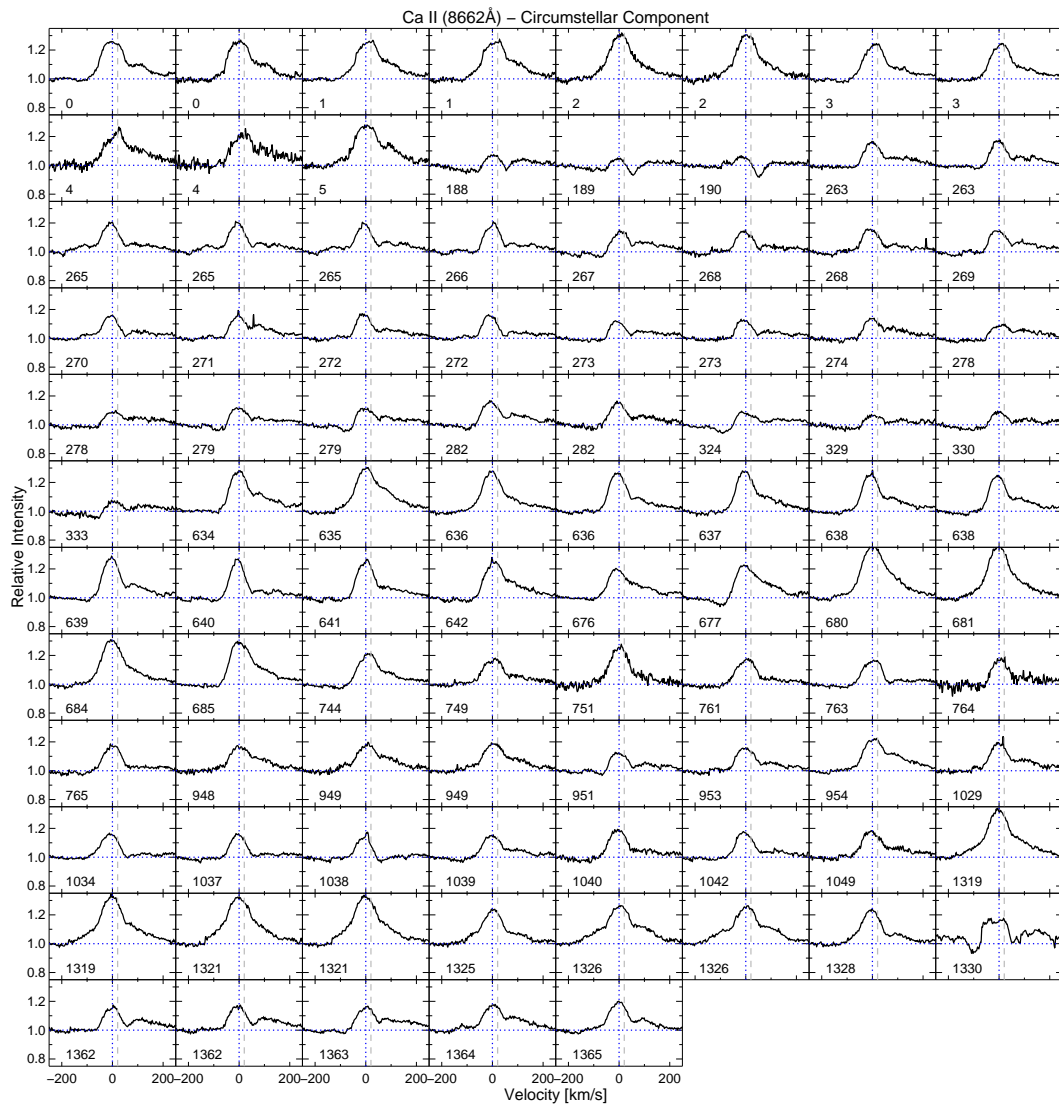


Figure C.10: Same as Fig. C.1 but for Ca II at $\lambda 8662\text{\AA}$.

Appendix D

Simulation of velocity correlation matrices

We conducted simulations for simplified line profile variations and their effect on the velocity correlation matrix as seen in real observations (Sec. 4.5.2). The aim is not to fully describe the physical processes causing the observed profiles variations but to give an idea about the dependencies and occurring correlations over the correlation matrix. For all calculations we consider 100 observations separated by one day and we assume a broad central emission described by a Gaussian, which peaks at 0 km s^{-1} . Each Gaussian is described by three parameters, namely amplitude (P_1), center (P_2), and width (P_3) of the Gaussian:

$$G = P_1 \cdot \exp \left[-0.5 \left(\frac{v - P_2}{P_3} \right)^2 \right], \quad (\text{D.1})$$

where v is the considered velocity range, which is -400 to $+400 \text{ km s}^{-1}$ in our example. The FWHM of the Gaussian is given by $2\sqrt{2\ln 2}P_3$. Gaussian noise is added in all cases. Red and blueshifted absorption components (RAC and BAC in the following) are constructed by adding Gaussians to the main Gaussian peak, which is in emission. The computation of the correlation matrix is as follows: the linear Pearson correlation coefficient r is computed for all combinations of velocity channels (x, y) over the entire line profile. The resulting matrices are symmetric across the main diagonal because of $r(x, y) = r(y, x)$. In addition, if $x = y$ then $r(x, y) = 1$, i.e. each matrix will have a main diagonal with $r = 1$. In the following, we list the different configurations and provide a contour plot of the velocity correlation matrix for each considered case.

Case 1 - Figure D.1

- trivial case
- single peak, P_1 , P_2 , and P_3 are constant over time
- $r = 1$ for $x = y$, red diagonal line, no other correlation present

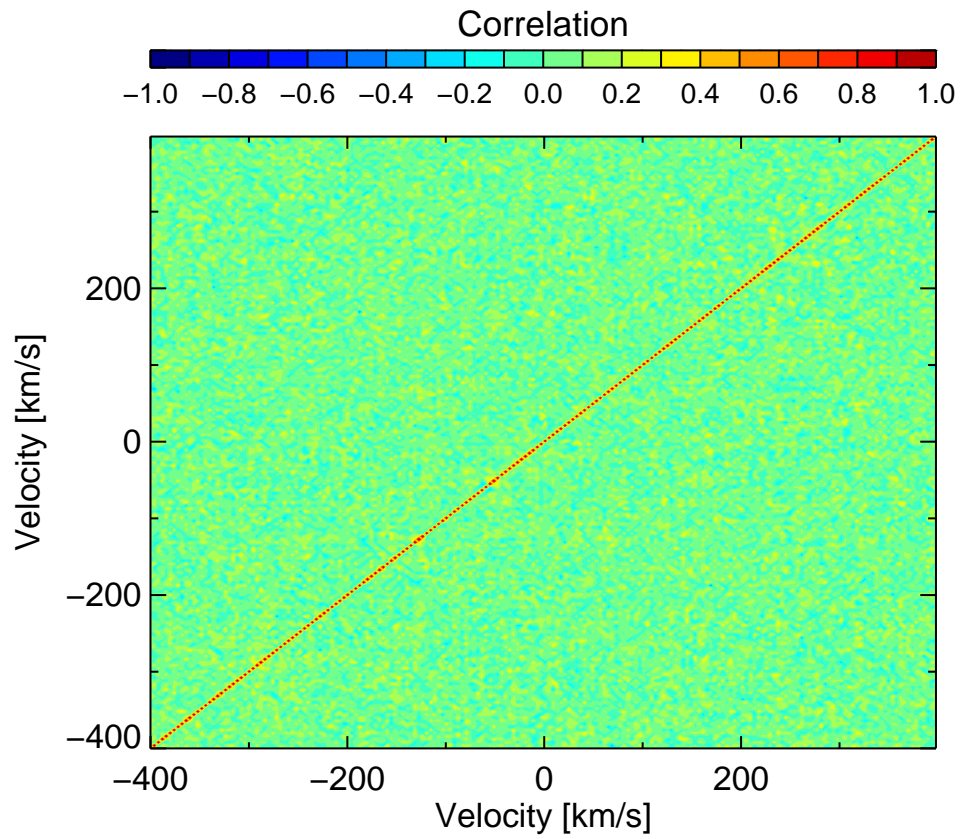


Figure D.1: Case 1.

Case 2 - Figure D.2

- trivial case
- single peak, P_2 , and P_3 are constant over time
- veiling added, i.e. only amplitude of Gaussian changes over time
- veiling effects the entire line profile, which results in a squarish correlation

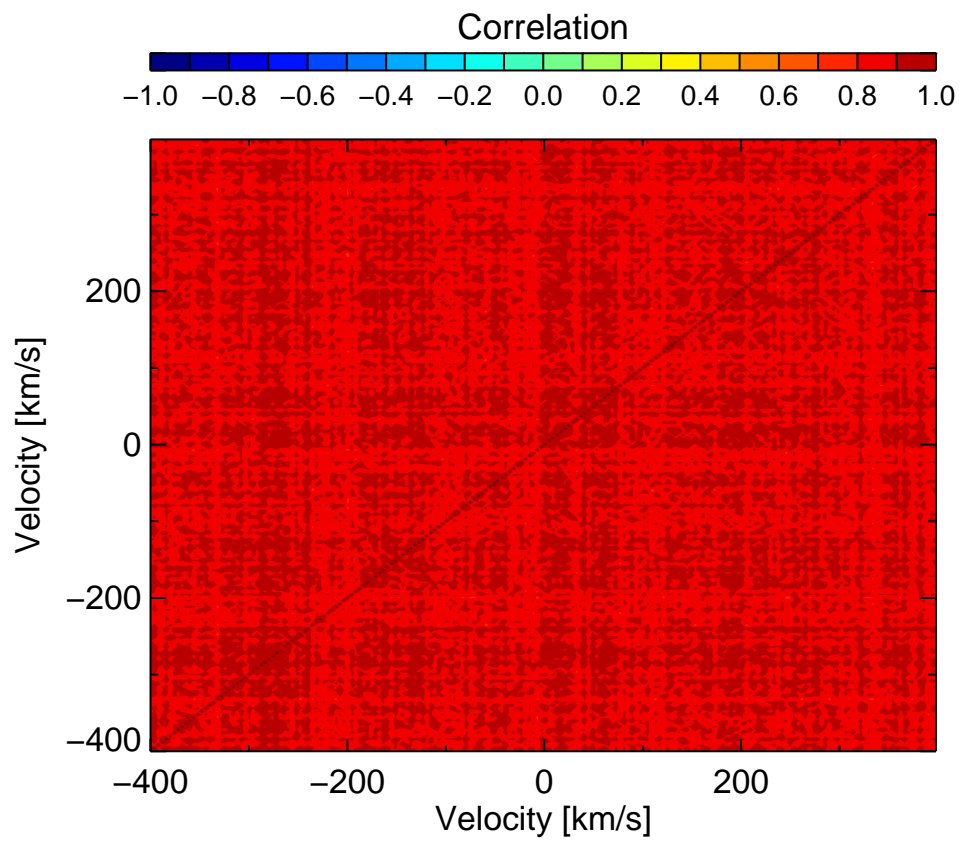


Figure D.2: Case 2.

Case 3 - Figure D.3

- main peak, P_1 , P_2 , and P_3 are constant over time
- subtraction of a broad centered Gaussian with varying amplitude affecting the central part of the main peak
- squarish plateau around $(x, y) = (0, 0) \text{ km s}^{-1}$
- extension of squarish plateau with 235 km s^{-1} corresponds to the range of variability introduced

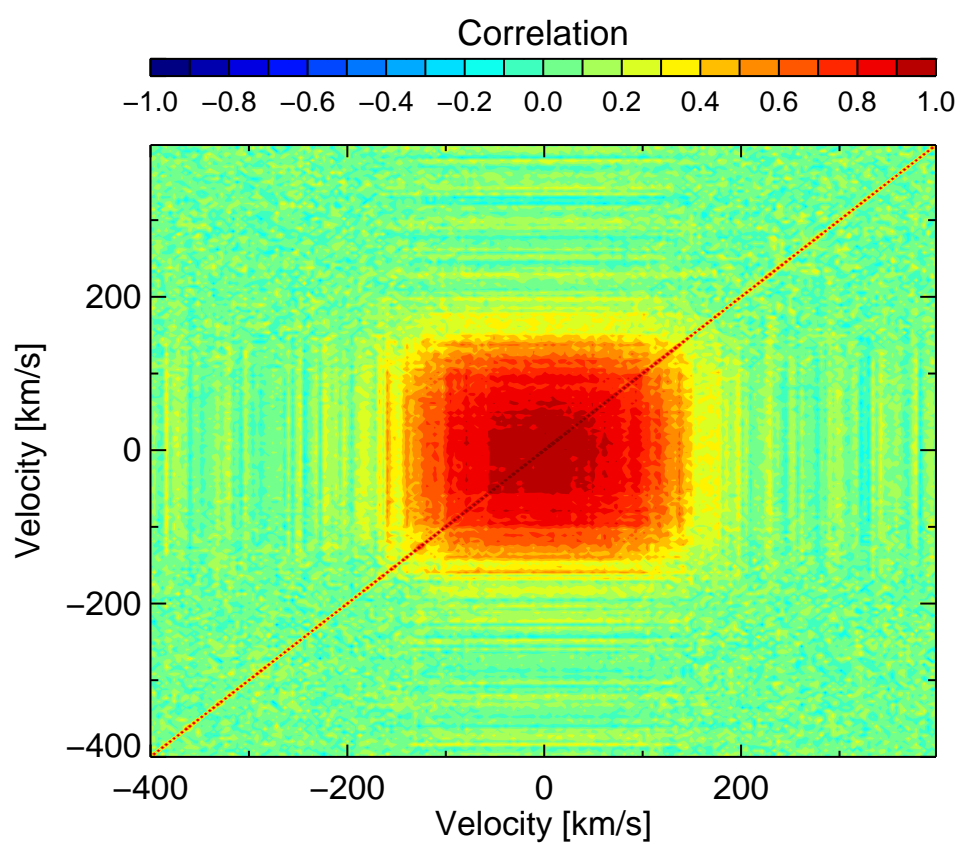


Figure D.3: Case 3.

Case 4 - Figure D.4

- main peak, P_1 , P_2 , and P_3 are constant over time
- BAC with variable P_1 ; P_2 , and P_3 are constant over time
- squarish plateau where BAC is located ($P_2 = -150 \text{ km s}^{-1}$)
- extension of squarish plateau corresponds to FWHM of BAC with 105 km s^{-1}

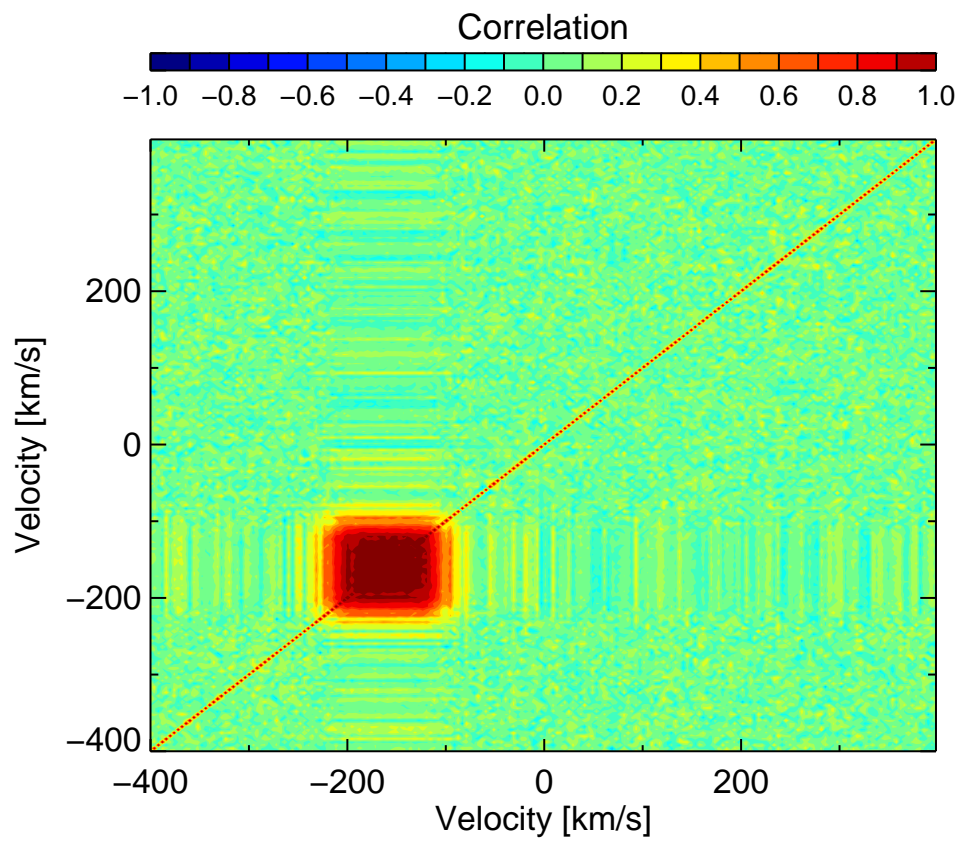


Figure D.4: Case 4.

Case 5 - Figure D.5

- main peak, P_1 , P_2 , and P_3 are constant over time
- BAC and RAC, simultaneous variation of P_1 ; P_2 , and P_3 are constant over time for both
- BAC centered at -150 km s^{-1} , RAC centered at 60 km s^{-1}
- squarish plateaus where BAC and RAC are located along the main diagonal
- additional squarish plateaus at $(x, y) = (-150, 65) \text{ km s}^{-1}$ and at $(x, y) = (65, 150) \text{ km s}^{-1}$ because BAC and RAC vary simultaneously but do not effect each other

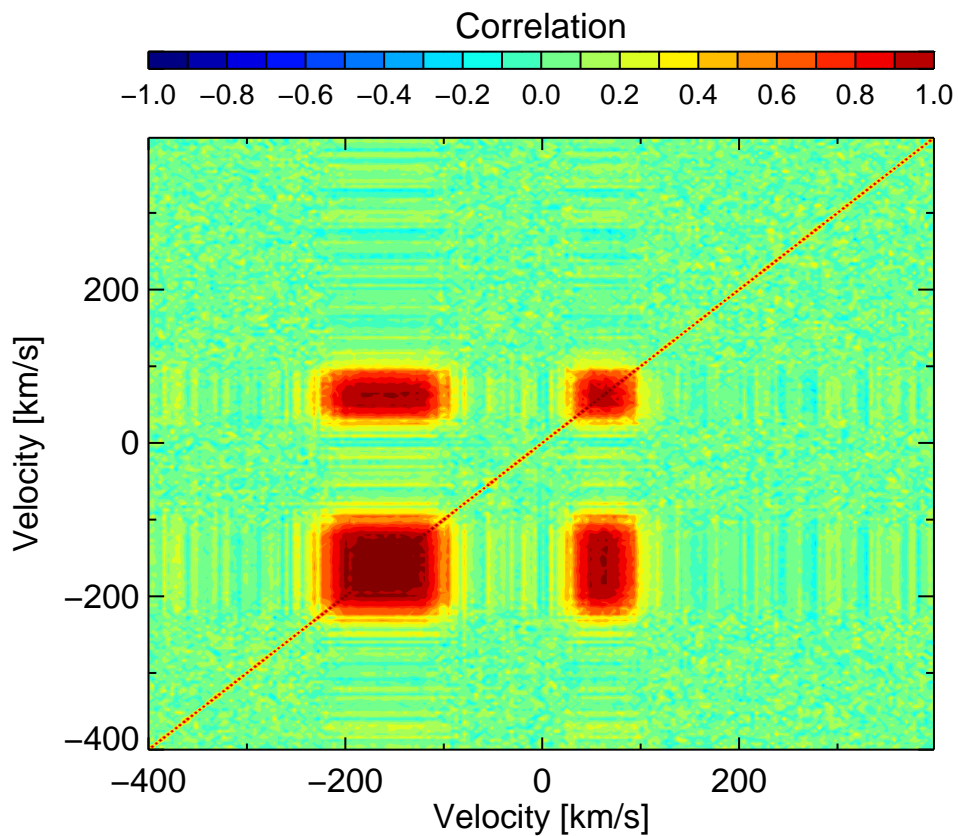


Figure D.5: Case 5.

Case 6 - Figure D.6

- same as case 5 but BAC and RAC are now anticorrelated, i.e. when BAC is growing, RAC vanishes and vice versa
- the squarish plateaus next to the main diagonal are now anticorrelated (blue colored)

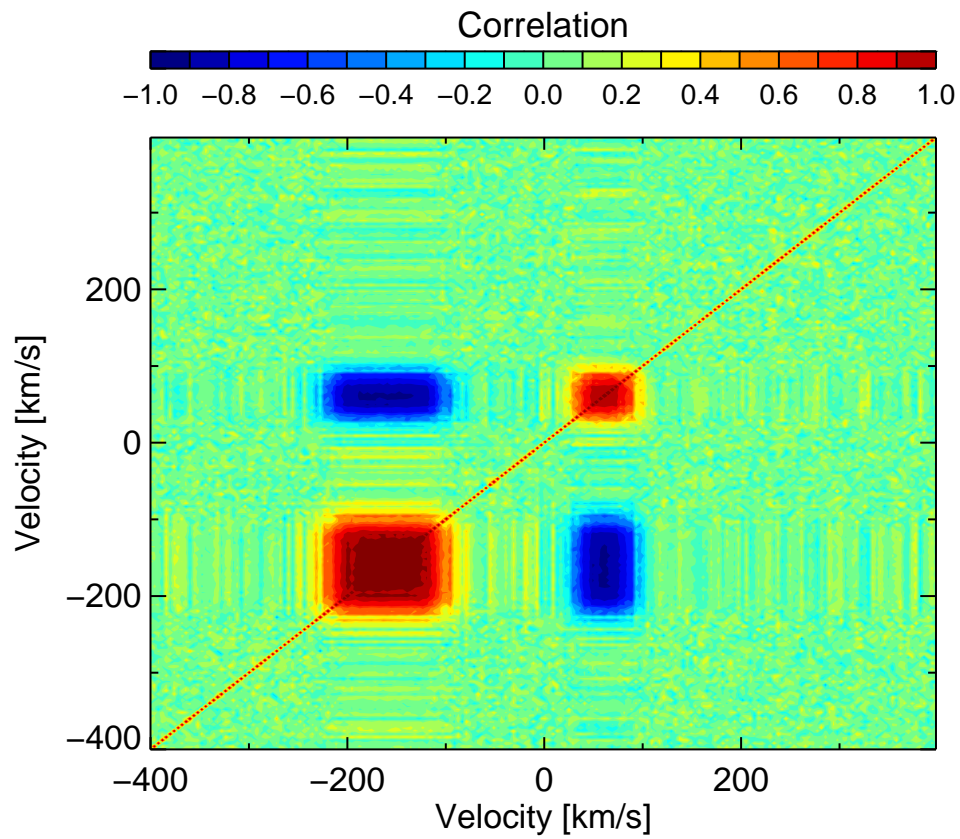


Figure D.6: Case 6.

Case 7 - Figure D.7

- same as case 5 but with additional veiling/variation of the main central Gaussian, i.e. subtraction of a broad Gaussian with periodically changing amplitude, which affects only the central part of the main Gaussian
- in addition to the four distinct plateaus such as in the 5th case, the correlation matrix shows a squarish correlation over a large velocity range, caused by the veiling

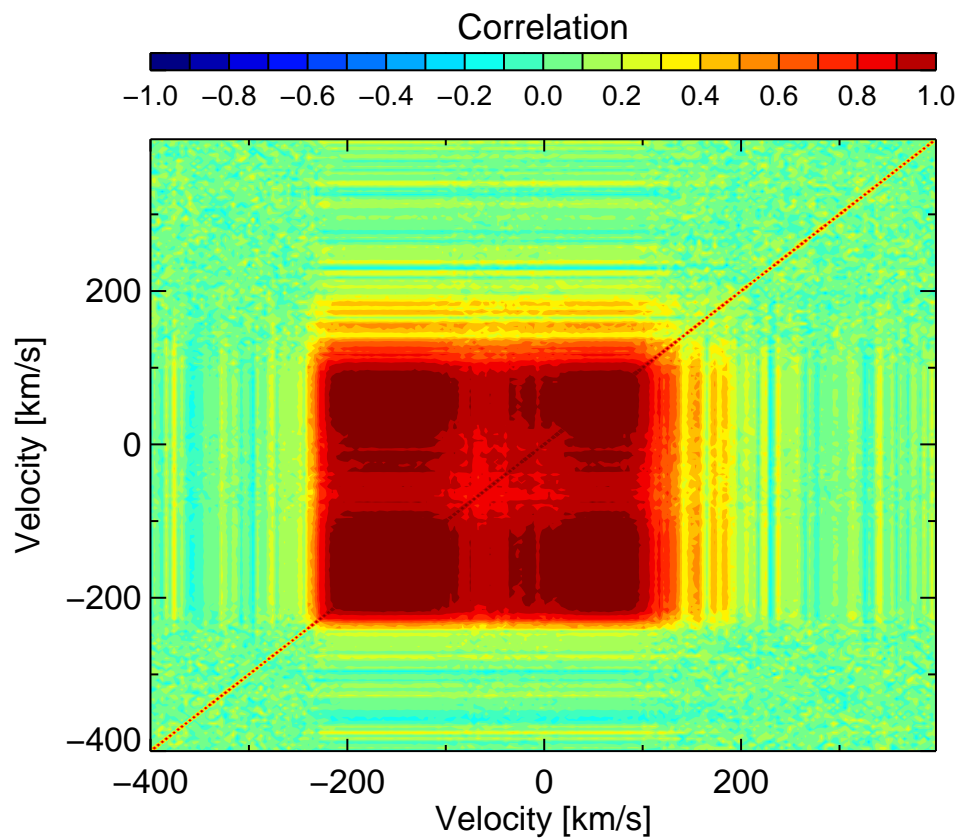


Figure D.7: Case 7.

Case 8 - Figure D.8

- same as case 4 but BAC also changes periodically its position between -200 and -50 km s^{-1}
- the correlation matrix shows an elongated area with positive correlation along the main diagonal
- additional plateaus with negative correlation at $(x, y) = (-200, -50) \text{ km s}^{-1}$ and at $(x, y) = (-50, -200) \text{ km s}^{-1}$ caused by the fact that BAC is moving from -200 to -50 km s^{-1} while its increasing its (negative) amplitude

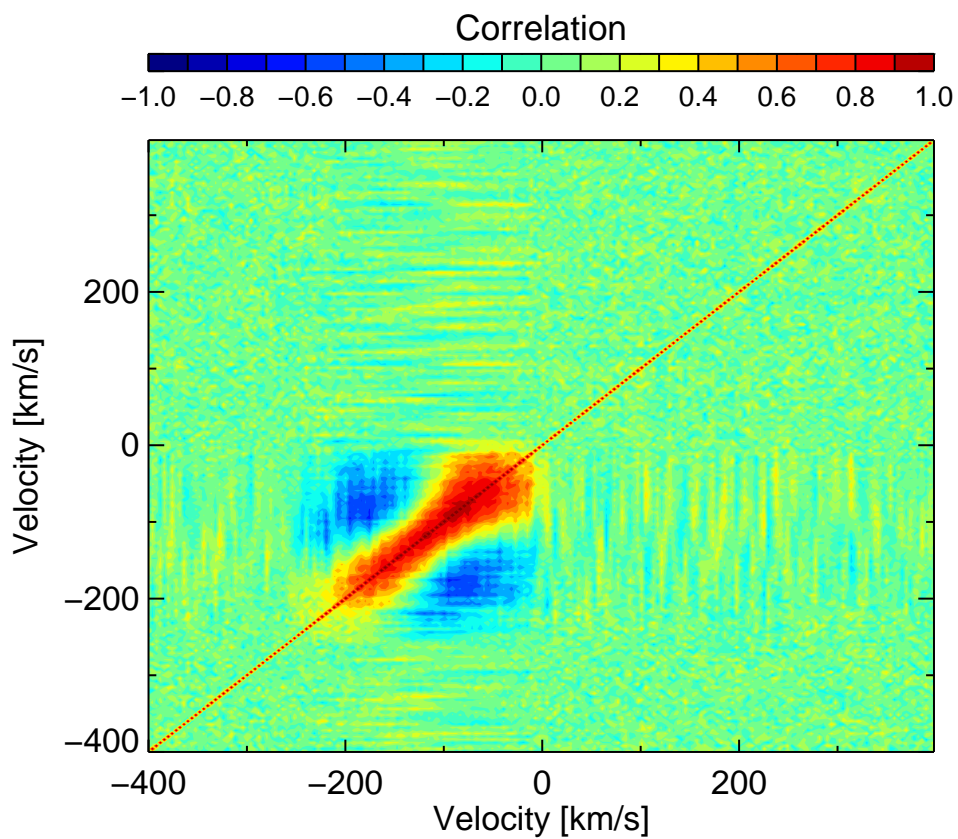


Figure D.8: Case 8.

Case 9 - Figure D.9

- main peak, P_1 , P_2 , and P_3 are constant over time but additional variation of the central part due to subtraction of a broad Gaussian with periodically changing amplitude
- BAC and RAC with constant amplitude but with periodically change of position
- the correlation matrix contains now almost all features from the previous cases
- depending which parameter varies the correlation pattern can appear shifted, more distorted or less significant

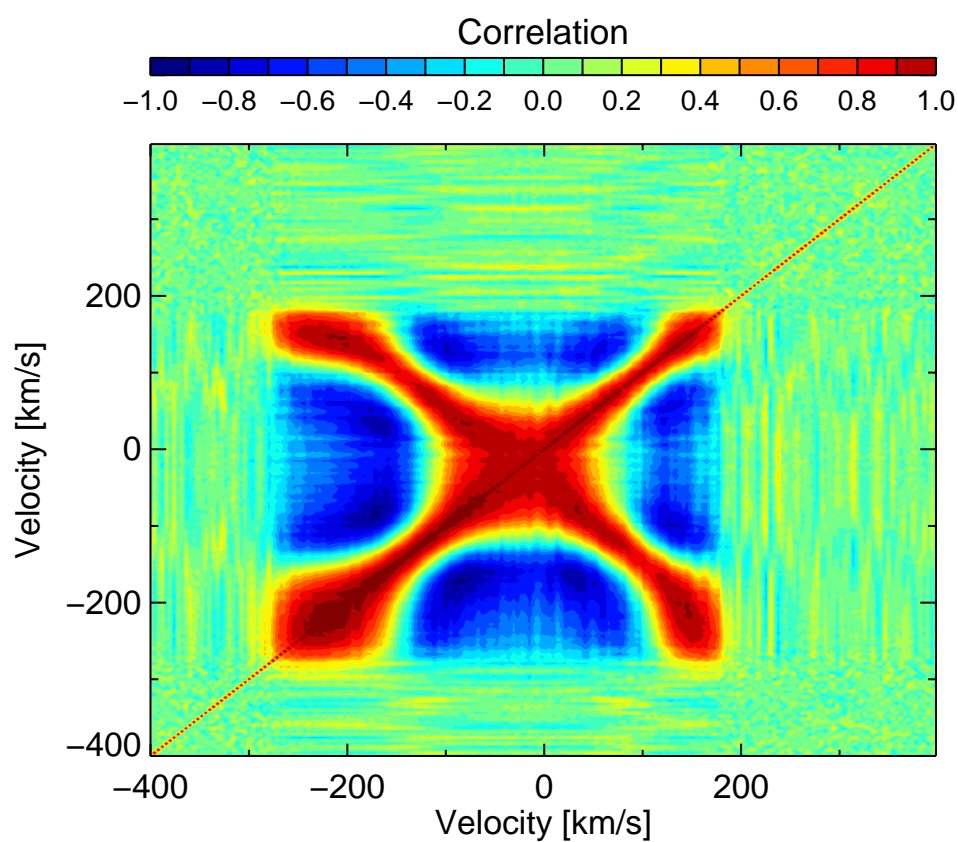


Figure D.9: Case 9.

Acknowledgements

I am very grateful to all the people who helped me to successfully realize this thesis. Their time, effort, and support are greatly appreciated.

In particular, I want to thank following people:

Prof. Dr. Thomas Henning, for giving me the opportunity to conduct this research under his supervision and for supplying me with new impulses when necessary.

Dr. Ralf Launhardt and Dr. Mario van den Ancker for their supervision, advice, and guidance over the years.

Dr. Francoise Delplancke-Ströbele for her supervision and guidance inside the VLTI group. Without her support the MIDI + PRIMA FSU-A mode would not have reached this advanced state.

Dr. Jörg-Uwe Pott and Dr. Sebastien Morel for the valuable discussions and their help bringing forth the MIDI + PRIMA FSU-A mode. In addition, I want to thank Jörg-Uwe Pott for proof-reading parts of my thesis.

Prof. Dr. Andreas Quirrenbach for agreeing to be my co-referee. I want to thank Prof. Dr. Thomas Henning, Prof. Dr. Andreas Quirrenbach, PD. Dr. Hubert Klahr, and Prof. Dr. Mario Trieloff for agreeing to be part of my examination committee.

I am grateful to the whole VLTI team in Garching and Chile who supported me with any interferometric related problem and who always made my stay in Garching and Paranal a great experience.

Finally, I would like to thank everyone at the Max Planck Institute for Astronomy and ESO for making the last four years so enjoyable!